Doctoral Dissertation
博士論文

Towards QCD-based equation of state of dense matter

（高密度物質状態方程式のQCDに基づく構築に向けて）

A Dissertation Submitted for the Degree of Doctor of Philosophy
December 2021

令和3年12月博士（理学）申請

Department of Physics, Graduate School of Science,
The University of Tokyo

東京大学大学院理学系研究科物理学専攻

Yuki Fujimoto

藤本　悠輝

Abstract

The equation of state (EoS) of the strongly-interacting cold and dense matter is a crucial ingredient for studying extreme astrophysical objects and phenomena such as neutron stars, core-collapse supernovae, neutron star binary mergers, etc. It also serves as an essential input for theoretical studies of the finite-density region of quantum chromodynamics (QCD); in this region very little is known up to now. The EoS of dense matter should be derived from QCD, but there are a plethora of technical difficulties which prevent us from QCD-based *ab initio* calculations. Nevertheless, the QCD-based calculation is still possible at high densities where the perturbative expansion in the strong coupling constant makes sense. In the conventional perturbative QCD (pQCD) calculations, however, the results are known to be plagued by a large uncertainty originating from the ambiguity in the choice of the renormalization scale. This scale variation uncertainty becomes larger as the density decreases, so that we cannot utilize the pQCD calculation at the realistic density realized inside neutron stars. The major driving force of this thesis is to lessen this scale variation uncertainty in the pQCD calculation.

To this end, we discuss the Hard Dense Loop (HDL) resummation at finite quark mass. In the preceding works, Hard Thermal Loop (which is the high-temperature counterpart of the HDL) resummation is recognized to improve the convergence of the perturbative expansion. We employ the HDL perturbation theory, which is one of the perturbative schemes to resum HDLs, and evaluate the EoS of dense QCD matter using this theory with a hope to alleviate the scale variation uncertainty. The finite bare quark mass is important for the quantitative construction of the EoS in realistic stellar environments, where the β equilibrium and electric charge neutrality conditions are maintained.

The resummation in the quark sector has the effect of lowering the baryon number density, and the EoS turns out to have much smaller uncertainty than the existing pQCD estimate. As a result, we can plot our numerical results on top of the existing constraints on the EoS from neutron star observations; our results favor smooth matching between the EoS from the resummed QCD calculation at high density and the extrapolated EoS from the nuclear matter density region. We discuss in some detail why the scale variation uncertainty is reduced, and write down the explicit condition for the reduction of the uncertainty. We also point out that the speed of sound in our EoS slightly exceeds the conformal limit; as the speed of sound is a measure for the stiffness of the EoS, surpassing the conformal limit brings about the qualitative difference in the behavior of the EoS.

Acknowledgment

I would like to acknowledge all the people who supported me during my graduate research.

First and foremost, I would like to dedicate my heartfelt gratitude to my supervisor Prof. Kenji Fukushima for leading me into this engrossing field of research, constant discussions on a broad range of topics (which proves that he is a versatile physicist), hands-on advice on how to write a paper, as well as for his continuous support and encouraging comments with which I could survive the whole period of my graduate studies even amidst the pandemic situation. I am grateful to my senior collaborator and friend Dr. Koichi Murase for our long-standing discussions on the DENSE collaboration, consultation about coding, heavy-ion physics, and many other things, and casual conversations. My deepest gratitude also goes to Prof. Muneto Nitta for discussions and very fruitful collaboration, which started from a single question in the seminar I gave at Keio University. I would also like to thank Prof. Yoshimasa Hidaka, Dr. Atsuki Hiraguchi, Prof. Kei Iida, and Prof. Wolfram Weise for the fruitful collaborations.

I would like to acknowledge my fellow colleagues in the nuclear theory group at The University of Tokyo for conversations and discussions, especially Dr. Yuya Abe, Shi Chen, Dr. Hideaki Iida, Zebin Qiu, and Takuya Shimazaki, for holding a seminar for reading the classical papers together; I have learned a lot from/with them.

I would like to express my gratitude to the dissertation defense committee, Prof. Takumi Doi, Prof. Aya Bamba, Prof. Kipp Cannon, Prof. Haozhao Liang, and Prof. Takashi Oka for a careful reading and very useful suggestions.

Throughout my graduate study, I have greatly benefited from Loïc Fernandez, Dr. Tyler Gorda, Daisuke Hagihara, Dr. Koichi Hattori, Prof. Tetsuo Hatsuda, Prof. Kenta Hotokezaka, Prof. Toru Kojo, Prof. Koutarou Kyutoku, Kentaro Nishimura, Prof. Akira Ohnishi, Prof. Shi Pu, Prof. Sanjay Reddy, Prof. Hiroyoshi Sakurai, Dr. Noriyuki Sogabe, Dr. Hiroyuki Tajima, Dr. Lingxiao Wang, Prof. Naoki Yamamoto, Prof. Di-Lun Yang, and Dr. Shigehiro Yasui for comments, conversations, and discussions.

I appreciate the support from the physics academic affairs office at The University of Tokyo.

Last but not least, I am indebted to my beloved family for their perpetual support.

The author is financially supported by Advanced Leading Graduate Course for Photon Science (ALPS) at The University of Tokyo and Japan Society for the Promotion of Science (JSPS) KAKENHI Grant No. 20J10506.

Contents

Abbreviations and symbols

2PI	Two-particle irreducible
2SC	Two-flavor superconductor
APR EoS	Akmal–Pandharipande–Ravenhall EoS
CFL	Color-flavor locking
CJT formalism	Cornwall–Jackiw–Tomboulis formalism
DL	Deep learning
EFT	Effective field theory
EoS	Equation of state
HIC	Heavy-ion collision
HTL / HDL	Hard thermal loop / Hard dense loop
HTLpt / HDLpt	HTL perturbation theory / HDL perturbation theory
Ld	Landau damping
LO	Leading order
NLO	Next-to-leading order
NNLO	Next-to-next-to-leading order
N^{n}LO	(Next-to-)^n leading order
PNM	Pure neutron matter
pQCD	Perturbative quantum chromodynamics
QCD	Quantum chromodynamics
QHC	Quark-hadron continuity
qp	Quasi-particles
se	Self-energy
SLy4 EoS	Skyrme Lyon 4 EoS
SNM	Symmetric nuclear matter
TOV equation	Tolman–Oppenheimer–Volkoff equation
χEFT	Chiral effective field theory

A	Nucleon number
c_s^2	Speed of sound squared
$D_{\mu\nu}$	Gluon propagator
$f_{\rm B}$	Bose-Einstein distribution, $f_{\rm B}(\omega) = 1/(e^{\omega/T} - 1)$
$f_{\rm F}$	Fermi-Dirac distribution, $f_{\rm F}(\omega) = 1/(e^{\omega/T} + 1)$
g	Strong coupling constant
L	Slope of the symmetry energy
m_f	Bare mass of flavor-f quark
$M_{\rm D}$	Debye mass
$M_{{\rm q}f}$	flavor-f quark screening mass
$M_\odot$	Solar mass, $M_\odot \simeq 1.99 \times 10^{30}\,{\rm kg}$
M–R	Mass-radius relationship of neutron stars
n	Quark number density
$n_{\rm B/Q}$	Baryon number / Charge density
n_0	Normal nuclear density, $n_0 \simeq 0.16\,{\rm fm}^{-3}$
N	Neutron number
$N_{\rm c/f}$	Number of colors / flavors
$O(\cdot)$	Order of $\cdot$
P	Pressure
$P_{\rm ideal}$	Pressure of the ideal quark gas, $P_{\rm ideal} = N_{\rm c} N_{\rm f} \mu^4/(12\pi^2)$
S_2 / S_v	Symmetry energy / Symmetry energy at $n_{\rm B} = n_0$, i.e., $S_v = S_2(n_0)$
S_f	Flavor-f quark propagator
T	Temperature
Z	Partition function / Proton number
α_s	Strong coupling constant, $\alpha_s = g^2/(4\pi)$
β	Inverse temperature, $\beta = 1/T$
δ	Isospin asymmetry parameter
ε	Energy density
Λ	Tidal deformability
$\bar{\Lambda}$	Renormalization scale
$\Lambda_{\overline{\rm MS}}$	$\overline{\rm MS}$ scale (throughout this work it is chosen as $\Lambda_{\overline{\rm MS}} = 378\,{\rm MeV}$)
$\Lambda_{\rm QCD}$	QCD scale
μ	Quark chemical potential
$\mu_{f/{\rm B/I/Q/S}/\ell}$	Flavor-f quark / baryon / isospin / charge / strangeness / lepton chemical potential
$\Pi_{\mu\nu}$	Gluon self-energy
ρ	Mass density
ρ_0	Normal nuclear mass density, $\rho_0 \simeq 2.7 \times 10^{17}\,{\rm kg/m}^3$
Σ_f	Self-energy of flavor-f quark
χ / $\chi_{\rm B}$	Quark / Baryon number susceptibility
$\hat{\ }$	Hard thermal loop quantity, e.g., $\hat{M}_{\rm D}$ is the Debye mass within the HTL approximation

Chapter 1

Introduction

In this work, we concern in specific the equation of state (EoS) of the strongly-interacting dense matter, which is the relation between thermodynamic properties such as the pressure P, the temperature T, the baryon chemical potential μ_{B}, the mass density ρ, the energy density ε, etc. We perform the *ab initio* calculation of the EoS [1] within the perturbative framework of Quantum Chromodynamics (QCD) [2–6] taking into account what is called the Hard Thermal Loop resummation [7].

Our primary concern seems to be rather technical and in a limiting situation, but in fact, it can influence a wide spectrum of research, and it will ultimately help us understand ourselves better. For example, the concept of mass is closely related to the phase transition in QCD; most of the visible universe is endowed with mass by the chiral symmetry breaking [8, 9]. Also, the recent multimessenger observation tells us that most of the rare metals around us including gold and platinum are coming from mergers of neutron star binaries, which are stars with the highest baryon density in the universe [10–12]. Interestingly enough, neutron stars are gold mines both in the literal and figurative sense.

1.1 Motivation and outstanding issues

Unraveling the properties and the phase structure (see Fig. 1.1 for the conjectured phase diagram) of dense matter subject to the strong interaction is a vital challenge in theoretical nuclear physics. To accomplish this goal, QCD—the first-principles theory of the strong interaction—should be the guiding principle. QCD has its own intrinsic scale $\Lambda_{\mathrm{QCD}} \sim 200\,\mathrm{MeV}$ that is adjusted, for instance, by the experiment (see the following subsection for details). The strong interaction becomes relevant when a matter is significantly compressed or heated up to the mass density or the temperature as high as Λ_{QCD}, namely, $\rho \sim \Lambda_{\mathrm{QCD}}^4$ or $T \sim \Lambda_{\mathrm{QCD}}$ in natural units. They are equivalent to $\rho \sim 10^{17}\,\mathrm{kg/m^3}$ or $T \sim 10^{12}\,\mathrm{K}$ in the ordinary SI units.

At such a high density or temperature, quarks and gluons, which are the elementary degrees of freedom of the strong interaction and are usually confined inside hadrons, can be liberated. In fact, from the inception of QCD, Collins and Perry have pointed out that the asymptotically-free nature

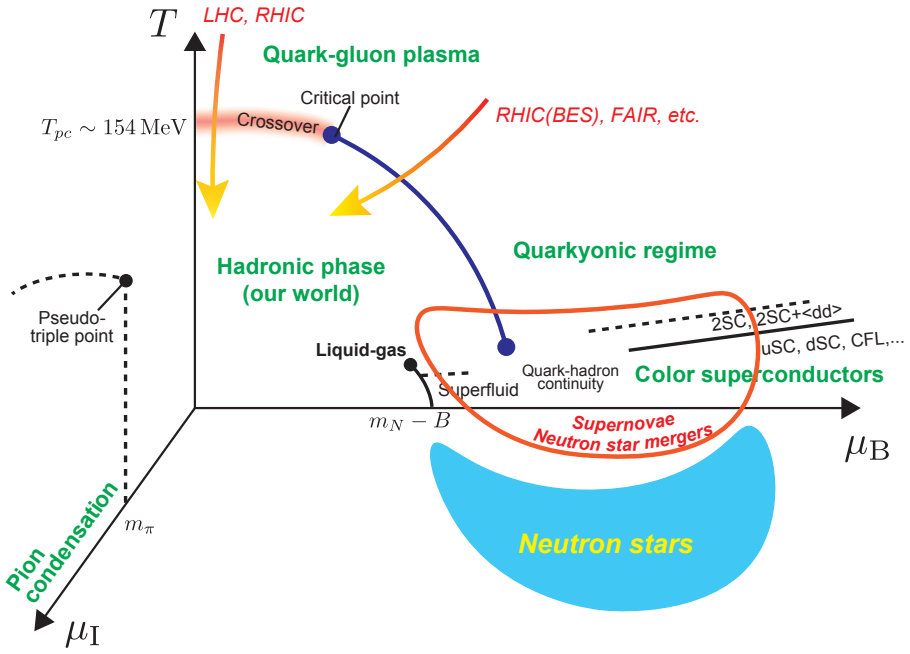

Fig. 1.1: Hypothetical QCD phase diagram.

of QCD [13, 14] allows for free quarks at sufficiently high densities [15] (see also Ref. [16] for the MIT bag model analysis and Ref. [17] for the earlier discussion based on quark model before QCD). Similarly, the deconfinement of quarks and gluons also occurs at high temperatures [18] (see also Ref. [19] for the earlier discussion in which the author coined the notion of limiting temperature, the deconfinement temperature in the modern sense).

In reality, however, it is difficult to reach such a high density on Earth. This is because of the repulsive core in the nuclear force between nucleons; the nuclear force, or a residual effect of the strong interaction on nucleons [20], is attractive at long range (∼1–2 fm) and repulsive at short range ($\lesssim 0.5$ fm). The long-range attraction binds the nucleons together forming a nucleus, and the combined effect with the short-range repulsion leads to the saturation of density inside a nucleus. The saturation density is $\rho_0 \simeq 2.7 \times 10^{17}\,\mathrm{kg/m^3}$ when expressed in terms of the mass density, and $n_0 \simeq 0.16\,(\mathrm{nucleons})/\mathrm{fm}^3$ in the baryon number density n_B. Unless we inject tremendous energy to overcome the repulsive core, we cannot reach the density above the saturation density ρ_0 or n_0.

Nevertheless, we can actually find such strongly interacting high-density matter in various extreme circumstances such as the astrophysical systems and the terrestrial facilities of heavy-ion colliders. The former systems include cores of neutron stars, neutron star binary mergers as well as core-collapse supernovae. Gravity pulls matter together in these environments so that the density can reach up to several times n_0. In the latter facilities such as the Relativistic Heavy Ion Collider (RHIC) at Brookhaven National Laboratory and the Large Hadron Collider (LHC) at CERN, we collide heavy nuclei at very high energies, so that the created matter—what is usually called the quark-gluon plasma (QGP)—reaches high density at collision center and is heated up simultaneously. These extreme

environments have been the major impetus for studying high-density QCD matter.

It is worthwhile emphasizing here the difference between the stellar matter and the usual nuclear matter with respect to the weak interaction. Neutrons undergo the β-decay as well as the inverse electron capture process owing to the large Fermi surface of neutrons, so that these two processes balance and the β-equilibrium is reached, i.e., $n \rightleftarrows p + e^- + \bar{\nu}_e$. In addition, the stellar matter is electrically neutral, so that chargeless neutrons are favored over positively-charged protons; a proton's charge is compensated by leptons. In such a way, large isospin imbalance $\mu_{\rm I} > 0$ is induced (see the $\mu_{\rm I}$-axis and the blue shaded region with a caption "Neutron stars" in Fig. 1.1). We thus have to consider the asymmetric nuclear matter, which has always the positive pressure and no density saturation. The symmetry energy is a parameter that governs the difference between the EoS of pure neutron (asymmetric) nuclear matter and that of symmetric matter.

Meanwhile, on the theory side, model studies point out exciting possibilities such as a first-order chiral phase transition and the associated critical endpoint(s) in the finite density region [21–25], and the color superconductivity, which is the superconducting states of quarks, with the various patterns of pairing [26–30] (see also Ref. [31] for the comprehensive review). Especially the critical point search is now under an extensive experimental investigation [32–34]. Also, based on the large-$N_{\rm c}$ limit of QCD, McLerran and Pisarski posited the existence of high-density yet confined matter, contrary to the idea of Collins and Perry [35]; quark degrees of freedom can come into play albeit the confinement, so this new regime of the matter is named Quarkyonic—a portmanteau word of quark and baryonic. Furthermore, an interesting possibility of a pion condensation is in the finite-$\mu_{\rm I}$ and $\mu_{\rm B} = 0$ region [36]. Based on these speculations, we depict the hypothetical QCD phase diagram in Fig. 1.1.

Despite all these efforts of scrutinizing the high-density matter both in the experimental/observational and theoretical aspects, very little is confirmed about the QCD phase structure up to now: (i) the liquid-gas transition of symmetric nuclear matter [37], (ii) the QGP generation at high temperatures [38], (iii) the quadrant-shape curve of the chemical freeze-out [39], whose shape is consistent with the QCD phase transition [40], and (iv) the crossover-type transition for thermal QCD at pseudo-critical temperature $T_{pc} \simeq 154\,\mathrm{MeV}$ and $\mu_{\rm B} = 0$ [41–43]. Aside from the (i) liquid-gas transition, all this knowledge are about the region at $T > 0$ and $\mu_{\rm B} \ll T$; there the high-quality experimental data and the precise lattice-QCD Monte Carlo calculations are available.

To better understand the finite-density region, a reliable—that is, model-independent and QCD-based—evaluation of the EoS of the dense matter is an urgent issue. It serves as an indispensable input for theoretical studies, e.g., for revealing the interior of neutron stars and for facilitating the core-collapse supernova simulations, to mention a few. Also, we are aware of the importance of the EoS by making an analogy to classical physics, in which the van der Waals type EoS plays an essential role in describing the realistic gas (see Ref. [44] for the modernized quantum formulation, and, e.g., Ref. [45] for its application to neutron star physics). In a more general sense, the significance of the EoS is not merely the problems which it solves, but the issues which it raises: for example, the above-mentioned QCD crossover transition has been recognized through the EoS calculations on the lattice at $\mu_{\rm B} = 0$ [41–43].

We are thus in need of the QCD-based EoS, but it is only available at limited ranges of densities at the moment: (a) *ab initio* methods using the nuclear force derived from Chiral Effective Theory (χEFT) with controlled uncertainty estimates [46–54] (see Ref. [55] for a recent review) at low-density range of $n_{\rm B} \sim 1$–$2\,n_0$, and (b) perturbative QCD (pQCD) calculations [56–64] (see Ref. [65] for a recent review) at asymptotically high densities of $n_{\rm B} \gtrsim 50\,n_0$. The intermediate density region around 2–10 n_0, which is relevant for the neutron star studies, still lacks reliable QCD-based calculations. Currently, the most advanced first-principles approach to QCD is the Monte-Carlo simulation of QCD on the lattice, but the lattice-QCD application to finite density systems is terribly hindered by the notorious sign problem (see the following subsection for details). This is why dense matter studies, especially in the context of neutron stars, still rely on phenomenological EoS constructions: (a) rather *ab initio* approaches based on the phenomenological nuclear interaction [66, 67] near the saturation density, (b) estimates employing the Skyrme interactions [68], (c) the relativistic mean-field theories [69], (d) the functional renormalization group with the chiral mean field model [70], etc. These phenomenological constructions cannot extrapolate up to the intermediate density region, as they cannot avoid the infamous problems such as the hyperon puzzle [71, 72] and the superluminal speed of sound violating causality [66], that is, the EoS is either too soft or stiff.

Therefore in this work, we take an alternative *yet QCD-based* approach: the pQCD calculation with resummation. As it is based on the first-principles theory, we are free from such infamous problems. It will be the central topic of this work, and we present the results based on this method (see Sec. 1.3 for the brief summary).

1.2 Quantum chromodynamics and resummations

As we have emphasized the virtue of QCD-based approaches in the previous subsection, let us now step back and recall some rudiments to better understand our results.

Quantum chromodynamics: The Lagrangian of QCD is given by

$$\mathcal{L}_{\rm QCD} = -\frac{1}{2}\,\mathrm{tr}(F^{\mu\nu}F_{\mu\nu}) + \sum_{f=1}^{N_{\rm f}} \bar{\psi}_f(i\gamma^\mu D_\mu - m_f)\psi_f\,, \tag{1.1}$$

where the field strength tensor is $F_{\mu\nu} \equiv \partial_\mu A_\nu - \partial_\nu A_\mu - ig[A_\mu, A_\nu]$ of the gluon field A_μ; it is endowed with a triple-valued charge called color. So A_μ is matrix valued, i.e., $A_\mu = A_\mu^a t^a$ with t^a being the generator of SU(3). The covariant derivative is defined as $D_\mu \equiv \partial_\mu - igA_\mu$, describing the minimal coupling between the gluon and quark field ψ_f with coupling strength g.

At the classical level, Eq. (1.1) is scale invariant in the chiral limit $m_f \to 0$. Upon quantization, however, the scale invariance is violated via the trace anomaly [73], which generates a dynamical dimensionful scale parameter $\Lambda_{\rm QCD}$ even for the pure gauge sector. This phenomenon is commonly referred to as dimensional transmutation.

The upshot of the dimensional transmutation is that the running coupling constant of QCD, $\alpha_s = g^2/(4\pi)$, becomes a function of the renormalization scale $\bar{\Lambda}$. Throughout this work, we employ the two-loop formula for the running coupling constant, which is

$$\alpha_s(\bar{\Lambda}) = \left[1 - \frac{2\beta_1}{\beta_0^2}\frac{\ln^2\left(\bar{\Lambda}^2/\Lambda^2_{\overline{\rm MS}}\right)}{\ln\left(\bar{\Lambda}^2/\Lambda^2_{\overline{\rm MS}}\right)}\right]\frac{4\pi}{\beta_0 \ln\left(\bar{\Lambda}^2/\Lambda^2_{\overline{\rm MS}}\right)}, \tag{1.2}$$

where

$$\beta_0 \equiv \frac{11}{3}N_{\rm c} - \frac{2}{3}N_{\rm f}, \tag{1.3}$$

$$\beta_1 \equiv \frac{17}{3}N_{\rm c}^2 - N_{\rm f}\frac{N_{\rm c}^2-1}{2N_{\rm c}} - \frac{5}{3}N_{\rm f}, \tag{1.4}$$

and $N_{\rm c}$ and $N_{\rm f}$ are the number of colors and flavors, respectively. They are the first two coefficients of the QCD beta function:

$$\frac{\partial}{\partial \ln \bar{\Lambda}^2}\left(\frac{\alpha(\bar{\Lambda})}{4\pi}\right) \equiv \beta(\alpha_s) = -\beta_0\left(\frac{\alpha_s}{4\pi}\right)^2 - \beta_1\left(\frac{\alpha_s}{4\pi}\right)^3 + O(\alpha_s^4), \tag{1.5}$$

and $-\beta_0 < 0$ means the asymptotic freedom [13, 14]. Here the scale parameter arising from the dimensional transmutation is denoted as $\Lambda_{\overline{\rm MS}}$, which is the $\overline{\rm MS}$ renormalization point. We will fix $\Lambda_{\overline{\rm MS}} = 378\,{\rm MeV}$ throughout, following the treatment of Ref. [60]. This value gives the $\alpha_s(\bar{\Lambda} = 2\,{\rm GeV}) = 0.2994$, which was the best experimental value at the time when Ref. [60] was published; we will use the slightly old value because we want to compare our results with those of Ref. [60].

Sign problem in lattice-QCD: The most dependable calculations of QCD thermodynamics come from lattice-QCD, but the finite-density region is currently out of reach due to the sign problem. We will explain how it arises in the presence of the chemical potential μ following the explanations in Refs. [74, 75]. In lattice-QCD, we use Monte-Carlo method to calculate the partition function in the Euclidean path integral formulation:

$$Z = \int \mathcal{D}U\mathcal{D}\bar{\psi}\mathcal{D}\psi e^{-S_E} = \int \mathcal{D}U e^{-S_G}\det\mathcal{M}(\mu), \tag{1.6}$$

where we understand $U = e^{iagA}$ as a link variable and a as a lattice spacing. The Euclidean action S_E of QCD is given by

$$S_E = S_G + \int_0^{1/T} d\tau \int_{\boldsymbol{x}} \bar{\psi}\mathcal{M}(\mu)\psi, \qquad \mathcal{M}(\mu) = \gamma_\mu^E D_\mu + m + \mu\gamma_4^E, \tag{1.7}$$

with S_G, τ, and γ_μ^E being the gauge part of the QCD action, the imaginary time, and the Euclidean gamma matrices, respectively.

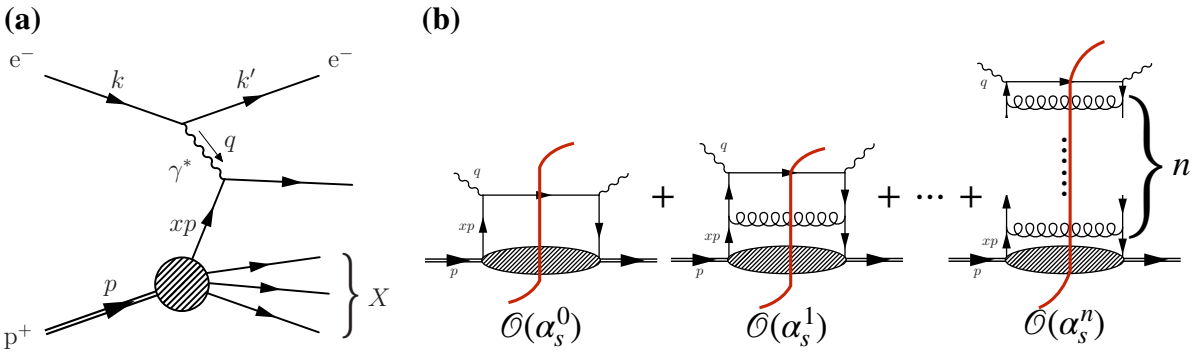

Fig. 1.2: Deep inelastic scattering. **(a)** Kinematics of deep inelastic electron scattering in the parton from a proton; **(b)** Resummation of the gluon ladder diagram. This type of "handbag" diagram combined with the cutting rule gives the total cross section.

The Dirac determinant $\det \mathcal{M}(\mu)$ in Eq. (1.6) becomes complex when μ is finite. The complex Dirac determinant ruins the importance sampling algorithm in the Monte Carlo simulation of the lattice QCD. It is due to the Metropolis step in the algorithm; in this step, we compare the probability weight of the different gauge link configuration, $\rho(U) \sim e^{-S_G} \det \mathcal{M}(\mu)$, so that the complex determinant does not make sense.

If $\mu = 0$, one can explicitly calculate that the Dirac matrix $\mathcal{M}$ fulfills the γ_5-pseudo Hermiticity,

$$\mathcal{M}^\dagger(0) = \gamma_5 \mathcal{M}(0) \gamma_5 \,. \tag{1.8}$$

It leads to the real and positive Dirac determinant: $\det \mathcal{M}(0) \geq 0$. So that lattice-QCD is applicable at $\mu = 0$. When $\mu \neq 0$, however, this relation is modified to $\mathcal{M}^\dagger(\mu) = \gamma_5 \mathcal{M}(-\mu^*)\gamma_5$ and thus leads to the complex Dirac determinant: $\det \mathcal{M}(\mu) \in \mathbb{C}$.

We note in passing that by introducing the isospin chemical potential $\mu_I \tau_3$ (τ is the isospin matrix) instead of μ, we can obtain the sign-problem free theory. This is because we find the same relation to Eq. (1.8) by replacing γ_5 with $\gamma_5 \tau_1$ [36], so that the isospin chemical potential μ_I can be simulated on lattice (see, e.g., Ref. [76] for the recent results). Generally speaking, Eq. (1.8) is an example of the pseudo Hermiticity. This notion is frequently discussed in the context of non-Hermitian physics [77], e.g., the PT symmetry such that γ_5 is replaced with the parity or time-reversal symmetries in Eq. (1.8) [78].

Resummation: In this thesis, our focus is on the improvement of the perturbation calculation of QCD thermodynamics by using the technique called resummation. Resummation is the modernized technique to improve the perturbative calculation in quantum field theories [79]. The progress in perturbation theory is not only in increasing a number of loops in Feynman diagrams giving a few powers of α_s, but also in taming large quantities; they are usually of the forms of single and double logarithms, and occur for each power of α_s. Taming large quantities entails resumming the perturbation series.

One of the renowned example of resummation is the Dokshitzer–Gribov–Lipatov–Altarelli–Pairsi

(DGLAP) evolution equation [80–82] of parton distribution functions (PDFs), $q_i(x, Q^2)$, in the deep inelastic scattering (DIS). The kinematics of DIS experiments are shown in Fig. 1.2 (a): we define the photon virtuality as $Q^2 \equiv -q^2$ and x is the longitudinal fraction of the incoming proton momentum carried by the struck parton[1]. The PDF $q_i(x, Q^2)$ expresses the probability that in the collision with scale Q^2 the proton contains a parton of specie i with the longitudinal fraction x. The DGLAP equation describes the slight violation of the Bjorken scaling, which comes from the QCD correction with a $\ln Q^2$ dependence. The Bjorken scaling is Q^2-independence of the structure function $F_2(x, Q^2)$, i.e., $F_2(x, Q^2) \to F_2(x)$. The structure function is given by the sum of the PDFs $F_2(x, Q^2) = x\sum_i e_i^2 q_i(x, Q^2)$. The $\ln Q^2$ dependence comes into play by considering the emission of an additional parton with a large transverse momentum k_T (see Fig. 1.2 (b) middle diagram); the probability of this emission is proportional to $\int^{Q^2} \alpha_s \frac{dk_\mathrm{T}^2}{k_\mathrm{T}^2} \sim \alpha_s \ln Q^2$. Although α_s is small, the extra parton production $\alpha_s \ln Q^2 \sim 1$ is large because of $\ln Q^2$, and thus we need resummation.

Let us turn back to the DGLAP equation to illustrate how resummation works. The DGLAP equation is

$$\frac{\partial}{\partial \ln Q^2} q_i(x, Q^2) = \alpha_s \sum_j P_{i\leftarrow j}\left(\frac{x}{\xi}\right) \otimes q_j(\xi, Q^2)\,, \tag{1.9}$$

where $P_{i\leftarrow j}(x/\xi)$ is the splitting kernel from the parton specie j to i [82], and $\otimes$ is the convolution with respect to ξ. The solution to this equation is

$$q(x, Q^2) \sim e^{\alpha_s \ln Q^2} = \sum_{n=0}^{\infty} f_n(x)\Big(\alpha_s \ln Q^2\Big)^n\,, \tag{1.10}$$

with $f_n(x)$ being a coefficient function. This corresponds to resummation of the all-order ladder diagrams as shown in Fig. 1.2 (b); we show the ladder diagrams with n extra parton emissions. All these diagrams contribute equally in pQCD, and the DGLAP equation handles them on the same footing. In this way, the perturbative correction is resummed into the PDF.

Similarly, there are varieties of resummations of large logarithms in the pQCD: Balitsky–Fadin–Kuraev–Lipatov (BFKL) [83–86] and Gribov–Levin–Ryskin–Mueller–Qiu (GLR–MQ) [87,88] equations, associated with the single and double logarithms $\ln(1/x)$ and $\ln Q^2 \ln(1/x)$, respectively. Also, Balitsky–Kovchegov (BK) [89,90] and Jalilian-Marian–Iancu–McLerran–Weigert–Leonidov–Kovner (JIMWLK) [91–97] equations resum the effect from the background gauge field; they dictate the nonlinear phenomenon of the gluon saturation [87], which lead to the appearance of the new dynamical scale Q_s in QCD [98] (see Refs. [99, 100] for the recent comprehensive textbook and review). Moreover, the concept of resummation is widespread; for example, the random phase approximation [101] is also a sort of resummation; Gell-Mann and Brueckner showed that it is sum of ring diagrams to infinite order [102].

[1] Strictly speaking, the Bjorken $x_\mathrm{Bj} = Q^2/(2p\cdot q)$, which is measured in the experiment, and the longitudinal fraction x are different. Nevertheless, they match in the naive parton model, and the difference can be quantified by the pQCD.

Hard thermal loops: The main focus of this work is the Hard Thermal Loop (HTL) resummation, or its high-density counter part Hard Dense Loop (HDL) resummation (we will use these terms interchangeably hereafter). In the thermal field theory calculations, theory usually has two parameters, which are the temperature T and the coupling constant g. So the energy scales can be divided into at least two scales: *hard* scale with momentum $k \sim T$ and *soft* scale with $k \sim gT$. This separation of scale is crucial in HTLs. HTL specifically refers to the loop integral with a loop momentum of the hard scale; it will give out the dominant T^2-dependent part only, because the loop integral is quadratic divergent, but it is effectively cut off with T by the Bose-Einstein/Fermi-Dirac distribution in thermal field theory calculations.

Historically speaking, the necessity of resummation has been recognized through the problem the gluon damping rate in thermal QCD. The gluon damping rate γ_g is proportional to the imaginary part of the gluon self-energy, and has the form $\gamma_g = Cg^2T/(8\pi)$. The problem was that 1-loop calculations gave gauge-dependent answers, i.e., the constant C would differ according to the gauge choice [103] (which was later proved to be a gauge-independent quantity [104]). This problem was put forward independently by Kalashnikov and Klimov [105] as well as by Gross, Pisarski and Yaffe [106]. A decade after, it was solved by Braaten and Pisarski [7, 107] following the paper by Pisarski [108], which identified the incompleteness of the preceding 1-loop calculations, and posed a resummation scheme to overcome such incompleteness (see Ref. [109] and references therein for more historic account). The gauge-independent result was obtained by replacing the bare gluon propagators and vertices with the effective HTL propagators and vertices by including HTL contributions from all orders in the loop expansion (see Sec. 3.2 for details).

The necessity of resummation can also be understood from $\hbar$-power counting following the argument in Ref. [109]. At finite temperature, $\hbar$ enters the theory as $g^2 \to g^2\hbar$ and $T \to T/\hbar$. At zero temperature, perturbative expansion in terms of g^2 simply counts the powers of $\hbar$. At finite temperature, however, $\hbar$ appears in both g^2 and T, so this naive power counting of g^2 does not work. The semi-classical limit is given by the divergent quantity in the limit of $\hbar \to 0$. Momenta of the order of $T/\hbar$ survives in the semi-classical limit. But unexpectedly, the same is also true for momenta of the order of $gT/\sqrt{\hbar}$. Therefore counting the powers of $1/\sqrt{\hbar}$ in the semi-classical limit is equal to classifying the scales of the order T, gT, etc.

1.3 Central results of this thesis

In this thesis, we will perform the pQCD calculation of the pressure of quarks with fermionic resummation. Our contributions are to take into account the bare quark mass effect explicitly within the formalism called the Hard Dense Loop perturbation theory (HDLpt) [110]. We think that the inclusion of the bare quark mass effect in the calculation is not so important, but the implications from the results are more illuminating.

Here, we shall first present our central results in Fig. 1.3, and postpone the technical details to the

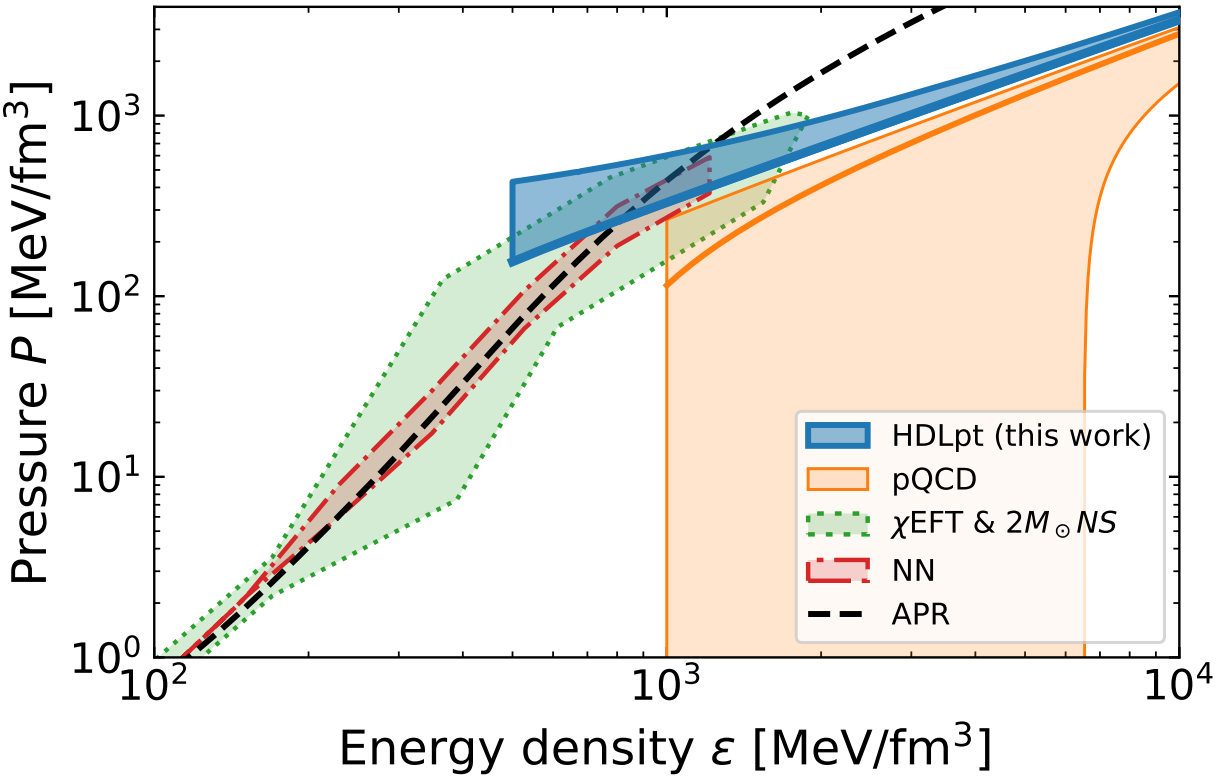

Fig. 1.3: Comparison of the EoS in this work (HDLpt) and other EoSs. The blue and the orange bands represent our results and the preceding results from Refs. [60, 61], respectively, with $\bar{\Lambda} = \mu - 4\mu$. The green band is the EoS extrapolated from the χEFT calculation so as to be consistent with the two-solar-mass pulsars [111, 112]. The red band shows the EoS inferred from the Neural Networks in the machine learning analysis of the neutron star observation [113]. The dashed black line is the APR EoS extrapolated from the nuclear side [66].

later chapters. On top of Fig. 1.3, our central results constitute the following key observations:

Key observations

(A) Reduction of the scale variation uncertainty

(B) Speed of sound exceeding the conformal limit

(C) Smooth matching between nuclear and quark matter EoS

In Fig. 1.3, we plot the various EoSs, which are the relation between the pressure P and the energy density ε. In order not to make the comparison on the figure too busy, we chose only a few representative EoSs from the nuclear side; namely, the EoS extrapolated from the χEFT calculation [111, 112] by the green band, the Neural Network output in the machine learning analysis [113] by the red band, and the standard nuclear EoS, for which we take the Akmal–Pandharipande–Ravenhall (APR) EoS [66], shown by the dashed line. We will explain in turn the above-mentioned key observations:

(A) Reduction of the scale variation uncertainty: The orange band in the density range, $\varepsilon > 10^3\,\mathrm{MeV/fm^3}$, depicts the results from the conventional pQCD calculation [60] for which we utilize the concise formula as given in Ref. [61]. Higher-order corrections could be added, but the uncertainty band is not much changed from Ref. [60]. As is obvious from the figure, the uncertainty band width abruptly diverges; for this reason it has been said that pQCD is reliable only at extreme high densities far from reality $n_\mathrm{B} \gtrsim 40\,n_0$.

This large uncertainty originates from the variation of the renormalization scale $\bar{\Lambda}$ in the coupling constant (see Eq. (1.2) above for the concrete expression and the meaning of $\bar{\Lambda}$). In principle, the value of physical observables should not depend on $\bar{\Lambda}$. Nonetheless, due to the truncation of the perturbative series at a finite order, the scale dependence enters theory. To evaluate the uncertainty associated with the scale variation, our standard practice is to vary $\bar{\Lambda}$ by a factor of two. The canonical choice for the scale $\bar{\Lambda}$ is $\bar{\Lambda} = 2\mu$ [60] with μ being the chemical potential of quarks; quarks are highly degenerate at $T = 0$ and $n_\mathrm{B} > n_0$, so that they form the Fermi sphere filled up to the momentum $k \sim \mu$. Therefore, the three orange lines in Fig. 1.3 for the conventional pQCD result correspond to the running coupling $\alpha_s(\bar{\Lambda} = \mu)$, $\alpha_s(\bar{\Lambda} = 2\mu)$, and $\alpha_s(\bar{\Lambda} = 4\mu)$, respectively; the lowermost line is for $\alpha_s(\bar{\Lambda} = \mu)$, which leads to the zero pressure—the breakdown of the pQCD—at the highest energy density among these three lines.

Now, a surprise comes from a blue narrow band that represents results from our HDLpt calculations: the uncertainty band is drastically reduced! One may wonder what causes such a drastic difference on Fig. 1.3. We can qualitatively understand this from the suppression of the baryon number density n_B at fixed μ owing to the resummation in the fermionic sector. The detailed account will be given in Chapter 6. We will also discuss the condition for the scale variation uncertainty to vanishes.

(B) Speed of sound exceeding the conformal limit: The EoS from our HDLpt calculation has a notable feature in addition to the reduced scale variation uncertainty. The speed of sound c_s^2 corresponds to the slope of the EoS. It is given by $c_s^2 = \partial P/\partial\varepsilon$. The behavior of the speed of sound can determine whether the EoS is "stiff" or "soft" (see the definition of this term in Sec. 2.1), and also it is relevant for neutron star physics as it can influence observables of neutron stars such as the stellar radius.

There is an empirical conjecture to claim that the speed of sound may not exceed the conformal limit [114]. The conformal limit, $c_s^2 = 1/3$, is the value of the speed of sound for the conformal theory. At asymptotically high density, all mass scales and interactions are negligible and c_s^2 approaches the conformal limit. In the conventional pQCD, the known correction to the conformal speed of sound $c_s^2 = 1/3$ is negative. Therefore the conformal bound is kept intact. We point out, however, our QCD-based calculation actually violate this conformal limit. Meanwhile, our attempt also revealed another subtleties related to the derivative of $\bar{\Lambda}$.

(C) Smooth matching between nuclear and quark matter EoS: This issue is closely related to the observation (A). The uncertainty bandwidth of the conventional pQCD abruptly diverges, and thus it is reliable only at extremely high densities far from reality. At a glance, indeed, we should understand how difficult it is to make a robust interpolation between the nuclear and the pQCD EoSs.

Now, another surprise in Fig. 1.3 comes from a blue narrow band that represents results from our HDLpt calculations: the HDLpt EoS appears to be merged into the nuclear EoSs smoothly in the intermediate density region! It should be noted that the APR EoS overshoots ours, but this is due to a well-known flaw in the APR EoS, i.e., superluminal speed of sound which violates causality.

1.4 Outline

This thesis is organized as follows.

Review part (Chapter 2 and 3): Chapter 2 offers a cursory look at the dense matter EoS studies from the viewpoint of nuclear experiments, astrophysical observations of neutron stars, and the theory calculations. Chapter 3 covers the relevant methods. We introduce the notion of hard thermal loops (HTLs) in Sec. 3.2, then we proceed to the survey on the various perturbative techniques to incorporate the HTL resummation including HTL perturbation theory (HTLpt) (Sec. 3.4), and the Φ-derivable approximation in the 2PI formalism (Sec. 3.5); these methods will be used in the later chapters.

Result part (Chapter 4 and 5): In Chapter 4, we calculate the EoS in the β equilibrium and charge neutral system. The method we use is the HTLpt, which was outlined in Sec. 3.4, and the inclusion of the bare mass of strange quarks is the novel extension in our calculation. In Chapter 5, we discuss some corrections to the results presented in the previous chapter. Also, we perform the EoS calculation under the Φ-derivable approximation in the 2PI formalism in Sec. 5.2.

Discussion part (Chapter 6, 7, and 8): Chapters 6, 7, and 8 are devoted to the discussion on the novel facets of our results. In Chapter 6, we discuss the reduction of the scale variation uncertainty in the HTL-resummed theories. In Chapter 7, we show the speed of sound in the HDLpt, which exceeds the conformal limit. We give a quick survey on the behavior of the speed of sound to understand why our result exceeding the conformal limit is relevant. Finally, in Chapter 8, we claim that our HDLpt calculation and the low-density nuclear matter EoSs smoothly match. It leads us to the physical picture that hadrons continuously melt into quarks. We also mention the relevance of our results to the astrophysics context.

Notations: Throughout this thesis, we use natural units $c = G = \hbar = k_{\mathrm{B}} = 1$ except in Chapter. 8, where cgs units are used.

We use the terminologies "Hard Thermal Loop (HTL)" and "Hard Dense Loop (HDL)" interchangeably. We will use the former when we discuss physics at high temperature, and the latter at low temperature and high density. However, the term HTL is also used even at low temperature and high density when we refer to the methodology of resummation itself, inasmuch as it is the original name coined by Braaten and Pisarski.

We will use the letter k and q for momenta and do not use p in order not to confuse with the pressure; the letter P is reserved for the pressure exclusively. Momenta in the Minkowski space is denoted with lower case letters, e.g. $k^\mu = (k^0, \boldsymbol{k})$, while those in the Euclidean space are denoted with upper case letters, e.g. $K_\mu = (k_4, \boldsymbol{k})$.

Extensive and intensive variables in thermodynamics are denoted by upper and lower case letters, respectively. However, there are exceptions to this rule, which are the pressure P and temperature T. These are denoted by upper case letters, albeit being the intensive variables.

Chapter 2

Review of the dense matter equation of state

In this chapter, we review the basic properties and the current status of the EoS. Particularly, we focus on the observable called the symmetry energy. There are diverse efforts towards revealing the EoS based on the terrestrial experiments including heavy-ion collisions, astrophysical observations, as well as theory calculations. We give a brief account of such efforts.

2.1 The basic properties of equation of state

Theoretical models usually calculate the total energy density ε of nuclear matter at given baryon density $n_{\rm B}$. See Fig. 2.1 for the recent calculation based on χEFT. It is expressed in terms of

$$\varepsilon(n_n, n_p) = n_{\rm B}\frac{E}{A} + m_n n_n + m_p n_p = n_{\rm B}\left(\frac{E}{A} + m_N\right), \tag{2.1}$$

where E/A is the energy per nucleon number A, and $m_{n/p}$ and $n_{n/p}$ are the mass and the density of neutrons/protons, respectively. If we define the nucleon mass as $m_N \simeq m_n \simeq m_p$ and the net baryon density as $n_{\rm B} = n_n + n_p$, then the energy density reduces to the RHS of Eq. (2.1).

From the total energy density or the energy per nucleon, we can calculate the pressure by the following formula

$$P(n_{\rm B}) = n_{\rm B}^2\frac{\partial}{\partial n_{\rm B}}\left(\frac{\varepsilon}{n_{\rm B}}\right) = n_{\rm B}^2\frac{\partial}{\partial n_{\rm B}}\left(\frac{E}{A}\right), \tag{2.2}$$

which follows from the thermodynamic relation $P = -\partial U/\partial V$ with $U = \varepsilon V$ and $V = 1/n_{\rm B}$ being the internal energy and the volume, respectively.

Let us now introduce the notion of the symmetry energy, which is important for discussing the dense matter EoS. We define the isospin asymmetry parameter as $\delta = (N-Z)/A = (n_n - n_p)/n_{\rm B}$. Then the energy per nucleon number A can be expanded around $\delta = 0$ as

$$\frac{E}{A}(n_{\rm B}, \delta) = \frac{E}{A}(n_{\rm B}, \delta = 0) + \delta^2 S_2(n_{\rm B}) + O(\delta^3). \tag{2.3}$$

Note that the term $\propto \delta$ vanishes because of the charge independence of nucleons. Namely, n and p

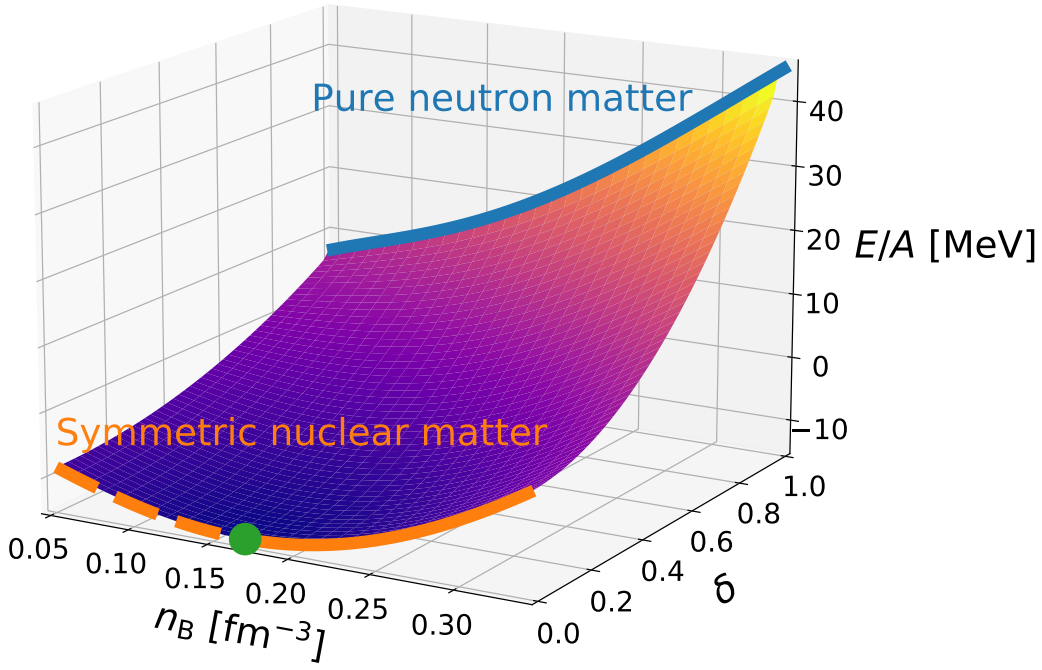

Fig. 2.1: Energy per nucleon E/A as a function of baryon density $n_{\rm B}$ and isospin asymmetry δ. This figure is plotted from the state of the art χEFT calculations of the density dependent $S_2(n_{\rm B})$ and E/A of SNM [54], using the tools available online in Ref. [115]. See text for description.

are symmetric under an exchange, so that the term subject to modification under the transformation $\delta \to -\delta$ is simply forbidden. The function $S_2(n_{\rm B})$—the coefficient of the δ^2-term—is commonly referred to as the symmetry energy.[1] Pure neutron matter (PNM) with $\delta = 1$ costs more energy than symmetric nuclear matter (SNM) with $\delta = 0$. The symmetry energy roughly measures the difference between the energy per nucleon in PNM and SNM:

$$S_2(n_{\rm B}) \simeq \frac{E_{\rm PNM}}{N}(n_{\rm B}, \delta = 1) - \frac{E_{\rm SNM}}{A}(n_{\rm B}, \delta = 0)\,. \tag{2.4}$$

Note that for PNM, the nucleon number A is replaced with the neutron number N as it comprises neutrons only. The density dependence of the symmetry energy is usually taken care of by the slope parameter L when expanding it around the saturation density n_0 (see, however, Ref. [116] for the recent discussion on the density-dependent parametrization of the nuclear symmetry energy)

$$S_2(n_{\rm B}) = S_v + \frac{L}{3}\left(\frac{n_{\rm B} - n_0}{n_0}\right) + O\Big((n_{\rm B}/n_0)^2\Big)\,. \tag{2.5}$$

This quantity is always positive because of the Pauli exclusion principle; PNM has larger energy than SNM.

[1] Strictly speaking, it is only valid in the isospin sector. Electromagnetism breaks the charge independence. So the Coulomb interaction gives rise to the $O(\delta)$ term, but its effect is nonetheless small and thus can be neglected.

For SNM part, we again expand around n_0

$$\frac{E_{\rm SNM}}{A}(n_{\rm B}) \equiv \frac{E}{A}(n_{\rm B}, \delta = 0) = -B + \frac{K_0}{18}\left(\frac{n_{\rm B} - n_0}{n_0}\right)^2 + O\Big((n_{\rm B}/n_0)^3\Big), \tag{2.6}$$

where $B \simeq -16\,\text{MeV}$ is the binding energy and K_0 is incompressibility of nuclear matter.

If we formulate everything in terms of derivatives, the symmetry energy parameters follows from

$$S_2(n_{\rm B}) = \frac{1}{2}\frac{\partial^2}{\partial\delta^2}\left[\frac{E}{A}(n_{\rm B}, \delta)\right]_{\delta=0}, \tag{2.7}$$

as

$$S_v = S_2(n_0), \quad L = 3n_0\left[\frac{\partial S_2(n_{\rm B})}{\partial n_{\rm B}}\right]_{n_{\rm B}=n_0}. \tag{2.8}$$

The SNM incompressibility is defined as

$$K_0 = 9n_0^2\frac{\partial^2}{\partial n_{\rm B}^2}\left[\frac{E_{\rm SNM}}{A}(n_{\rm B})\right]_{n_{\rm B}=n_0} \tag{2.9}$$

Up to now, we have referred to the notion of the saturation density n_0 without an explanation, but let us step back and give a brief account of this. The saturation density is the density at which nuclear matter is self-bound, i.e., stable at zero pressure. In Fig. 2.1, at $\delta = 0$, we have marked the minimum of the binding energy with green blob, the stable density region with positive pressure (plotted with the solid line), and the unstable region with negative pressure (plotted with the dashed line). From the behavior of the pressure is given in Eq. (2.2), we can identify the saturation point as the minimum of E/A as a function of $n_{\rm B}$; at this point, $n_{\rm B} = n_0$, matter has zero pressure and the (negative) binding energy $E/A = -B \simeq 16\,\text{MeV}$. This is also the reason why the $n_{\rm B}$-term is vanishing in Eq. (2.6). From Eq. (2.2), it is easy to understand that matter is unstable with negative pressure below n_0 since E/A is a decreasing function with respect to $n_{\rm B}$.

In QCD thermodynamics, at the first point, we calculate the pressure $P(\mu)$ as a function of chemical potential (or the grand potential Ω) from the grand canonical partition function $Z(\mu)$:

$$P(\mu) = \frac{T}{V}\ln Z(\mu)\left(= -\frac{\Omega}{V}\right). \tag{2.10}$$

Then the number density n and energy density ε are calculated accordingly from the thermodynamic relations:

$$n = \frac{\partial P}{\partial \mu}, \quad \varepsilon = -P + \mu n. \tag{2.11}$$

Here we introduce the idea of stiffness. The incompressibility defined in Eq. (2.9) is one measure

for this. Another frequently used measure is the speed of sound (squared):

$$c_s^2 = \frac{\partial P}{\partial \varepsilon} \,. \tag{2.12}$$

This corresponds to the slope of the EoS expressed in terms of $P - \varepsilon$ relation. Stiffness means the same as in our daily life: easily compressible matter is called soft and vice versa as stiff. That is, the soft matter has a small change in pressure when changing the (energy) density, while the stiff matter has a larger change in pressure.

2.2 The status of experimental/observational diagnosis of the EoS

Experimental and observational data available from the extreme environments provide us with useful constraints on possible EoSs so that some theoretical scenarios can be excluded/accepted. The most well-known and successful example along these lines is the discovery of two-solar-mass ($2\,M_\odot$) neutron stars [117–120], which turns down scenarios leading to soft EoS. That is, it is unlikely for the dense matter to accommodate a strong first-order phase transition [121] nor condensations of exotic degrees of freedom (see, however, Refs. [122,123] for the measurements of the Landau-Migdal parameters; these values may still facilitate the pion condensation).

In Figs. 2.2 and 2.3, we summarize the currently obtained constraints on the EoS both either experiments or observations. Still, the uncertainty of the estimated EoS from various sources is quite large, so it is still inconclusive from the experiments/observations what is the precise form of the EoS. Nonetheless, it is beneficial at this moment to distinguish what is known and what is not known. In the following, we briefly review what we can learn about the EoS from such opportunities.

2.2.1 Terrestrial experiments and the S_v–L correlation

There is a linear correlation between S_v and L parameters [135–137] as can be seen clearly in Fig. 2.2. To comprehend this correlation, it is instructive to explain in the spirit of the Bethe-Weizsäcker mass formula

$$E(N,Z) = a_{\rm vol}A - a_{\rm surf}A^{2/3} - a_{\rm C}\frac{Z^2}{A^{1/3}} - a_{\rm sym}(A)\delta^2 A + \Delta E(N,Z)\,. \tag{2.13}$$

In the liquid *droplet* model [138], the coefficient of the symmetric term can be expressed as

$$a_{\rm sym}^{\rm droplet}(A) = \frac{S_v}{1 - \frac{S_s}{S_v}A^{-1/3}} \,. \tag{2.14}$$

As a finite nucleus has a surface, the additional surface symmetry energy parameter arises in this expression. Note that the liquid *droplet* model is different from the liquid *drop* model in the sense that it can describe neutron skins in neutron-abundant nuclei under the variation of δ; it is practically

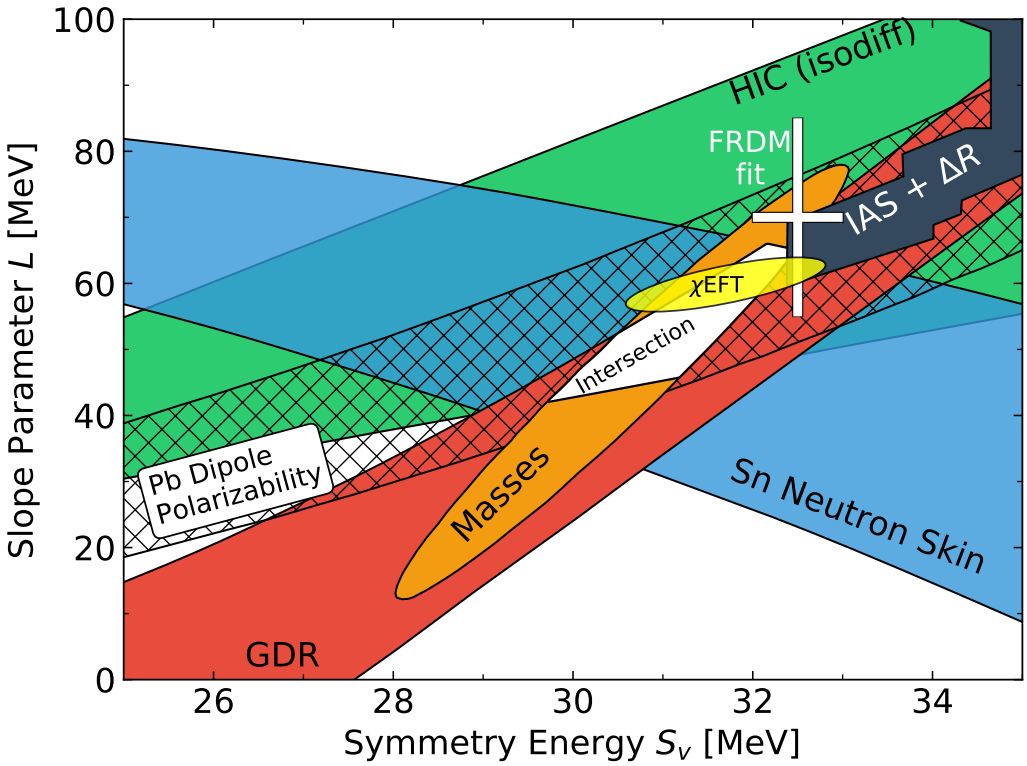

Fig. 2.2: Summary plot of the experimental constraints on the S_v–L relation. Experimental constraints are adapted from nuclear masses [124, 125], neutron-skin thickness of Sn isotopes [126], the dipole polarizability of ^{208}Pb [127, 128], giant dipole resonances (GDR) [129], isobaric analog states and isovector skins (IAS+ΔR) [130], and isospin diffusion in heavy-ion collisions (HIC (isodiff)) [131]. The overlapping region is filled with white color. The 68 % contour from the recent χEFT calculation [54] is also overlaid. This figure is reproduced from Refs. [54, 132–134] using the code provided in Ref. [115].

more improved treatment compared with the liquid drop model.

There is a strong correlation between S_v and S_s. This correlation is apparent: the heavy nuclei with $A \approx 200$ and largest asymmetries requires $a_{\rm sym}^{\rm droplet} = S_v/(1 - S_s A^{-1/3}/S_v) = a_{\rm sym} = \text{const}$, where $a_{\rm sym}$ is the usual liquid drop model parameter, so that S_v and S_s/S_v are linearly correlated.

Now the S_v–S_s correlation can be translated into the S_v–L correlation by utilizing the density dependence of S_s. The surface energy term S_s has the density dependence because it reflects the varying density within a nucleus, so that the correction to S_v is necessary. Thus, S_s depends also on S_v and L, and we can write $S_s(S_v, L)$. For example, the approximate form of S_s/S_v has indeed been found in Ref. [132]:

$$\frac{S_s}{S_v} \simeq 0.646 + \frac{S_v}{97.9\,\text{MeV}} + 0.436\frac{L}{S_v} + 0.0873\left(\frac{L}{S_v}\right)^2 . \tag{2.15}$$

Therefore, there is a strong correlation between S_v and L and it can be justified from the fundamental mass formula. The various quantities in nuclear physics are dependent on S_v and S_s, so their measured values are sensitive to the symmetry energy. Below is an incomplete list of nuclear structure and reaction quantities sensitive to the symmetry energy:

Nuclear masses: As the S_v–L correlation is related to the mass formula, the most straightforward and tightest constraints on the symmetry energy are obtained by a least-squares fit to the nuclear masses across the chart of nuclides. Kortelainen et al. [124] fitted nuclear masses and charge radii resulting in $S_v \simeq 30.5 \pm 3.1\,\text{MeV}$ and $L \simeq 45 \pm 40\,\text{MeV}$ (see the orange ellipse in Fig. 2.2). Also, the finite-range droplet model (FRDM) predicts the values of $S_v \simeq 32.5 \pm 0.5\,\text{MeV}$ and $L \simeq 70 \pm 15\,\text{MeV}$ [125] (see the white error bar in Fig. 2.2).

Neutron-skin thickness: The neutron-skin thickness is defined as

$$\Delta r_{np} \equiv \langle r_n^2 \rangle^{1/2} - \langle r_p^2 \rangle^{1/2} . \tag{2.16}$$

The strong correlation between S_v and S_s (and thus S_v and L) and Δr_{np} can be seen in the liquid droplet model prediction

$$\Delta r_{np} \simeq \frac{2r_0}{3}\frac{S_s\delta}{S_v + S_s A^{-1/3}} . \tag{2.17}$$

By using this relation, the fit of the neutron-skin data of Sn isotopes gives the negative correlation between S_v–L [126] (see the blue region in Fig. 2.2). Also, the neutron-skin thickness of ^{208}Pb has been recently measured in the PREX-II experiment [139], leading to the stiff values of $S_v \simeq 38.1 \pm 4.7\,\text{MeV}$ and $L = 106 \pm 37\,\text{MeV}$ [140], which are inconsistent with the intersection of the currently obtained constraints, see Fig. 2.2. It is, however, still under an intense debate: by taking into account the dipole polarizability (see below), L is subject to significant change [141], which is at odds with the analysis of Ref. [140] (see also Ref. [142]).

Dipole polarizability: The dipole polarizability is the linear response of a nucleus in an excited state caused by an external dipole electric field. The dipole polarizability α_D is related to the inverse energy-weighted photo absorption cross section $\sigma_{\rm abs}(\omega)$

$$\alpha_D = \frac{\hbar c}{2\pi^2 e^2}\int d\omega\,\frac{\sigma_{\rm abs}(\omega)}{\omega^2}\,. \tag{2.18}$$

The liquid droplet model predicts the correlation between S_v and S_s in the form of

$$\alpha_D = \frac{AR^2}{20S_v}\left(1+\frac{5}{3}\frac{S_s}{S_v}A^{-1/3}\right), \tag{2.19}$$

where $R = r_0 A^{1/3}$ is the nuclear radius. The experimental study [127] put a constraint on α_D of ^{208}Pb. The relation between α_D and Δr_{np} was found in Ref. [128], and by using the relation between Δr_{np} and S_v as well as L [126], the S_v–L correlation was obtained as in Fig. 2.2.

Giant dipole resonance: A good measure for the mean excitation energy of the giant dipole resonance is $E_{-1} = \sqrt{m_1/m_{-1}}$, where m_{-1} and m_1 are the inverse energy-weighted and the energy-weighted sum rule, respectively. Given that F is the physical operator that excites a 1p-1h state from $|0\rangle$ to its eigenstates $|n\rangle$ with an excitation energy E_n and $\omega_n = E_n - E_0$, the m_p sum rule is defined by $m_p = \sum_{n>0}|\langle n|F|0\rangle|^2\omega_n^p$. Hydrodynamic model [143] predicts

$$E_{-1} = \sqrt{\frac{6\hbar^2(1+\kappa)}{m_N R^2}\frac{S_v}{1+5A^{-1/3}S_s/S_v}}\,, \tag{2.20}$$

where κ is what is commonly referred to as the enhancement factor. It was shown in Ref. [129] that Eq. (2.20) is strongly correlated with the symmetry energy at the subnuclear density $n_{\rm B} \simeq 0.1\,{\rm fm}^{-3}$ (see the red shaded region in Fig. 2.2).

2.2.2 Heavy-ion collisions

The nuclear observables given above are useful in constraining the symmetry energy $S_2(n_{\rm B})$, however, they are only measured at the subnuclear density $n_{\rm B} \lesssim n_0$. Heavy-ion collisions provide a useful probe to study the symmetry energy at the supranuclear density since there are abundant hadrons produced in the collisions with densities higher than n_0. Although the heavy-ion collision is a very complex experiment, the final state particles allow us a simple and clean statistical interpretation, e.g., by using a simple statistical hadronization model [39]. Densities of protons and neutrons in the central collisions are sensitive to the value of the symmetry energy. Generally speaking, to extract information of the symmetry energy study from the heavy-ion collision dynamics, one needs to rely on the specific transport model. So the model-dependence should be carefully examined, and this invoked intensive comparisons between different codes [144–147] over the last two decades, which lead to the improved reliability of the theory calculations.

There are isospin-sensitive observable such as (a) isospin diffusion, (b) π^-/π^+ ratio, and (c) anisotropic collective flows, to mention a few (see Ref. [148] and references therein for a more detailed account).

Isospin diffusion: In the isospin diffusion process, the symmetry energy exerts the exchange of neutrons and protons between nuclei in a heavy-ion collision. This diffusion process forces the isospin asymmetry of the target and projectile to be equal after the collision.

Isospin transport ratio $R_i(X)$ is defined as follows in order to separate the diffusion effects from the others. For the isospin observable X, mixed collisions of neutron-rich nuclei A and neutron-deficient nuclei B, $A+B$ or $B+A$, are scaled with the symmetric collisions, $A+A$ and $B+B$:

$$R_i(X) = \frac{2X - (X_{A+A} + X_{B+B})}{X_{A+A} - X_{B+B}} \tag{2.21}$$

This measure takes the value $R_i = \pm 1$ if there is no diffusion and $R_i = 0$ if the isospin equilibrium is reached.

In Fig. 2.2, we plot the symmetry energy from the measurement of isospin diffusion transport ratios in ^{112}Sn + ^{124}Sn and ^{124}Sn + ^{112}Sn collisions at the energy of 50 MeV/A [131]; in these data, the variable X is taken to be as what is called the isoscaling parameters [149] scaled with the symmetric collisions of neutron-rich and deficient nuclei, i.e., ^{124}Sn + ^{124}Sn and ^{112}Sn + ^{112}Sn.

π^-/π^+ ratio: The π^-/π^+ ratio in heavy-ion collisions has a strong dependence on the isospin asymmetry (see, e.g., for Refs. [150–153]). At the intermediate energy region of $\sim$ 300 MeV/A, inelastic heavy-ion collisions produce the Δ resonance which decays into the nucleon by emitting pions. The charged pion ratio, π^-/π^+, depends on the ratio of protons and neutrons in a way [154]:

$$\pi^-/\pi^+ = \frac{5N^2 + NZ}{5Z^2 + NZ} \simeq \frac{n_n^2}{n_p^2}\,. \tag{2.22}$$

Recent experiment charged pion production in Sn isotope collisions infer the symmetry energy constraints at $n_{\rm B} \simeq 1.5 n_0$ of $32.5 < S_v < 38.1$ MeV and $42 < L < 117$ MeV [155]. This data is not shown in Fig. 2.2 not to make the figure busy, nevertheless, it has an overlap with the currently obtained constraints.

Anisotropic collective flows: Anisotropic collective flows have been used as a probe to extract the dense QCD matter EoS [156] (see, e.g., Refs. [157, 158] for the recent updates). Flows are described by the corresponding coefficients in the Fourier components of the azimuthal angle distribution of measured particles:

$$\frac{dN}{d\phi} \propto 1 + 2\sum_{n=1}^{\infty} v_n \cos n\phi \tag{2.23}$$

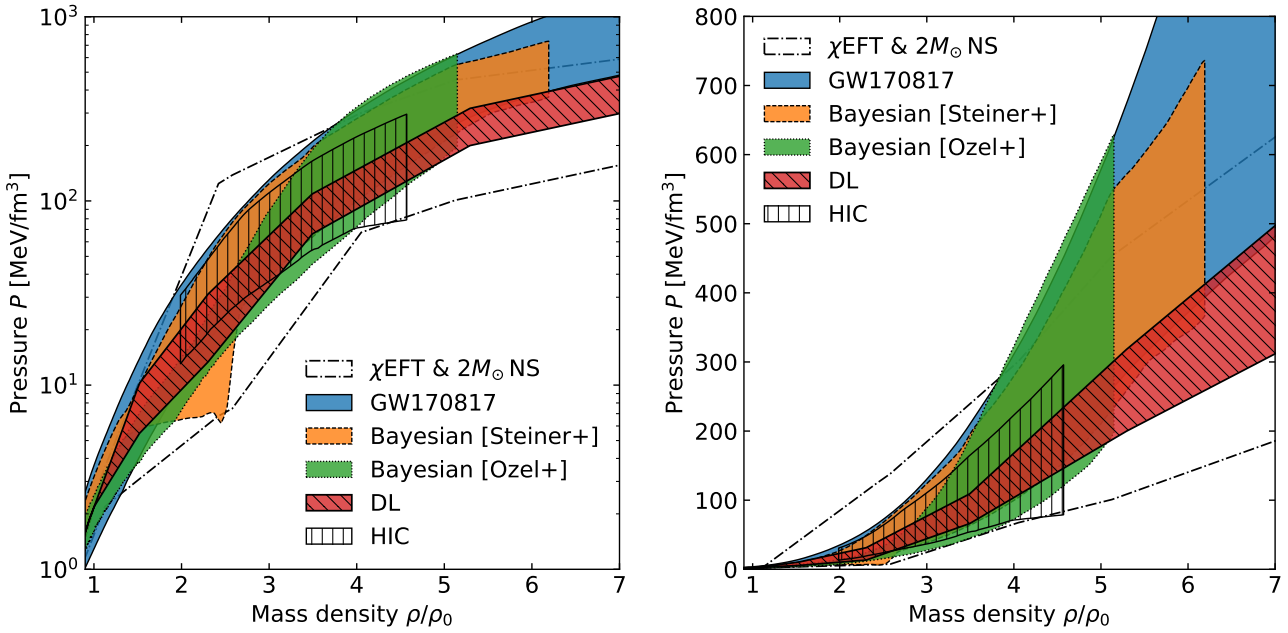

Fig. 2.3: Summary plot of the observational and the experimental constraints on the P–ρ relation. The left and right panels are essentially the same, but the pressure is plotted in a log scale (left) and a linear scale (right). Observational constraints are derived from the $2\,M_\odot$ consistent extrapolation of the χEFT theory calculation [112], GW170817 [160], two independent Bayesian analyses [161, 162], and deep learning (DL) [113, 163]. Also, the collective flow constraint from HICs is overlaid [159] (see Sec. 2.2.2 for details).

where $v_1 \equiv \langle \cos\phi \rangle$ is the directed flow, and $v_2 \equiv \langle \cos 2\phi \rangle$ is the elliptic flow. The mean transverse momentum per nucleon projected onto the reaction plane is $\langle p_x/A \rangle$. It can be related to the directed flow through $v_1 = \langle p_x/p_T \rangle$ with $p_T \equiv \sqrt{p_x^2 + p_y^2}$ being the transverse momentum. The directed transverse flow F is then defined by

$$F = \left. \frac{d\langle p_x/A \rangle}{d(y/y_{\rm cm})} \right|_{y/y_{\rm cm}=1} , \tag{2.24}$$

where y is the rapidity and $y_{\rm cm}$ is that of particles at rest in the center of mass frame. By combining v_2 and F, which are obtained in Au-Au collisions with energies $\sim$ 0.15–10 GeV/A, Danielewicz et al. [159] put a constraint on the EoS at densities $n_{\rm B} = 2$–$4.5\,n_0$ (see the hatched region in Fig. 2.3). We note, however, that this result is extrapolated from the hot SNM to the cold PNM, so that it may be subject to substantial systematic uncertainties; the experiments are only targeting the symmetric matter at high temperatures.

2.2.3 Neutron star observations

Several observational data of neutron stars are now available from (i) the radius determination of neutron stars in quiescent low-mass X-ray binaries (qLMXBs) and thermonuclear bursters [161, 165–168] (see reviews [162, 169, 170] for discussions on the methods and associated uncertainties), (ii) the

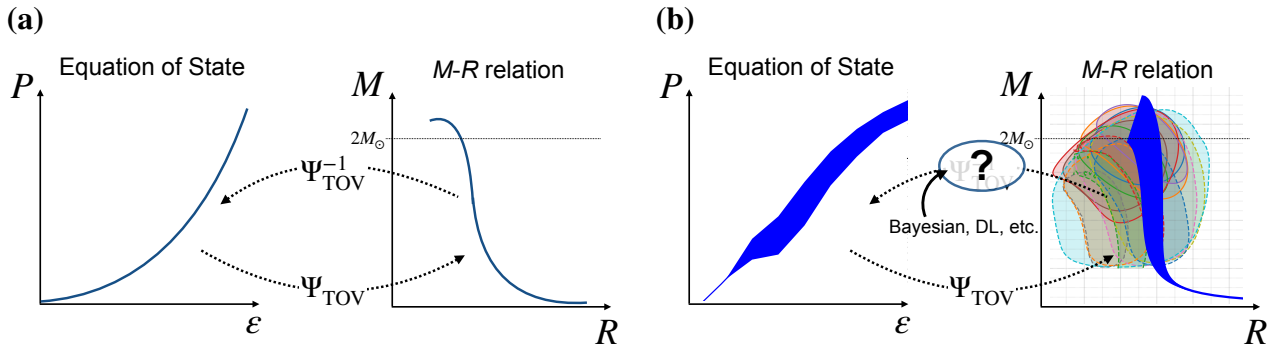

Fig. 2.4: Schematic figure of the relation between the EoS and M–R of neutron stars. **(a)** Ideal situation where the one-to-one correspondence between the EoS and M–R is established [164]; **(b)** Realistic situation with observational uncertainty; $\Psi_{\rm TOV}$ is straightforward to calculate (blue shaded region in M–R is calculated from the EoS), but $\Psi^{-1}_{\rm TOV}$ is very non-trivial. Data are from Ref. [162].

mass measurements of the $2\,M_\odot$ pulsars by Shapiro delay [117–120], (iii) detection of gravitational waves from binary neutron star mergers or the binary black hole neutron star merger by the LIGO-Virgo collaboration [160, 171, 172], and (iv) the pulsar timing measurements in the X-ray wavelength by the NICER [173–176]. Typical observable quantities of neutron stars are mass M, radius R, compactness M/R, tidal deformability Λ (and their variants, e.g., Love number k_2), etc. For instance, the tidal deformability is extracted from the gravitational wave signals from binary neutron star mergers, and the NICER particularly aims at the compactness M/R. An EoS-insensitive universal relation between the observables such as the I-Love-Q relation [177, 178], which connects the moment of inertia I, the Love number k_2, and the quadrupole moment Q, can be useful in constraining the EoS (see Refs. [179, 180] and reference therein for further discussions).

There are diverse statistical technologies to extract the most likely EoS from the observational data. Here we give a brief synopsis of this problem of extracting the EoS as shown in Fig 2.4. Let us consider particularly the pairs of stellar mass-radius relation, M–R, for example. In principle, the method presented below works for other kinds of observables as well. The M–R can be calculated from the EoS using the general relativistic structural equation, i.e., Tolman–Oppenheimer–Volkoff (TOV) equation [181, 182] (see Appendix B.1.1 for details). We will express the *inverse* operation of solving the TOV equation as $\Psi^{-1}_{\rm TOV}$. As in Fig. 2.4 (a), ideally, the $\Psi^{-1}_{\rm TOV}$ is straightforward since there is a one-to-one correspondence between the EoS and M–R [164]. In reality, however, the M–R data include the observational uncertainties as shown in Fig. 2.4 (b), so that the one-to-one correspondence is obscured. To this end, we need to rely on the statistical method to perform the regression from M–R to the EoS. The traditional approach is the Bayesian inference [161, 165, 166, 183–188] and the Gaussian processes [189–191]. On top of that, the newly developed comprehensive technique devising deep learning [113, 163, 192] (see also Refs. [193–195] for related works) serves as a complementary tool to tackle this problem; this method is advantageous because it depends on a prior distribution for the EoS probability distributions only *implicitly* while the other approaches explicitly assume the prior.

In Fig. 2.3, we plot the selected results[2]. The most conservative observational constraint (see χEFT & $2\,M_\odot$ NS in Fig. 2.3) is obtained solely from the $2\,M_\odot$ constraint, and up to $n_\mathrm{B} \simeq n_0$, we assume the EoS calculated within the χEFT [112]. Steiner, Lattimer, and Brown [161] analyzed four neutron stars in qLMXBs (in the globular clusters M13, ω Cen, NGC 6397, and X7 in 47 Tuc) as well as four thermonuclear bursters (4U 1608–522, KS 1731–260, EXO 1745–248, and 4U 1820–30) using the Bayesian inference. The result in Fig. 2.3 (see the orange region) shows the 68 % contour of their result. Özel et al. [162, 167, 168] also employed Bayesian inference but analyzed additionally four qLMXBs (in the globular clusters M28, M30, NGC 6304, and X5 in 47 Tuc) as well as two thermonuclear bursters (SAX J1748.9-2021 and 4U 1724−207) on top of the previously mentioned eight stars. In Fig. 2.3, we show the contour of e^{-1} of the maximum likelihood (see the gree region). Fujimoto, Fukushima, and Murase [113, 163] utilize deep learning (DL) to cope with the NICER data of J0030+0451 [173] and the above-mentioned fourteen stars (see the red hatched region in Fig. 2.3). The Bayesian analysis from GW170817 [160] is plotted with the blue region in the figure. We note that in the right panel of Fig. 2.3, we plot the pressure in the linear scale, and it explains that the high-density region has still large uncertainty.

2.3 The status of QCD-based theoretical calculations

As mentioned earlier, at $T = 0$ and $n_\mathrm{B} \gtrsim n_0$, the QCD-based *ab initio* methods are only available at limited density regions at the moment. Fig. 2.5 is the summary plot of the status quo. The available calculations include:

- $n_\mathrm{B} \gtrsim 50\,n_0$: pQCD calculations [56–64]
- $n_\mathrm{B} \lesssim 2\,n_0$: Many-body methods combined with the perturbative χEFT nuclear forces [46–54]

The intermediate density region around 2–10 n_0, which is relevant for the neutron star studies, still lacks reliable QCD-based calculations. The region enclosed by the dashed line in Fig. 2.5 is the allowed region of polytropic extrapolation from χEFT [112]; outside this region is rejected by the $2\,M_\odot$ constraints of neutron star observations. As mentioned above, currently the most advanced lattice-QCD calculation is still beyond reach at high densities.

2.3.1 Perturbative QCD calculation

To sharpen novelties in our work, let us briefly summarize what has been understood so far. The pQCD calculation is the expansion with respect to the strong coupling constant α_s. The α_s expansion

[2]Strictly speaking, the EoSs in Fig. 2.3 from the Bayesian (Steiner et al.) [161] and the HIC [159] are presented in the form of P–n_B relation, so they are different from the P–ρ relation. However, the deviation from $m_n n_\mathrm{B}$ and $\rho c^2 = \varepsilon$ is confirmed to be small, which is proportional to E/N, so we neglect this subtle difference (see, e.g., Ref. [112] for actual numbers in the χEFT calculation). Henceforth, this subtle difference will be neglected in the schematic illustrations, and n_B, ρ, and ε are used interchangeably.

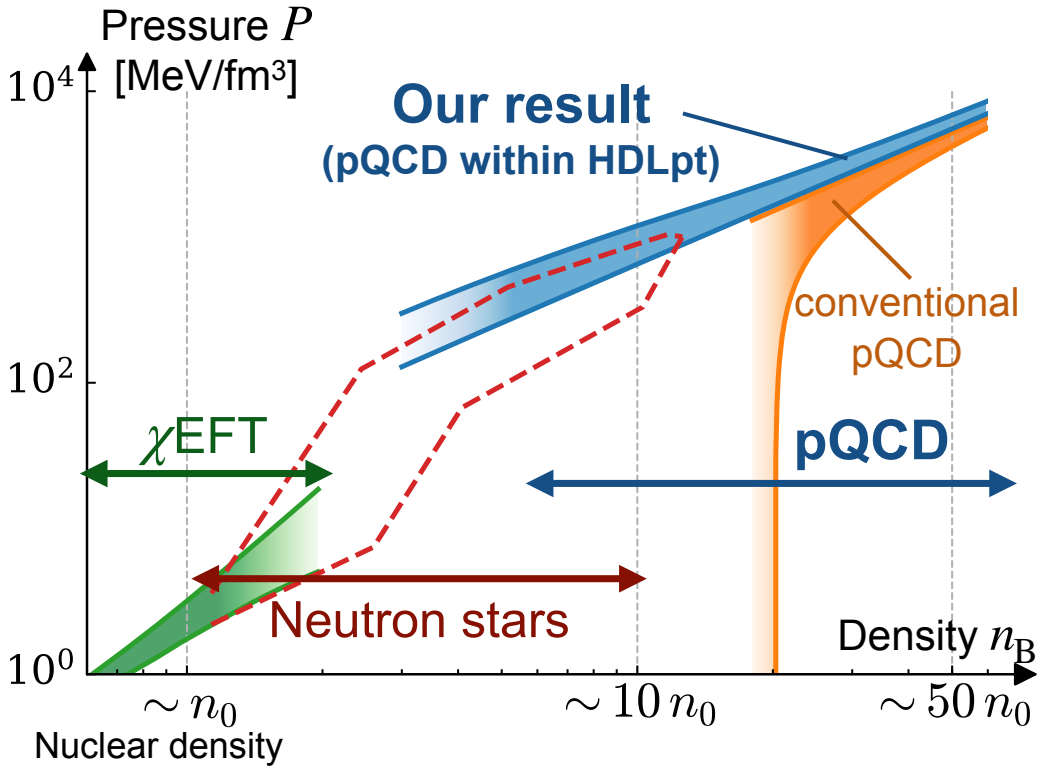

Fig. 2.5: Status of the QCD-based theoretical calculations. The χEFT result of PNM is adapted from Ref. [53] and the conventional pQCD result is from Ref. [60] using the concise fitting formula provided in Ref. [61]. The region enclosed by the dashed line is the extrapolation compatible with the $2\,M_\odot$ constraints from the χEFT calculation [112]. Our result is from Ref. [1].

of the pressure can be summarized as:

$$P = \overbrace{P_{\rm ideal}}^{\substack{\rm LO\\(1\text{-loop})}} + \overbrace{P_1^{\rm const}}^{\substack{\rm NLO\\(2\text{-loop})}}\alpha_s + \overbrace{P_2^{\rm const}}^{\substack{\rm NNLO\\(3\text{-loop})}}\alpha_s^2 + \overbrace{P_3^{\rm const}}^{\substack{\rm N^3LO\\(4\text{-loop})}}\alpha_s^3 + P_2^{\rm LL}\ \alpha_s^2\ln\alpha_s + P_3^{\rm NLL}\ \alpha_s^3\ln\alpha_s + P_3^{\rm LL}\ \alpha_s^3\ln^2\alpha_s\,, \tag{2.25}$$

where the pressure of the ideal Fermi gas, which is at the leading-order (LO), is

$$P_{\rm ideal} = \frac{N_{\rm c}N_{\rm f}}{12\pi^2}\mu^4\,, \tag{2.26}$$

with μ being the quark chemical potential. The next-to-leading order (NLO) coefficient $P_1^{\rm const}$ has been known since 1960; Refs. [196, 197] are the earliest literature to the best of our knowledge (see also Ref. [198]). The monumental works by Freedman and McLerran in 1976 [56–58] and by Baluni in 1977 [59] revealed the coefficients $P_2^{\rm const}$ and $P_2^{\rm LL}$ in Eq. (2.25); they performed the next-to-next-to-leading order calculations for massless QCD from the 3-loop Feynman diagrams.

Since their heroic achievement, we had to wait for about three decades until the pQCD EoS was augmented with the strange quark mass $m_{\rm s} \neq 0$ and applied to the neutron star phenomenology [60]. The earlier pQCD application can be found in Ref. [199] and the substantial strange mass effect was pointed out in Ref. [200].

Currently, the theoretical efforts are progressing toward further higher-order next-to-next-to-next-to-leading-order ($\rm N^3LO$) calculations [62–64] with the hope for better convergence. We note that this situation is very different from the finite-temperature case, where the perturbation theory breaks down above the three-loop order due to Linde's problem [201]. Linde's problem is caused by the chromomagnetic screening at the ultra-soft scale, which can only be obtained non-perturbatively. On the other hand, at zero temperature, the magnetic gluons are never screened, so that there is no Linde's problem and one can go beyond the three-loop order. Since the $\alpha_s^2\ln\alpha_s$ term is coming from the plasmon ring diagram, Gorda et al. [62] identified the leading-log (LL) term at $\rm N^3LO$, which takes the form of $\alpha_s^3\ln^2\alpha_s$, from the similar consideration of the ring diagram. Moreover, Fernandez and Kneur [202] adds all the leading-log terms and next-to-leading-log (NLL) terms, i.e., $\alpha_s^n\ln^{n-1}\alpha_s$ and $\alpha_s^n\ln^{n-2}\alpha_s$, up to infinite order based on the renormalization group optimization method [203]. All the known coefficients in Eq. (2.25) are summarized in Table 2.1.

In parameter space $T > 0$ and $\mu/T < 1$, where the lattice-QCD simulation is at work, the validity of alternative theoretical approaches has been tested. In particular, the Hard Thermal Loop perturbation theory (HTLpt) is the most promising resummation scheme [65, 204–215] that confronts the lattice-QCD results at high temperatures. In this approach, the pressure with the HTL-resummation is evaluated up to the three-loop order, i.e., NNLO. Another approach is based on the Φ-derivable approximation [216–222] in the two-particle-irreducible (2PI) skeleton expansion of the thermodynamic potential [223–225].

	Value	References
$P_1^{\rm const}$	$-\frac{2}{\pi}P_{\rm ideal}$	Akhiezer & Peletminskii (1960) [196] Salpeter (1961) [197]
$P_2^{\rm const}$	$-\frac{1}{\pi^2}\Big(18-11\ln 2+\beta_0\ln\frac{\bar{\Lambda}}{\mu}$ $-0.536N_{\rm f}+N_{\rm f}\ln\frac{N_{\rm f}}{\pi}\Big)P_{\rm ideal}$	Freedman & McLerran (1976) [56–58] Baluni (1977) [59]
$P_2^{\rm LL}$	$-\frac{N_{\rm f}}{\pi^2}P_{\rm ideal}$	
$P_3^{\rm LL}$	$-\frac{11(N_{\rm c}^2-1)N_{\rm f}}{32\pi^3}P_{\rm ideal}$	Gorda, Kurkela, Romatschke, Säppi & Vuorinen [62]

Table 2.1: The known pressure coefficients in Eq. (2.25) from massless pQCD evaluated within $\overline{\rm MS}$ scheme. The numerical values are for $N_{\rm c}=N_{\rm f}=3$ unless specified otherwise.

From the success of HTLpt and Φ-derivable approach at high T, it is natural anticipation that the same machinery of resummation would cure the convergence problem at high baryon density or large quark chemical potential μ as well, which may reduce the scale variation uncertainty. Indeed, the parallelism between the high T and high μ cases has been established based on the transport equation approach in Ref. [226]; the high-density counterparts of HTLs are called Hard Dense Loops (HDLs). As long as a resummation prescription in the quark sector is concerned, more simply, we can just take the $T\to 0$ limit of HTLpt to introduce "HDLpt" as considered in Ref. [227] (see also Ref. [206], and we note that the term "HDLpt" was first introduced in Ref. [110]). The existing NLO and NNLO calculations, however, involves the expansion of integrals with respect to the parameter $M_{\rm D}^2/T^2$, where $M_{\rm D}^2\propto g^2T^2$ is the Debye mass. Therefore, it is not straightforward to take $T\to 0$ limit in the existing calculations of HTLpt.

Besides, the HTL approximation usually neglects the bare quark mass and only the screening masses of quarks enter expressions used in Refs. [206,227]. Later on, extensive discussions about the EoS and the quark star properties have been addressed in Ref. [110]. As seen in Fig. 2 of Ref. [110], however, the HDLpt hardly remedies the convergence problem associated with the uncertainty of the scale $\bar{\Lambda}=\mu$–4μ in the running coupling constant $\alpha_s(\bar{\Lambda})$. In this work, we quantify the resummation effects on the EoS of cold and dense quark matter at high baryon density $n_{\rm B}$ or the energy density ε with the bare quark mass dependence for the first time.

The conventional pQCD calculation at the NNLO order or higher also involves the HTL resummation. As a matter of fact, in such calculations, the HTL resummation is not just an improvement, but necessary to circumvent the IR divergence. At NNLO, the HTL resummation does not include the vertex correction but just summing the plasmon ring diagrams to infinite orders. This sort of HTL resummation in the primitive form can be found in the earliest work by Gell-Mann and Brueckner, Freedman and McLerran, as well as Baluni. Along this line, now Gorda et al. [63, 64] include the

vertex correction as well at N^{3}LO. The pressure at N^{3}LO in Eq. (2.25) can be reorganized in to

$$P_3^{\rm const} + P_3^{\rm NLL} \ln \alpha_s + P_3^{\rm LL} \ln^2 \alpha_s = P_3^{\rm soft} + P_3^{\rm mixed} + P_3^{\rm hard} , \tag{2.27}$$

where the superscript "soft", "mixed", and "hard" refer to the scale of loop momentum k: as HTL involves the isolation of the soft and hard scales, $g\mu$ and μ, so that the diagrams only with $k \sim g\mu$ gives $P_3^{\rm soft}$, the diagrams only with $k \sim \mu$ gives $P_3^{\rm hard}$, and the diagrams with mixed loop momenta $k \sim \mu$ and $g\mu$ gives $P_3^{\rm mixed}$. Up to now, $P_3^{\rm soft}$ is obtained [63, 64], but the full $O(\alpha_s^3)$ result is still incomplete.

2.3.2 Chiral effective field theory and other calculations

As it is not the central topic of this thesis, we will only introduce the selected results of χEFT calculations. The virtue of the χEFT calculations is that they allow for the controlled uncertainty estimates; the uncertainty is dominated by the low energy constants that determine the leading two-pion-exchange three-body forces. The stellar matter EoS has been obtained up to NNLO [111, 112], and now the N^{3}LO calculations are available for PNM [54] and also for stellar matter [228].

As repeatedly mentioned, we cannot apply the lattice-QCD for calculating the QCD thermodynamics at $T = 0$ and $\mu > 0$. Nevertheless, an alternative approach based on lattice-QCD is possible. One can circumvent the sign problem by not calculating the EoS directly, but by calculating the EoS from the nuclear force obtained by lattice-QCD [229]; in this method, the lattice-QCD is used secondarily for the EoS calculation:

Also, a holographic approach to the EoS calculation is also possible, which can treat the strong-coupling gauge theory non-perturbatively. The gravity dual of QCD may probably exist, but it is currently out of reach, so the computation is carried out only for QCD-like theories (see Ref. [230] for the recent review).

Chapter 3

Review of QCD thermodynamics and resummation schemes

In this chapter, we will briefly mention the notion of HTL and various resummation schemes to include the HTL effect. First of all, the path integral expression for the partition function in imaginary time is formulated, which is needed for the EoS calculation. Then, the HTLs are exemplified by showing explicit calculations. The HTL resummation schemes introduced here are (i) the Braaten-Pisarski effective theory scheme, (ii) screened perturbation theory application to the HTL resummation (which is also called the HTL perturbation theory), and (iii) the 2PI expansion of thermodynamics with Φ-derivable approximation. The latter two, i.e., (ii) and (iii) are the methods we use in the later chapters.

3.1 Imaginary time formalism and path integrals for partition functions

In this thesis, we study QCD thermodynamics in a grand canonical ensemble. Thermal equilibrium is specified by temperature T (or the inverse temperature $\beta \equiv 1/T$) and the chemical potential μ_f for flavor-f quarks. Other relevant parameters are the bare flavor-f quark mass m_f.

The expectation value of time-independent operators $\hat{O}$ in the grand canonical ensemble is given by

$$\langle \hat{O} \rangle = \mathrm{tr}\left[\hat{\rho}\,\hat{O}\right], \tag{3.1}$$

where the density operator $\hat{\rho}$ and the partition function Z takes the form

$$\hat{\rho} = \frac{1}{Z} e^{-\beta(\hat{H}-\mu_f \hat{N}_f)}, \quad Z(T,\mu_f) = \mathrm{tr}\, e^{-\beta(\hat{H}-\mu_f \hat{N}_f)}. \tag{3.2}$$

The flavor-f quark number operator, which is conjugate to the chemical potential μ_f, is

$$\hat{N}_f = \int_{\boldsymbol{x}} \bar{\psi}_f \gamma^0 \psi_f . \tag{3.3}$$

In the path integral formalism, the matrix element of time evolution operators $e^{-i\hat{H}(t_f-t_i)}$ can be expressed as

$$\langle\varphi_f|e^{-i\hat{H}(t_f-t_i)}|\varphi_i\rangle = \int_{\varphi(t_i)=\varphi_i}^{\varphi(t_f)=\varphi_f} \mathcal{D}\varphi(\boldsymbol{x},t)\, e^{iS(\varphi)}\,, \tag{3.4}$$

where $iS(\varphi)$ is the action in the Minkowski space:

$$iS(\varphi) = i\int_{t_i}^{t_f} dt \int_{\boldsymbol{x}} \mathcal{L}_M(\boldsymbol{x},t)\,. \tag{3.5}$$

The Lagrangian in the Minkowski space is denoted as $\mathcal{L}_M$. Now, we can naturally generalize it to thermal equilibrium (as the operator $\mathcal{O}$ is now time independent, one can Wick rotate safely) by changing $t_i \to 0$, $t_f \to -i\beta$, and $t \to -i\tau$ in the path integral expression.

$$\langle\varphi_f|\,\hat{\rho}\,|\varphi_i\rangle = \frac{1}{Z}\langle\varphi_f|e^{-\beta\hat{H}}|\varphi_i\rangle = \frac{1}{Z}\int_{\varphi(0)=\varphi_i}^{\varphi(-i\beta)=\varphi_f} \mathcal{D}\varphi(\boldsymbol{x},t\to-i\tau)\, e^{-S_E(\varphi)}\,, \tag{3.6}$$

where the Euclidean action is defined as

$$iS(\varphi) \to -S_E(\varphi) = -\int_0^\beta d\tau \int_{\boldsymbol{x}} L_E(\boldsymbol{x},\tau)\,, \quad L_E \equiv -\mathcal{L}_M(t\to-i\tau)\,. \tag{3.7}$$

By setting $\varphi_i = \varphi_f$, which leads to $\langle\varphi_i|\hat{\rho}|\varphi_i\rangle = 1$, we finally arrive at the path integral representation of the partition function

$$Z = \int_{\varphi(\tau=\beta)=\varphi(\tau=0)} \mathcal{D}\varphi(\boldsymbol{x},\tau)\, e^{-S_E(\varphi)}\,. \tag{3.8}$$

We have now considered the bosonic φ and it should fulfill the periodic boundary condition at $\tau = \beta$: $\varphi(\tau=\beta) = \varphi(\tau=0)$. For fermion field ψ, the boundary condition is modified to the anti-periodic condition: $\psi(\tau=\beta) = -\psi(\tau=0)$[1]. In QCD, the gauge should be fixed carefully, but here we do not turn to this issue and follow the standard treatment as in Refs. [232, 233]. Since fields $\varphi(\tau)$ or $\psi(\tau)$ are either periodic or anti-periodic ($\varphi(\beta) = \varphi(0)$ or $\psi(\beta) = -\psi(0)$) in the imaginary time formalism, the Fourier transform is taken over a finite interval $\tau \in [0,\beta]$, so that it becomes a Fourier sum with a discrete frequency:

$$\varphi(\tau,\boldsymbol{x}) = T\sum_{n=-\infty}^{n=\infty} \tilde{\varphi}(\omega_n,\boldsymbol{x})e^{i\omega_n\tau}, \quad \omega_n = 2n\pi T\,, \tag{3.9}$$

$$\psi(\tau,\boldsymbol{x}) = T\sum_{n=-\infty}^{n=\infty} \tilde{\psi}(\omega_n,\boldsymbol{x})e^{i\tilde{\omega}_n\tau}, \quad \tilde{\omega}_n = (2n+1)\pi T\,, \tag{3.10}$$

where ω_n and $\tilde{\omega}_n$ are called (bosonic and fermionic) Matsubara frequencies.

Utilizing the path integral above, one can derive the conventional Feynman rules also in the imag-

[1] Interesting, the Fadeev-Popov ghost field, which is the grassmanian but bosonic degrees of freedom (scalar), follows the *periodic* condition [231].

inary time formalism. The procedure to calculate higher orders of perturbation theory is straightforward.

- Firstly, we split the Euclidean action S_E in the path integral into the free part and the interacting part:
$$S_E = S_E^{(\text{free})} + S_E^{(\text{int})} . \tag{3.11}$$

- Inside the path integral we expand e^{-S_E} in powers of $S_E^{(\text{int})}$. That is,
$$Z = \int_{\varphi(\tau=\beta)=\varphi(\tau=0)} \mathcal{D}\varphi\, e^{-S_E} \simeq \int_{\varphi(\tau=\beta)=\varphi(\tau=0)} \mathcal{D}\varphi\, e^{-S_E^{(\text{free})}} \left[1 - S_E^{(\text{int})} + \frac{1}{2}(S_E^{(\text{int})})^2 - \frac{1}{6}(S_E^{(\text{int})})^3 + \cdots\right] . \tag{3.12}$$

- Build the loop expansion with the propagators and vertices. When we perform the loop integral, we also sum over the Matsubara frequencies.

  The Euclidean propagator for bosons is
$$\langle\tilde{\varphi}(k_n, \boldsymbol{k})\tilde{\varphi}(q_n, \boldsymbol{q})\rangle = \beta\delta_{k_n+q_n,0}(2\pi)^3\delta^3(\boldsymbol{k}+\boldsymbol{q})\frac{1}{k_n^2 + E_k^2} , \tag{3.13}$$
  where k_n and q_n are bosonic Matsubara frequencies and $E_k = \sqrt{\boldsymbol{k}^2 + m^2}$. The fermionic Euclidean propagator is
$$\langle\tilde{\psi}(\tilde{k}_n, \boldsymbol{k})\tilde{\bar{\psi}}(\tilde{q}_n, \boldsymbol{q})\rangle = \beta\delta_{\tilde{k}_n+\tilde{q}_n,0}(2\pi)^3\delta^3(\boldsymbol{k}+\boldsymbol{q})\frac{-(i\gamma^0\tilde{k}_n - \boldsymbol{\gamma}\cdot\boldsymbol{k})}{\tilde{k}_n^2 + E_k^2} , \tag{3.14}$$
  where the fermionic Matsubara frequency reads $\tilde{k}_n = (2n+1)\pi T + i\mu$. The Feynman rules for vertices can be read out from field theory at $T = 0$.

- When taking the Matsubara sum, the conventional procedure is to convert it to the contour integral by using the Bose-Einstein distribution $f_{\text{B}}(\omega)$ and the Fermi-Dirac distribution $f_{\text{F}}(\omega)$, which are defined as
$$f_{\text{B}}(\omega) \equiv \frac{1}{e^{\beta\omega} - 1} , \quad f_{\text{F}}(\omega) \equiv \frac{1}{e^{\beta\omega} + 1} . \tag{3.15}$$
  It is possible because the Bose-Einstein and the Fermi-Dirac distributions possess poles at $2n\pi T$ and $(2n+1)\pi T$, which exactly coincide with the bosonic and fermionic Matsubara frequencies, respectively. See Sec. 4.2 for the concrete procedure.

3.2 Hard thermal loops

Hard thermal loops (HTLs) refer to the diagrams that the "hard" loop momentum of the scale T saturate the loop integral; it gives the leading behavior in temperature $\propto T^2$. This leading behavior is

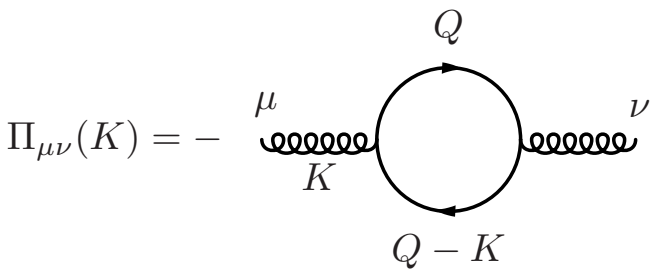

Fig. 3.1: One-loop contribution to the gluon self-energy $\Pi_{\mu\nu}(K)$.

due to the quadratic divergence in the loop integral: at finite temperature, this quadratic UV divergence $\propto k^2$ is cut off at $\lesssim T$ by either the Bose-Einstein or the Fermi-Dirac distribution.

3.2.1 Hard thermal loop approximation

The leading behavior in temperature $\propto T^2$ is extracted with ease in the HTL approximation. The HTL approximation has already been employed in various literature [234–237] (see also Refs. [238, 239]) even before the concept of HTL; the interpretation of the approximation was clarified later by Braaten and Pisarski [7, 108, 240] (see, e.g., Ref. [241] for the comprehensive review; some of the discussion below follows this paper).

Now let us take the quark-loop contribution to the gluon self-energy diagram shown in Fig. 3.1 as an example of the HTL approximation. The approximation can be defined by the following steps:

HTL approximation

(1) Consider *soft* external momentum of the scale $K \sim gT$. Neglect all the external momenta in numerators (which is $\not{K}$).

(2) Sum over all Matsubara frequencies $\tilde{\omega}_n$ inside the loops (precisely speaking, this step does not involve any approximations, but it is anyways necessary for the HTL approximation).

(3) Expand the spatial component of external momenta over the loop momenta (which is k/q), then integrate over *hard* spatial loop momenta $q \sim T$.

3.2.2 Gluon self-energy in the HTL approximation

We will demonstrate the HTL approximation by computing the gluon self-energy diagram shown in Fig. 3.1. We treat quarks as massless for simplicity. Using the Feynman rules in the above-mentioned imaginary time and the path integral formalism, one can express it as

$$\Pi_{\mu\nu}(K) = g^2 \frac{N_\mathrm{f}}{2} \sum\!\!\!\!\!\!\int_Q \frac{\mathrm{tr}[\gamma_\mu^E \not{Q} \gamma_\nu^E (\not{Q} - \not{K})]}{Q^2 (Q-K)^2} \,, \tag{3.16}$$

where we define the Euclidean momenta as $K_\mu = (k_4, \boldsymbol{k}) = (-\omega, \boldsymbol{k})$ and $Q_\mu = (-\tilde{\omega}_n, \boldsymbol{q})$ with $K^2 = \omega^2 + \boldsymbol{k}^2$ and $Q^2 = \tilde{\omega}_n^2 + \boldsymbol{q}^2$. We will also denote $\hat{\boldsymbol{q}} = \boldsymbol{q}/q$. We use the following shorthand notation for the Matsubara sum and spatial integration:

$$\sum\!\!\!\!\!\!\int_Q \equiv T\sum_n \int_{\boldsymbol{q}}, \quad \int_{\boldsymbol{q}} \equiv \int \frac{d^3\boldsymbol{q}}{(2\pi)^3}\,. \tag{3.17}$$

Also, we define the Euclidean Dirac matrices γ_μ^E as $\gamma_0^E \equiv i\gamma_0$ and $\gamma_i^E \equiv \gamma_i$, so that they follow the anti-commutation relation $\{\gamma_\mu^E, \gamma_\nu^E\} = -2\delta_{\mu\nu}$.

HTL approximation: Step (1) neglect the soft scale in the numerator In this step, we neglect the $\not{K}$-term in the nominator corresponding to the soft external momentum and carry out the Dirac algebra. It leads to

$$\begin{aligned}
\Pi_{\mu\nu}(K) &\simeq g^2\frac{N_\mathrm{f}}{2}\sum\!\!\!\!\!\!\int_Q \frac{8Q_\mu Q_\nu - 4Q^2\delta_{\mu\nu}}{Q^2(Q-K)^2}\,,\\
&= 4g^2N_\mathrm{f}\sum\!\!\!\!\!\!\int_Q \frac{Q_\mu Q_\nu}{Q^2(Q-K)^2} - 2\delta_{\mu\nu}g^2N_\mathrm{f}\sum\!\!\!\!\!\!\int_Q \frac{1}{(Q-K)^2}\,,\\
&= 4g^2N_\mathrm{f}\sum\!\!\!\!\!\!\int_Q \frac{Q_\mu Q_\nu}{(\tilde{\omega}_n^2+E_{\boldsymbol{q}}^2)[(\tilde{\omega}_n-\omega)^2+E_{\boldsymbol{q}-\boldsymbol{k}}^2]} - 2\delta_{\mu\nu}g^2N_\mathrm{f}\sum\!\!\!\!\!\!\int_Q \frac{1}{\tilde{\omega}_n^2+E_{\boldsymbol{q}}^2}\,,\\
&\equiv I_{\mu\nu} - \delta_{\mu\nu}J\,.
\end{aligned} \tag{3.18}$$

In the last line, we have defined the integrals $I_{\mu\nu}$ and J.

HTL approximation: Step (2) carry out Matsubara sum In this step, we carry out the Matsubara sum for the integral $I_{\mu\nu}$ and J. The Matsubara sum is performed by the usual contour integral technique. As emphasized above, there is no approximation in this step, but it is necessary for the later step of the approximation.

Firstly, the frequency sum for J can be evaluated as [232]:

$$J = 2g^2N_\mathrm{f}\sum\!\!\!\!\!\!\int_Q \frac{1}{\tilde{\omega}_n^2+E_{\boldsymbol{q}}^2} = 2g^2N_\mathrm{f}\int_{\boldsymbol{q}}\frac{1}{2E_{\boldsymbol{q}}}[1-2f_\mathrm{F}(E_{\boldsymbol{q}})]\,. \tag{3.19}$$

Next, we evaluate the Matsubara sum for the (ij)-component of the integral $I_{\mu\nu}$:

$$\begin{aligned}
I_{ij} &= 4g^2N_\mathrm{f}\sum\!\!\!\!\!\!\int_Q \frac{q_iq_j}{(\tilde{\omega}_n^2+E_{\boldsymbol{q}}^2)[(\tilde{\omega}_n-\omega)^2+E_{\boldsymbol{q}-\boldsymbol{k}}^2]}\\
&= -\frac{g^2N_\mathrm{f}}{2\pi^2}\int\frac{q^2dqd\Omega}{4\pi}\frac{q^2\hat{q}_i\hat{q}_j}{E_{\boldsymbol{q}}E_{\boldsymbol{k}-\boldsymbol{q}}}\left[(1-f_\mathrm{F}(E_{\boldsymbol{q}})-f_\mathrm{F}(E_{\boldsymbol{q}-\boldsymbol{k}}))\left(\frac{1}{i\omega-E_{\boldsymbol{q}}-E_{\boldsymbol{q}-\boldsymbol{k}}}-\frac{1}{i\omega+E_{\boldsymbol{q}}+E_{\boldsymbol{q}-\boldsymbol{k}}}\right)\right.\\
&\qquad\left.-(f_\mathrm{F}(E_{\boldsymbol{q}})-f_\mathrm{F}(E_{\boldsymbol{q}-\boldsymbol{k}}))\left(\frac{1}{i\omega+E_{\boldsymbol{q}}-E_{\boldsymbol{q}-\boldsymbol{k}}}-\frac{1}{i\omega-E_{\boldsymbol{q}}+E_{\boldsymbol{q}-\boldsymbol{k}}}\right)\right]\,,
\end{aligned} \tag{3.20}$$

where we defined as

$$E_{\boldsymbol{q}} = q, \quad E_{\boldsymbol{q}-\boldsymbol{k}} = |\boldsymbol{q}-\boldsymbol{k}|, \quad \cos\theta = (\boldsymbol{k}\cdot\boldsymbol{q})/(kq), \quad d\Omega = d\cos\theta d\phi\,. \tag{3.21}$$

Similarly, the Matsubara sum for the $(4i)$-component of the integral can be evaluated as:

$$\begin{aligned} I_{4i} &= 4g^2N_{\rm f}\sum\!\!\!\!\!\!\int_Q \frac{\tilde{\omega}_n q_i}{(\tilde{\omega}_n^2+E_{\boldsymbol{q}}^2)[(\tilde{\omega}_n-\omega)^2+E_{\boldsymbol{q}-\boldsymbol{k}}^2]} \\ &= \frac{g^2N_{\rm f}}{2\pi^2}\int\frac{q^2dqd\Omega}{4\pi}\frac{iq\hat{q}_i}{E_{\boldsymbol{k}-\boldsymbol{q}}}\left[(1-f_{\rm F}(E_{\boldsymbol{q}})-f_{\rm F}(E_{\boldsymbol{q}-\boldsymbol{k}}))\left(\frac{1}{i\omega-E_{\boldsymbol{q}}-E_{\boldsymbol{q}-\boldsymbol{k}}}+\frac{1}{i\omega+E_{\boldsymbol{q}}+E_{\boldsymbol{q}-\boldsymbol{k}}}\right)\right. \\ &\qquad \left.+(f_{\rm F}(E_{\boldsymbol{q}})-f_{\rm F}(E_{\boldsymbol{q}-\boldsymbol{k}}))\left(\frac{1}{i\omega+E_{\boldsymbol{q}}-E_{\boldsymbol{q}-\boldsymbol{k}}}+\frac{1}{i\omega-E_{\boldsymbol{q}}+E_{\boldsymbol{q}-\boldsymbol{k}}}\right)\right]. \end{aligned} \tag{3.22}$$

By using the relation $\tilde{\omega}_n^2 = Q^2 - \boldsymbol{q}^2$, (44)-component of the integrals can be related to J and I_{ij}, which are already obtained above:

$$I_{44} = 2J - \delta_{ij}I_{ij}\,. \tag{3.23}$$

HTL approximation: Step (3) carry out loop integral over the hard scale In this step, we will treat q is large, which is the origin of the term "hard thermal loop." We will only keep terms that depend on T and those that do not are simply dropped.

Firstly, J from Eq. (3.19) can further be approximated as

$$J \simeq 2g^2N_{\rm f}\int_{\boldsymbol{q}}\frac{1}{E_{\boldsymbol{q}}}f_{\rm F}(E_{\boldsymbol{q}}) = -N_{\rm f}\frac{g^2T^2}{12} \tag{3.24}$$

Supposing that q is large, we expand $E_{\boldsymbol{q}-\boldsymbol{k}}$ in terms of k/q, so that

$$E_{\boldsymbol{q}-\boldsymbol{k}} = |\boldsymbol{q}-\boldsymbol{k}| = q\sqrt{1-2(\boldsymbol{q}\cdot\boldsymbol{k})/q^2+k^2/q^2} \simeq q - k\cos\theta\,, \tag{3.25}$$

$$f_{\rm F}(E_{\boldsymbol{q}-\boldsymbol{k}}) \simeq f_{\rm F}(q-k\cos\theta) \simeq f_{\rm F}(q) - k\cos\theta\frac{df_{\rm F}(q)}{dq}\,. \tag{3.26}$$

And the denominators of Eqs. (3.20) and (3.22) significantly simplify, and take the form

$$i\omega + E_{\boldsymbol{q}} - E_{\boldsymbol{q}-\boldsymbol{k}} \simeq i\omega - \boldsymbol{k}\cdot\hat{\boldsymbol{q}} = K\cdot\hat{Q}\,, \tag{3.27}$$

where we define $\hat{Q}_\mu = (-i, \hat{\boldsymbol{q}})$. Using this relation, we can approximate Eq. (3.20) as

$$\begin{aligned} I_{ij} &\simeq -\frac{g^2N_{\rm f}}{\pi^2}\int\frac{q^2dqd\Omega}{4\pi}\hat{q}_i\hat{q}_j\left(\frac{f_{\rm F}(q)}{q}-\frac{df_{\rm F}(q)}{dq}+\frac{df_{\rm F}(q)}{dq}\frac{i\omega}{K\cdot\hat{Q}}\right) \\ &= -N_{\rm f}\frac{g^2T^2}{12}\delta_{ij} + N_{\rm f}\frac{g^2T^2}{6}\int\frac{d\Omega}{4\pi}\frac{i\omega}{K\cdot\hat{Q}}\hat{q}_i\hat{q}_j\,, \end{aligned} \tag{3.28}$$

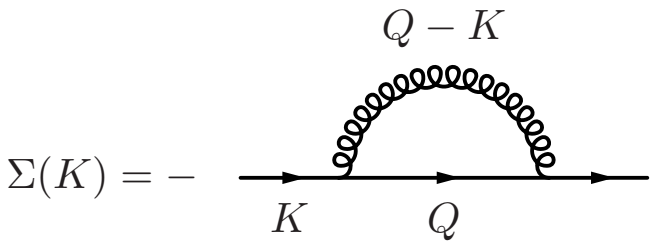

Fig. 3.2: One-loop contribution to the quark self-energy $\Sigma(K)$.

and Eq. (3.22) as

$$\begin{aligned} I_{4i} &\simeq -\frac{g^2 N_\mathrm{f}}{\pi^2}\int \frac{q^2 dq d\Omega}{4\pi}\hat{q}_i \frac{df_\mathrm{F}(q)}{dq}\frac{\omega}{K\cdot\hat{Q}} \\ &= N_\mathrm{f}\frac{g^2T^2}{6}\int\frac{d\Omega}{4\pi}\frac{\omega\hat{q}_i}{K\cdot\hat{Q}}\,. \end{aligned} \tag{3.29}$$

Plugging all these integrals J and $I_{\mu\nu}$ in Eq. (3.18), we finally get the quark-loop contribution to the gluon self-energy in the HTL approximation:

$$\hat{\Pi}_{\mu\nu} = \hat{M}_\mathrm{D}^2\int\frac{d\Omega}{4\pi}\left(\delta_{\mu 4}\delta_{\nu 4} + \frac{i\omega\hat{Q}_\mu\hat{Q}_\nu}{K\cdot\hat{Q}}\right). \tag{3.30}$$

Note that the caret in $\hat{\Pi}$ means that it is the HTL quantity, which is evaluated in the HTL approximation. The coefficient $\hat{M}_\mathrm{D}$ in front is the QCD Debye mass which takes the form by including the additional contributions from gluon-loops and quark chemical potential:

$$\hat{M}_\mathrm{D}^2 \equiv \frac{g^2}{3}\left(N_\mathrm{c}+\frac{1}{2}N_\mathrm{f}\right)T^2 + \frac{g^2 N_\mathrm{f}}{2\pi^2}\mu^2\,. \tag{3.31}$$

Note that this is also the HTL quantity with a caret symbol.

3.2.3 Quark self-energy

We compute the quark self-energy diagram shown in Fig. 3.2. Here we also include the bare quark masses m_f. It can be calculated similarly to the gluon self-energy case:

$$\Sigma_f(K) = -g^2 C_F \sum\!\!\!\!\!\!\int_Q \frac{\gamma_\mu^E \not{Q} \gamma_\mu^E}{(\tilde{\omega}_n^2 + E_{\boldsymbol{q}}^2)[(\tilde{\omega}_n-\omega)^2 + E_{\boldsymbol{q}-\boldsymbol{k}}^2]}\,. \tag{3.32}$$

By performing Matsubara sum, we arrive at

$$\begin{aligned}\Sigma_f(K) = -g^2 C_F \int_q \frac{1}{E_q E_{q-k}} \Bigg\{ & \frac{f(-E_q, \boldsymbol{q})}{i\omega + E_q + E_{q-k}} \Big[1 + f_{\rm B}(E_{q-k}) - f_{\rm F}(E_q - \mu_f)\Big] \\ & + \frac{f(-E_q, \boldsymbol{q})}{i\omega + E_q - E_{q-k}} \Big[f_{\rm F}(E_q - \mu_f) + f_{\rm B}(E_{q-k})\Big] \\ & + \frac{f(E_q, \boldsymbol{q})}{i\omega - E_q + E_{q-k}} \Big[-f_{\rm F}(E_q + \mu_f) - f_{\rm B}(E_{q-k})\Big] \\ & + \frac{f(E_q, \boldsymbol{q})}{i\omega - E_q - E_{q-k}} \Big[-1 - f_{\rm B}(E_{q-k}) + f_{\rm F}(E_q + \mu_f)\Big] \Bigg\} , \end{aligned} \tag{3.33}$$

where $E_q = \sqrt{\boldsymbol{q}^2 + m_f^2}$ and $E_{q-k} = |\boldsymbol{q} - \boldsymbol{k}|$. We define the function f in the nominators as

$$f(\pm E_q, \boldsymbol{q}) = (D-2)\Big[\pm E_q \gamma^0 + \boldsymbol{q}\cdot\boldsymbol{\gamma}\Big] + D m_f \mathbf{1} , \tag{3.34}$$

with $D = 4 - 2\epsilon$ being the dimension of the Minkowski theory. Note that the Dirac matrices are now in the Minkowskian convention.

We will again carry out the HTL approximation by expanding E_q and E_{q-k} in terms of the hard loop momentum q:

$$E_q = \sqrt{\boldsymbol{q}^2 + m_f^2} \simeq q, \quad E_{q-k} \simeq q - k\cos\theta \tag{3.35}$$

In the strict sense, neglecting the bare quark mass m_f is not the HTL approximation; the bare quark mass does not follow the soft gT or hard T scales in the HTL hierarchy, so the full m_f-dependence in E_q can be kept intact. It is, however, customary to neglect m_f as well in the HTL approximation, as $m_f \ll \mu_f$ in any cases.

After analytic continuation to the Minkowski space, we obtain the quark self-energy expression

$$\hat{\Sigma}_f(k_0, k) = \hat{M}_{{\rm q}f}^2 \int \frac{d\Omega}{4\pi} \frac{\not{y}}{k_\mu y^\mu} , \tag{3.36}$$

where we define a light-like vector $y^\mu = (1, \hat{\boldsymbol{y}})$. The coefficient $\hat{M}_{{\rm q}f}$ in front is the quark screening mass:

$$\hat{M}_{{\rm q}f}^2 \equiv \frac{g^2}{8} \frac{N_{\rm c}^2 - 1}{2N_{\rm c}} \left(T^2 + \frac{\mu_f^2}{\pi^2} \right) . \tag{3.37}$$

3.2.4 Need for resummation

We can understand why we need HTL resummation by the simple comparison between the kinetic term and the interaction, or the fluctuation term. Let us consider the minimal coupling in QCD:

$$\partial_\mu + igA_\mu \sim k_\mu + ig\bar{A} , \tag{3.38}$$

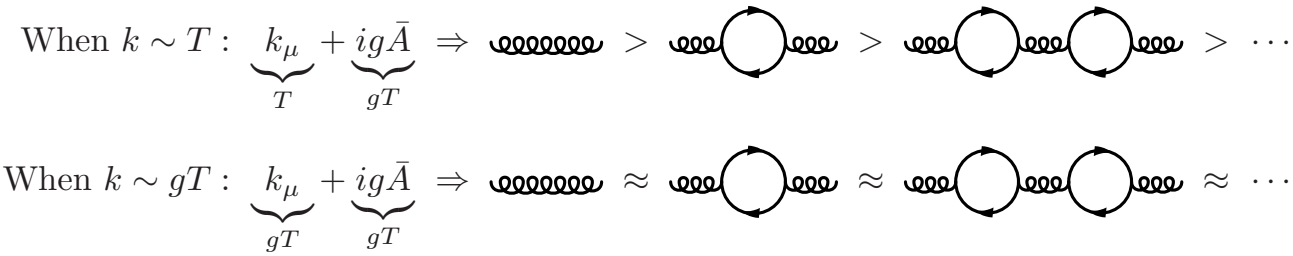

Fig. 3.3: Diagrammatic argument of the need for HTL resummation.

where the first term corresponds to the momentum in the kinetic term; it is the momentum that appears as the external momentum in the Feynman diagram. The second term corresponds to the typical gauge fluctuations. We define it as $\bar{A} \equiv \sqrt{\langle A^2 \rangle_T} \sim \sqrt{\hat{\Pi}}/g$. From the calculations in the preceding subsections, we already know that the gluon self-energy has the scale $\hat{\Pi} \sim g^2 T^2$. Therefore, the typical gauge fluctuations $\bar{A} \sim T$. If the magnitude of the kinetic term is larger than the interaction term, i.e. $k_\mu \gg ig\bar{A}$, then one can treat this mode perturbatively.

We will now refer to Fig. 3.3 for the explanation. When the kinetic term is of the scale of $k \sim T$, then the typical gauge fluctuation is of the scale of T, so that the condition $k_\mu \gg ig\bar{A}$ is satisfied. If we roughly evaluate the diagram above in Fig. 3.3, then one obtains

$$\begin{aligned} &\frac{1}{k^2} + \frac{1}{k^2}\Pi\frac{1}{k^2} + \frac{1}{k^2}\Pi\frac{1}{k^2}\Pi\frac{1}{k^2} + \cdots \\ &\sim \frac{1}{T^2} + \frac{1}{T^2}(gT)^2\frac{1}{T^2} + \frac{1}{T^2}(gT)^2\frac{1}{T^2}(gT)^2\frac{1}{T^2} + \cdots \\ &\sim \frac{1}{T^2} + \frac{g^2}{T^2} + \frac{g^4}{T^2} + \cdots . \end{aligned} \tag{3.39}$$

There is a clear hierarchy in the g^2-expansion, so that the diagrams can be perturbatively treated.

However, when the momentum is of the scale of $k \sim gT$ (see the lower panel of Fig. 3.3), then the magnitude of the kinetic term and the interaction term becomes similar: $k_\mu \sim ig\bar{A}$. Then the upshot is,

$$\begin{aligned} &\frac{1}{k^2} + \frac{1}{k^2}\Pi\frac{1}{k^2} + \frac{1}{k^2}\Pi\frac{1}{k^2}\Pi\frac{1}{k^2} + \cdots \\ &\sim \frac{1}{(gT)^2} + \frac{1}{(gT)^2}(gT)^2\frac{1}{(gT)^2} + \frac{1}{(gT)^2}(gT)^2\frac{1}{(gT)^2}(gT)^2\frac{1}{(gT)^2} + \cdots \\ &\sim \frac{1}{(gT)^2} + \frac{1}{(gT)^2} + \frac{1}{(gT)^2} + \cdots . \end{aligned} \tag{3.40}$$

All the diagrams, with an arbitrary number of loops, shown below in Fig. 3.3 contribute equally. This schematic calculation clearly delineates that the gluon self-energy $\Pi_{\mu\nu}$ is the same order of magnitude as the bare propagator. Therefore, these diagrams should be treated on the same footing, and thus added up to infinite orders. This is the essential ideal of the HTL resummation. If we resum all the

HTL diagrams, what we get is the resummed full propagator:

$$\frac{1}{k^2}+\frac{1}{k^2}\Pi\frac{1}{k^2}+\frac{1}{k^2}\Pi\frac{1}{k^2}\Pi\frac{1}{k^2}+\cdots=\frac{1}{k^2-\Pi}\,. \tag{3.41}$$

We have only shown the calculation of the gluon self-energy, but the same discussion applies to the quark self-energy Σ. Moreover, the three-, and four-gluon vertices Γ are also of the same order of magnitude as the bare propagator and the bare vertices. It is true when all external momenta are of the soft scale gT, and this separation of the scale is crucial in the HTL machinery. The HTL resummation can be regarded as the generalization of the Gell-Mann–Brueckner type resummation, in which only the resummation of the propagator is concerned, but the HTL resummation is somewhat different as it also involves the vertex correction.

Here, several comments are in order. The HTLs are independent of the gauge fixing methods. This has been verified by the explicit calculations [7,242], and the general proof has been given by Blaizot and Iancu within the kinetic theory approach in Refs. [243,244]. The gauge-fixing independent nature of HTLs demonstrates that only physical excitations contribute to the collective motions.

We also note that the major impetus for pursuing the HTL resummation was to solve the convergence problem of the EoS of hot QCD matter. It has been known since the old-time that the EoS exhibits the highly oscillatory behavior. That is, if we compute the hot QCD EoS in the perturbative expansion with respect to g, then the behavior completely changes order by order (see, e.g., [245,246] for the $O(g^5)$ calculations). The pressure P normalized with the free gas value $P_{\rm SB}$ is always $P/P_{\rm SB}<1$ for $O(g^2)$ calculation. Things change drastically for the $O(g^3)$ and $O(g^4)$ calculations; the normalized pressure always exceeds the unity, i.e., $P/P_{\rm SB}>1$. If we include the $O(g^5)$ contribution, however, then it again shows $P/P_{\rm SB}<1$ behavior. We were not able to go beyond $O(g^5)$ perturbatively due to Linde's problem. It was a big problem in the late 1990s, and now it seems to be solved after the reliable lattice-QCD calculations [42,43] have come out. The approaches mentioned in the following sections, especially the HTL perturbation theory, concern the convergence problem in QCD thermodynamics. Finally, we note that there seems to be no such convergence problem at $T=0$ and $\mu>0$: the higher-order perturbative correction does not change the behavior of the pressure as drastically as in the finite-temperature QCD.

3.3 Braaten-Pisarski resummation scheme

From the discussion in the last subsection, we see the necessity of resummation. Thus, we need to develop the effective expansion in terms of the effective, or dressed, propagators and vertices. In this section, we will briefly mention a systematic reorganization of the perturbative series put forth by Braaten and Pisarski [7,108,240], which takes into account the effective propagators and vertices.

We will first explain the effective action for the HTL resummation. Then we will proceed to the elementary building blocks of the Braaten-Pisarski scheme, which are the dressed propagators and vertices; these can be derived from the HTL effective action.

The HTL effective action, which was firstly discovered by Taylor and Wong [247], can be divided into the gluon and quark part:

$$\mathcal{L}_{\mathrm{HTL}} = \mathcal{L}_{\mathrm{HTL,\,g}} + \mathcal{L}_{\mathrm{HTL,\,q}}\,. \tag{3.42}$$

The expression of the quark self-energy in Eq. (3.36) suggests the form of the quark part of the HTL Lagrangian:

$$\mathcal{L}_{\mathrm{HTL,\,q}} = \hat{M}_{\mathrm{q}f}^2 \bar{\psi}(k) \int \frac{d\Omega}{4\pi} \frac{\not{y}}{y^\mu k_\mu} \psi(-k)\,. \tag{3.43}$$

As the inverse Fourier transform implies that $p_\mu \to -i\partial_\mu$, this can be made into the real space

$$\mathcal{L}_{\mathrm{HTL,\,q}} = i\hat{M}_{\mathrm{q}f}^2 \bar{\psi}(x) \int \frac{d\Omega}{4\pi} \frac{\not{y}}{y^\mu \partial_\mu} \psi(x)\,. \tag{3.44}$$

This expression is still gauge-variant, so in order to maintain the gauge-invariance, we will replace ∂_μ with the covariant derivative D_μ

$$\mathcal{L}_{\mathrm{HTL,\,q}} = i\hat{M}_{\mathrm{q}f}^2 \bar{\psi}(x) \int \frac{d\Omega}{4\pi} \frac{\not{y}}{y \cdot D} \psi(x)\,. \tag{3.45}$$

Gluon effective action can be derived likewise. Using the gluon-self energy expression in Eq. (3.30),

$$\mathcal{L}_{\mathrm{HTL,\,g}} = \frac{1}{2} \operatorname{tr} A_\mu \hat{\Pi}_{\mu\nu} A_\nu\,, \tag{3.46}$$

from which we will obtain after the similar calculation above,

$$\mathcal{L}_{\mathrm{HTL,\,g}} = -\frac{1}{2} \hat{M}_{\mathrm{D}}^2 \operatorname{tr} \int \frac{d\Omega}{4\pi} F_{\mu\rho} \frac{y^\rho y^\sigma}{(y \cdot D)^2} F^\mu_{\ \sigma}\,. \tag{3.47}$$

Finally we obtain the HTL effective Lagrangian:

$$\mathcal{L}_{\mathrm{HTL}} = -\frac{1}{2} \hat{M}_{\mathrm{D}}^2 \operatorname{tr} \left(F_{\mu\rho} \left\langle \frac{y^\rho y^\sigma}{(y \cdot D)^2} \right\rangle_y F^\mu_{\ \sigma} \right) + i\hat{M}_{\mathrm{q}f}^2 \bar{\psi}_f \left\langle \frac{\not{y}}{y \cdot D} \right\rangle_y \psi_f\,, \tag{3.48}$$

where $y = (1, \hat{\boldsymbol{y}})$ is the light-like vector. We understand $\langle \cdots \rangle_y$ as the average over the $\hat{\boldsymbol{y}}$ direction, i.e., carrying out the $d\Omega$ integration. The definitions of the QCD Debye mass $\hat{M}_{\mathrm{D}}$ and the quark screening mass $\hat{M}_{\mathrm{q}f}$ are given in Eqs. (3.31) and (3.37), respectively. This effective Lagrangian is proven to be gauge-invariant [247] (see also Refs. [248, 249] for its connection to the Chern-Simons action).

From this Lagrangian, one can derive the gluon and quark dressed inverse propagators D and S_f

$$\begin{aligned} D_{\mu\nu}^{-1}(\omega, k) &= D_{0,\mu\nu}^{-1}(\omega, k) + \hat{\Pi}_{\mu\nu}(k)\,, \\ S_f^{-1}(\omega, k) &= S_0^{-1}(k) + \hat{\Sigma}_f(\omega, k)\,. \end{aligned} \tag{3.49}$$

where $D_{0,\mu\nu}^{-1}$ and S_0^{-1} are the gluon and quark free inverse propagators. We can also derive the dressed

vertices such as

$$^*\Gamma^a_\mu(k;q_1,q_2) = t^a\gamma_\mu + \hat{\Gamma}^a_\mu(k;q_1,q_2)\,, \tag{3.50}$$

from the effective Lagrangian. Indeed, from $\delta\mathcal{L}_{\mathrm{HTL,\,q}}/\delta\bar{\psi}\delta\psi\delta A_\mu$, one can obtain

$$\hat{\Gamma}^a_\mu(k;q_1,q_2) = -\hat{M}^2_{\mathrm{q}f}t^a\int\frac{d\Omega}{4\pi}\frac{y_\mu\not{y}}{(q_1\cdot y)(q_2\cdot y)}\,. \tag{3.51}$$

In the Braaten-Pisarski scheme, when we calculate the Feynman diagrams we use different propagators and vertices according to the scale of the loop momentum involved. Namely, for hard modes, we simply apply the bare propagators and vertices, while for soft modes we use the dressed propagators and vertices. In this scheme, we supplement the bare QCD Lagrangian with the HTL Lagrangian:

$$\mathcal{L}_{\mathrm{QCD}} = \mathcal{L}_{\mathrm{QCD}} + \mathcal{L}_{\mathrm{HTL}} - \mathcal{L}_{\mathrm{HTL}} = \mathcal{L}_{\mathrm{eff}} + \Delta\mathcal{L}\,, \tag{3.52}$$

and the added part will be regarded as the HTL effective theory while the subtraction is regarded as a counter term to avoid double counting of the HTLs.

We note that the recent enterprise on the pQCD calculation at $T = 0$ [62–64] and $T \lesssim g\mu$ [250] adopt this HTL-resummation scheme. Their physical picture is that the quarks are filled up to μ_f in the Fermi sphere, so that the low momentum quarks are Pauli blocked. Therefore they only consider the hard mode for the quarks, and no resummation is included in the quark sector.

3.4 Screened perturbation theory: HTL perturbation theory

Another way to include the HTL-resummation effect is the HTL perturbation theory (HTLpt). Later on in this thesis, we will use this approach. It is considered as an application of the screened perturbation theory to QCD.

To see how the screened perturbation theory works, let us first take the massless scalar theory as an example. The Minkowskian Lagrangian for the massless scalar theory reads:

$$\mathcal{L} = \frac{1}{2}\partial_\mu\phi\partial^\mu\phi - \frac{\lambda}{4!}\phi^4\,. \tag{3.53}$$

At non-finite temperature, it is well known that the conventional perturbative expansion is spoiled by the IR divergence (see, e.g., Ref. [233] for the standard discussion). Nevertheless, this IR divergence can be removed by resumming the higher-order ring diagrams that generate a thermal screening mass of order $m_{\mathrm{eff}} \sim gT$, which results in the perturbative series with an expansion in powers of $\sqrt{\lambda}$, not λ.

Alternatively, this screening effect can also be reproduced by using the screened perturbation theory [251], or more systematically by using the optimized perturbation theory [252] (we note that this is the field-theoretical analog of the variational perturbation theory à la Feynman and Kleinert [253]). In these theories, we include the screening effect by supplementing the effective mass term $-\frac{1}{2}m^2_{\mathrm{eff}}\phi^2$

into the original theory and subtracting the effective term so that the total Lagrangian does not change:

$$\mathcal{L} = \underbrace{\frac{1}{2}\partial_\mu\phi\partial^\mu\phi - \frac{1}{2}m_{\rm eff}^2\phi^2}_{\mathcal{L}'_{\rm (free)}} + \underbrace{\frac{1}{2}m_{\rm eff}^2\phi^2 - \frac{\lambda}{4!}\phi^4}_{\mathcal{L}'_{\rm (int)}} . \tag{3.54}$$

Now we treat the $\mathcal{L}'_{\rm (free)}$ as the free theory and $\mathcal{L}'_{\rm (int)}$ as an interaction of order λ. The effects of the $m_{\rm eff}^2$ term in $\mathcal{L}'_{\rm (free)}$ contributes to all orders, but the systematic subtracted by the $m_{\rm eff}^2$ term in $\mathcal{L}'_{\rm (int)}$. In this approach, the parameter $m_{\rm eff}^2$ is arbitrary; the gap equation to determine this parameter as a function of g^2 and T has been obtained. We note that this also remedies the convergence problem.

Now we apply this idea to QCD and the HTL Lagrangian. We will regard the HTL screening effect as the effective mass in the screened perturbation theory. After reorganizing the Lagrangian as

$$\mathcal{L} = \mathcal{L}_{\rm QCD}^{\rm (free)} + \mathcal{L}_{\rm HTL} - \mathcal{L}_{\rm HTL} + \mathcal{L}_{\rm QCD}^{\rm (int)} = \mathcal{L}'^{\rm (free)} + \mathcal{L}'^{\rm (int)} \tag{3.55}$$

the new free theory includes the HTL contribution. It seems to be the same as the Braaten-Pisarski scheme, but the difference lies in that the HTLpt uses the $\mathcal{L}'^{\rm (free)}$ at any momentum scale.

The drawback of this approach is that the UV structure is modified, so that the additional divergent terms appear. There is still no rigorous proof on the renormalizability of $\mathcal{L}'_{\rm (free)}$, nevertheless, we assume that new divergence can be subtracted with additional counter terms. See Ref. [254] for a more detailed review. More details will be given in the next chapter, and the concrete calculations will also be shown there.

3.5 Φ-derivable approximation in the 2PI expansion

A systematic way to incorporate the screening effects in the thermodynamics is to use a formalism in which the grand potential $\Omega = -PV$ is expressed in terms of the dressed Green's function. Such a formalism, also referred to as the effective action for composite operators, has been recognized in non-relativistic systems in condensed matter physics [216, 223, 224, 255], then later applied to relativistic field theories [225] by Cornwall, Jackiw, and Tomboulis; it is thus also referred to as Cornwall-Jackiw-Tomboulis (CJT) formalism in some literature. This has been applied to QCD in the context of HTL resummation by Blaizot, Iancu, and Rebhan [218–221] and independently by Peshier [222]. In this formalism, the grand potential reads

$$\beta\Omega[D, S] = \frac{1}{2}\,\mathrm{tr}\ln D^{-1} - \frac{1}{2}\,\mathrm{tr}\,\Pi D - \mathrm{tr}\ln S^{-1} + \mathrm{tr}\,\Sigma S + \Phi[D, S]\,, \tag{3.56}$$

where D and S are the gluon and quark full propagators; they are expressed in terms of the gluon and quark self-energies Π and Σ through Schwinger-Dyson equations (it is also commonly referred to as

the gap equations)

$$\begin{aligned} D_{\mu\nu}^{-1} &= D_{0,\mu\nu}^{-1} + \Pi_{\mu\nu}\,, \\ S_f^{-1} &= S_0^{-1} + \Sigma_f\,. \end{aligned} \tag{3.57}$$

We understand the trace in Eq. (3.56) is taken over all the configuration space such as momenta, Matsubara modes, flavors, colors, etc. Higher-order corrections $\Phi[D,S]$ are given in terms of two-particle irreducible (2PI) skeleton diagrams, in which all lines are the full propagators instead of the bare ones. The 2PI vacuum diagrams up to two-loop order in QCD are shown as

$\Phi[D,S] = -\frac{1}{12}$ 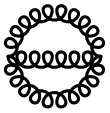 $-\frac{1}{8}$ 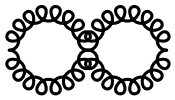 $+\frac{1}{2}$ 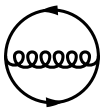 $+\cdots$ (3.58)

The self-energies are obtained from $\Phi[D,S]$ upon variation of D and S:

$$\Pi_{\mu\nu} \equiv 2\frac{\delta\Phi[D,S]}{\delta D_{\mu\nu}}\,, \quad \Sigma \equiv \frac{\delta\Phi[D,S]}{\delta S}\,. \tag{3.59}$$

The self-energies here are functionals of the full propagators, and they satisfy the SD equations of Eq. (3.57). These relations Eqs. (3.57) and (3.59) together define the propagators and self-energies in a self-consistent manner.

The procedure above outlines the Φ-derivable, or self-consistent, approximations; these relations lead the full propagators to fulfill the variational equations such that $\Omega[D,S]$ is stationary under the variations of D and S at fixed D_0 and S_0, i.e.,

$$\frac{\delta\Omega[D,S]}{\delta D} = 0\,, \quad \frac{\delta\Omega[D,S]}{\delta S} = 0\,. \tag{3.60}$$

The basic ingredient of the Φ-derivable approximation scheme is this stationary property.

Another virtue of the stationary condition in Eq. (3.60) is the simplification in the expression of density. It is defined by

$$n = -\left.\frac{\partial(\Omega/V)}{\partial\mu}\right|_T\,. \tag{3.61}$$

After the conventional contour deformation, the Matsubara sum becomes the continuous integral, and density takes the form of

$$n = -2\int\frac{d^4k}{(2\pi)^4}\frac{\partial f_{\rm F}(\omega-\mu)}{\partial\mu}\,\mathrm{tr}\Big[\mathrm{Im}\ln S^{-1}(\omega,k) - \mathrm{Im}\,\Sigma(\omega,k)\,\mathrm{Re}\,S(\omega,k)\Big] + n'\,, \tag{3.62}$$

where the imaginary part of the function is defined as follows

$$\mathrm{Im}\,S^{-1}(\omega,k) \equiv \mathrm{Im}\,S^{-1}(\omega+i0^+,k) = \frac{1}{2i}\,\mathrm{Disc}\,S^{-1}(\omega,k)\,. \tag{3.63}$$

The term n', originating from the residual interaction between the quasi-particles [217], is given by

$$n' \equiv -\left.\frac{\partial(T\Omega)}{\partial\mu}\right|_{D,S} + 2\int \frac{d^4k}{(2\pi)^4}\frac{\partial f_{\rm F}(\omega-\mu)}{\partial\mu}\,{\rm tr}[{\rm Re}\,\Sigma\,{\rm Im}\,S\,] = 0\,. \tag{3.64}$$

It is proven to be $n' = 0$ up to $O(g^3)$. Although $\Phi[D, S\,]$ contributes to Ω already at $O(g^2)$, this cancellation postpones the Φ-contribution beyond $O(g^3)$. The advantage of this approach is that the $O(g^2)$ results for the derivative quantity of Ω can be obtained without explicitly calculating the $O(g^2)$ diagrams. This cancellation has been proven in QED [217] and in QCD [220].

Here, several remarks are in order. We note that the self-consistently resummed expression of density in Eq. (3.62) is UV finite; the divergence is tamed by the Fermi-Dirac distribution. The Φ-derivable approximation in principle introduces the gauge dependence because the vertices are not dressed, but it has been shown that the gauge dependence is suppressed at the stationary point [256]. Nevertheless, it does not matter in the actual QCD calculations because more approximation is involved, and only the gauge-invariant HTLs are used. This approach is named as "approximately self-consistent resummation" by Blaizot, Iancu, and Rebhan [220]; we still use the self-consistent formalism, but we make an approximation to the solution of the gap equations (3.57) as it is almost impossible to analytically solve these equations in QCD.

In this thesis, we will briefly mention the results obtained in this formalism as a crosscheck to the HTLpt, but there is an ambiguity in the EoS arising from the treatment of the constant term, so we do not get deeply involved in this formalism.

Chapter 4

EoS construction from pQCD with HDL-resummation

In this chapter, we perform the actual calculation for the EoS. From the technical point of view, we adopt the resummation schemes in the gluon sector as prescribed in Ref. [204, 205] and in the quark sector as in Ref. [227] with our own extension to cope with the strange quark mass. Our expressions are given in the form of exact integrations without any expansion in terms of the screening mass as in Ref. [213]. We construct our EoS in the β equilibrium and charge neutral system.

4.1 Pressure of quark matter from HDLpt

In the $T \to 0$ limit the HDLpt pressure, $P_{\rm HDLpt}$, is given by the gluon loop and the quark loop with the self-energy insertions; namely,

$$P_{\rm HDLpt} = (N_{\rm c}^2 - 1)P_{\rm g} + N_{\rm c} \sum_{f=u,d,s} P_{{\rm q},f} + \Delta P_{\rm g,q}\,, \tag{4.1}$$

where $\Delta P_{\rm g}$ and $\Delta P_{\rm q}$ are the counter terms that subtract the ultraviolet divergences.

Gluon pressure $P_{\rm g}$: The gluon part with an appropriate subtraction by $\Delta P_{\rm g} \propto 1/\epsilon$ (where the spatial dimensions are $d = 3 - 2\epsilon$ in the dimensional regularization) is

$$P_{\rm g} = \frac{M_{\rm D}^4}{64\pi^2}\left(\ln\frac{\bar{\Lambda}}{M_{\rm D}} + C_{\rm g}\right). \tag{4.2}$$

A constant, $C_{\rm g}$, is an integral over a function involving the gluon self-energy and numerically estimated as $C_{\rm g} \approx 1.17201$ in the dimensional regularization. Here, $M_{\rm D}$ is the gluon screening mass induced by μ, i.e.,

$$M_{\rm D}^2 \equiv \frac{2\alpha_s}{\pi}\sum_f \mu_f^2\,. \tag{4.3}$$

We note that the bare quark masses in the hard loops are neglected commonly in the HTL approximation (see Ref. [232] for a standard textbook). The gluon sector is intact, so we just employ the expressions given in Refs. [204, 205, 213, 215]. See Appendix A for the complete calculation.

Quark pressure $P_{\mathrm{q},f}$: The quark part appears from the flavor-f quark loop, i.e.,

$$P_{\mathrm{q},f} = \mathrm{tr}\ln S_f^{-1}\,, \tag{4.4}$$

where the inverse dressed propagator S_f^{-1} is

$$S_f^{-1} = \not{k} - m_f - \Sigma(k_0, \boldsymbol{k})\,, \tag{4.5}$$

$$k_0 = i\tilde{\omega}_n + \mu_f\,, \tag{4.6}$$

for flavor-f quarks with $\tilde{\omega}_n \equiv (2n+1)\pi T$ being the fermionic Matsubara frequency. For the expression of the self-energy Σ, whose explicit from was given in Sec. 3.2.3, we need to introduce the following notations according to Refs. [213, 227], i.e.,

$$A_0(k_0, k) \equiv k_0 - \frac{M_{\mathrm{q}f}^2}{k_0}\widetilde{\mathcal{T}}(k_0, k)\,, \tag{4.7}$$

$$A_{\mathrm{s}}(k_0, k) \equiv k + \frac{M_{\mathrm{q}f}^2}{k}\left[1 - \widetilde{\mathcal{T}}(k_0, k)\right]\,, \tag{4.8}$$

and the flavor-f quark screening mass is

$$M_{\mathrm{q}f}^2 \equiv \frac{\alpha_s}{2\pi}\frac{N_{\mathrm{c}}^2 - 1}{2N_{\mathrm{c}}}\mu_f^2\,. \tag{4.9}$$

The fermionic HTL function in $d = 3 - 2\epsilon$ spatial dimensions is defined as

$$\widetilde{\mathcal{T}}(k_0, k) \equiv \frac{\Gamma(\frac{d}{2})}{\Gamma(\frac{1}{2})\Gamma(\frac{d-1}{2})}\int_{-1}^{1} dz\,(1-z^2)^{\frac{d-3}{2}}\frac{k_0}{k_0 - kz} = {}_2F_1\left(\frac{1}{2}, 1; \frac{3}{2} - \epsilon; \frac{k^2}{k_0^2}\right), \tag{4.10}$$

which arises from the angular integration in Eq. (3.36). Then, the self-energy for flavor-f quarks is expressed as

$$\not{k} - \Sigma(k_0, k) = A_0(k_0, k)\gamma^0 - A_{\mathrm{s}}(k_0, k)\boldsymbol{\gamma}\cdot\hat{\boldsymbol{k}}\,. \tag{4.11}$$

The paramount advance in this work is the inclusion of bare mass m_f, and the quark pressure deviates from Refs. [213, 227]. Let us first write down our final expression and then explain the notations next. In the flavor-f quark sector the pressure contribution reads:

$$P_{\mathrm{q},f} = M_{\mathrm{q}f}^4\left[C_{\mathrm{q}}(\eta_f) + D_{\mathrm{q}}(\eta_f)\ln\frac{\bar{\Lambda}}{M_{\mathrm{q}f}}\right] + P_{\mathrm{qp},f} + P_{\mathrm{Ld},f}\,. \tag{4.12}$$

We introduced $C_{\rm q}$ and $D_{\rm q}$ as functions of $\eta_f \equiv 1+m_f^2/(2M_{{\rm q}f}^2)$. These definitions involve the following functions:

$$f_\pm(\bar{\omega},\eta_f) = \frac{\eta_f \pm \eta'(\bar{\omega},\eta_f)}{1+\bar{\omega}^2}\,, \tag{4.13}$$

$$\eta'(\bar{\omega},\eta_f) = \sqrt{\eta_f^2-(1+\bar{\omega}^2)\left[(1-\widetilde{\mathcal{T}}(i\bar{\omega},1))^2+\frac{\widetilde{\mathcal{T}}^2(i\bar{\omega},1)}{\bar{\omega}^2}\right]}\,, \tag{4.14}$$

where $\bar{\omega}$ is a dimensionless and continuous variable. Then, $C_{\rm q}$ and $D_{\rm q}$ are given by

$$\begin{aligned} C_{\rm q}(\eta_f) &= \sum_{\chi=\pm}\frac{1}{4\pi^3}\int_0^\infty d\bar{\omega}\left(f_\chi^2\ln f_\chi - \frac{\partial f_\chi^2}{\partial\epsilon}\right)+\left(\frac{5}{4}-\ln 2\right)D_{\rm q}(\eta_f) \\ &= \sum_{\chi=\pm}\frac{1}{4\pi^3}\int_0^\infty d\bar{\omega}\left(f_\chi^2\ln f_\chi - \frac{\partial f_\chi^2}{\partial\epsilon}\right)-\frac{1}{2\pi^2}\left(\frac{5}{4}-\ln 2\right)(\eta_f^2-1)\,, \end{aligned} \tag{4.15}$$

$$\begin{aligned} D_{\rm q}(\eta_f) &= -\sum_{\chi=\pm}\frac{1}{2\pi^3}\int_0^\infty d\bar{\omega}\, f_\chi^2 \\ &= -\frac{1}{2\pi^2}(\eta_f^2-1)\,. \end{aligned} \tag{4.16}$$

We note that $D_{\rm q}(\eta_f\to 1)\to 0$ and $C_{\rm q}(\eta_f\to 1)\approx -0.03653$ as is consistent with Ref. [213]. We also note that the subtraction at finite m_f is mass dependent, i.e.,

$$\Delta P_{\rm q} = M_{{\rm q}f}^4 D_{\rm q}(\eta_f)\frac{1}{2\epsilon}\,. \tag{4.17}$$

Quasi-particle contribution $P_{{\rm qp},f}$ to the quark pressure: The next term, $P_{{\rm qp},f}$, in Eq. (4.12) is the quasi-particle contribution given by

$$P_{{\rm qp},f} = \frac{1}{\pi^2}\int_0^\infty dk\,k^2\sum_{\chi=\pm 1}[(\mu_f-\omega_{f\chi})\theta(\mu_f-\omega_{f\chi})] - \frac{\mu_f^4}{12\pi^2}\,. \tag{4.18}$$

We note that the ideal term $\propto -\mu_f^4$ in the above expression arises in the calculation as we doubly pick up two pole contributions at $\omega_{f\pm}$. In Ref. [227] the quasi-particle contribution was defined by taking the $M_{{\rm q}f}^2$ derivative/integration, so that only the difference from the ideal term was considered by construction, and the ideal term was not subtracted but added. Here, the quasi-particle poles, $\omega_{f\pm}$, are solutions of the following implicit equations, i.e.,

$$A_0(\omega_{f\pm},k) \mp \sqrt{m_f^2+A_{\rm s}^2(\omega_{f\pm},k)} = 0\,, \tag{4.19}$$

or writing it down more explicitly

$$\omega_{f\pm} - \frac{M_{\mathrm{q}f}^2}{k} Q_0\left(\frac{\omega_{f\pm}}{k}\right) \mp \sqrt{m_f^2 + \left[k - \frac{M_{\mathrm{q}f}^2}{k} Q_1\left(\frac{\omega_{f\pm}}{k}\right)\right]^2} = 0\,, \tag{4.20}$$

where

$$Q_0(x) \equiv \frac{1}{2}\ln\left(\frac{x+1}{x-1}\right), \quad Q_1(x) \equiv xQ_0(x) - 1\,, \tag{4.21}$$

are the Legendre functions. These Legendre functions arise from the HTL function (4.10) in the limit of $\epsilon \to 0$.

Landau damping contribution $P_{\mathrm{Ld},f}$ to the quark pressure: Finally, the last term in Eq. (4.12) represents the contribution from the Landau damping, which reads:

$$P_{\mathrm{Ld},f} = -\frac{1}{\pi^3}\int_0^{\mu_f} d\omega \int_\omega^\infty dk\, k^2\, \theta_{\mathrm{q}f}(\omega, k; m_f, M_{\mathrm{q}f}^2)\,. \tag{4.22}$$

The integrand is given by $\tan\theta_{\mathrm{q}f} = \mathcal{Y}/\mathcal{X}$ where

$$\mathcal{X} = k^2 - \omega^2 + m_f^2 + 2M_{\mathrm{q}f}^2 + \frac{M_{\mathrm{q}f}^4}{k^2}\left\{1 - \frac{2\omega}{k}Q_0(k/\omega) - \frac{k^2-\omega^2}{k^2}\left[Q_0^2(k/\omega) - \frac{\pi^2}{4}\right]\right\}, \tag{4.23}$$

$$\mathcal{Y} = \frac{\pi M_{\mathrm{q}f}^4}{k^2}\left[\frac{\omega}{k} + \frac{k^2-\omega^2}{k^2}Q_0(k/\omega)\right]. \tag{4.24}$$

In this case $k \geq \omega$ holds and the argument of Q_0 should be k/ω, not ω/k.

In Fig. 4.1, we show a breakdown of each contribution to the pressure for the massless bare quarks. The pressure is normalized with the ideal gas value: $P_{\mathrm{ideal}} = N_{\mathrm{c}}N_{\mathrm{f}}\mu_f^4/(12\pi^2)$. For the illustration purpose, we plot the massless bare quark pressure, but the behavior is the same for the massive bare quark pressure: quasiparticles dominate the pressure.

4.2 Details of the integration

Here, we will elaborate on the details of integration that appear in the derivation of Eq. (4.12) in the previous section. The quark part of the pressure appears from the flavor-f quark loop:

$$P_{\mathrm{q},f}(T,\mu_f) = \mathrm{tr}\ln S_f^{-1} \tag{4.25}$$

$$= \sum\!\!\!\!\!\!\int_{\{K\}} \ln\det\left[\not{k} - m_f - \Sigma(i\tilde{\omega}_n + \mu_f, k)\right]$$

$$= 2\sum\!\!\!\!\!\!\int_{\{K\}} \ln\left[A_S^2(i\tilde{\omega}_n + \mu_f, k) + m_f^2 - A_0^2(i\tilde{\omega}_n + \mu_f, k)\right], \tag{4.26}$$

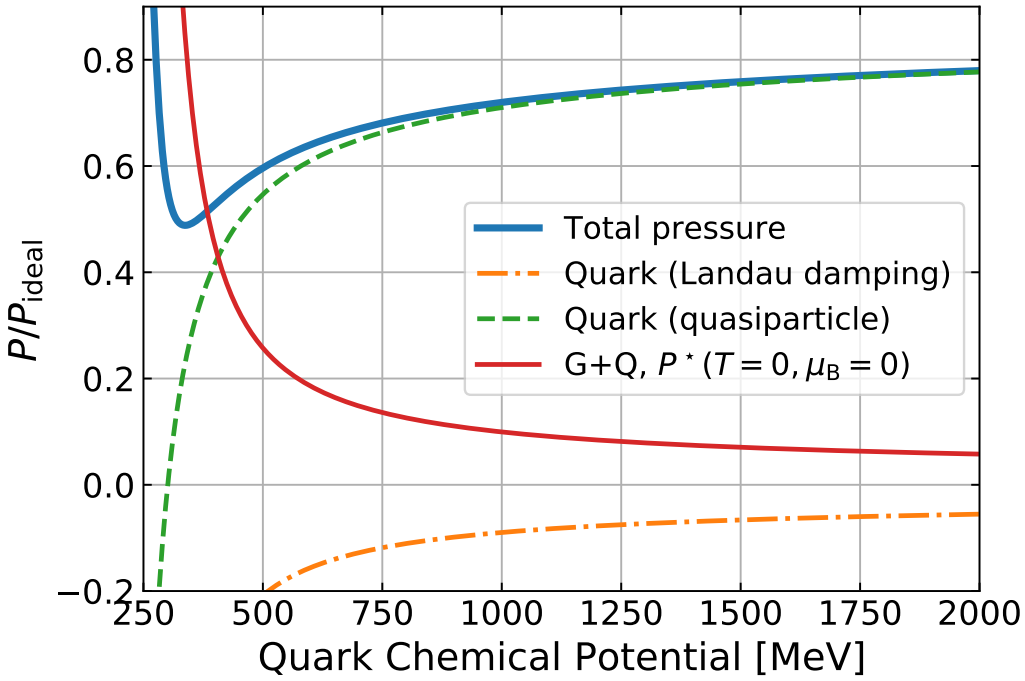

Fig. 4.1: A breakdown of each contribution to the pressure. The pressure is normalized with the ideal gas value. For the illustration purpose, the plot is in the massless limit of bare quarks, but the same holds for the massive bare quarks.

where we write the sum-integral as $\oint\!\!\!\!\!\!\sum_{\{K\}} = T\sum_{\tilde{\omega}_n}\int_{\boldsymbol{k}}$ in $d = 3-2\epsilon$ spatial dimensions for the momentum integration. The functions A_0 and A_S are defined above. We note that $P_{\mathrm{q},f}$ in Eq. (4.25) can be regarded as a leading contribution in the 2PI formalism.

We recast the Matsubara sum into the contour integral along with C as depicted in the left panel of Fig. 4.2. We can deform the contour C into $C_{\mathrm{qp}} \cup C_{\mathrm{Ld}}$, see the right panel of Fig. 4.2. We identify the terms from C_{qp} and C_{Ld} with the quasi-particle contribution and the Landau damping contribution, respectively, according to Refs. [206, 213]:

$$P_{\mathrm{qp/Ld},f}(T,\mu_f) = \int_{\boldsymbol{k}} \oint_{C_{\mathrm{qp/Ld}}} \frac{d\omega}{2\pi i} \ln\left[A_s^2(\omega,k) + m_f^2 - A_0^2(\omega,k)\right] \tanh\left(\frac{\beta(\omega-\mu_f)}{2}\right). \tag{4.27}$$

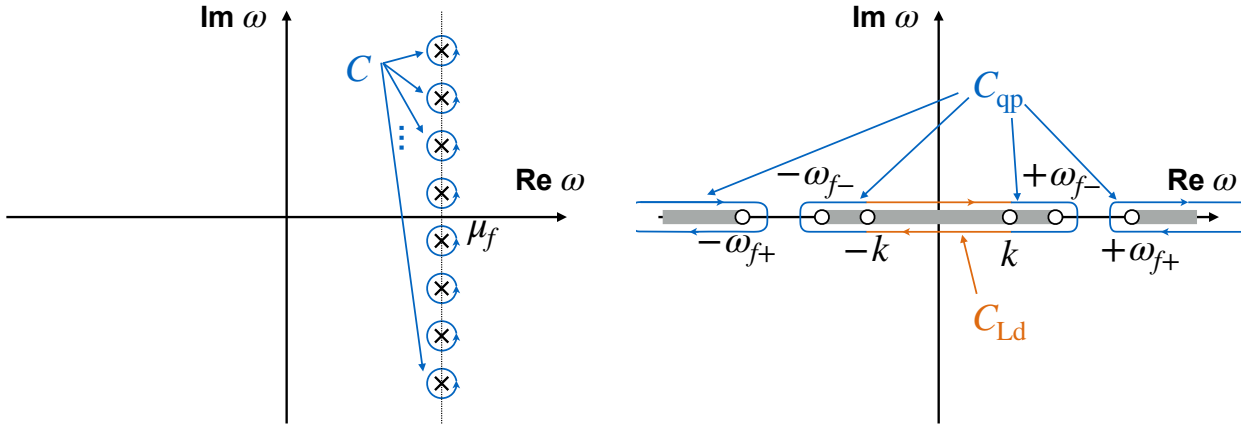

Fig. 4.2: (Left) Original contour C corresponding to the Matsubara sum. (Right) Deformed contours, $C_{\rm qp}$ and $C_{\rm Ld}$.

Quasi-particle contribution: The quasi-particle contribution to the integral (see the right panel of Fig. 4.2) is

$$\begin{aligned}
P_{{\rm qp},f} =& \int_{\boldsymbol{k}} \left\{ \int_{\tilde{\omega}_{f+}}^{\infty} \frac{d\omega}{2\pi} \left[\text{Disc} \arg\left(A_s^2(\omega,k) + m_f^2 - A_0^2(\omega,k) \right) \right] \left[\tanh\left(\frac{\beta(\omega-\mu_f)}{2} \right) - \tanh\left(\frac{\beta(-\omega-\mu_f)}{2} \right) \right] \right. \\
&\left. + \int_{k}^{\tilde{\omega}_{f-}} \frac{d\omega}{2\pi} \left[\text{Disc} \arg\left(A_s^2(\omega,k) + m_f^2 - A_0^2(\omega,k) \right) \right] \left[\tanh\left(\frac{\beta(\omega-\mu_f)}{2} \right) - \tanh\left(\frac{\beta(-\omega-\mu_f)}{2} \right) \right] \right\} \\
=& \int_{\boldsymbol{k}} \left\{ \int_{\tilde{\omega}_{f+}}^{\infty} \frac{d\omega}{2\pi} (-2\pi) \left[2 - \frac{2}{e^{\beta(\omega-\mu_f)}+1} - \frac{2}{e^{\beta(\omega+\mu_f)}+1} \right] + \int_{k}^{\tilde{\omega}_{f-}} \frac{d\omega}{2\pi} (2\pi) \left[2 - \frac{2}{e^{\beta(\omega-\mu_f)}+1} - \frac{2}{e^{\beta(\omega+\mu_f)}+1} \right] \right\} \\
=& 2 \int_{\boldsymbol{k}} \sum_{\chi,s=\pm} T \ln\left[1 + e^{-\beta(\omega_{f\chi}+s\mu_f)} \right] - 2 \int_{\boldsymbol{k}} \sum_{s=\pm} T \ln\left[1 + e^{-\beta(k+s\mu_f)} \right] + 2 \int_{\boldsymbol{k}} \left[\omega_{f+}(k) + \omega_{f-}(k) - k \right],
\end{aligned} \tag{4.28}$$

where we defined as $\text{Disc}\, f(\omega) \equiv f(\omega + i0^+) - f(\omega - i0^+)$, used $A_{0,s}^2(\omega,k) = A_{0,s}^2(-\omega,k)$, and dropped an irrelevant infinity from the upper bound of the ω-integration. The dispersion relation for quarks $\omega_{f\pm}$ is obtained by solving Eq. (4.20) above. For the moment we can drop the third term in Eq. (4.28) that is independent of T and μ_f (which will be reassembled later). Finally, we obtain:

$$P_{{\rm qp},f}(T=0,\mu_f) = \frac{1}{\pi^2} \int_0^{\infty} dk\, k^2 \sum_{\chi=\pm 1} \left[(\mu_f - \omega_{f\chi}) \theta(\mu_f - \omega_{f\chi}) \right] - \frac{\mu_f^4}{12\pi^2}, \tag{4.29}$$

which completes the derivation of Eq. (4.18) above. The $s=-1$ term in the sum of Eq. (4.28) vanishes at $T \to 0$ because of the step function $\theta(-\mu_f - \omega_{f\chi})$.

Landau damping contribution: The Landau damping contribution to the integral is

$$\begin{aligned} P_{\mathrm{Ld},f} &= \int_{\boldsymbol{k}} \int_{-k}^{k} \frac{d\omega}{2\pi} \operatorname{Disc} \arg\left(A_s^2(\omega,k) + m_f^2 - A_0^2(\omega,k)\right) \tanh\left(\frac{\beta(\omega-\mu_f)}{2}\right) \\ &= -\frac{1}{\pi} \int_{\boldsymbol{k}} \int_0^k d\omega\, 2\theta_{\mathrm{q}f}(\omega,k;m_f^2,M_{\mathrm{q}f}^2) \left[\frac{1}{e^{\beta(\omega-\mu_f)}+1} + \frac{1}{e^{\beta(\omega+\mu_f)}+1} - 1\right]. \end{aligned} \tag{4.30}$$

In the last line we introduced [with $\mathcal{X}$ and $\mathcal{Y}$ defined in Eqs. (4.23) and (4.24) above, respectively]:

$$\begin{aligned} 2\theta_{\mathrm{q}f} &= 2\arctan \mathcal{Y}/\mathcal{X} = \operatorname{Disc} \arg\left(A_s^2(\omega,k) + m_f^2 - A_0^2(\omega,k)\right) \\ &= \operatorname{Disc} \arctan\left\{\frac{\operatorname{Im}\left[A_s^2(\omega,k) + m_f^2 - A_0^2(\omega,k)\right]}{\operatorname{Re}\left[A_s^2(\omega,k) + m_f^2 - A_0^2(\omega,k)\right]}\right\} \\ &= \operatorname{Disc} \arctan\left\{\frac{\frac{M_{\mathrm{q}f}^4}{k^2}\left[-2\operatorname{Im}\left({}_2F_1(\frac{1}{2},1;\frac{3}{2};\frac{k^2}{\omega^2})\right) - \frac{k^2-\omega^2}{\omega^2}\operatorname{Im}\left({}_2F_1(\frac{1}{2},1;\frac{3}{2};\frac{k^2}{\omega^2})^2\right)\right]}{k^2-\omega^2+m_f^2+2M_{\mathrm{q}f}^2 + \frac{M_{\mathrm{q}f}^4}{k^2}\left[1-2\operatorname{Re}\left({}_2F_1(\frac{1}{2},1;\frac{3}{2};\frac{k^2}{\omega^2})\right) - \frac{k^2-\omega^2}{\omega^2}\operatorname{Re}\left({}_2F_1(\frac{1}{2},1;\frac{3}{2};\frac{k^2}{\omega^2})^2\right)\right]}\right\} \\ &= 2\arctan\left\{\frac{\frac{M_{\mathrm{q}f}^4}{k^2}\left[-2\left(-\frac{\pi\omega}{2k}\right) - \frac{k^2-\omega^2}{\omega^2}\left(-\frac{\pi\omega^2}{2k^2}\ln\left(\frac{k+\omega}{k-\omega}\right)\right)\right]}{k^2-\omega^2+m_f^2+2M_{\mathrm{q}f}^2 + \frac{M_{\mathrm{q}f}^4}{k^2}\left[1-2\frac{\omega}{2k}\ln\left(\frac{k+\omega}{k-\omega}\right) - \frac{k^2-\omega^2}{\omega^2}\frac{\omega^2}{4k^2}\left[\ln\left(\frac{k+\omega}{k-\omega}\right)^2 - \pi^2\right]\right]}\right\}. \end{aligned} \tag{4.31}$$

Again, we only keep the T and μ_f dependent parts in Eq. (4.30), so that the $T \to 0$ limit leads to

$$P_{\mathrm{Ld},f}(T=0,\mu_f) = -\frac{1}{\pi^3}\int_0^{\mu_f} d\omega \int_\omega^\infty dk\, k^2\, \theta_{\mathrm{q}f}(\omega,k;m_f,M_{\mathrm{q}f}^2), \tag{4.32}$$

which completes the derivation of Eq. 4.22 in the previous section.

T- and μ_f- independent term: We here reassemble the T and μ_f independent terms that we dropped above. To this end, it is convenient to think of the $T = \mu_f = 0$ limit in Eq. (4.26), in which the Matsubara sum reduces to $T\sum_n \to \int_{-\infty}^{\infty}\frac{d\bar\omega}{2\pi}$, so that the pressure reads:

$$\begin{aligned} P_{\mathrm{q}f}^\star &= 2\int_{-\infty}^{\infty}\frac{d\bar\omega}{2\pi}\int_{\boldsymbol{k}} \ln\left[A_S^2(i\bar\omega,k) + m_f^2 - A_0^2(i\bar\omega,k)\right] \\ &= 4\int_0^{\infty}\frac{d\bar\omega}{2\pi}\int_{\boldsymbol{k}} k\ln\left\{(1+\bar\omega^2)k^2 + m_f^2 + 2M_{\mathrm{q}f}^2 + \frac{M_{\mathrm{q}f}^4}{k^2}\left[\left(1-\widetilde{\mathcal{T}}(i\bar\omega,1)\right)^2 - \frac{\widetilde{\mathcal{T}}^2(i\bar\omega,1)}{\bar\omega^2}\right]\right\} \\ &= -\frac{\bar\Lambda^{2\epsilon}e^{\gamma_{\mathrm{E}}\epsilon}}{4\pi^{5/2}}\frac{\Gamma(2-\epsilon)\Gamma(\epsilon-2)}{\Gamma(\frac{3}{2}-\epsilon)}M_{\mathrm{q}f}^{4-2\epsilon}\int_0^\infty d\bar\omega\left[\left(f_+(\bar\omega,\eta_f)\right)^{2-\epsilon} + \left(f_-(\bar\omega,\eta_f)\right)^{2-\epsilon}\right], \end{aligned} \tag{4.33}$$

where we used the following integral:

$$\int_0^\infty dk\, k^\alpha \ln(k^2+m^2) = \frac{\Gamma\left(\frac{1+\alpha}{2}\right)\Gamma\left(\frac{1-\alpha}{2}\right)}{1+\alpha} m^{1+\alpha}. \tag{4.34}$$

The function $f_{\pm}(\bar{\omega}, \eta_f)$ with $\eta_f \equiv 1 + m_f^2/(2M_{\mathrm{q}f}^2)$ is defined as in Eqs. (4.13) and (4.14) above. The limit of $\epsilon \to 0$ gives:

$$\begin{aligned} P_{\mathrm{q}f}^{\star} =& -\frac{M_{\mathrm{q}f}^4}{4\pi^3}\left(\frac{1}{\epsilon} + \ln\frac{\bar{\Lambda}^2}{M_{\mathrm{D}}^2} + \frac{5}{2} - 2\ln 2\right)\left[\sum_{\chi=\pm}\int_0^{\infty} d\bar{\omega}\, f_{\chi}^2 - \epsilon\sum_{\chi=\pm}\int_0^{\infty} d\bar{\omega}\left(f_{\chi}^2 \ln f_{\chi} - 2f_{\chi}\frac{\partial f_{\chi}}{\partial \epsilon}\right)\right] \\ =& M_{\mathrm{q}f}^4\left[C_{\mathrm{q}}(\eta_f) + D_{\mathrm{q}}(\eta_f)\ln\frac{\bar{\Lambda}}{M_{\mathrm{q}f}}\right] + M_{\mathrm{q}f}^4 D_{\mathrm{q}}(\eta_f)\frac{1}{2\epsilon}\,. \end{aligned} \tag{4.35}$$

The constants C_{q} and D_{q} are defined in Eqs. (4.15) and (4.16) in the previous section, respectively. The ultraviolet divergence is subtracted by the term ΔP_{q} in Eq. (4.1) above:

$$\Delta P_{\mathrm{q}} = M_{\mathrm{q}f}^4 D_{\mathrm{q}}(\eta_f)\frac{1}{2\epsilon}\,. \tag{4.36}$$

In this way the above procedures complete the derivation of Eq. (4.12) in the previous section.

4.3 EoS construction in β equilibrium

In Introduction, we emphasized the difference between the symmetric matter and the asymmetric stellar matter. For matter in stellar environments, such as the neutron star matter, the crucial point was to consider the cold catalyzed matter, which is under the β equilibrium and electric charge neutrality conditions. Our novel contribution of this work lies in taking into account the bare mass of strange quarks; it is crucial for the quantitative calculation of the cold catalyzed matter.

4.3.1 β equilibrium, charge neutrality, and the strange quark mass

β equilibrium: The β equilibrium is reached via the following weak reactions:

$$\begin{aligned} d &\rightleftarrows u + e^- + \bar{\nu}_e\,, \\ s &\rightleftarrows u + e^- + \bar{\nu}_e\,. \end{aligned} \tag{4.37}$$

These processes imply the relations between quark chemical potentials as

$$\begin{aligned} \mu_d &= \mu_u + \mu_e\,, \\ \mu_s &= \mu_u + \mu_e\,. \end{aligned} \tag{4.38}$$

We assume that neutrinos escape quickly from the system so that we can neglect their contributions. In general, the chemical potential of flavor-f quarks, μ_f can be expressed in terms of the linear combination of the (quark, electric charge, strangeness) chemical potentials, $(\mu, \mu_{\mathrm{Q}}, \mu_{\mathrm{S}})$, namely,

$$\mu_f = N_f\,\mu + Q_f\,\mu_{\mathrm{Q}} + S_f\,\mu_{\mathrm{S}}\,, \tag{4.39}$$

where N_f, Q_f, and S_f are the quark number, electric charge, and strangeness of the flavor-f quark, respectively. Owing to the fact $Q_u = 2/3$, $Q_d = -1/3$, and $Q_s = -1/3$, as well as the difference between Q_u and Q_d, the charge chemical potential is proportional to the isospin chemical potential $\mu_{\rm I}$. Each quark chemical potential reads

$$\mu_u = \mu + \frac{2}{3}\mu_{\rm Q}\,, \quad \mu_d = \mu - \frac{1}{3}\mu_{\rm Q}\,, \quad \mu_s = \mu - \frac{1}{3}\mu_{\rm Q} - \mu_{\rm S}\,. \tag{4.40}$$

The electron chemical potential is $\mu_e = -\mu_Q$ as electrons carry neither the quark number nor strangeness and are negatively charged. Plugging these quark chemical potentials in the beta equilibrium condition of Eq. (4.38) fixes the strangeness chemical potential to zero:

$$\mu_{\rm S} = 0\,. \tag{4.41}$$

And the quark chemical potentials in β equilibrium becomes

$$\mu_u = \mu + \frac{2}{3}\mu_Q\,, \quad \mu_d = \mu_s = \mu - \frac{1}{3}\mu_Q\,. \tag{4.42}$$

Charge neutrality: The charge chemical potential μ_Q in Eq. (4.42) remains as a free parameter; the (local) charge neutrality fixes $\mu_{\rm Q}$ as a function of μ. The charge neutrality condition is

$$n_Q(\mu, \mu_{\rm Q}) - n_e(\mu_{\rm Q}) = 0\,, \tag{4.43}$$

where $n_e(\mu_{\rm Q}) \equiv \mu_e^3/(3\pi^2) = -\mu_{\rm Q}^3/(3\pi^2)$ is the electron density neglecting masses and interactions of electrons. Also, n_Q is the charge density of quark matter:

$$n_Q = \frac{\partial P}{\partial \mu_{\rm Q}} = \frac{2}{3}n_u - \frac{1}{3}n_d - \frac{1}{3}n_s\,, \tag{4.44}$$

with n_u, n_d, and n_s being the density of u, d, and s quark, respectively.

In the fictitious world in which all u, d, and s quarks are massless, the β equilibrium and charge neutrality conditions are automatically satisfied; the absence of the bare quark mass significantly simplifies technicalities as well as the realization of the β equilibrium. With an equal amount of u, d, and s quarks (that is automatically the case if their masses are all neglected), the electric charge neutrality follows from Eq. (4.44) as it is, even without electrons.

For quantitative descriptions of the neutron star phenomenology, however, we need to take account of the strange quark mass and solve the β equilibrium condition. In this sense, the number of flavors of the system with the non-zero strange quark mass is sometimes denoted as $N_{\rm f} = 2 + 1$, while the massless strange case is denoted as $N_{\rm f} = 3$. One of the novel parts of this work is the inclusion of the bare quark mass, and we have already written down the explicit expressions in the quark sector. In our notation for flavor-f quarks the bare mass is m_f and the screening mass is $M_{{\rm q}f}$.

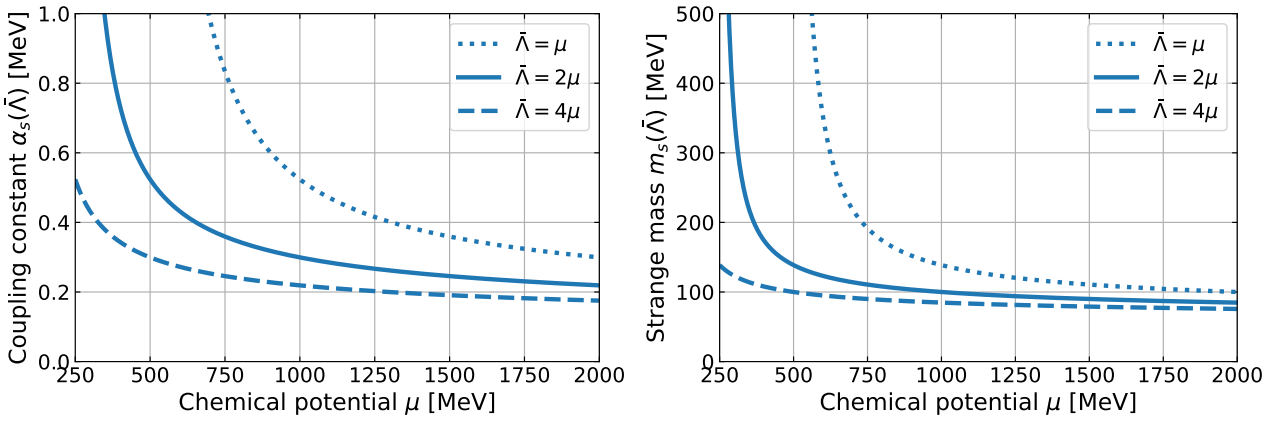

Fig. 4.3: The running of the coupling constant $\alpha_s(\bar{\Lambda})$ (left) and bare mass of strange quarks $m_s(\bar{\Lambda})$ (right).

Bare mass of strange quarks: The bare quark mass of flavor-f is scale dependent (see the right panel of Fig. 4.3 for the behavior of the running mass) as

$$m_f(\bar{\Lambda}) = m_f(2\text{GeV})\left[\frac{\alpha_s(\bar{\Lambda})}{\alpha_s(2\,\text{GeV})}\right]^{\gamma_0/\beta_0}\frac{1+\mathcal{A}(\bar{\Lambda})}{1+\mathcal{A}(2\,\text{GeV})}\,. \tag{4.45}$$

Here, the coupling constant $\alpha_s(\bar{\Lambda})$ (see the left panel of Fig. 4.3 for its behavior) was already introduced in Eq. (1.2)

$$\alpha_s(\bar{\Lambda}) = \left[1-\frac{2\beta_1}{\beta_0^2}\frac{\ln^2\left(\bar{\Lambda}^2/\Lambda^2_{\overline{\text{MS}}}\right)}{\ln\left(\bar{\Lambda}^2/\Lambda^2_{\overline{\text{MS}}}\right)}\right]\frac{4\pi}{\beta_0\ln\left(\bar{\Lambda}^2/\Lambda^2_{\overline{\text{MS}}}\right)}\,. \tag{1.2}$$

The coefficient β_0 was already introduced in Eq. (1.3):

$$\beta_0 \equiv \frac{11}{3}N_\text{c} - \frac{2}{3}N_\text{f}\,, \tag{1.3}$$

and $\gamma_0 \equiv 3(N_\text{c}^2-1)/(2N_\text{c})$. The two-loop corrections to the bare mass appear in

$$\mathcal{A}(\bar{\Lambda}) \equiv A_1\frac{\alpha_s(\bar{\Lambda})}{\pi} + \frac{A_1^2+A_2}{2}\left(\frac{\alpha_s(\bar{\Lambda})}{\pi}\right)^2 \tag{4.46}$$

with

$$A_1 \equiv -\frac{\beta_1\gamma_0}{2\beta_0^2} + \frac{\gamma_1}{4\beta_0}\,, \tag{4.47}$$

$$A_2 \equiv \frac{\gamma_0}{4\beta_0^2}\left(\frac{\beta_1^2}{\beta_0}-\beta_2\right) - \frac{\beta_1\gamma_1}{8\beta_0^2} + \frac{\gamma_2}{16\beta_0}\,. \tag{4.48}$$

For β_2, γ_1, and γ_2, the general expressions are complicated, and we refer to numerical values, $\beta_2 = 3863/24$, $\gamma_1 = 182/3$, and $\gamma_2 = 8885/9 - 160\zeta(3) \approx 794.9$ for $N_\text{c} = N_\text{f} = 3$. More general and

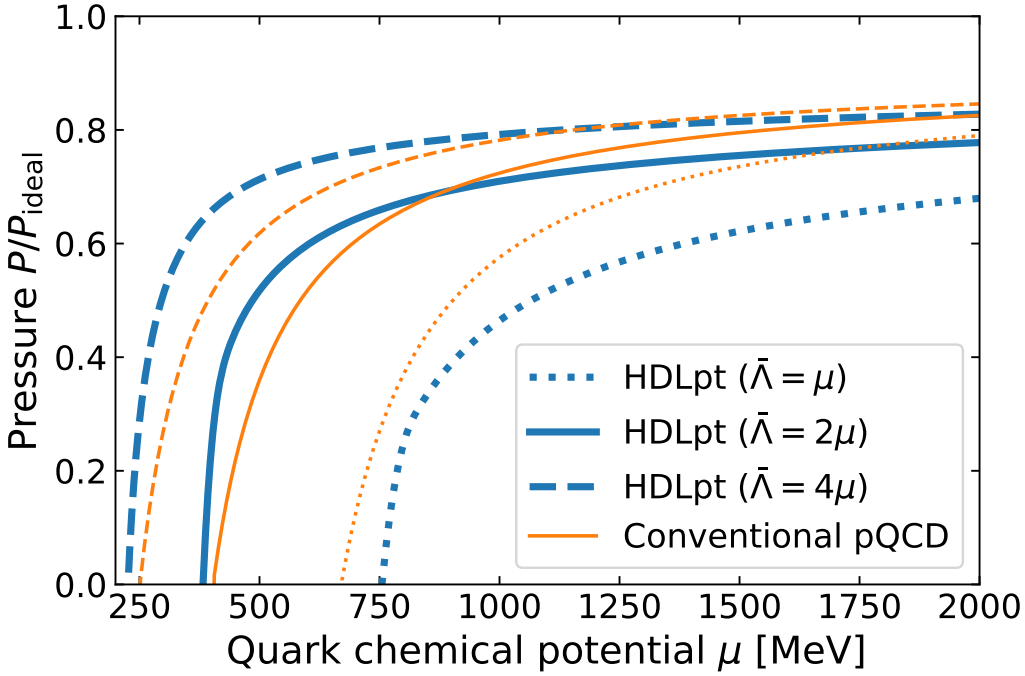

Fig. 4.4: The EoS expressed in the form of $P(\mu)$.

complete expressions can be found, e.g., in Ref. [257]. For actual numerical calculations, we took $m_u = m_d = 0$ and $m_s(2\text{GeV}) = 100\,\text{MeV}$. For N_c and N_c in $\alpha(\bar{\Lambda})$ and $m_s(\bar{\Lambda})$ we took $N_\text{c} = N_\text{f} = 3$.

4.3.2 Numerical results of the EoS

In Fig. 4.4, we show the EoS in the form of $P(\mu)$; the pressure is normalized with the ideal gas value $P_\text{ideal}(\mu) = N_\text{c} N_\text{f} \mu^4/(12\pi)^2$. It is evident that the scale variation uncertainty in HDLpt is not small as compared with the conventional pQCD results. As we show later, however, the scale variation uncertainty in $P(\varepsilon)$ from our HDLpt calculation is significantly smaller than that of the conventional pQCD. Therefore, it is a quite nontrivial discovery that the scale variation uncertainty in $P(\varepsilon)$ is significantly smaller than that in $P(\mu)$.

In Fig. 4.5, we show the EoS in the form of $P(\varepsilon)$. This is derived from the $P(\mu; \bar{\Lambda})$ through the relation $\varepsilon(\mu) = -P(\mu) + \mu(\partial P/\partial\mu)$. We note that $\bar{\Lambda} = \xi\mu$ ($\xi = 1, 2, 4$) is only substituted at the end of the calculation (see Sec. 6.4 for the detailed discussion). This is essentially the same plot as Fig. 1.3 in the previous section with an extended region of the energy density. Because of the uncertainty out of control at lower energy density, it is reasonable to truncate the plot around $\varepsilon \simeq 500\ \text{MeV}/\text{fm}^3$.

It seems that even around the energy density $\varepsilon \simeq 150\,\text{MeV}/\text{fm}^3$, which roughly corresponds to the saturation density n_0, the perturbative calculation still makes sense. Nevertheless, it is absurd to use the quark EoS to describe neutron stars around the saturation density, as the natural degrees of freedom here are nucleons. Thus, whether the EoS from the pQCD calculation is reliable or not should be determined from the other external information.

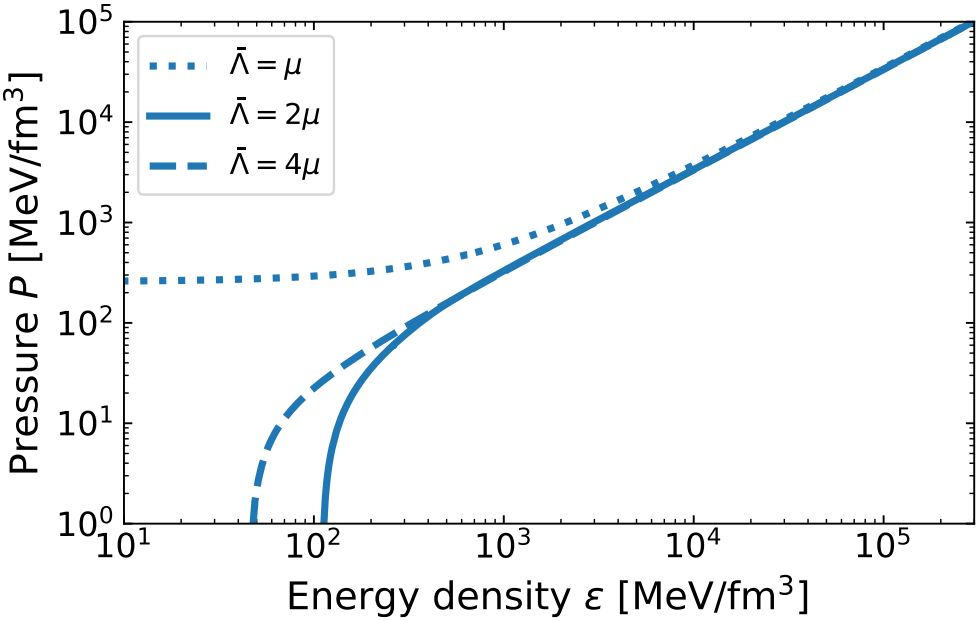

Fig. 4.5: The same as Fig. 1.3 with an extended region of the energy density.

4.3.3 The effect of the bare mass of strange quarks

In this subsection, we quantify the effect of the bare mass of strange quarks on the EoS. We note that the bare mass of strange quarks is handled under the HDL approximation. For the complete treatment, in which the expression of pressure is very complicated, see Sec. 5.1.2.

In Fig. 4.6, $N_{\rm f} = 3$ refers to the HDLpt in the massless limit, while $N_{\rm f} = 2+1$ means that the HDLpt with the strange quark mass in β equilibrium. The left panel of Fig. 4.6 shows the effect of the bare strange quark mass on the P–μ relation. The finite mass in the calculation leads to that the pressure goes to zero at a larger value of μ, while some of the $N_f = 3$ results go beyond one. The result for $N_f = 2 + 1$ is more natural because the baryon onset point corresponds to $\mu_{\rm B} = m_N - B \simeq 930\,{\rm MeV}$, which is equivalent to $\mu \simeq 300\,{\rm MeV}$; at this point, the pressure becomes zero. Of course, we do not expect that the pQCD calculation is valid down to the nuclear matter region, nevertheless, it is interesting to observe that the $N_f = 2 + 1$ results reproduce the EoS such that the pressure onset is around $\mu \simeq 300\,{\rm MeV}$.

The right panel of Fig. 4.6 shows the effect of the bare strange quark mass on the P–ε relation. By comparing $N_f = 2 + 1$ and $N_f = 3$ results, one can see that the finite mass has the effect of reducing the scale variation uncertainty at higher energy density.

In Fig. 4.7, we also plot the ratio of the strange quark density out of the total quark density, $Y_s = n_s/n$ (which is equivalent to the negative strangeness fraction, because the strangeness of the strange quark is defined as $S = -1$). From this plot, we can quantify at which density the strangeness comes into play with a hope to quantitatively account for the hyperon puzzle from the quark matter

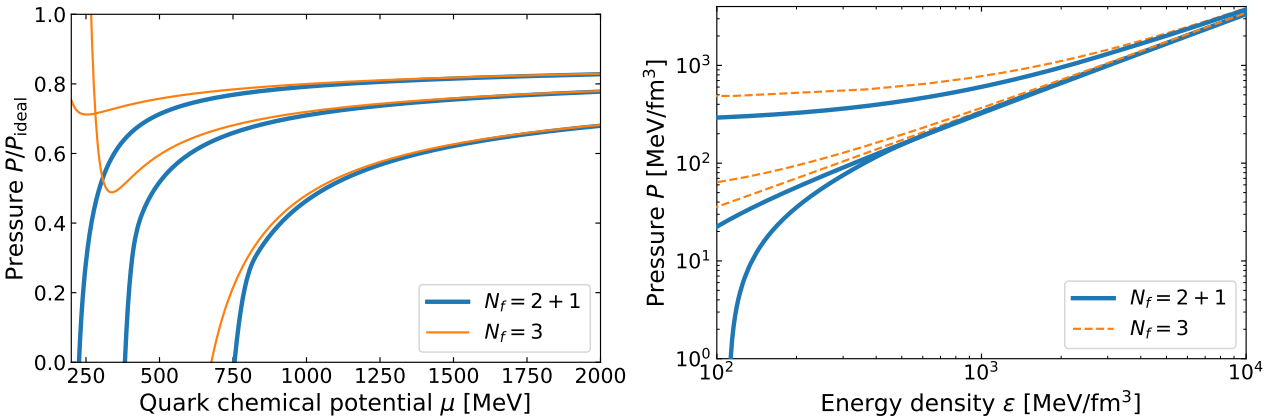

Fig. 4.6: The effect of the bare quark on the P–μ relation (left) and the P–ε relation (right). $N_{\rm f} = 3$ refers to the EoS in the massless limit, while $N_{\rm f} = 2 + 1$ means that the EoS with the strange quark mass in β equilibrium.

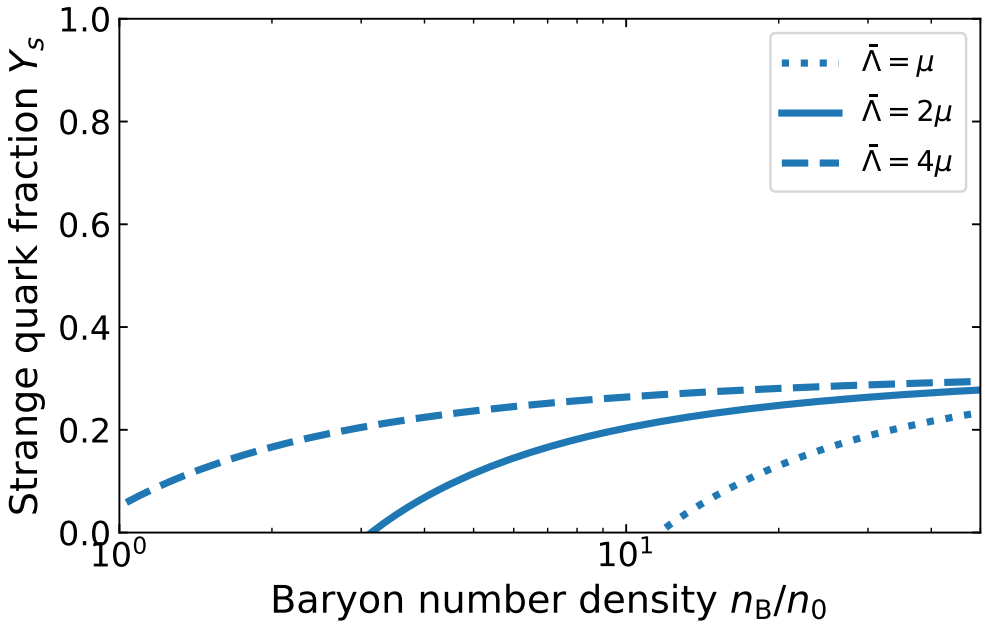

Fig. 4.7: The ratio of the strange quark density out of the total quark density, $Y_s = n_s/n$.

side. In the actual calculation, uncertainties in the onset density of the strangeness turn out to be very large due to the running of the strange quark mass as shown in Fig. 4.3, so that it cannot be applied to solve the hyperon puzzle. This large uncertainty may be mitigated by taking into account the bare quark mass dependence in the self-energy (see Sec. 5.1.2).

Chapter 5

Some corrections and alternative approach

In this chapter, we turn to two corrections and an alternative approach to the HDLpt calculation in the previous chapter. The two corrections include an *ad hoc* correction to match with the existing pQCD results and the mass correction to the self-energy in the full propagator. The calculation in the 2PI formalism is also performed under the Φ-derivable approach.

5.1 Corrections to the HDLpt

In this section, we show two corrections to the HDLpt calculation. One is the *ad hoc* $O(\alpha_s)$ correction to mitigate the mismatch with the conventional pQCD result. The other is the bare quark mass effect in the self-energy, which is resummed in the full propagator. We neglect it when performing the HTL approximation, but we can keep the full dependence of the bare quark mass. Nevertheless, this correction is negligible, but we show it for completeness.

5.1.1 $O(\alpha_s)$ correction

The HDLpt has a deviation of $O(\alpha_s)$ in the pressure from the conventional pQCD calculation. For analytical simplicity, we will show the calculation in the massless case only. It is known that the expansion of P_{HDLpt} in powers of $M_{\mathrm{q}f}/\mu_f \ll 1$ gives, for $N_{\mathrm{c}} = 3$ [227]:

$$\frac{P_{\mathrm{HDLpt}}}{P_{\mathrm{ideal}}} = 1 - 6\frac{M_{\mathrm{q}f}^2}{\mu_f^2} + O\left(\frac{M_{\mathrm{q}f}^4}{\mu_f^4}\right) = 1 - 4\frac{\alpha_s}{\pi} + O(\alpha_s^2)\,, \tag{5.1}$$

where the ideal pressure is $P_{\mathrm{ideal}} = N_{\mathrm{c}} N_{\mathrm{f}} \mu_f^4/(12\pi^2)$.

The leading correction to P_{ideal} comes from the quasi-particle contribution in P_{HDLpt}, and integration is saturated around the hard momentum scale $k \sim \mu$. The explicit description is as follows. When $k \gg M_{\mathrm{q}f}$, the dispersion relation of quasi-particles, which is the solution to Eq. (4.20), can be

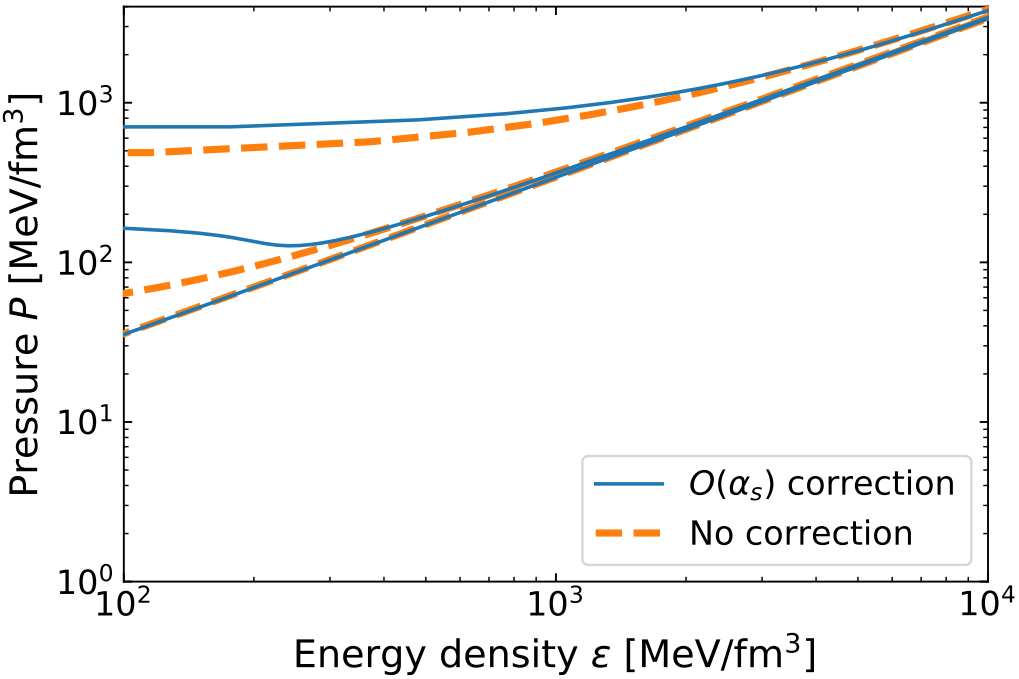

Fig. 5.1: EoS from the HDLpt with and without the $O(\alpha_s)$ correction.

approximated as [232]

$$\omega_{f+} \approx k + \frac{M_{\mathrm{q}f}^2}{k}\,, \quad \omega_{f-} \approx k + 2k\exp\left(-\frac{2k^2}{M_{\mathrm{q}f}^2} - 1\right). \tag{5.2}$$

Substituting this expression in to the quasi-particle contribution,

$$P_{\mathrm{qp},f} = \frac{1}{\pi^2}\int_0^\infty dk\, k^2 \sum_{\chi=\pm1}[(\mu_f - \omega_{f\chi})\theta(\mu_f - \omega_{f\chi})] - \frac{\mu_f^4}{12\pi^2}\,. \tag{5.3}$$

By approximating the step function as $\theta(\mu_f - \omega_{f\chi}) \approx \theta(\mu_f - k)$, we get the leading correction

$$\begin{aligned} P_{\mathrm{qp},f} &\approx \frac{1}{\pi^2}\int^{\mu_f} dk\, k^2\left(\mu_f - k - \frac{M_{\mathrm{q}f}^2}{k}\right) + \frac{1}{\pi^2}\int^{\mu_f} dk\, k^2\left[\mu_f - k - 2k\exp\left(-\frac{2k^2}{M_{\mathrm{q}f}^2} - 1\right)\right] - \frac{\mu_f^4}{12\pi^2}\,, \\ &\approx \frac{1}{\pi^2}\left(\frac{k^3}{3}\mu_f - \frac{k^4}{4} - \frac{k^2}{2}M_{\mathrm{q}f}^2\right)\Bigg|^{\mu_f} + \frac{1}{\pi^2}\left(\frac{k^3}{3}\mu_f - \frac{k^4}{4}\right)\Bigg|^{\mu_f} - \frac{\mu_f^4}{12\pi^2}\,, \\ &= \frac{\mu_f^4}{12\pi^2}\left(1 - 6\frac{M_{\mathrm{q}f}^2}{\mu_f^2}\right) = P_{\mathrm{ideal}}\left(1 - 4\frac{\alpha_s}{\pi}\right). \end{aligned} \tag{5.4}$$

We note that this equation explains why the ideal pressure $\mu_f^4/(12\pi^2)$ should be subtracted in Eq. (4.18): from both quasi-particle branches, ω_{f+} and ω_{f-}, there is the over counted ideal pressure contribution, so one of them should be subtracted.

The conventional pQCD result is [56–59]

$$\frac{P_{\rm pQCD}}{P_{\rm ideal}} = 1 - 2\frac{\alpha_s}{\pi} + O(\alpha_s^2)\,. \tag{5.5}$$

Therefore we can match the $O(\alpha_s)$ terms of the HDLpt with the conventional pQCD result by adding the following *ad hoc* correction to $P_{\rm HDLpt}$:

$$P_{\rm corr} = 2\frac{\alpha_s}{\pi}P_{\rm ideal}\,, \tag{5.6}$$

which was introduced in Ref. [227].

In Fig. 5.1, we quantify the effect of this $O(\alpha_s)$ correction. We only calculate it in the massless limit because the qualitative feature is already captured in the massless limit (of course the strange quark mass becomes important when discussing the *quantitative* feature). The EoS does not change its form drastically, in particular for $\bar{\Lambda} = 4\mu$, which is the bottom-most line in the figure. It is natural as larger $\bar{\Lambda}$ means the smaller α_s, so that the effect of $O(\alpha_s)$ correction becomes also smaller. This *ad hoc* correction can be naturally reproduced by going to the next order in the perturbative expansion [207, 208].

5.1.2 Bare quark mass contribution to the self-energy

In this subsection, we will see how the derivation given in Sec. 4.2 changes if we keep the bare quark mass m_f in the self-energy expression of Eq. (3.33). We note that the dispersion relation of the massive quarks has previously been studied in Refs. [258–261] (see also Ref. [262] for the recent development based on the effective theory). Unlike in Sec. 4.2, when we keep the bare quark mass, then there is an additional constant term in the self-energy expression:

$$\Sigma(k_0, \boldsymbol{k}) = \Sigma_0(k_0, k)\gamma^0 - \Sigma_{\rm s}(k_0, k)\boldsymbol{\gamma}\cdot\hat{\boldsymbol{k}} - \Sigma_{\rm m}\,. \tag{5.7}$$

The last term arises owing to the mass correction; it can be verified shortly after by seeing it is proportional to m_f itself. If we neglect the bare mass in the loop, then $\Sigma_{\rm m} = 0$. Now with the bare mass correction, the inverse propagator in Eq. (4.11) modifies its form to

$$S_f^{-1}(k_0, k) = A_0(k_0, k)\gamma^0 - A_{\rm s}(k_0, k)\boldsymbol{\gamma}\cdot\hat{\boldsymbol{k}} - A_{\rm m}\,, \tag{5.8}$$

where we define

$$A_0 = k_0 - \Sigma_0, \quad A_{\rm s} = k - \Sigma_{\rm s}, \quad A_{\rm m} = m_s - \Sigma_{\rm m}\,. \tag{5.9}$$

If we evaluate each term in Eq. (5.7) under the HDL approximation at $T = 0$ but keeping the bare mass correction intact, i.e., applying the following approximation to Eq. (3.33)

$$E_{\boldsymbol{q}} = \sqrt{\boldsymbol{q}^2 + m_f^2}\,, \quad E_{\boldsymbol{q}-\boldsymbol{k}} \simeq q - k\cos\theta\,. \tag{5.10}$$

Note that preceding section, $E_{\boldsymbol{q}}$ was approximated as $E_{\boldsymbol{q}} \simeq q$. We obtain after long calculations (we evaluate in $3-2\epsilon$ spatial dimension)

$$\hat{\Sigma}_0(k_0,k) = \frac{4(1-\epsilon)\Gamma(\frac{3}{2})}{(4\pi)^{2-\epsilon}\Gamma(\frac{3}{2}-\epsilon)} g^2 \int_0^{\sqrt{\mu_f^2-m_f^2}} dq\, \frac{q^{1-2\epsilon}}{k_0+E_q-q}\, {}_2F_1\left(\frac{1}{2},1;\frac{3}{2}-\epsilon;\frac{k^2}{(k_0+E_q-q)^2}\right), \tag{5.11}$$

$$\hat{\Sigma}_{\rm s}(k_0,k) = \frac{4(1-\epsilon)\Gamma(\frac{3}{2})}{(4\pi)^{2-\epsilon}\Gamma(\frac{3}{2}-\epsilon)} \frac{g^2}{k} \int_0^{\sqrt{\mu_f^2-m_f^2}} dq\, \frac{q^{2-2\epsilon}}{E_q}\left[{}_2F_1\left(\frac{1}{2},1;\frac{3}{2}-\epsilon;\frac{k^2}{(k_0+E_q-q)^2}\right)-1\right], \tag{5.12}$$

$$\hat{\Sigma}_{\rm m}(k_0,k) = \frac{4(2-\epsilon)\Gamma(\frac{3}{2})}{(4\pi)^{2-\epsilon}\Gamma(\frac{3}{2}-\epsilon)} g^2 m_f \int_0^{\sqrt{\mu_f^2-m_f^2}} dq\, \frac{q^{1-2\epsilon}}{E_q(k_0+E_q-q)}\, {}_2F_1\left(\frac{1}{2},1;\frac{3}{2}-\epsilon;\frac{k^2}{(k_0+E_q-q)^2}\right). \tag{5.13}$$

In the limit $\epsilon \to 0$, it becomes

$$\hat{\Sigma}_0(k_0,k) = \frac{g^2}{4\pi^2} \int_0^{\sqrt{\mu_f^2-m_f^2}} dq\, \frac{q}{k_0+E_q-q}\, {}_2F_1\left(\frac{1}{2},1;\frac{3}{2};\frac{k^2}{(k_0+E_q-q)^2}\right), \tag{5.14}$$

$$\hat{\Sigma}_{\rm s}(k_0,k) = \frac{g^2}{4\pi^2 k} \int_0^{\sqrt{\mu_f^2-m_f^2}} dq\, \frac{q^2}{E_q}\left[{}_2F_1\left(\frac{1}{2},1;\frac{3}{2};\frac{k^2}{(k_0+E_q-q)^2}\right)-1\right], \tag{5.15}$$

$$\hat{\Sigma}_{\rm m}(k_0,k) = \frac{m_f g^2}{2\pi^2} \int_0^{\sqrt{\mu_f^2-m_f^2}} dq\, \frac{q}{E_q(k_0+E_q-q)}\, {}_2F_1\left(\frac{1}{2},1;\frac{3}{2};\frac{k^2}{(k_0+E_q-q)^2}\right). \tag{5.16}$$

Note that this expression can also be obtained from the HTL effective Lagrangian with the bare quark mass given in Ref. [263], in which he assumes $E_{\boldsymbol{q}} \simeq q + m_f^2/(2q)$.

We can check that these expressions recover the familiar expression in the massless limit $m_f \to 0$, namely,

$$\hat{\Sigma}_0(k_0,k) \xrightarrow{m_f\to 0} \frac{g^2}{4\pi^2 k_0} \int_0^{\mu_f} dq\, q\, {}_2F_1\left(\frac{1}{2},1;\frac{3}{2};\frac{k^2}{k_0^2}\right) = \frac{M_{{\rm q}f}^2}{k_0}\, {}_2F_1\left(\frac{1}{2},1;\frac{3}{2};\frac{k^2}{k_0^2}\right), \tag{5.17}$$

$$\hat{\Sigma}_{\rm s}(k_0,k) \xrightarrow{m_f\to 0} \frac{g^2}{4\pi^2 k} \int_0^{\mu_f} dq\, q\left[{}_2F_1\left(\frac{1}{2},1;\frac{3}{2};\frac{k^2}{k_0^2}\right)-1\right] = \frac{M_{{\rm q}f}^2}{k}\left[{}_2F_1\left(\frac{1}{2},1;\frac{3}{2};\frac{k^2}{k_0^2}\right)-1\right], \tag{5.18}$$

$$\hat{\Sigma}_{\rm m}(k_0,k) \xrightarrow{m_f\to 0} 0\,. \tag{5.19}$$

In the massless case, as was seen in Eq. (3.36), there was the simple factorization into the radial integration, which leads to the quark screening mass $\hat{M}_{{\rm q}f}$, and the angular integration. However, this feature is lost in the massive case. This disastrously complicates the expression of the self-energy.

Now the branch cut of $\hat{\Sigma}$, which was shown in Fig. 4.2, is modified to the $-k-m_f < \omega < k+k_F-\mu_f$ with $k_F = \sqrt{\mu_f^2-m_f^2}$ being the Fermi momentum. It also complicates the quasi-particle contribution

to the pressure as

$$P^{\text{massive}}_{\text{qp},f}(T=0,\mu_f) = \frac{1}{\pi^2}\int_0^\infty dk\, k^2 \sum_{\chi=\pm1}\left[(\mu_f-\omega_{f\chi})\theta(\mu_f-\omega_{f\chi})\right] - \frac{(2\mu_f-k_F)^4}{12\pi^2}\,, \tag{5.20}$$

where $\omega_{f\chi}$ are the solution of

$$0 = A_0(\omega_{f\pm},k) \mp \sqrt{A^2_{\text{m}}(\omega_{f\pm},k)+A^2_{\text{s}}(\omega_{f\pm},k)}\,. \tag{5.21}$$

The Landau damping contribution to the pressure can be generalized to

$$P^{\text{massive}}_{\text{Ld},f}(T=0,\mu_f) = \frac{1}{\pi}\int_{\boldsymbol{k}}\int_{-k-m_f}^{k+k_F-\mu_f} d\omega\, 2\theta^{\text{massive}}_{\text{q}f}\theta(\mu_f-\omega)\,, \tag{5.22}$$

where $2\theta^{\text{massive}}_{\text{q}f}$ is defined as

$$2\theta^{\text{massive}}_{\text{q}f} = \arctan\left\{\frac{\text{Im}\left[A^2_{\text{s}}(\omega,k)+A^2_{\text{m}}(\omega,k)-A^2_0(\omega,k)\right]}{\text{Re}\left[A^2_{\text{s}}(\omega,k)+A^2_{\text{m}}(\omega,k)-A^2_0(\omega,k)\right]}\right\}. \tag{5.23}$$

The imaginary of $A^2_{\text{s}}+A^2_{\text{m}}-A^2_0$ can only be evaluated numerically, so that these expressions cannot be simplified further.

We have shown this calculation for completeness, but we posit that neglecting the bare quark mass in the HTL approximation is not a large effect. It is indeed the standard practice to drop the bare quark mass in this approximation. Thus, we do not go into further details and leave the numerical evaluation of this effect for the future.

5.2 Φ-derivable approximation in the 2PI expansion

The advantage of the 2PI formalism is that one can reproduce the perturbative result beyond two-loop order without calculating two-loop diagrams directly. The expression of density was already given in Eq. (3.62) above. It is

$$n_{\Phi,f}(T,\mu_f) = -2\int_{\boldsymbol{k}}\int\frac{d\omega}{2\pi}\frac{\partial f_{\text{F}}(\omega-\mu_f)}{\partial\mu_f}\,\text{tr}\left[\text{Im}\ln S^{-1} - \text{Im}\,\Sigma\,\text{Re}\,S\right]. \tag{5.24}$$

By using the identity

$$\text{Im}\ln S^{-1}(\omega,k) = \arctan\left(\frac{\text{Im}\,S^{-1}}{\text{Re}\,S^{-1}}\right) - \pi\,\text{sgn}(\omega)\theta(-\,\text{Re}\,S^{-1})\,, \tag{5.25}$$

we can split the first term of the trace in Eq. (5.24) into two terms, namely, the Landau-damping contribution, $n_{\text{Ld},f}$, and the quasi-particles contribution, $n_{\text{qp},f}$. In fact, these terms are exactly the same

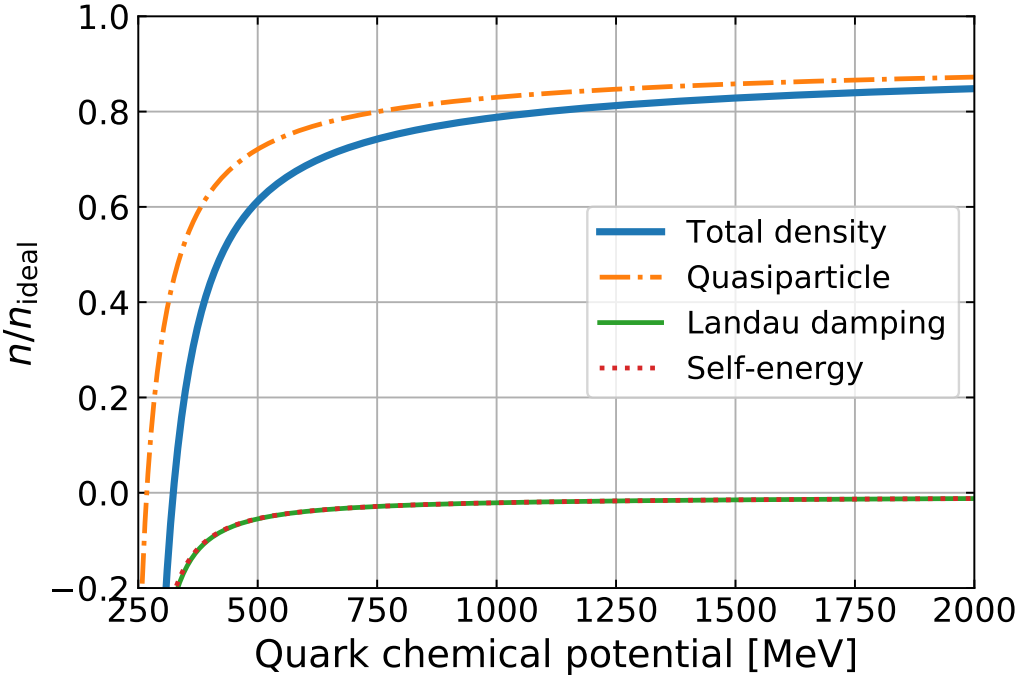

Fig. 5.2: A breakdown of each contribution to the pressure in the Φ-derivable approximation.

as the one evaluated in HDLpt in the preceding section. The only difference between the HDLpt and the Φ-derivable approximation resides in the second term of the trace in Eq. (5.24), i.e., the self-energy contribution $n_{\mathrm{se},f}$. Thus, the Φ-derivable approximate expression of the density, $n_{\Phi,f}$ (5.24) can be recast in the form

$$n_{\Phi,f}(T,\mu_f) = N_{\mathrm{c}} \sum_{f=u,d,s} \left(n_{\mathrm{qp},f} + n_{\mathrm{Ld},f} + n_{\mathrm{se},f} \right) . \tag{5.26}$$

The contribution from each term is depicted in Fig. 5.2. As in the case of the HDLpt, the quasi-particle contribution is dominant.

The quasi-particle and Landau-damping contributions can be simply given by just taking the derivative of Eq. (4.18) and (4.22) with respect to μ_f with keeping $M_{\mathrm{q}f}$ constant

$$\begin{aligned} n_{\mathrm{qp},f}(T,\mu_f) &= \left(\frac{\partial P_{\mathrm{qp},f}}{\partial \mu_f} \right)_{M_{\mathrm{q}f}} \\ &= -\frac{1}{\pi^2} \int_0^\infty dk\, k^2 \sum_{\chi,s=\pm} \frac{s}{e^{\beta(\omega_{f\chi}+s\mu_f)}+1} - \left(\frac{\mu_f T^2}{3} + \frac{\mu_f^3}{3\pi^2} \right) , \end{aligned} \tag{5.27}$$

$$\begin{aligned} n_{\mathrm{Ld},f}(T,\mu_f) &= \left(\frac{\partial P_{\mathrm{Ld},f}}{\partial \mu_f} \right)_{M_{\mathrm{q}f}} \\ &= -\frac{1}{\pi^3} \int_0^\infty d\omega \frac{\partial}{\partial \mu_f} \left[\frac{1}{e^{\beta(\omega-\mu_f)}+1} + \frac{1}{e^{\beta(\omega+\mu_f)}+1} \right] \int_\omega^\infty dk\, k^2\, \theta_{\mathrm{q}f}(\omega,k;m_f,M_{\mathrm{q}f}^2) . \end{aligned} \tag{5.28}$$

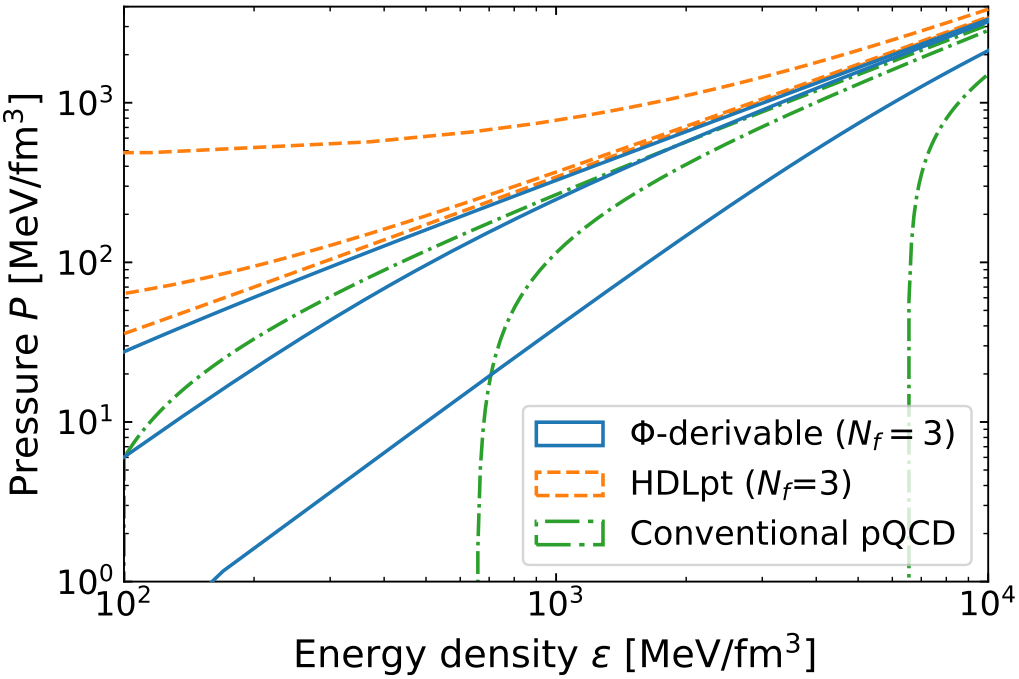

Fig. 5.3: $P(\varepsilon)$ evaluated within the Φ-derivable approach.

In the $T = 0$ limit, they become

$$n_{\mathrm{qp},f}(T=0,\mu_f) = \frac{1}{\pi^2}\int_0^\infty dk\, k^2 \sum_{\chi=\pm1} \theta(\mu_f - \omega_{f\chi}) - \frac{\mu_f^3}{3\pi^2}\,, \tag{5.29}$$

$$n_{\mathrm{Ld},f}(T=0,\mu_f) = -\frac{1}{\pi^3}\int_{\mu_f}^\infty dk\, k^2\, \theta_{\mathrm{q}f}(\mu_f,k;m_f,M_{\mathrm{q}f}^2)\,. \tag{5.30}$$

Performing the similar calculation in Sec. 4.2, we can obtain the expression for $n_{\mathrm{se},f}(T,\mu_f)$

$$n_{\mathrm{se},f}(T,\mu_f) = -\frac{1}{\pi^3}\int_0^\infty d\omega \frac{\partial}{\partial\mu_f}\left[\frac{1}{e^{\beta(\omega-\mu_f)}+1} + \frac{1}{e^{\beta(\omega+\mu_f)}+1}\right]\int_\omega^\infty dk\, k^2 \frac{\mathcal{Y}\left[\mathcal{X} - \frac{\pi^2 M_{\mathrm{q}f}^4}{2k^4}(k^2-\omega^2)\right]}{\mathcal{X}^2+\mathcal{Y}^2}\,, \tag{5.31}$$

where the functions $\mathcal{X}$ and $\mathcal{Y}$ are defined in Eqs. (4.23) and (4.24). In $T = 0$ limit, it becomes

$$n_{\mathrm{se},f}(T=0,\mu_f) = -\frac{1}{\pi^3}\int_{\mu_f}^\infty dk\, k^2 \left.\frac{\mathcal{Y}\left[\mathcal{X} - \frac{\pi^2 M_{\mathrm{q}f}^4}{2k^4}(k^2-\omega^2)\right]}{\mathcal{X}^2+\mathcal{Y}^2}\right|_{\omega=\mu_f}\,. \tag{5.32}$$

This completes the derivation of three terms in Eq. (5.26).

From the density $n_{\Phi,f}$, we can compute the pressure

$$P_{\Phi,f}(\mu_f;\bar{\Lambda}) = -B + \int_{\mu_0(\bar{\Lambda})}^{\mu_f} d\mu'\, n_{\Phi,f}(\mu';\bar{\Lambda})\,, \tag{5.33}$$

where $\mu_0(\bar{\Lambda})$ is the point that $n_{2\mathrm{PI},f}$ becomes zero for the given value of $\bar{\Lambda} = \xi\mu$, i.e., $n_{\Phi,f}(\mu_0(\bar{\Lambda});\bar{\Lambda}) = 0$. There is an ambiguity in the constant term in the above expression; it may be regarded as the bag constant in the MIT bag model [264, 265], which quantifies the energy difference in the pressure of hadronic matter and quark matter. Nevertheless, we can set the constant $B = 0$, and then evaluate the relation between P and the energy density ε as in Fig. 5.3. The pressure values are different between the Φ-derivable approximation and the HDLpt results, due to the difference in the constant terms, but still, the scale variation uncertainty is smaller than the conventional pQCD.

These results imply that resummation both in the HDLpt and the Φ-derivable approximation somehow alleviates the scale variation uncertainty. The difference between the HDLpt and the Φ-derivable approximation is due to the treatment of the vacuum term, in other words, the μ- and T-independent term, which is denoted as $P^\star$ in Sec. 4.2. In the former scheme, it evaluates the vacuum term utilizing the dimensional regularization, while the latter simply throws away this contribution since we only calculate the density that depends on μ and T; the pressure is evaluated indirectly through the integration of the density. This treatment of the vacuum terms is by no means trivial, so it is worth further investigation, and we leave it as future work. In this thesis, we regard the HDLpt calculation as our primary result and the Φ-derivable approximation as the complementary approach, so that we do not go into the details.

Chapter 6

Reduction of scale variation uncertainty

The surprising feature of our HDLpt calculations is the reduction of scale variation uncertainty in the EoS expressed in the form of $P(\varepsilon)$. In this chapter, we explain what is the origin of such a drastic difference, and then write down the condition for the reduction of uncertainty. We put a caveat on the treatment of the μ-dependence in the coupling constant.

6.1 Origin of the scale variation uncertainty in pQCD

In principle, the value of physical observables should not depend on the renormalization scale $\bar{\Lambda}$. Here, however, the pressure–energy density relation depends on the value of $\bar{\Lambda}$; it can be identified as the effect of truncation of the perturbative series at a certain order.

The scale variation uncertainty originates from the NNLO or beyond in the conventional pQCD calculation, i.e., 3-loop order, or $O(\alpha_s^2)$. Up to NLO, the quark pressure and density reads

$$P = P_{\text{ideal}}\left[1 - 2\frac{\alpha_s(\bar{\Lambda})}{\pi}\right], \tag{6.1}$$

$$n = n_{\text{ideal}}\left[1 - 2\frac{\alpha_s(\bar{\Lambda})}{\pi}\right], \tag{6.2}$$

where $P_{\text{ideal}} = \mu^4/(12\pi^2)$ and $n_{\text{ideal}} = \mu^3/(3\pi^2)$. Owing to the same perturbative coefficients, the relation $P(n)$ or $P(\varepsilon)$ does not depend on $\bar{\Lambda}$ at all. Indeed, if we calculate the speed of sound, then it is always constant $c_s^2 = 1/3$.

At NNLO, the quark pressure and the reads

$$P = P_{\text{ideal}}\left[1 - 2\frac{\alpha_s(\bar{\Lambda})}{\pi} + \left(C(\alpha_s) + \beta_0 \ln\frac{\bar{\Lambda}}{\mu}\right)\left(\frac{\alpha_s(\bar{\Lambda})}{\pi}\right)^2\right], \tag{6.3}$$

$$n = \frac{\partial P}{\partial \mu} = n_{\text{ideal}}\left[1 - 2\frac{\alpha_s(\bar{\Lambda})}{\pi} + \left(C(\alpha_s) + \beta_0 \ln\frac{\bar{\Lambda}}{\mu} \underbrace{- \frac{\beta_0}{4}}\right)\left(\frac{\alpha_s(\bar{\Lambda})}{\pi}\right)^2\right], \tag{6.4}$$

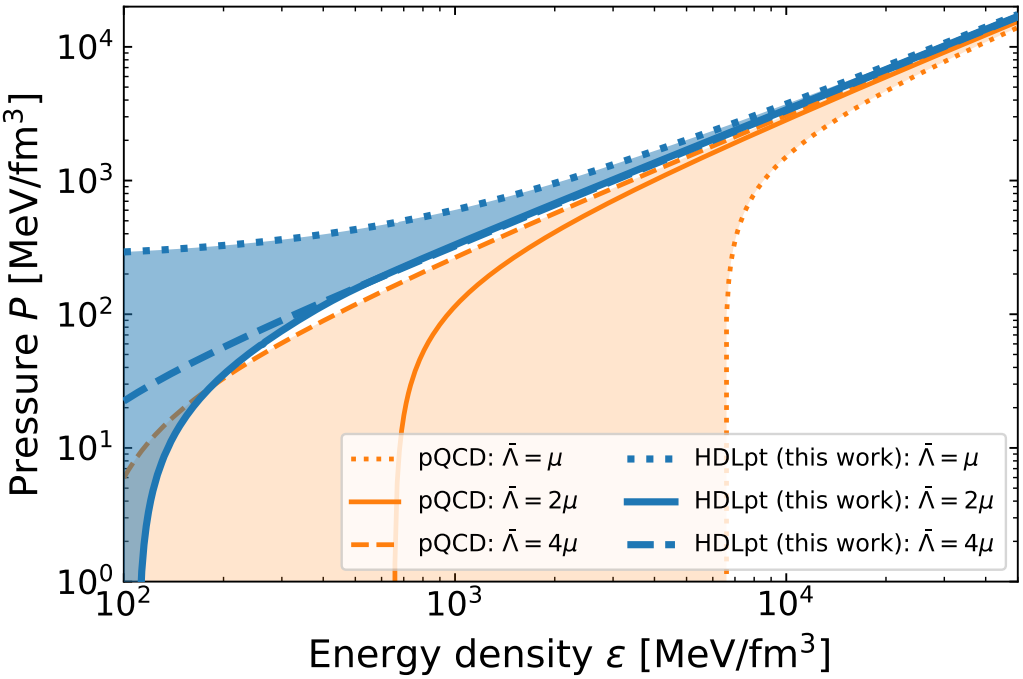

Fig. 6.1: Scale variation uncertainty for the conventional pQCD and the HDLpt (our result) calculations.

where the constant irrelevant to the discussion here is defined as $C(\alpha_s) = 18 - 11\ln 2 - 0.536N_\mathrm{f} + N_\mathrm{f}\ln(N_\mathrm{f}\alpha_s/\pi)$. The term marked with the under brace in Eq. (6.4) is responsible for the $\bar{\Lambda}$-dependence in the $P(n)$-relation or the $P(\varepsilon)$-relation. This under-braced term arises from the $\ln\mu$ contribution in the expression, so the $\ln\mu$ term is the very reason for the scale variation uncertainty. Note that even if we substitute $\bar{\Lambda} = \xi\mu$ ($\xi = 1, 2, 4$) first, then take the derivative of P with respect to μ, one will still get the term that will produce the deviation from the pressure expression as in Eq. (6.4). It is related to whether we resum $\ln\mu$ dependence in α_s or not (see Sec. 6.4 for details).

6.2 Heuristic interpretation

One may wonder what causes such a drastic difference in the scale variation uncertainty in Fig. 6.1. We can qualitatively understand this from Fig. 6.2 (top) in which the baryon number density n_B as a function of the quark chemical potential μ is plotted.

Because the HDLpt sums the quark loops up, n_B is the most sensitive quantity affected by the resummation in the quark sector. It is an interesting and reasonable observation that n_B is suppressed at fixed μ after the resummation: thermodynamic quantities are dominated by quark quasi-particles (see Fig. 4.1), and in HDLpt, quark excitations are more screened by self-energy insertions, as compared to pQCD treatments. Therefore, on Fig. 6.1, the corresponding μ for a given ε becomes larger, and the corresponding running coupling $\alpha_s(\bar{\Lambda} = \xi\mu)$, where $\xi = 1, 2, 4$, is smaller. This qualitative argument partially accounts for the reduction of the uncertainty band, but not fully yet. As shown in Fig. 6.2,

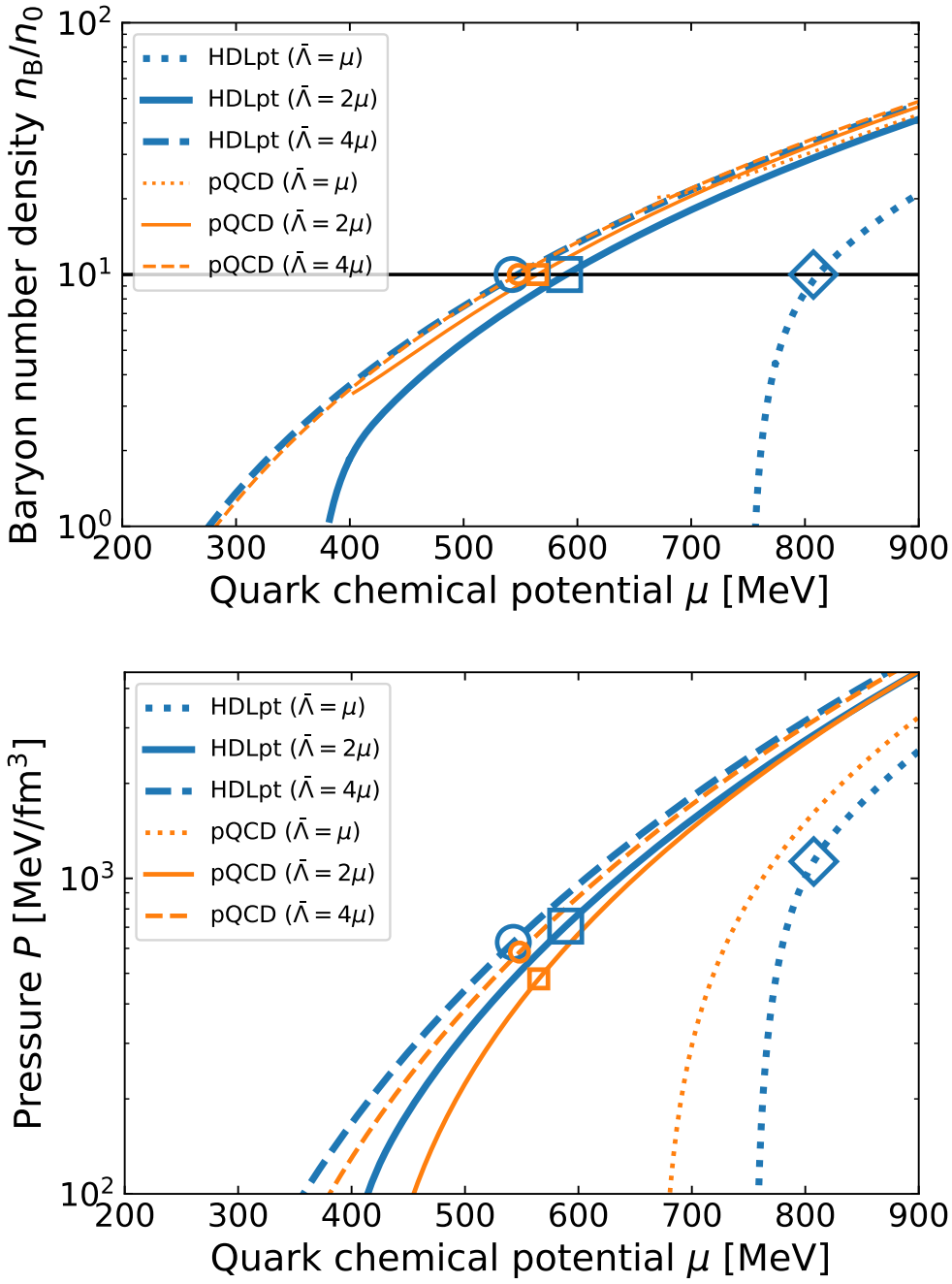

Fig. 6.2: Baryon number density (top) and pressure (bottom) as functions of the quark chemical potential. In the figure pQCD refers to the results from Refs. [60, 61] and HDLpt to our results.

if we plot the pressure P, the baryon number density $n_{\rm B}$, and the energy density ε as functions of μ, respectively, the uncertainty bands are wider than Fig. 6.1. In Fig. 6.2 (top), we overlay a horizontal line at $n_{\rm B} = 10\, n_0$ to find the values of the corresponding μ for different $\bar{\Lambda}$. The values of P at these μ's are shown in Fig. 6.2 (bottom) with the same markers. Importantly, the marker for $P(\bar{\Lambda} = \mu)$ is out of the plot range. This $P(\bar{\Lambda} = \mu)$ one was the most problematic, which was actually the source of the large uncertainty in the conventional pQCD calculation. Owing to the suppression in $n_{\rm B}$ leads to the situation that $P(\varepsilon)$ with $\bar{\Lambda} = \mu$ and that with $\bar{\Lambda} = 4\mu$ happen to stay close, which narrows the uncertainty band on Fig. 6.1. There might be a deep reason (e.g., scaling properties) for this behavior, and further investigations are in progress.

6.3 Scale independence condition

For the astrophysical application, we need $P(\varepsilon)$ or $P(n_{\rm B})$ rather than $P(\mu)$. Here we formulate the scale independence condition for $P(\varepsilon)$ or $P(n_{\rm B})$.

6.3.1 P–$n_{\rm B}$ relation

The condition that $P(n_{\rm B}; \bar{\Lambda}) \equiv P(\mu_{\rm B}(n_{\rm B}; \bar{\Lambda}); \bar{\Lambda})$ is insensitive to the scale $\bar{\Lambda}$ is

$$0 = \frac{dP(n_{\rm B}; \bar{\Lambda})}{d\bar{\Lambda}} = \frac{\partial P(\mu_{\rm B}(n_{\rm B}; \bar{\Lambda}); \bar{\Lambda})}{\partial \bar{\Lambda}} + \frac{\partial P(\mu_{\rm B}(n_{\rm B}; \bar{\Lambda}); \bar{\Lambda})}{\partial \mu_{\rm B}} \frac{\partial \mu_{\rm B}(n_{\rm B}; \bar{\Lambda})}{\partial \bar{\Lambda}} \tag{6.5}$$

At this point we require $d\mu_{\rm B}/d\bar{\Lambda} = 0$, where $\mu_{\rm B}$ is the function of $n_{\rm B}$ and takes a certain value at fixed $\mu^*_{\rm B}$, i.e.,

$$\mu_{\rm B}(n_{\rm B}(\mu^*_{\rm B}; \bar{\Lambda}); \bar{\Lambda}) = \mu^*_{\rm B}\,. \tag{6.6}$$

Then, taking the derivative with respect to $\bar{\Lambda}$ on the both hand sides leads to

$$\frac{\partial \mu_{\rm B}}{\partial \bar{\Lambda}} + \frac{\partial \mu_{\rm B}}{\partial n_{\rm B}} \frac{\partial n_{\rm B}}{\partial \bar{\Lambda}} = 0\,. \tag{6.7}$$

We plug this expression into Eq. (6.5), and obtain

$$\frac{\partial P(\mu_{\rm B}; \bar{\Lambda})}{\partial \bar{\Lambda}} - \frac{n_{\rm B}(\mu_{\rm B}; \bar{\Lambda})}{\chi_{\rm B}(\mu_{\rm B}; \bar{\Lambda})} \frac{\partial n_{\rm B}(\mu_{\rm B}; \bar{\Lambda})}{\partial \bar{\Lambda}} = 0\,, \tag{6.8}$$

where $\mu_{\rm B} = 3\mu$ is the baryochemical potential and $\chi_{\rm B} \equiv \partial n_{\rm B}/\partial \mu_{\rm B}$ is the baryon number susceptibility. Using the expression of the speed of sound (7.2), one can put it in the form

$$\frac{\partial P(\mu_{\rm B}; \bar{\Lambda})}{\partial \bar{\Lambda}} - c_s^2 \mu_{\rm B} \frac{\partial n_{\rm B}(\mu_{\rm B}; \bar{\Lambda})}{\partial \bar{\Lambda}} = 0\,. \tag{6.9}$$

6.3.2 P–ε relation

We can also derive such a condition for $P(\varepsilon;\bar{\Lambda}) \equiv P(\mu_{\rm B}(\varepsilon;\bar{\Lambda});\bar{\Lambda})$ likewise. It is

$$0 = \frac{dP(\varepsilon;\bar{\Lambda})}{d\bar{\Lambda}} = \frac{\partial P(\mu_{\rm B}(\varepsilon;\bar{\Lambda});\bar{\Lambda})}{\partial\bar{\Lambda}} + \frac{\partial P(\mu_{\rm B}(\varepsilon;\bar{\Lambda});\bar{\Lambda})}{\partial\mu_{\rm B}}\frac{\partial\mu_{\rm B}(\varepsilon;\bar{\Lambda})}{\partial\bar{\Lambda}}\,. \tag{6.10}$$

Using the relation similar to Eq. (6.7):

$$\frac{\partial\mu_{\rm B}}{\partial\bar{\Lambda}} + \frac{\partial\mu_{\rm B}}{\partial\varepsilon}\frac{\partial\varepsilon}{\partial\bar{\Lambda}} = 0\,, \tag{6.11}$$

we finally arrive at

$$\frac{\partial P(\mu_{\rm B};\bar{\Lambda})}{\partial\bar{\Lambda}} - c_s^2\frac{\partial\varepsilon(\mu_{\rm B};\bar{\Lambda})}{\partial\bar{\Lambda}} = 0\,. \tag{6.12}$$

By substituting the thermodynamic relation $\varepsilon = -P + \mu_{\rm B}n_{\rm B}$, the condition becomes

$$\left(1+c_s^2\right)\frac{\partial P(\mu_{\rm B};\bar{\Lambda})}{\partial\bar{\Lambda}} - c_s^2\mu_{\rm B}\frac{\partial n_{\rm B}(\mu_{\rm B};\bar{\Lambda})}{\partial\bar{\Lambda}} = 0\,. \tag{6.13}$$

Furthermore, in the most of the pQCD calculation, it can be approximated as $c_s^2 \approx 1/3$, thus,

$$\frac{4}{3}\frac{\partial P(\mu_{\rm B};\bar{\Lambda})}{\partial\bar{\Lambda}} - \frac{1}{3}\mu_{\rm B}\frac{\partial n_{\rm B}(\mu_{\rm B};\bar{\Lambda})}{\partial\bar{\Lambda}} = \frac{1}{3}\left(4-\mu_{\rm B}\frac{\partial}{\partial\mu_{\rm B}}\right)\frac{\partial P(\mu_{\rm B};\bar{\Lambda})}{\partial\bar{\Lambda}} = 0\,. \tag{6.14}$$

The last equation shows that the reduction of the scale uncertainty in $P(\varepsilon)$ is automatically satisfied given that $P(\mu_{\rm B}) \propto \mu_{\rm B}^4$.

In any of the cases for $P(\varepsilon)$ or $P(n_{\rm B})$, the essential observation is that the cancellation between the scale dependence in P and $n_{\rm B}$ is enough to reduce the scale dependence. In the conventional argument, however, the reduction of the scale variation error in $P(\mu)$, that is $\partial P/\partial\bar{\Lambda} = 0$, has been the central issue. Here we point out that $\partial P/\partial\bar{\Lambda} = 0$ is only a sufficient condition for Eqs. (6.9), (6.12), and (6.13). Albeit $\partial P/\partial\bar{\Lambda} \neq 0$, the inclusion of the latter terms, such as $\propto \partial n_{\rm B}/\partial\bar{\Lambda}$ and $\propto \partial\varepsilon/\partial\bar{\Lambda}$, can cancel the scale-dependence; Fig. 6.2 is the concrete realization of such cancellation.

6.4 Issues related to differentiating the μ-dependence in α_s

In this section, we mention the subtleties related to the μ-derivative to be fair. We take the μ-derivative when we derive the number density from the pressure. As repeatedly mentioned above, in our conventional prescription, the renormalization scale $\bar{\Lambda}$ in the coupling constant $\alpha_s(\bar{\Lambda})$ is chosen to be $\bar{\Lambda} = \xi\mu$, where $\xi = 1, 2, 4$. In principle, physical observables should not depend on the choice of the parameter $\bar{\Lambda}$, so this is merely a matter of convention for parametrization. On the other hand, it is nonetheless customary to take $\bar{\Lambda}$ as the typical scale of the system, so that μ is an appropriate choice; for example, in the DGLAP equation in the high-energy pQCD context, Q^2-dependence (see

the definition of Q^2 in Sec. 1.2) is included in the coupling constant, $\alpha_s(Q^2)$, and this Q^2-dependence is also resummed through the Q^2-evolution equation.

Therefore here comes the subtlety: should we also differentiate the μ-dependence in the coupling constant $\alpha_s(\xi\mu)$ when we derive the density? Generally speaking, there is no definite answer to this question; this is something that cannot be determined from principle but requires the comparison of specific calculations. In this thesis, we posit that we should *not* differentiate the μ-dependence in the coupling constant. In the following, we will see how differentiating the μ-dependence in the coupling constant affects the EoS. Then we give a convincing argument why we should not take the μ-derivative for the coupling constant; we will give a couple of justifications in the spirit of the approximately self-consistent resummation, as well as based on the thermodynamic consistency.

Let us firstly take the NNLO expression of the quark pressure.

$$P = P_{\rm ideal}\left[1 - 2\frac{\alpha_s(\bar{\Lambda})}{\pi} + \left(C + N_{\rm f}\ln\frac{\alpha_s(\bar{\Lambda})}{\pi} + \beta_0\ln\frac{\bar{\Lambda}}{\mu}\right)\left(\frac{\alpha_s(\bar{\Lambda})}{\pi}\right)^2\right], \tag{6.15}$$

where the constant irrelevant to the discussion here is defined as $C = 18 - 11\ln 2 - 0.536N_{\rm f} + N_{\rm f}\ln N_{\rm f}$ (note that the definition is different from the one given in Sec. 6.1). If we do not differentiate the μ-dependence in the coupling constant, then the number density becomes

$$n = \frac{\partial P}{\partial\mu} = n_{\rm ideal}\left[1 - 2\frac{\alpha_s(\bar{\Lambda})}{\pi} + \left(C + N_{\rm f}\ln\frac{\alpha_s(\bar{\Lambda})}{\pi} + \beta_0\ln\frac{\bar{\Lambda}}{\mu} - \frac{\beta_0}{4}\right)\left(\frac{\alpha_s(\bar{\Lambda})}{\pi}\right)^2\right]. \tag{6.16}$$

On the other hand, if we differentiate the μ-dependence in the coupling constant, which requires the QCD beta function, then the number density is

$$\begin{aligned} n = \frac{dP}{d\mu} &\equiv \frac{\partial P}{\partial\mu} + \frac{\partial P}{\partial\bar{\Lambda}}\bigg|_{\bar{\Lambda}=\xi\mu}\frac{\partial(\xi\mu)}{\partial\mu} \\ &= n_{\rm ideal}\left[1 - 2\frac{\alpha_s(\bar{\Lambda})}{\pi} + \left(C + N_{\rm f}\ln\frac{\alpha_s(\bar{\Lambda})}{\pi} + \beta_0\ln\frac{\bar{\Lambda}}{\mu} - \frac{\beta_0}{4}\right)\left(\frac{\alpha_s(\bar{\Lambda})}{\pi}\right)^2\right] + O(\alpha_s^3), \end{aligned} \tag{6.17}$$

where we used $\dfrac{\partial\alpha_s(\bar{\Lambda})}{\partial\bar{\Lambda}} = -\dfrac{\beta_0}{\bar{\Lambda}}\dfrac{\alpha_s^2}{2\pi} + O(\alpha_s^3)$ in Eq. (1.5). In this case, the expression of the running coupling constant $\alpha_s(\bar{\Lambda} = \xi\mu)$ incorporates the resummation of $\ln\mu$ terms through the renormalization group equation [58] as is apparent from Eq. (1.2).

Regardless of whether we differentiate α_s with respect to μ or not, these expressions match at the given order of the perturbation theory. But the latter includes the higher-order terms that are beyond the accuracy of the current calculation, which might ruin the thermodynamic consistency [60].

The effect of differentiating α_s with respect to μ is significant when we perform the actual calculation of the EoS. In Figs. 6.3 and 6.4, we plot such an example ($dP/d\mu$ and $\partial P/\partial\mu$ are the ones that does and does not include the μ-differentiation in α_s, respectively). In Fig. 6.3, in which the EoS in the form of $P(\varepsilon)$ is plotted, the scale variation uncertainty becomes as large as that of the conventional

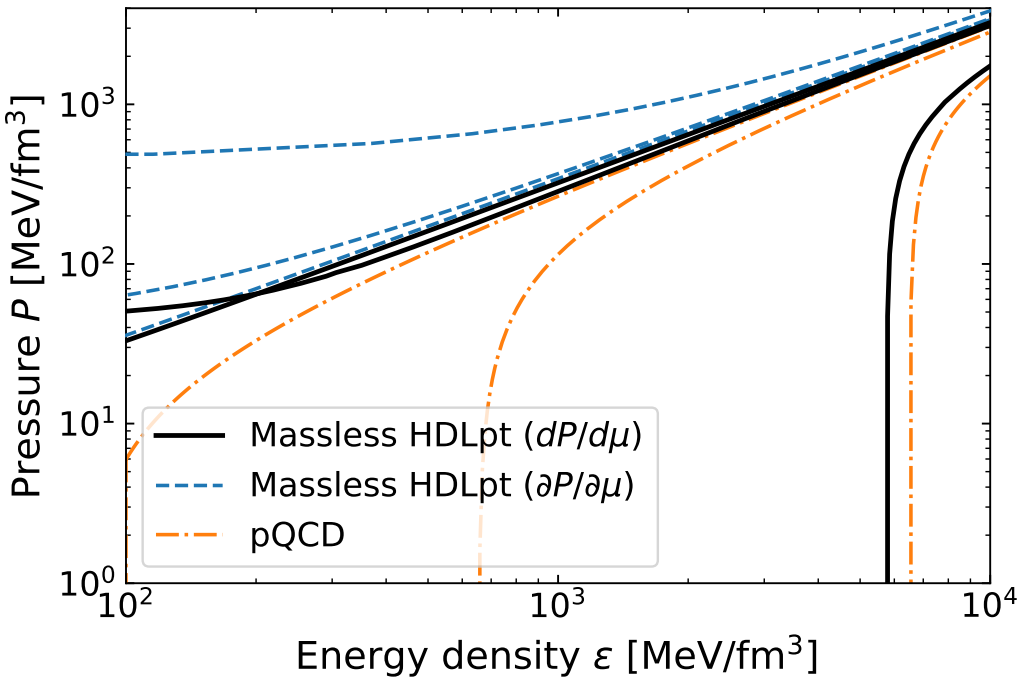

Fig. 6.3: Comparing the effect on the EoS of whether we differentiate μ-dependence in α_s or not. We perform the specific calculation within the massless limit of the HDLpt. The one marked with $dP/d\mu$ refers to the result of differentiating μ-dependence in α_s, and $\partial P/\partial\mu$ refers to not differentiating. We overlay the conventional pQCD result for reference.

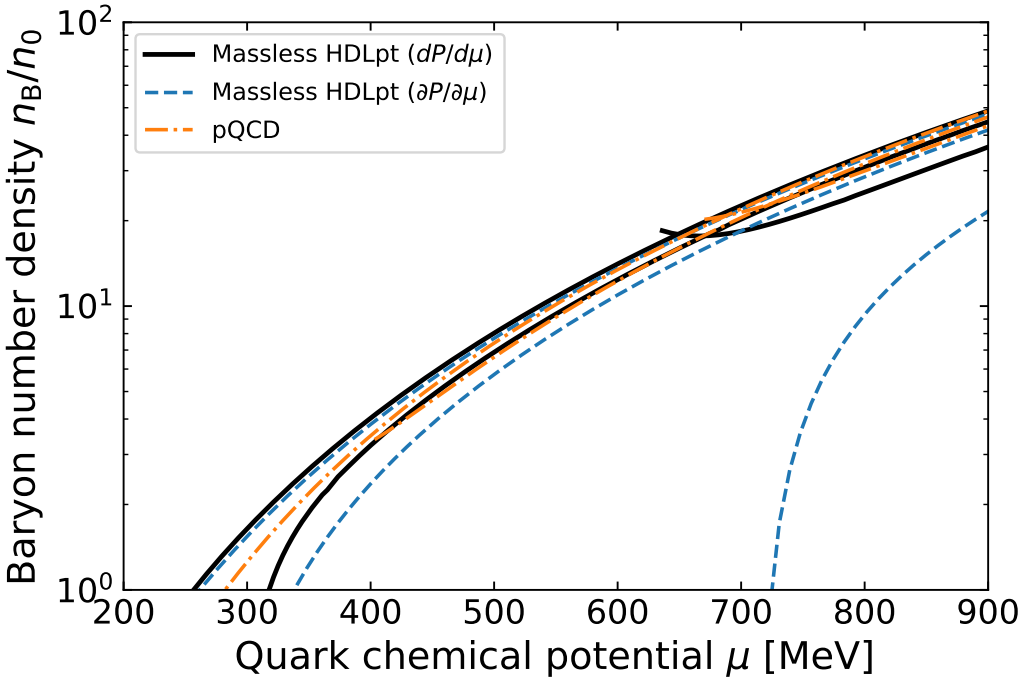

Fig. 6.4: The EoS calculated within the same setup as Fig. 6.3 but plotted as the relation between n_B and μ.

pQCD calculation. Particularly, $\bar{\Lambda} = \mu$ looks very similar to that of the pQCD calculation, which may suggest that the breakdown of the pQCD calculation for $\bar{\Lambda} = \mu$ originates from the coupling constant. Fig. 6.4 shows the $n_{\rm B}(\mu)$ relation and the baryon number density suppression is suppressed for $dP/d\mu$ case.

Here, we give two justifications for not taking the μ-derivative for the coupling constant.

The first justification is based on the thermodynamic consistency [60]. As already shown above, if we differentiate the μ-dependence in the coupling constant, we will get the uncontrolled higher-order terms in the density. These unwanted terms go beyond the perturbation order considered and are typically ill-behaved. If we just drop these higher-order terms, then it implies $Nd\mu \neq VdP$; it is a violation of thermodynamic consistency, so we cannot drop these terms. The simplest solution to this is just to treat the coupling constant as constant, namely, do not differentiate the μ-dependence inside α_s. As was already mentioned above, Eqs. (6.16) and (6.17) show that the expressions of the density match at the given order of the perturbation theory regardless of whether we differentiate α_s with respect to μ or not. In fact, this matching is not a mere coincidence. The $\ln\mu$ terms responsible for the scale variation uncertainty in Eq. (6.16) stem from the vacuum polarization diagrams; they are the same diagrams for the evaluation of the QCD beta function, so the diagrammatic consideration ensures this matching. To further verify the matching beyond the NNLO, we need explicit calculation with four-loop diagrams along the line of Ref. [64], which is left for future work. Nevertheless, the matching favors not to differentiate the μ-dependence in the coupling constant.

In passing, we note that this matching also explains why in Figs. 6.3 and 6.4 the massless HDLpt results with differentiating the μ-dependence in α_s [$dP/d\mu$ in Figs. 6.3 and 6.4] and the conventional pQCD results show the similar behavior; in particular the massless HDLpt ($dP/d\mu$) result for $\bar{\Lambda} = \mu$ breaks down around $\varepsilon \simeq 6 \times 10^3\,\mathrm{MeV/fm^3}$.

The second justification is based on the pressure expression in the HDLpt calculation. In the HDLpt, the $\ln\mu$ term responsible for the scale variation uncertainty enters the expression through a log of the screening mass $\ln M_{{\rm q}f} \sim \ln(g\mu)$. Taking the μ-derivative of α_s is equivalent to setting $\bar{\Lambda} \sim \xi\mu$, so the additional $\ln\mu$ appears; it will lead to the double counting of $\ln\mu$. Thus in the HDLpt, we should not differentiate α_s with respect to μ.

Based on these two justifications, in this thesis, we take the perspectives that we do not take the μ-derivative of α_s.

Chapter 7

Speed of sound

The EoS from our resummed perturbation theory has a notable feature in addition to the smaller uncertainty. Here we discuss the speed of sound that could exceed the conformal limit and the robustness of this behavior against the various corrections.

7.1 Overview of the speed of sound

In this section, we discuss the behavior of the speed of sound (squared), whose definition is given by

$$c_s^2 \equiv \frac{\partial P}{\partial \varepsilon}\,. \tag{7.1}$$

By using the thermodynamic relation $\varepsilon = -P = \mu n = -P + \mu_{\rm B} n_{\rm B}$ it can be recast in the form

$$c_s^2 = \frac{n}{\mu\chi} = \frac{n_{\rm B}}{\mu_{\rm B}\chi_{\rm B}}\,, \tag{7.2}$$

where $\mu_{\rm B} = 3\mu$ is the baryochemical potential as well as $\chi \equiv \partial n/\partial\mu$ and $\chi_{\rm B} \equiv \partial n_{\rm B}/\partial\mu_{\rm B}$ are the quark and baryon number susceptibilities. Rewriting this expression in the following form

$$\left(\mu_{\rm B}\frac{\partial}{\partial\mu_{\rm B}} - \frac{1}{c_s^2}\right) n_{\rm B} = 0\,, \tag{7.3}$$

implies that c_s^2 is related to the effective degrees of freedom of the system. For the ideal Fermi gas, $c_s^2 = 1/3$ and it is indeed $n_{\rm B} \propto \mu_{\rm B}^3$. It is more illuminating if we express the baryon number density as $n_{\rm B} = N(\mu_{\rm B})\mu_{\rm B}^3/(6\pi^2)$ with $N(\mu_{\rm B})$ being the number of degrees of freedom of the system, e.g., polarization, flavor, color, etc. Then the speed of sound can further be altered into the expression

$$c_s^2 = \frac{1}{3}\left(1 + \frac{\mu_{\rm B}}{3N}\frac{dN}{d\mu_{\rm B}}\right)^{-1}\,. \tag{7.4}$$

This implies that if the degrees of freedom increase with increasing chemical potential, i.e. $dN/d\mu_{\rm B} < 0$, then $c_s^2 < 1/3$ holds.

7.1.1 Conformal limit and pQCD calculation

In the conventional pQCD calculation up to $O(\alpha_s^2)$, the value of the speed of sound is almost $1/3$. This value, $c_s^2 \approx 1/3$, is commonly referred to as the conformal limit since it is the value in the conformal theory; in this limit, the EoS reads $P = \varepsilon/3$. In the high-density limit in QCD, asymptotically, all mass scales and interactions are negligible and the conformal limit should be eventually saturated. In the $O(\alpha_s^2)$ pQCD calculation, the first correction from the conformal limit is negative, so that the conformal limit is approached from $c_s^2 < 1/3$ with increasing density. The pQCD expression up to $O(\alpha_s^2)$ for the number density is [56–59]

$$n^{(2)}_{\rm pQCD}(\mu,\bar{\Lambda}) = n_{\rm ideal}\left[1 - 2\frac{\alpha_s}{\pi} - \left(\frac{61}{4} - 11\ln 2 - 0.369N_{\rm f} + N_{\rm f}\ln\frac{N_{\rm f}\alpha_s}{\pi} + \beta_0\ln\frac{\bar{\Lambda}}{\mu}\right)\left(\frac{\alpha_s}{\pi}\right)^2\right]. \tag{7.5}$$

The derivative with respect to μ reads

$$\mu\frac{\partial n^{(2)}_{\rm pQCD}(\mu,\bar{\Lambda})}{\partial\mu} = 3n^{(2)}_{\rm pQCD} + \beta_0\left(\frac{\alpha_s}{\pi}\right)^2 n_{\rm ideal}\,. \tag{7.6}$$

Plugging these expressions in Eq. (7.2), one obtains

$$c_s^2 = \frac{1}{3}\frac{n^{(2)}_{\rm pQCD}/n_{\rm ideal}}{n^{(2)}_{\rm pQCD}/n_{\rm ideal} + \frac{\beta_0}{3}\left(\frac{\alpha_s}{\pi}\right)^2} < \frac{1}{3}\,. \tag{7.7}$$

Alternatively, one can differentiate μ-dependence inside the coupling constant $\alpha_s(\bar{\Lambda} = \xi\mu)$ ($\xi = 1, 2, 4$)

$$\begin{aligned}\mu\frac{dn^{(2)}_{\rm pQCD}(\mu,\bar{\Lambda}=\xi\mu)}{d\mu} &\equiv \mu\frac{\partial n^{(2)}_{\rm pQCD}(\mu,\bar{\Lambda}=\xi\mu)}{\partial\mu} + \mu\frac{\partial n^{(2)}_{\rm pQCD}(\mu,\bar{\Lambda}=\xi\mu)}{\partial\bar{\Lambda}}\frac{\partial(\xi\mu)}{\partial\mu}\,,\\ &= 3n^{(2)}_{\rm pQCD} + \beta_0\left(\frac{\alpha_s}{\pi}\right)^2 n_{\rm ideal} + O(\alpha_s^3)\,.\end{aligned} \tag{7.8}$$

Plugging these expressions in Eq. (7.2), one obtains the same expression as above up to $O(\alpha_s^2)$

$$c_s^2 = \frac{1}{3}\frac{n^{(2)}_{\rm pQCD}/n_{\rm ideal}}{n^{(2)}_{\rm pQCD}/n_{\rm ideal} + \frac{\beta_0}{3}\left(\frac{\alpha_s}{\pi}\right)^2} < \frac{1}{3}\,. \tag{7.9}$$

Even if we take the derivative with respect to μ inside $\alpha_s(\xi\mu)$ or not, the expression of c_s^2 becomes the same up to $O(g^2)$. The very existence of the term $\frac{\beta_0}{3}\left(\frac{\alpha_s}{\pi}\right)^2$ in the denominator ensures that the speed of sound is always less than $1/3$, and approaches the conformal limit from below with increasing

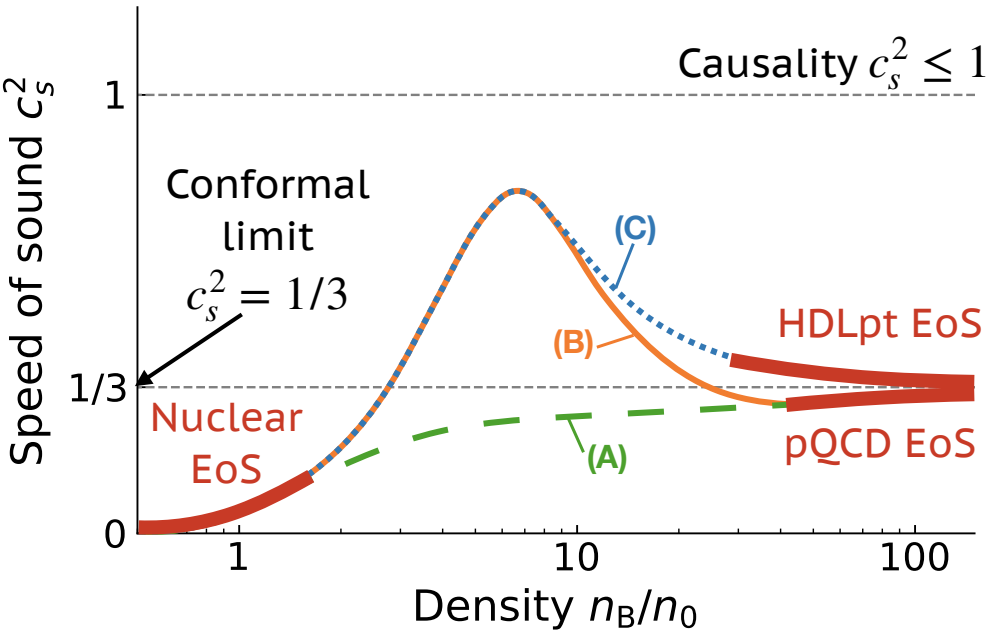

Fig. 7.1: A few possible scenarios for the speed of sound based on the current understanding of its behavior: Scenario (A) refers to the case the conformal limit is always respected. Scenario (B) has the peak in the speed of sound, which violates the conformal limit. Scenario (C) resembles to (B), but the higher density region is different.

density.

It is also interesting to observe that the coefficient is closely related to the asymptotic freedom: β_0 is the first coefficient in the beta function of QCD as is given in Eq. (1.3). The origin of this behavior can be ascribed to the different term depending on whether we differentiate μ-dependence inside $\alpha_s(\xi\mu)$ or not: If we differentiate μ-dependence inside $\alpha_s(\xi\mu)$, the first coefficient of n, i.e. $-2/\pi$, as well as β_0 in Eq. (1.5) is responsible for this behavior. If not, then the term $\beta_0 \ln \bar{\Lambda}/\mu$ at $O(\alpha_s^2)$ is the origin. In the former case, one can state it as the "one-loop" effect, but the latter is the pure "two-loop" effect.

7.1.2 A few scenarios for the speed of sound

Fig. 7.1 summarizes the current state of the speed of sound based on several theory calculations (see Ref. [266] for the recent review). Other than the conformal limit mentioned above, there is an obvious bound of the causality, which forces the speed of sound to be less than the speed of light: $c_s^2 < 1$. There are two established boundary conditions both in lower and higher density terrains: in the lower density region $n_B \simeq 1$–$2\,n_0$, it is almost consensus that the speed of sound is $c_s^2 \ll 1/3$. On the other hand, at the higher density region, in which $n_B \gtrsim 10\,n_0$, the speed of sound approaches $c_s^2 \simeq 1/3$ either from below or above. Also, the recent neutron star observations rule out the strong first-order phase transitions [267]; strong first-order phase transition means that c_s^2 goes to zero. There

may still be a weak first order phase transition [163], but we will assume that the speed of sound can roughly be regarded as the continuous function of density. As shown in Fig. 7.1, its behavior can be classified into a few scenarios:

(A) The speed of sound is always below $c_s^2 = 1/3$. This scenario is based on an empirical conjecture that the speed of sound does not exceed the conformal limit.

(B) The speed of sound has a peak at moderate densities, and it goes below the conformal limit at large densities.

(C) The speed of sound has also a peak at moderate densities, but it is kept above the conformal limit at large densities.

The problem with scenario (A) is that at low densities the value of c_s^2 should be sufficiently large, which means that the EoS should be stiff, otherwise the heavy neutron stars cannot be supported. It is likely that c_s^2 exceeds $1/3$ from the recent neutron star observations [53, 228], so in this sense, scenarios (B) and (C) are more realistic ones.

7.2 The speed of sound in HDL-resummed theories

7.2.1 HDLpt

We calculated the speed of sound within the HDLpt, which is depicted in Fig. 7.2. To make clear the relevance to the neutron star environment, we chose the horizontal axis as the baryon number density $n_{\rm B}$ in the unit of the normal nuclear density n_0.

There is an empirical conjecture to claim that the speed of sound may not exceed the conformal limit $c_s^2 = 1/3$. As was already explained, in the pQCD calculation, the conformal limit is approached from $c_s^2 < 1/3$ with increasing density. Also at finite temperature, the lattice-QCD results demonstrate that the conformal bound $c_s^2 < 1/3$ holds [42, 43]. Known examples of QCD calculations seem to respect the conformal limit (see, however, Ref. [36] for an exception at finite isospin chemical potential). However, no field-theoretical proof exists to guarantee $c_s^2 < 1/3$. The recent analysis based on neutron star data, especially the two-solar-mass condition, indeed suggest a possibility of $c_s^2 > 1/3$ at sufficiently high baryon density [53, 114, 228, 268]. Moreover, theoretical consideration also points to an inevitable peak in the speed of sound [269–271] as in the scenario (B) and (C) in Fig. 7.1.

Figure 7.2 shows that our resummed EoS slightly violates the conformal bound and c_s^2 approaches $1/3$ from above. It is evident that our result is a counterexample to the conjecture of $c_s^2 < 1/3$. The quantitative difference is numerically small between EoSs from our HDLpt and pQCD, and the violation of the conformal bound is tiny, but this comparison on Fig. 7.2 implies that one should be careful about the robustness of the speed of sound bound (see, for example, discussions in Refs. [272, 273]). Our finding also opens up a possibility of scenario (C) in Fig. 7.1. If the speed of sound is the

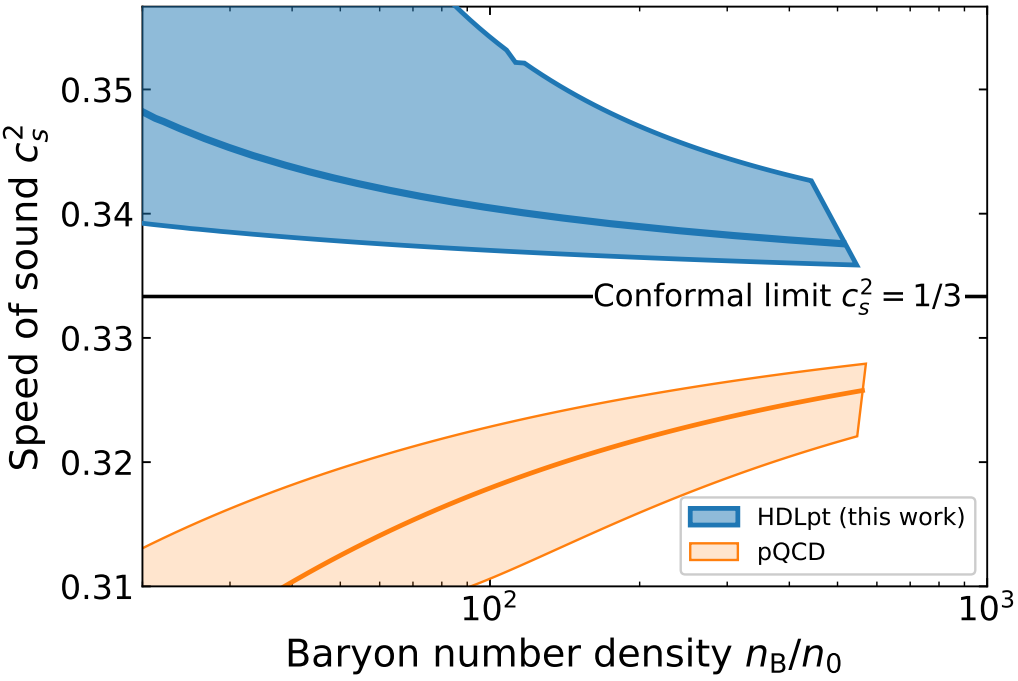

Fig. 7.2: Speed of sound c_s^2 from the EoSs; the blue band represent the results from our HDLpt EoS (evaluated in the massless limit), and the orange band from the pQCD for reference.

continuous function of n_B, then at some point the speed of sound should exceed the conformal limit, which may lead to the peak structure as shown in Fig. 7.1.

7.2.2 HDLpt with the $O(\alpha_s)$ correction

The HDLpt has a deviation of $O(\alpha_s)$ in the pressure from the conventional pQCD calculation as mentioned earlier in Sec. 5.1.1. Also, as was discussed in Sec. 7.1.1, the fact that $c_s^2 < 1/3$ can be ascribed to the $O(\alpha_s)$ coefficient of the pressure. Here, in order to check the robustness of our result, we add the *ad hoc* correction term $P_{\rm corr} = (2\alpha_s/\pi)P_{\rm ideal}$ [227] to $P_{\rm HDLpt}$ to mitigate the difference in the $O(\alpha_s)$ coefficient. In Fig. 7.3 we plot the speed of sound evaluated by $P_{\rm HDLpt}$ and $P_{\rm HDLpt} + P_{\rm corr}$ both in the massless case. Fig. 7.3 clearly shows that even with the $P_{\rm corr}$ correction, the speed of sound still approaches $c_s^2 = 1/3$ from above as the density increases. We verify that our HDLpt predicts $c_s^2 > 1/3$ even if we add a correction to match the $O(\alpha_s)$ terms; this implies that $c_s^2 > 1/3$ could be attributed to the higher order effects from the resummation.

7.2.3 Φ-derivable approximation in the 2PI expansion

In Fig. 7.4 we plot the speed of sound evaluated in the Φ-derivable approximation in the 2PI formalism. Since the expression of the speed of sound only involves the density and its derivative, the speed of sound is insensitive to the ambiguity in the constant in Eq. (5.33), so this is more reliable than, e.g., $P(\varepsilon)$ relation. It is very surprising to see that the speed of sound from the Φ-derivable approach is exactly $c_s^2 = 1/3$. This may imply the conformal nature of the theory. We are still not

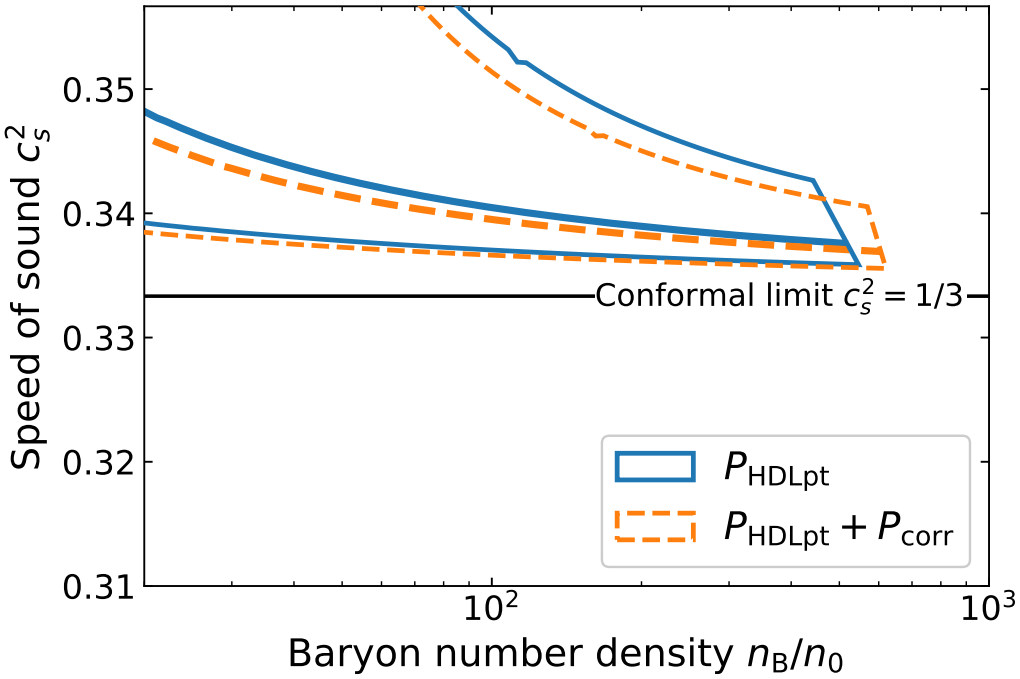

Fig. 7.3: Comparison between the speed of sound evaluated from P_{HDLpt} and $P_{\mathrm{HDLpt}} + P_{\mathrm{corr}}$.

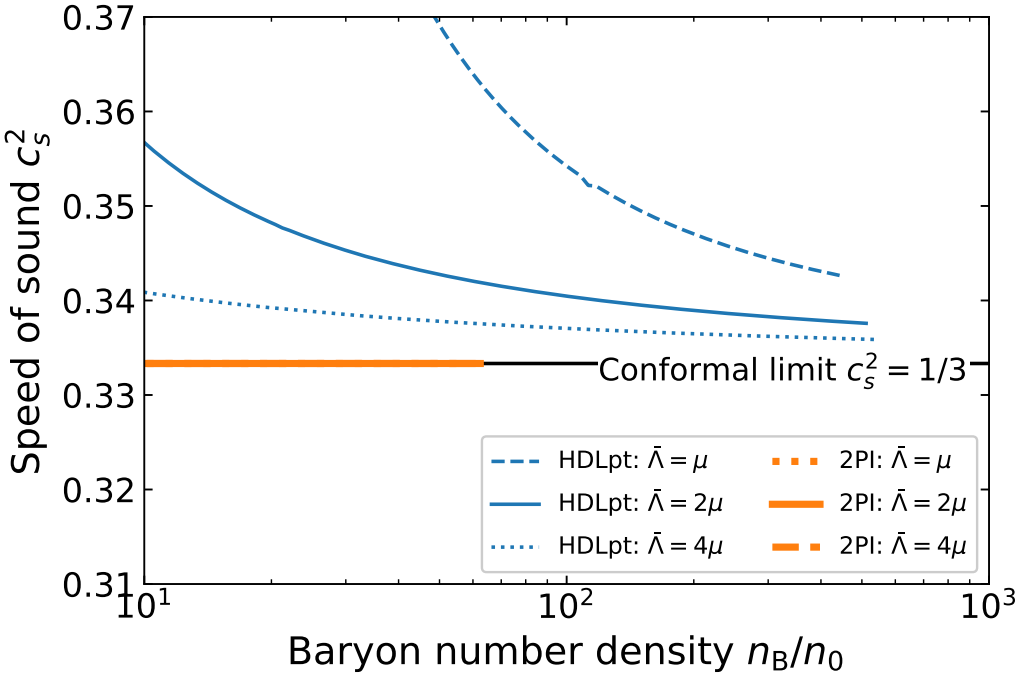

Fig. 7.4: Comparison of the speed of sound from the HDLpt and the Φ-derivable approach in the 2PI formalism.

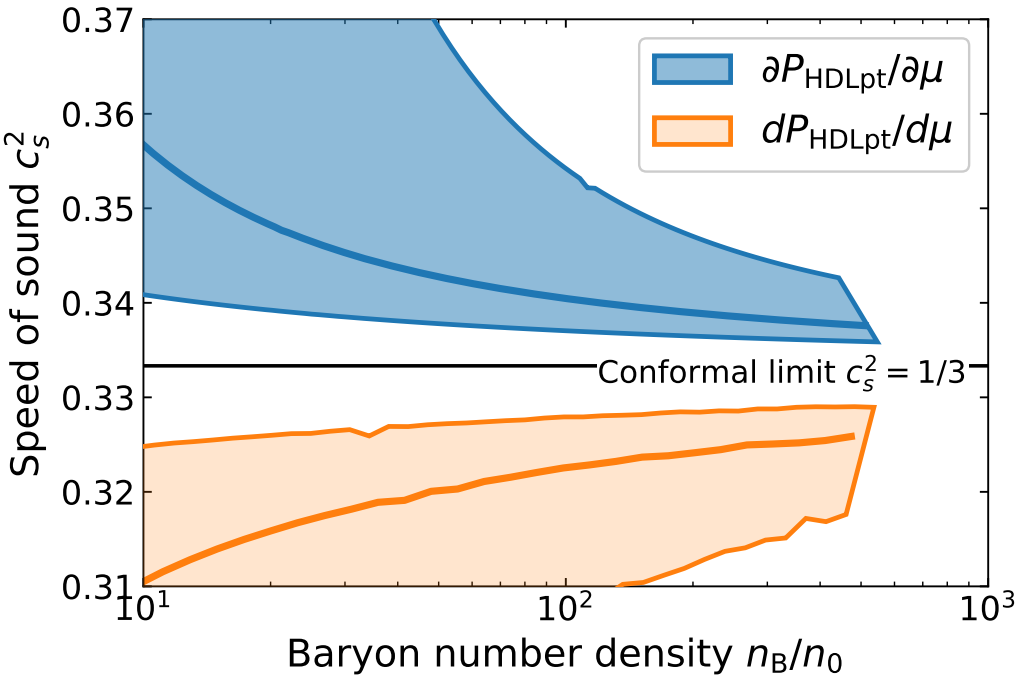

Fig. 7.5: The speed of sound evaluated in the HDLpt with ($dP_{\rm HDLpt}/d\mu$) and without ($\partial P_{\rm HDLpt}/\partial\mu$) including the differentiation of α_s with respect to μ.

aware of its origin, and further investigation is in order.

7.3 Issues related to differentiating the μ-dependence in α_s

As in Sec. 6.4, differentiating the μ-dependence in α_s has also a large effect on the speed of sound. From the discussion in Sec. 7.1.1, the behavior of the speed of sound is not affected by taking the μ-derivative inside α_s, i.e., it is always $c_s^2 < 1/3$.

However, for the HDLpt calculation, the behavior changes drastically. In Fig. 7.5, we plot the speed of sound evaluated in the HDLpt. The one marked with $dP_{\rm HDLpt}/d\mu$ (orange shaded region) takes into account the derivative of the μ-dependence in the coupling constant α_s: the speed of sound is always less than the conformal limit, i.e., $c_s^2 < 1/3$. This behavior can be understood in the following manner. From the $M_{{\rm q}f}/\mu$ expansion of the HDLpt pressure $P_{\rm HDLpt}$, we know that the first correction has a negative coefficient. Since it shares the same structure of the expression as the conventional pQCD calculation, then it is natural to observe $c_s^2 < 1/3$. In short, this can be ascribed to the combined effect of the negative coefficient of $P_{\rm HDLpt}$ at $O(\alpha_s)$ as well as the first negative coefficient of the QCD beta function.

The one marked with $\partial P_{\rm HDLpt}/\partial\mu$ (blue shaded region) is the same as in Fig. 7.2. In the case of the conventional pQCD, the behavior of the speed of sound does not change irrespective of whether we differentiate α_s with respect to μ or not. On the other hand, it is interesting to observe that the behavior of the speed of sound in the HDLpt becomes completely different by changing the way of

taking the derivative. Again we emphasize that our assumption is *not* to differentiate μ-dependence in α_s, throughout this thesis (see Sec. 6.4 for the justification).

Chapter 8

Smooth matching between nuclear and quark matter EoS

In this chapter, we will discuss the phase transition from hadronic matter to quark matter in neutron stars. A cursory look is provided on why the first-order phase transition is disfavored and the crossover transition is more favored. Then, we will turn to a bit of theory to justify the crossover transition at high density. Finally, we will construct the EoS solely from the QCD boundary conditions to prove that the pQCD is useful in constraining the EoS, and calculate the stellar observables such as the mass, radius, and tidal deformability of neutron stars.

8.1 Hadron-to-quark transition in neutron stars

In Fig. 8.1, we plot the astrophysical constraint on the EoS from different neutron stars, and also the conventional nuclear matter EoS. DL refers to the deep learning analysis [113, 163], and GW170817 refers to the Bayesian analysis from the neutron star merger event [160]. APR is one of the nuclear matter EoS, which is conventionally used in a wide context [66]. On the other hand, in the high-density region, we plot our HDLpt results which are evaluated in the β equilibrium and charge neutral system with taking the strange mass effect into account.

In the figure, around the density range $\rho \simeq 3$–$8\,\rho_0$, one can clearly see the smooth matching between the EoSs extrapolated from the lower density and the EoS of quark matter calculated from the HDLpt. This implies that if there is a phase transition from hadronic matter to the quark matter, then there is no large gap in the EoS; the energy density gap with the constant pressure generally means the first-order phase transition. The smooth matching favors a crossover transition from the hadronic matter to the quark matter, which is also observed in the high-temperature QCD (see Fig. 8.2). There may still be a possibility of a weak first-order transition within the allowed range of the EoS. Nonetheless, the strong first-order phase transition is excluded, so that it suggests some underlying physics that hadrons steadily melt into quarks as the density increases.

Here, let us now review how the hadron-to-quark first-order or crossover transitions are dealt

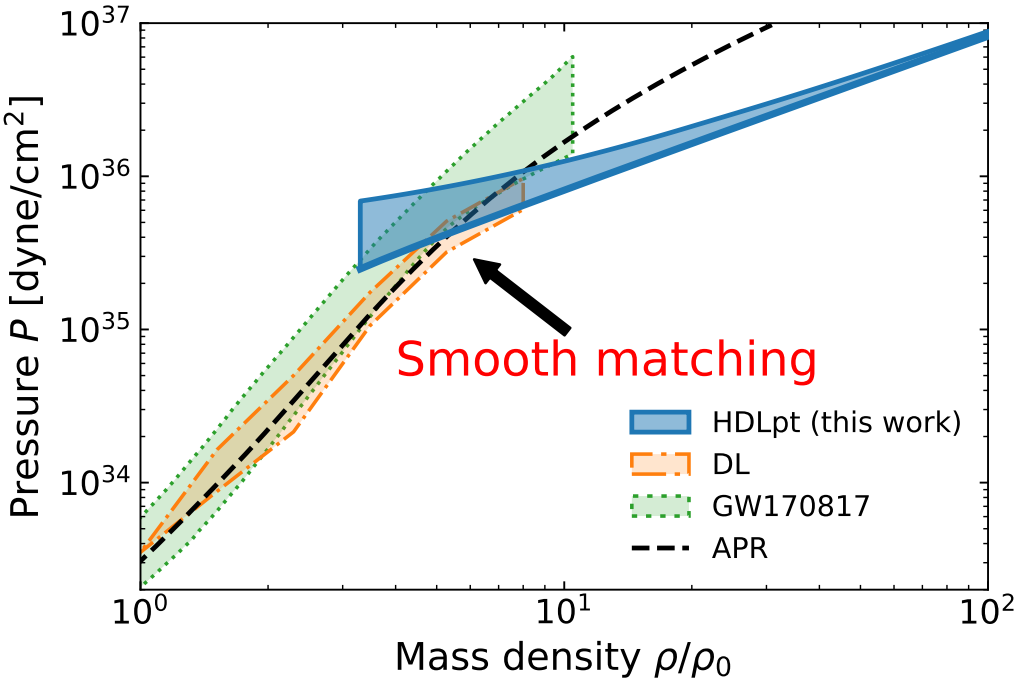

Fig. 8.1: Smooth matching between the hadronic EoS and the quark EoS.

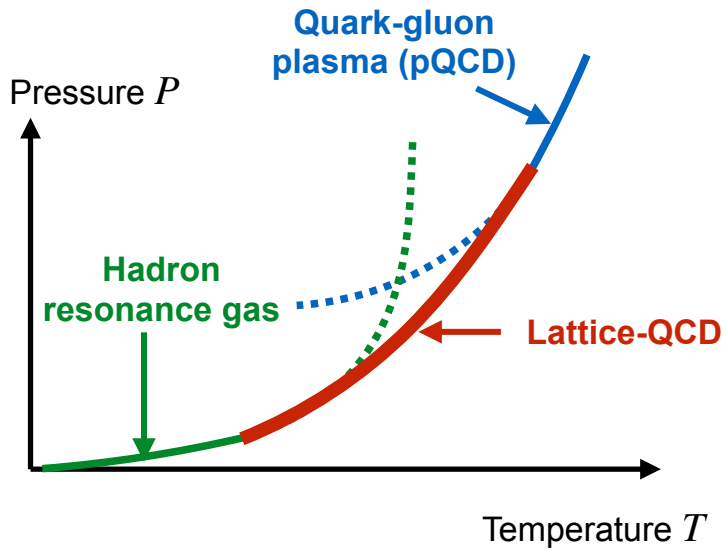

Fig. 8.2: The schematic figure of the EoS of the high temperature QCD matter. At lower temperatures, the EoS based on the hadron resonance gas model works well, but it becomes divergent once the quark-gluon matter sets in. At higher temperatures, pQCD calculations such as the one from the HTLpt is available. The Lattice-QCD calculation reveals that the transition from the hadron resonance gas to the quark-gluon plasma is crossover-type.

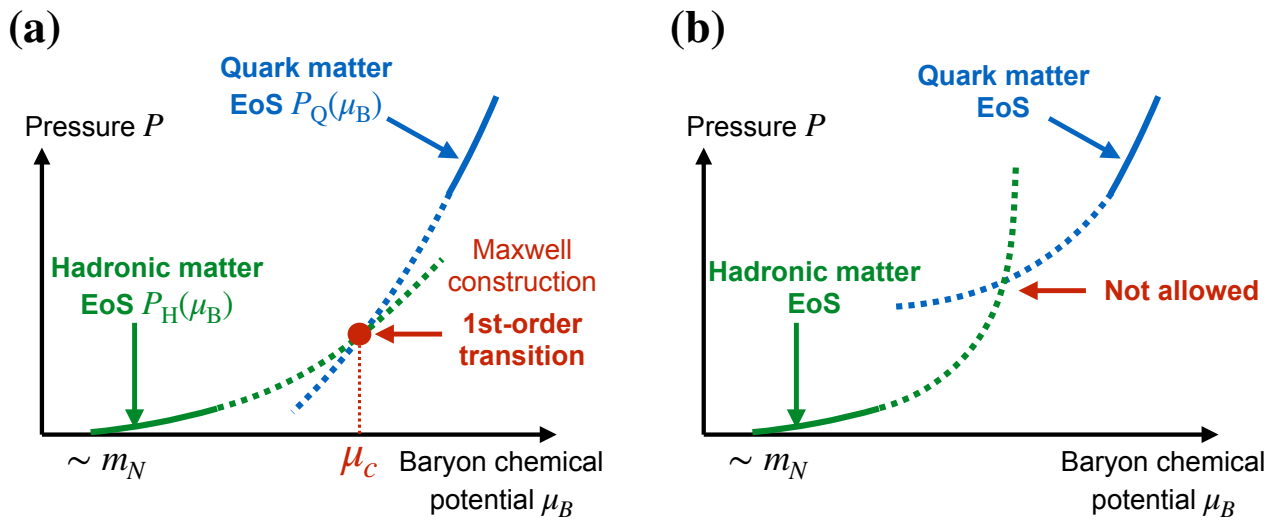

Fig. 8.3: The schematic figure of the EoS construction for hybrid star matter. We connect the hadronic EoS and the quark EoS; **(a)** We extrapolate the hadronic EoS up and the quark EoS down to the densities where they meet. The EoS is built upon the Maxwell construction. **(b)** This case is not allowed. See text for further details.

with in the theoretical treatment (see Ref. [274] for the recent comprehensive review). We note in passing that in this section, we generally use the term "hadronic matter" instead of nuclear matter because *hyperons*—which are baryons (=fermionic hadrons) containing strange quarks inside—may also appear. Particularly, we will review how to construct the EoS for the matter inside "hybrid stars," which are neutron stars with a quark matter core inside.

8.1.1 Maxwell construction for the first-order phase transition

Firstly, we will turn to the problems of the hadron-to-quark first-order phase transition by taking the Maxwell construction as an actual example. Historically speaking, for the quark matter description, the standard choice was to utilize the MIT bag model [264, 265]; in this model, quarks are confined inside a limited space named the "bag," and the non-perturbative confining effects are accounted by the so-called bag constant B, which quantifies the energy difference between the QCD and the ordinary vacua. In the traditional argument, e.g. Refs. [16, 275], a quark core of neutron stars is treated as a giant MIT bag. In such a treatment, the EoS of hybrid star matter is constructed by connecting the hadronic matter EoS and the quark matter EoS. For the quark matter EoS, other models such as the Nambu–Jona-Lasinio (NJL) models [8, 276–278] are also frequently used.

The schematic figure in Fig. 8.3 depicts the typical construction based on the traditional point of view. In Fig. 8.3 (a), we show the Maxwell construction for the hadron-to-quark phase transition. We extrapolate the hadronic EoS, $P_{\rm H}(\mu_{\rm B})$, up and the quark EoS, $P_{\rm Q}(\mu_{\rm B})$, down to the densities where they meet. At this point, we impose the Gibbs condition between the hadronic and quark phases, i.e.,

$$\mu_{\rm B}^{\rm hadron} = \mu_{\rm B}^{\rm quark} \equiv \mu_c\,, \qquad P_{\rm H}(\mu_c) = P_{\rm Q}(\mu_c)\,, \tag{8.1}$$

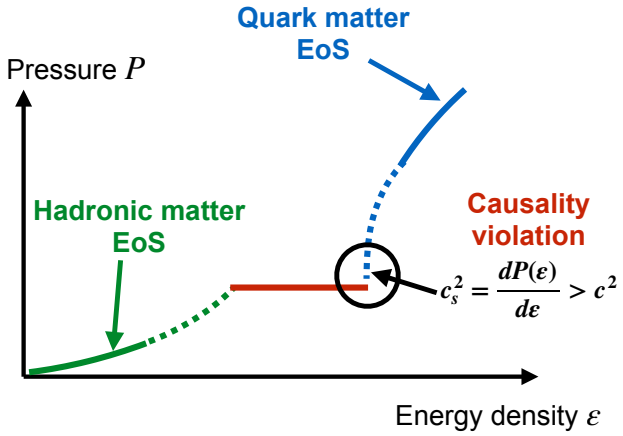

Fig. 8.4: The general problem with the Maxwell construction between the hadronic and quark matter EoS. This EoS, which is plotted in the form of $P(\varepsilon)$ corresponds to that in Fig. 8.3 (a), which is plotted in the form of $P(\mu_{\rm B})$. At the high-density end of the plateau in the energy density, the EoS rises abruptly, so that the causality violation $c_s^2 > 1$ easily occur.

where $\mu_{\rm B}^{\rm hadron}$ and $\mu_{\rm B}^{\rm quark}$ are the baryon chemical potential of the hadronic and quark matter, respectively. In addition, we require the conditions

$$P_{\rm H} > P_{\rm Q} \quad (\mu_{\rm B} < \mu_c)\,, \qquad P_{\rm H} < P_{\rm Q} \quad (\mu_{\rm B} > \mu_c)\,, \tag{8.2}$$

in order for the hadronic matter to be realized at low densities and the quark matter to be at high densities. With these conditions fulfilled, we build the EoS based on the Maxwell construction. There can arise such a situation as in Fig. 8.3 (b), in which the hadronic matter EoS diverges. It is not allowed as in the conventional construction of the EoS outlined above, as it does not satisfy the condition (8.2). In reality, however, it is actually the case for high-temperature QCD, so here is the problem of the Maxwell construction.

There is also another problem related to the Maxwell construction of Fig. 8.3 (a). Fig. 8.4 clearly illustrates what is the problem. In Fig. 8.4, the EoS is plotted in the form of $P(\varepsilon)$ corresponds to that in Fig. 8.3 (a), which is plotted in the form of $P(\mu_{\rm B})$. The hadron-to-quark phase transition in Fig. 8.3 (a), which is marked as a cusp with the red dot, corresponds to an energy density jump in Fig. 8.4 by a factor of two or so. At the high-density end of the energy density jump, the EoS rises abruptly, so that there can arise the acausal behavior, $c_s^2 > 1$, at this point easily. Also, the Maxwell construction requires infinite surface tension at the boundary between the hadronic and quark matter. Moreover, the EoS with a strong first-order phase transition becomes soft, so it cannot support heavy neutron stars with masses $\sim 2\,M_\odot$. It is clearly in tension with the current observations, so this is the reason why the strong first-order phase transition is excluded.

For simplicity, here we have only shown the Maxwell construction, but one can generalize this to the globally charge neutral construction by relaxing the Gibbs condition in Eq. (8.1) because there are

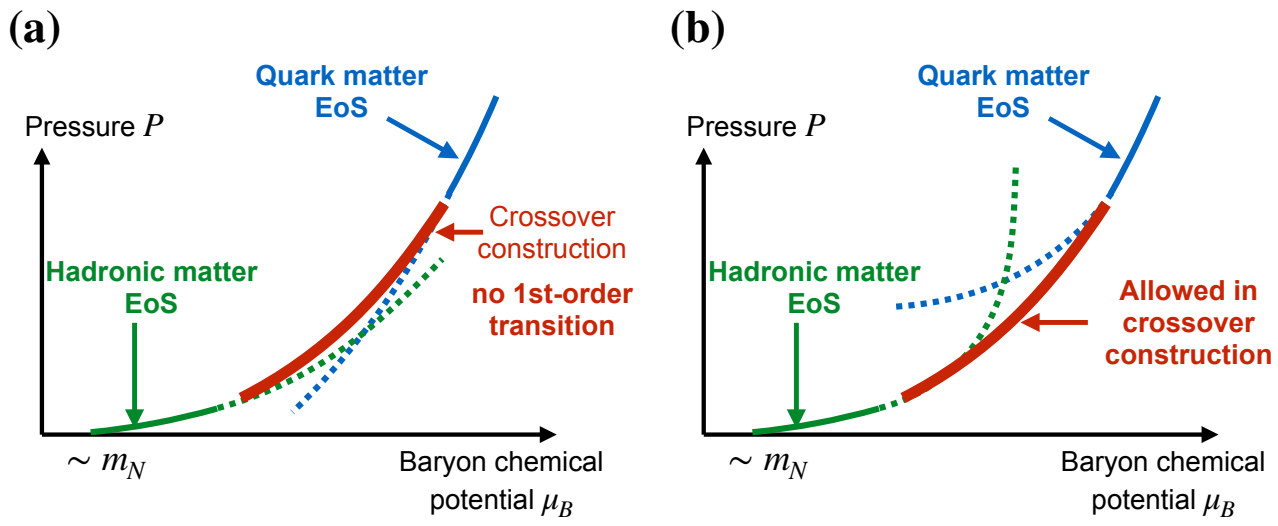

Fig. 8.5: The schematic figure of the three-window, or the quark-hadron continuity construction of the EoS. We divide the chemical potential into three windows: (i) hadronic region, (ii) crossover region, and (iii) quark region. In the the hadronic EoS (green line) and the quark EoS (blue line) are interpolated by the smooth function (red thick line); **(a)** The typical crossover construction without the first-order phase transition; **(b)** The crossover construction also works for the situation which was not allowed in the Maxwell construction. See text for further details.

multiple conserved charges in neutron stars such as the baryon number and the electric charge [279].

8.1.2 Three-window construction for hadron-to-quark crossover

The problems of the Maxwell construction mentioned in the preceding subsection can be remedied by using the three-window construction [280–283]. This construction is also referred to as the quark-hadron continuity construction. The schematic figure in Fig. 8.5 depicts the typical three-window construction of the EoS. In this construction, we divide the regions of the chemical potential into three windows: (i) hadronic region, (ii) crossover region, and (iii) quark region. In regions (i) and (iii), we cut off the hadronic and quark EoS at a certain value of the chemical potential. Then, by using the smooth function in the region (ii), we interpolate between the hadronic EoS in the region (i) and the quark EoS in (iii). The crossover construction in Fig. 8.5 (a), corresponding to Fig. 8.3 (a), induces no first-order phase transition in the EoS. We note that by using the function with a cusp instead of the smooth one, then we can also have the first-order transition in the three-window construction. The advantage of this construction lies in Fig. 8.5 (b), which was forbidden in the Maxwell construction as it does not satisfy the condition (8.2). Indeed, Fig. 8.5 (b) is exactly the case for the high-temperature QCD (compare with Fig. 8.2), in which the precise form of the EoS is known from the reliable lattice-QCD calculations.

In short, the three-window construction is a more general prescription for interpolating between the hadronic and the quark EoS; it allows the EoS to have either the crossover or the first-order transition. As we can avoid a first-order transition in the three-window modeling, it can cure the

acausal behavior in the Maxwell construction, which is generally the problem of the EoS with a first-order transition. Also, the EoS constructed by the three-window modeling can support the massive $2\,M_\odot$ neutron stars. Actually, this was the exact driving force to consider the crossover-type EoS. Now various phenomenological EoSs (QHC18 [274], QHC19 [284], and QHC21 [285]) are constructed in this construction by taking the realistic nuclear matter EoS (Togashi EoS) [67] or the χEFT EoS [228] for the hadronic EoS, as well as the NJL model for the quark EoS.

Underlying physics behind this three-window crossover construction is the concept called Quark-hadron continuity, which we will turn to in the next section.

8.2 Underlying idea of the crossover: Quark-hadron continuity

In the high-density crossover transition, the hadronic matter is smoothly bridged to quark matter. Color superconductivity gives us an insight into the idea that hadronic matter and quark matter are continuously connected; Schäfer and Wilczek coined the term "Quark-hadron continuity" (QHC) for such idea [286]. The idea of QHC can be attributed to the same symmetry breaking patterns and low-lying excitations in both quark and hadronic phases. In a three-flavor symmetric case, color-flavor locking (CFL) occurs [30], and the idea of QHC is established [286] (see, however, Refs. [287–290] for recent discussions under the existence of the non-Abelian vortices). By contrast, in the two-flavor case, the concept of QHC between nuclear matter and two-flavor color superconductor (2SC) is invalidated due to the apparent difference in the global symmetries. However, it has been pointed out that the QHC can still be maintained in the two-flavor case by the present author and collaborators [291, 292]. The essential point is that the two-flavor stellar matter is highly asymmetric as repeatedly mentioned above and neutron abundant.

In this section, we introduce the QHC scenarios in some detail. We will only stick to the QHC although many other scenarios that realize the crossover transition such as ones based on Quarkyonic matter [35, 269, 283, 293–296], quantum percolation [297] as well as hidden topology change [298], to mention a few. For the three-flavor symmetric case, the physical picture of QHC is that the hyperon superfluid and the CFL color superconductor are indistinguishable. For the two-flavor case, the QHC picture is that we cannot distinguish the ${}^3P_2$ neutron superfluid [299, 300], which is believed to occur inside neutron stars and the conventional 2SC color superconductor with an additional component of the $\langle dd\rangle$ diquark condensation.

In the conventional color superconductor, a diquark condensate in ${}^1S_0$ channel is formed

$$\langle \hat{q}^\top_{\alpha A} C\gamma^5 \hat{q}_{\beta B}\rangle \propto \epsilon_{\alpha\beta\gamma}\epsilon_{ABC}\langle \hat{\Phi}^{\gamma C}\rangle\,, \tag{8.3}$$

where the charge conjugation matrix $C \equiv i\gamma^0\gamma^2$ is inserted to form a Lorentz scalar. Greek $(\alpha, \beta, \ldots)$ and capital $(A, B, \ldots)$ indices represent color and flavor, respectively[1]. The color-superconducting phase can be thought of as a Higgs phase of QCD. Diquarks play here the same role as the Higgs

[1]Note that the flavor index was f in the above.

boson does in the electro-weak sector of the standard model. It has previously been shown in lattice gauge theories that the confinement phase and the Higgs phase are connected without a phase boundary [301]. Owing to this fact, we cannot distinguish between the hadronic (confinement) phase and the color superconductor (Higgs) phase as long as the global symmetries are the same in both phases; this is the essence of the QHC.

The symmetry of QCD comprises local gauge symmetry, chiral symmetry and baryon number symmetry: $\mathcal{G}_{\rm QCD} = [{\rm SU}(3)_{\rm C}] \times {\rm SU}(N_{\rm f})_{\rm L} \times {\rm SU}(N_{\rm f})_{\rm R} \times {\rm U}(1)_{\rm B}$. Neglecting the strange (s) quark mass, the chiral part of $\mathcal{G}_{\rm QCD}$ can be ideally treated as $N_{\rm f} = 3$. In reality, however, s is much heavier than the up (u) and the down (d) quarks ($m_s/m_{u,d} \sim 30$), so it is more natural to consider isospin-symmetric $N_{\rm f} = 2$ systems.

$N_{\rm f} = 3$ case: In this case, the quark matter is the CFL color superconductor. The CFL ansatz for the diquark condensate Eq. (8.3) reads $\langle\hat{\Phi}^{\alpha A}\rangle = \delta^{\alpha A}\Delta_{\rm CFL}$. The pattern of symmetry breaking in the CFL phase is $\mathcal{G}_{\rm QCD} \to \mathcal{G}_{\rm CFL}$, where $\mathcal{G}_{\rm CFL} = {\rm SU}(3)_{\rm C+L+R}$ is the residual symmetry in the CFL phase. The residual global symmetry in the CFL phase $\mathcal{G}_{\rm CFL}$ is the same as that of the hadronic phase, where the chiral and the baryon number symmetries are spontaneously broken. This led us to the observation of the QHC.

Local gauge symmetry cannot be broken spontaneously [302]. It means that the Higgs mechanism alone, which is a *fictitious* breaking of gauge symmetry, cannot be captured by any gauge-invariant order parameter. Here, however, global symmetry breaking occurs simultaneously in $\mathcal{G}_{\rm QCD} \to \mathcal{G}_{\rm CFL}$, thus this global sector can still be captured by gauge-invariant order parameters. We can construct such order parameters by saturating gauge indices of diquark operator (8.3) in two ways, either symmetrically or anti-symmetrically. Then, each of which captures the breaking of the chiral (${\rm SU}(N_{\rm f})_{\rm L} \times {\rm SU}(N_{\rm f})_{\rm R}$) and superfluid (${\rm U}(1)_{\rm B}$) sector of the QCD symmetry $\mathcal{G}_{\rm QCD}$ [303].

$$\text{Chiral}: \quad \mathcal{M} = \delta^{\beta}_{\alpha}\delta^{\beta'}_{\alpha'}(\bar{q}^{\alpha}\bar{q}^{\alpha'})(q_{\beta}q_{\beta'}) \propto (\bar{q}^{\alpha}q_{\alpha})(\bar{q}^{\alpha'}q_{\alpha'})\,, \tag{8.4}$$

$$\text{Superfluid}: \quad \Upsilon = \epsilon^{\alpha\beta\gamma}\epsilon^{\alpha'\beta'\gamma'}(q_{\alpha}q_{\alpha'})(q_{\beta}q_{\beta'})(q_{\gamma}q_{\gamma'}) \propto (\epsilon^{\alpha\beta\gamma}q_{\alpha}q_{\beta}q_{\gamma})(\epsilon^{\alpha'\beta'\gamma'}q_{\alpha'}q_{\beta'}q_{\gamma'})\,. \tag{8.5}$$

Superfluid order parameter Υ takes a similar expectation value in both the quark and the hadronic phases because of the QHC. In the hadronic phase, as it is obvious from the RHS of Eq. (8.5) above, it can be interpreted as $\Upsilon \propto \Lambda\Lambda$ with $\Lambda \sim uds$. This is the order parameter for the hyperon superfluidity.

$N_f = 2$ case: The 2SC ansatz for the diquark condensate (8.3) reads

$$\langle\hat{\Phi}^{\alpha A}\rangle = \delta^{\alpha 3}\delta^{A3}\Delta_{\rm 2SC} \equiv \Phi^{\alpha}_{\rm 2SC}\,, \tag{8.6}$$

where we assumed the unitary gauge-fixing. The residual symmetry in the 2SC phase is $\mathcal{G}_{\rm 2SC} = [{\rm SU}(2)_{\rm C}] \times {\rm SU}(2)_{\rm L} \times {\rm SU}(2)_{\rm R} \times {\rm U}(1)_{\rm B}$, which is apparently different from the hadronic phase. However, aside from the 2SC condensate $\Phi^{\alpha}_{\rm 2SC}$, it is still possible to consider an additional two-flavor diquark

condensate in order for the QHC to be maintained. Here we focus on the superfluid aspect of the QHC. We describe neutrons by a quark-diquark structure $n = \epsilon^{\alpha\beta\gamma}(u_\alpha^\top C\gamma^5 d_\beta)d_\gamma$. The order parameter for ${}^3P_2$ neutron superfluidity is

$$\Upsilon_{nn} \equiv n^\top C\gamma^i \nabla^j n\,. \tag{8.7}$$

By rearranging the valence quark content in Υ_{nn}, we get

$$\Upsilon_{nn} \propto \epsilon^{\alpha\beta\gamma}\epsilon^{\alpha'\beta'\gamma'}(u_\alpha^\top C\gamma^5 d_\beta)(u_{\alpha'}^\top C\gamma^5 d_{\beta'})(d_\gamma^\top C\gamma^i\nabla^j d_{\gamma'})\,. \tag{8.8}$$

The first two terms in parentheses are identical to the 2SC condensate $\Phi^\gamma_{\rm 2SC}$ in Eq. (8.6), while the last term $d_\gamma^\top C\gamma^i\nabla^j d_{\gamma'}$ is the novel element here. If we take the expectation value of Υ_{nn} in the mean-field approximation, Υ_{nn} takes the value

$$\langle\Upsilon_{nn}\rangle \approx \Phi^\alpha_{\rm 2SC}\Phi^{\alpha'}_{\rm 2SC}\langle d_\alpha^\top C\gamma^i\nabla^j d_{\alpha'}\rangle\,, \tag{8.9}$$

where we have neglected the crystalline condensation. The last term in the angle brackets of the above expression is the diquark condensate of d-quarks, which is paired in the ${}^3P_2$ channel. We call this phase 2SC+$\langle dd\rangle$ phase. The residual symmetry in the 2SC+$\langle dd\rangle$ phase is the same as neutron matter, hence the QHC holds. We note in passing there appears a new topological excitation called the non-Abelian Alice strings [304–306] appears in this novel phase.

We can draw a connection between the microscopic ${}^3P_2$ diquark condensate and the macroscopic value of the EoS. We considering the four-fermion coupling interaction in the ${}^3P_2$ diquark channel, i.e.,

$$\hat{\mathcal{I}}_P = (\bar\psi\gamma^i\nabla^j C\bar\psi^\top)(\psi^\top C\gamma_i\nabla_j\psi)\,. \tag{8.10}$$

By Fierz rearranging this $\hat{\mathcal{I}}_P$ term, one finds a term with a direct correspondence to the energy-momentum tensor in the fermionic sector, $T^{\mu\nu} = \bar\psi i\gamma^\mu\partial^\nu\psi$. For matter in equilibrium, $T^{\mu\nu} = \mathrm{diag}[\varepsilon, P, P, P]$, with the energy density ε and the pressure P of fermionic matter. Extracting only the contribution relevant for the energy-momentum tensor, the tree-level expectation value of $\hat{\mathcal{I}}_P$ reads

$$\langle\hat{\mathcal{I}}_P\rangle \approx \frac{3}{4}P^2\,. \tag{8.11}$$

It is evident from this expression that the ${}^3P_2$ diquark interaction couples to the pressure which is a macroscopic quantity.

8.3 Phenomenological application

In this section, we discuss the phenomenological application of our results, i.e., the HDLpt calculation of the quark matter EoS. In specific, we calculate the observables of neutron stars or hybrid

stars as we take into account the effect of the quark matter EoS.

Combined with the EoS, the mass and radius of neutron stars are obtained by solving the TOV equation[2]:

$$\frac{dP}{dr} = -\frac{m\varepsilon}{r^2}\left(1+\frac{P}{\varepsilon}\right)\left(1+\frac{4\pi r^3 P}{m}\right)\left(1-\frac{2m}{r}\right)^{-1}, \tag{8.12}$$

$$m(r) = 4\pi\int_0^r r'^2 dr'\,\varepsilon(r'), \tag{8.13}$$

where r is the radial distance from the stellar center and $m(r)$ is the mass enclosed within the radius r. This is an initial problem with the initial conditions set at the center of the star $r = 0$: $P(r = 0) = P_c$ and $m(r = 0) = 0$. The central pressure P_c is a free parameter. After solving the initial value problem, we further solve $P(r = R) = 0$ to find the radius. Then, the mass of a neutron star is given by $M = m(r = R)$.

Another important observable of neutron stars is tidal deformability, Λ, which quantifies the deformation caused by the tidal force when two neutron stars merge. Tidal deformability can be obtained by solving the following equation [307, 308] combined with the TOV equation:

$$\frac{dH}{dr} = \beta \tag{8.14}$$

$$\begin{aligned}\frac{d\beta}{dr} = {}& 2\left(1-\frac{2m}{r}\right)^{-1} H\left\{2\pi\left[5\varepsilon+9P+(\varepsilon+P)\frac{d\varepsilon}{dP}\right]+\frac{3}{r^2}+2\left(1-\frac{2m}{r}\right)^{-1}\left(\frac{m}{r^2}+4\pi r^2 P\right)^2\right\}\\ &+\frac{2\beta}{r}\left(1-\frac{2m}{r}\right)^{-1}\left\{-1+\frac{m}{r}+2\pi r^2(\varepsilon-P)\right\}.\end{aligned} \tag{8.15}$$

Again this is an initial value problem with the initial condition $H(r = 0) = \beta(r = 0) = 0$ (see also Eq. (B.30) for the practical value used for the initial value). From M, R, H, and β obtained above, we can calculate the tidal deformability as

$$\begin{aligned}\Lambda = {}& \frac{16}{15}(1-2C)^2[2+2C(y-1)-y]\\ &\times\Big\{2C[6-3y+3C(5y-8)]+4C^3[13-11y+C(3y-2)+2C^2(1+y)]\\ &\qquad+3(1-2C)^2[2-y+2C(y-1)]\ln(1-2C)\Big\}^{-1},\end{aligned} \tag{8.16}$$

where C and y are defined as $C \equiv M/R$ and $y \equiv R\beta(R)/H(R)$, respectively. See Appendix B for the complete derivation of these equations.

In the following two subsections, we will quantify the effect of the QCD EoS on neutron star observables. The effect of the pQCD branch seems to be tiny when we connect the pQCD calculation directly to the nuclear matter EoS. However, as the pQCD EoS becomes soft with $c_s^2 = 1/3$ at high

[2]Practically, it is more convenient to formulate it in terms of enthalpy $\eta \equiv (\varepsilon + P)/n_{\rm B}$ instead of radius r.

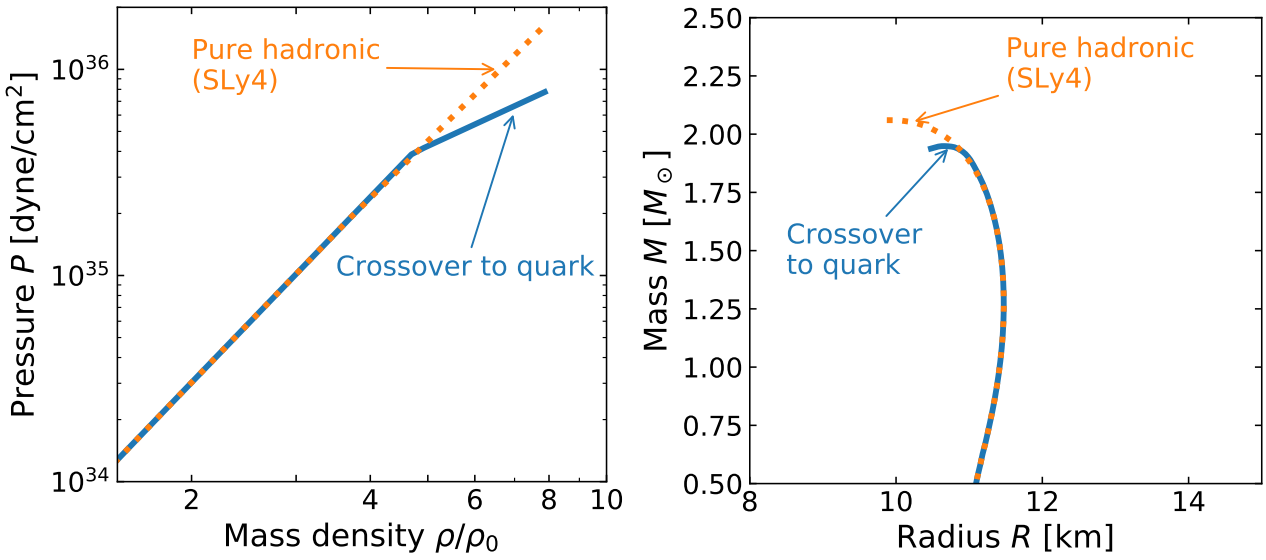

Fig. 8.6: (Left) Pure hadronic EoS (SLy4) and the hadronic EoS connected to the quark EoS. (Right) Corresponding M–R relation.

	P_1[dyne/cm^2]	Γ_1	ρ_1	Γ_2	ρ_2	Γ_3
Pure hadronic (SLy4)	2.42×10^{34}	3.01	$1.85\,\rho_0$	2.99	$3.70\,\rho_0$	2.85
Crossover to quark	2.42×10^{34}	3.01	$1.85\,\rho_0$	2.99	$4.72\,\rho_0$	1.33

Table 8.1: Parameters of piecewise polytropic EoSs in cgs units.

densities, it can be very useful constraining the global trend of the EoS.

8.3.1 Connecting hadronic EoS and quark EoS

For numerical simplicity, we use the piecewise polytrope parametrization of the EoS [309]. We divide the density range into a certain number of segments. In this subsection, we take it as three, and in the next subsection, we take it as four. For the mass density ρ in the range $[\rho_{i-1},\rho_i]$ $(i=1,2,\ldots)$, the EoS is expressed by a polytrope

$$P(\rho) = K_i\rho^{\Gamma_i}\,, \qquad \rho_{i-1}\le\rho\le\rho_i\,, \tag{8.17}$$

where Γ_i is the adiabatic index of the i-th piece. The corresponding energy density in the range $\rho_{i-1}<\rho<\rho_i$ is given by

$$\varepsilon(\rho) = (1+a_i)\rho + \frac{K_i\rho^{\Gamma_i}}{\Gamma_i-1}, \qquad a_i = \frac{\varepsilon(\rho_{i-1})}{\rho_{i-1}} - 1 - \frac{K_i\rho_{i-1}^{\Gamma_i-1}}{\Gamma_i-1}\,. \tag{8.18}$$

Below the density ρ_1, we connect the crust EoS, which is $P(\rho)=K_{\rm crust}\rho^{1.36}$ with $K_{\rm crust}=4.00\times10^{-8}$ in cgs units (see Ref. [309] for details). In this subsection, we consider three polytropic regions, which is specified by the six parameters in cgs units: $(P_1,\Gamma_1,\rho_1,\Gamma_2,\rho_2,\Gamma_3)$ with $P_1\equiv P(\rho_1)$.

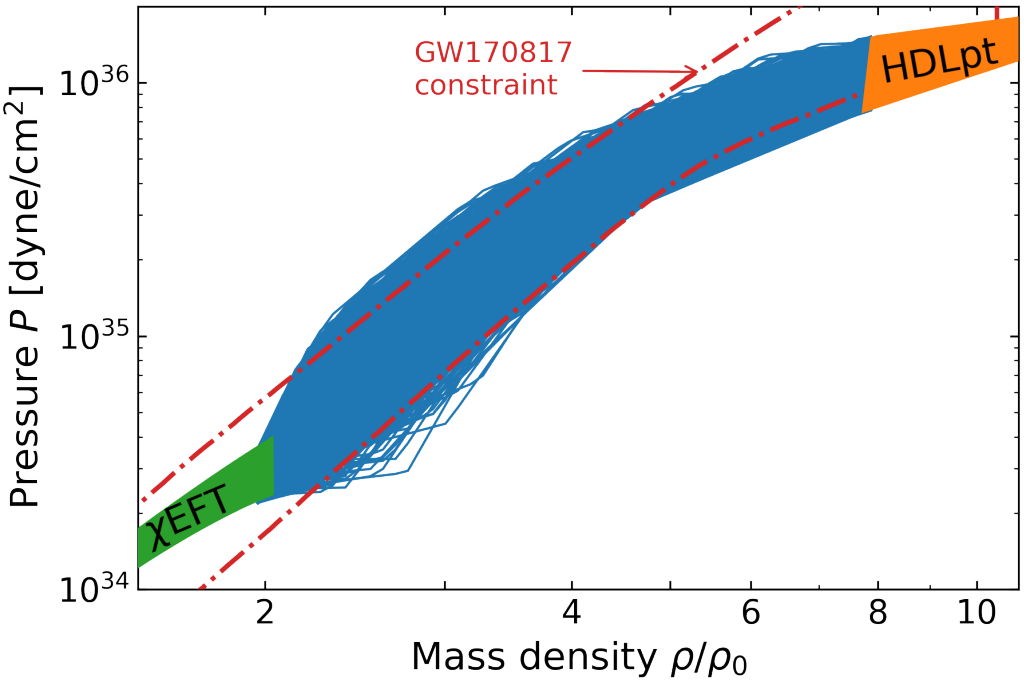

Fig. 8.7: Constraints on the EoS put solely by QCD boundary condition combined with a minimal $2\,M_\odot$ constraint.

Under these setups, we compare the pure hadronic EoS, which is taken to be SLy4 [68], and the EoS with the hadron-to-quark crossover. The crossover EoS is constructed by finding the density where these two EoSs, which are SLy4 and the HDLpt EoS, meet in the P–ρ plane. The fitted parameters for each EoS are given in Table 8.1; The only difference is in the third segment, and the crossover EoS has the rapid softening feature. Precisely speaking, since there is a gap in the derivative quantity such as the adiabatic index, it is not the crossover transition, but the second-order phase transition. Nonetheless, we cannot get the smooth EoS within the piecewise polytropic parametrization, we call it the crossover EoS (see, however, Ref. [310] for the generalized parametrization, which allows for the continuous adiabatic index).

In Fig. 8.6, we compare the pure hadronic EoS and the crossover EoS. From the M–R relation in the right panel, one can see that the effect of the quark matter is very tiny. At least within the current precision of the observation, we cannot distinguish these two cases.

8.3.2 QCD constraints on the EoS

In the preceding subsection, we saw that the effect of the quark matter calculation on a specific EoS is very slight. However, we point out that it can still be useful for constraining the allowed EoS regions in the P–ρ plane.

The strategy is to set the boundary conditions from the QCD calculations: at lower density side, we use the χEFT calculation [228] up to $\rho \simeq 2\rho_0$, and at higher density side, we use our HDLpt calculation down to $\rho \simeq 8\rho_0$. Then, in the intermediate density range $2\rho_0 < \rho < 8\rho_0$, we interpolated

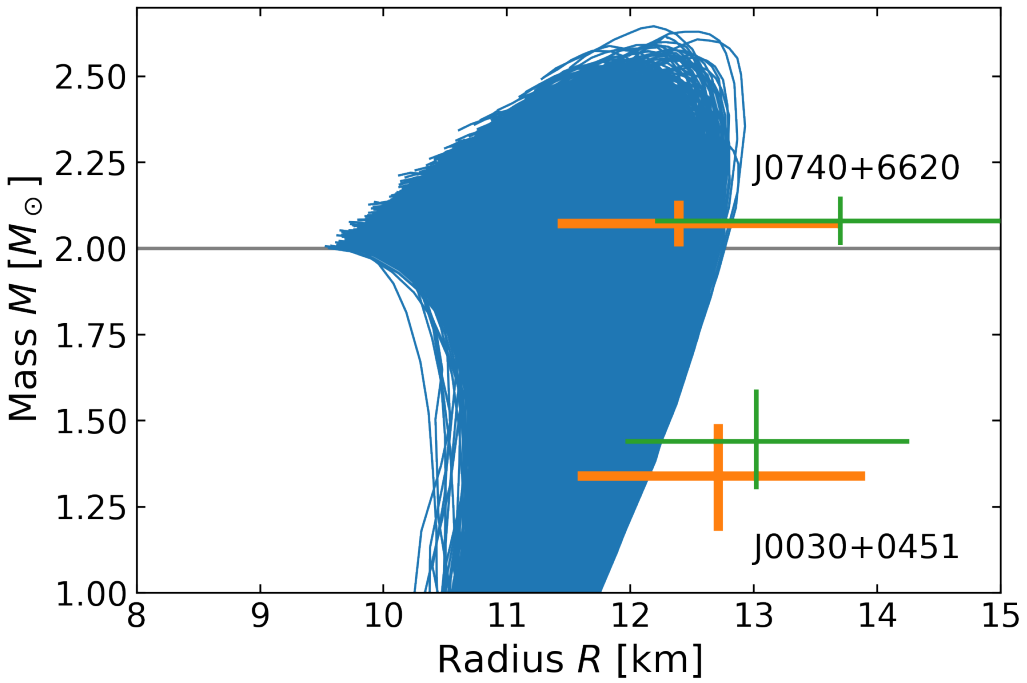

Fig. 8.8: M–R relation corresponding to Fig. 8.7. The radius constraints from the NICER collaboration are overlaid: J0030+0451 at $M = 1.4\,M_\odot$ [173, 174], and J0740+6620 at $M = 2\,M_\odot$ [175, 176].

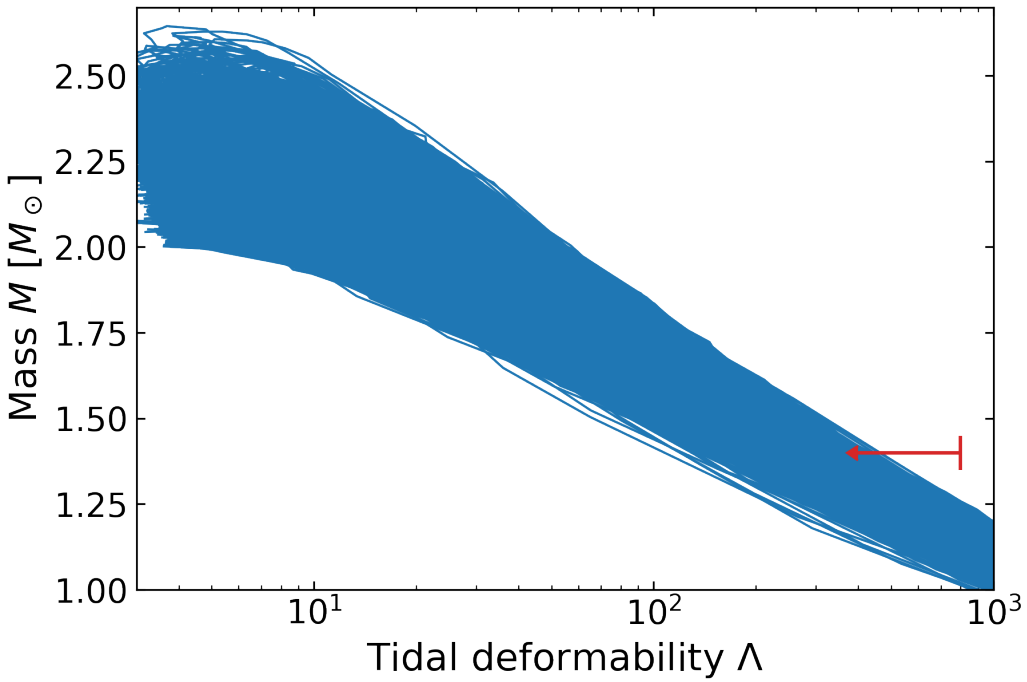

Fig. 8.9: Tidal deformability corresponding to Fig. 8.7. The red arrow is the constraint from GW170817.

between these boundary conditions using the piecewise polytropes. We generate numerous piecewise polytropes with the parameters chosen at random. Here, we take the number of pieces as four with the adiabatic index in the last piece fixed to $\Gamma_4 = 1.33$; this value is chosen to match the quark matter value given in Table 8.1. This program has been initiated by Kurkela, Vuorinen, and their collaborators [311]; up to now, they have subsequently developed the method to get the EoS constraint from the tidal deformability [312] or to use the speed of sound for the parametrization [272, 313].

In Fig. 8.7, we plot 10,000 randomly generated piecewise polytropic EoSs interpolating between the χEFT and the HDLpt calculations. Fig. 8.8 and Fig. 8.9 are the corresponding M–R relation and the tidal deformability. We reject EoSs with a maximum mass less than $2\,M_\odot$; one can clearly see it in Fig. 8.8, in which all M–R relation reaches beyond $2\,M_\odot$. In this sense, we can say this is the most conservative constraint on the EoS based on the theory calculations with the minimal observational criterion. Even so, the magnitude of the allowed region is comparable to the observational constraint from the GW170817 event [160]. We would like to emphasize here that the theory calculation, particularly the pQCD calculations at high densities, can still be useful for constraining the possible EoSs.

In Fig. 8.7, we see the kink around $\rho = 4$–$6\,\rho_0$. This global tendency, which is quantified more quantitatively by the speed of sound or the adiabatic index, is related to the emergence of quark matter inside neutron stars [272].

In this subsection, we have mentioned briefly how the pQCD calculations are useful in constraining the EoS, and further studies on this issue can be found, e.g., in Ref. [314].

Chapter 9

Conclusions

In this thesis, the equation of state (EoS) of the strongly interacting dense matter is studied comprehensively relying on the QCD-based approach. Our machinery is the perturbation theory with resummation, and to be more specific, it is what is called the Hard Dense Loop perturbation theory (HDLpt). With the application to neutron star physics in mind, we take into account the effect of a bare mass of strange quarks. The inclusion of the bare quark mass effect is important for the quantitative description of the β equilibrium and charge neutral stellar system, but it hardly affects the qualitative feature of the EoS.

What is more crucial is the effect of resummation in the quark sector. Previously, the conventional perturbative QCD (pQCD) calculations are plagued with large scale variation uncertainty. In principle, the pQCD results should not depend on the choice of the renormalization scale, $\bar{\Lambda}$, but the truncation of the perturbative series at a finite order causes the uncertainty depending on the choice of $\bar{\Lambda}$. We find that this scale variation uncertainty is lessened in the EoS when it is expressed as the relation between the pressure, P, and the energy density, ε. This P–ε relation is important for the astrophysical application. Since the scale variation uncertainty is lessened, now we can compare our pQCD calculation with the EoS constrained by astrophysical observations; we found that there is a smooth matching between these EoSs. It may imply there is a smooth crossover transition from nuclear matter to quark matter. We also found the counterexample to the empirical theorem stating that the speed of sound, c_s^2, should always be less than the conformal limit, $c_s^2 = 1/3$, by explicitly showing $c_s^2 > 1/3$ in our calculation.

In Chapter 1, we gave a brief introduction to motivate why we study strongly interacting dense matter by putting an emphasis on the advantage of QCD-based approaches with resummation.

In Chapter 2, we offered a cursory look at the dense matter EoS studies. After briefly explaining the basic properties of the EoS, we presented the constraints on the EoS from nuclear experiments and astrophysical observations of neutron stars. We then reviewed the status of the theory calculation, particularly the pQCD calculations of the EoS. In Chapter 3, we covered the necessary perturbative methods to calculate QCD thermodynamics incorporating the hard thermal loop (HTL) resummation. We introduced the notion of HTLs and the need for resummation in Sec. 3.2. Then, we mentioned the

various techniques such as HTL perturbation theory (HTLpt) (Sec. 3.4), and the Φ-derivable approximation in the 2PI formalism (Sec. 3.5), which were used in the later chapters. For completeness, we also mentioned the resummation scheme à la Braaten and Pisarski in Sec. 3.3.

In Chapter 4, based on the method we introduced in Sec. 3.4, we calculated the EoS in the form of $P(\mu)$, which is the relation between the pressure and chemical potential, μ. In Sec. 4.1, all the necessary formulae were given, and details of the integration, which arises from the Matsubara summation, were supplemented in Sec. 4.2 for reference. Then the EoS construction in the β equilibrium and charge neutral system was explained in Sec. 4.3 along with the numerical results for the $N_{\rm f} = 2 + 1$ quarks. In Chapter 5, we discussed two corrections to the results presented in the previous chapter; they are an *ad hoc* $\mathcal{O}(\alpha_s)$ correction to match with the conventional pQCD coefficient as well as the bare mass correction in the self-energy expression used in the HDLpt, which turned to be negligible in our case. Also, for comparison, we performed the EoS calculation in the alternative resummation method of the Φ-derivable approximation in the 2PI formalism in Sec. 5.2.

In Chapters 6, 7, and 8, we discussed the novel facets of our results. Chapter 6 was devoted to the reduction of the scale variation uncertainty in the HTL-resummed theories. A heuristic interpretation was given by scrutinizing the relations between P, μ, and the baryon density, $n_{\rm B}$. Then, we explicitly wrote down the condition in order for the scale variation uncertainty to vanish. Thermodynamics involves differentiation with respect to μ. There can also arise a μ-dependence in the coupling constant, and the treatment of this μ-dependence is subtle. In Sec. 6.4, after describing the subtle feature of this point, we justify our assumption of not differentiating the μ-dependence in the coupling constant by stating that this is merely a convention of the parametrization. In Chapter 7, we discussed the behavior of the speed of sound in the HDLpt. We gave a quick survey on a few conventional scenarios describing the behavior of the speed of sound to fully appreciate our result. Main results, i.e. the violation of the conformal limit, were shown in Sec. 7.2 again with a caveat on the subtleties related to differentiating μ-dependence in the coupling constant in Sec. 7.3. Finally, in Chapter 8, we showed the smooth matching between our HDLpt EoS and the low-density nuclear matter EoSs. Inspired by this behavior of the EoS, we are led to the physical picture of quark-hadron continuity, which states that hadrons deconfine smoothly into quarks with increasing density, thus the hadron-to-quark transition becomes crossover-type. In Sec. 8.1, we reviewed the general remarks on the EoS construction with crossover, and in Sec. 8.2 we introduced the quark-hadron continuity concept, in which the present author and collaborators contributed. Finally in Sec. 8.3 the pQCD calculation is applied to constraining the neutron star observables to illustrate the usefulness of the pQCD results.

Novelties of our work lie in the following points.

First of all, the inclusion of bare quark mass effect both in the HDLpt and in the 2PI expansion, as discussed in Sec. 4.1 and 5.2, is newness in the technicalities. This allows us to construct the EoS in a realistic stellar environment, in which the strange quarks are heavier than u and d quarks.

This is just the extension of the preceding works; previously there have been calculations using the HDLpt in the massless limit of bare quarks such as in Refs. [110,227]. Our primary new findings were

not the calculations themselves, but rather the implications from the results of the above calculations. The one is the reduction of the scale variation uncertainty when viewed in the relation $P(\varepsilon)$. Usually in the community of pQCD thermodynamics, what they care about is the $P(\mu)$-relation as they calculate this quantity directly. For the phenomenological application, however, more important is $P(\varepsilon)$, so that the reduction of the uncertainty is more demanding in this expression. We have given explicit conditions for the reduction of the scale variation uncertainty in Sec. 6.3. We have also mentioned the issues related to differentiating μ-dependence in the coupling constant in Sec. 6.4. This issue has been alluded to in various literature as in Ref. [60], but to the best of our knowledge, this is the first time that these issues are stated with an explicit calculation at least in this context.

The upshot of this reduction of the uncertainty is the smooth matching between our calculation and the nuclear matter EoS. The possibility of the crossover transition at high densities has been thoroughly investigated in recent years, but our direct comparison allows us to see clearly the crossover tendency in the EoS. We note, however, that the analyses in Sec. 8.3 is not new; it is the direct application of the program initiated in Ref. [311].

The behavior of the speed of sound surpassing the conformal limit is also a notable issue. As we have explained, there is an empirical conjecture stating that the bound for the speed of sound is the conformal limit. This conjecture significantly affects the neutron star structure, and in recent years, there has been a variety of negative results on this conjecture from the astrophysical point of view. Our calculation serves as the counterexample for such conjecture.

The advantage of our calculations is the inclusion of resummation in the quark sector, which was absent in the conventional pQCD calculations [56–64]. As has been discussed in the 2PI expansion, the self-consistent resummation scheme itself is non-perturbative and robust.

To be fair, we also raise the drawback of our approach; our calculation is still at the leading order, and we are throwing away some known contributions in the pQCD results. For further systematic studies, we definitely need to go to higher orders in the coupling constant expansion, to contrast on equal footing with the existing results. In any case, a complementary approach other than the conventional pQCD is demanding.

This is the first step towards the QCD-based construction of the EoS in all the density regions. The significance of the EoS is not merely the problems that it solves, but the issues which it raises. We believe this will eventually help us understand the finite density region of QCD, which still remains as a terra incognita.

There are several directions we can take for future works.

First of all, the most critical is the higher-order calculations. The LO calculation still works well sometimes, but in order to settle things fully, the higher-order calculations are inevitable.

Fixing the renormalization scale appropriately is another issue. It has been argued that there are typical scale setting methods suggested in the various literature [315]. The application of such meth-

ods is worth further investigation. Also, now we are only considering resummation in the chromo-electric sector of QCD, but the chromomagnetic sector, whose scale is softer than the former, should also be taken into account. Color superconductivity is recognized to be arising from the long-range interaction in the chromomagnetic sector [316], and incorporating the gap in color superconductors may have a large effect on the EoS.

We can think of the application of our calculation to several dynamical phenomena. One is neutron star merger simulations emitting gravitational waves. It would be very interesting to consider how the crossover transition can be detected in the gravitational wave observatories. Also, our formulation also works at finite temperature, so that we can apply it to the context of heavy-ion collisions. High baryon density QGP matter is currently probed in the beam energy scan program at the RHIC [317], so it is of utmost importance to take advantage of such data. In this thesis, we considered the possibility of hybrid stars, which are neutron stars with quark cores inside. The compact stellar object may be solely made of strange quark matter [318–320], which is called quark stars. The existence of quark stars is still inconclusive, but at least the quark stars are inconsistent with the recent observations of compact stellar objects; the bag model description of quark stars with different values of the bag constant B [264, 265, 278, 321] will all lead to the smaller radius and maximum mass, which are inconsistent with the recent observations, thus the observed compact objects cannot be regarded as quark stars. Nonetheless, in current years, terrestrial experiments look for a somewhat different form of the strange quark matter in nuclear colliders; they are called metastable exotic multi-hypernuclear objects (MEMO) [322], and they can be regarded as a strangelet, or a nugget of the strange quark matter. Our quantitative study in the strangeness sector may also be useful in studying such objects.

Appendix A

Gluon calculations

We will supplement the pressure of gluons in Eq. 4.2 of the main text. It was already derived in, e.g., Ref. [204].

$$P_{\rm g} = \frac{M_{\rm D}^4}{64\pi^2}\left(\ln\frac{\bar{\Lambda}}{M_{\rm D}} + C_{\rm g}\right). \tag{4.10}$$

The gluon pressure can be split into the transverse gluon part and the longitudinal gluon part:

$$P_{\rm g}(T,\mu_f) \equiv (2-2\epsilon)P_{\rm T}(T,\mu_f) + P_{\rm L}(T,\mu_f)\,, \tag{A.1}$$

where the transverse gluon contribution $P_{\rm T}$ and the longitudinal contribution $P_{\rm L}$ are

$$P_{\rm T}(T,\mu_f) = -\frac{1}{2}\sum\!\!\!\!\!\!\int_K \ln\left[K^2 + \Pi_{\rm T}(i\omega_n,k)\right]\,, \tag{A.2}$$

$$P_{\rm L}(T,\mu_f) = -\frac{1}{2}\sum\!\!\!\!\!\!\int_K \ln\left[k^2 + \Pi_{\rm L}(i\omega_n,k)\right]\,. \tag{A.3}$$

$$\tag{A.4}$$

We define the transverse and longitudinal gluon self-energy appearing in the expression of the pressures as

$$\Pi_{\rm T}(i\omega_n,k) \equiv -\frac{\hat{M}_{\rm D}^2}{2-2\epsilon}\frac{\omega_n^2}{k^2}\left[1 - \frac{\omega_n^2+k^2}{\omega_n^2}\mathcal{T}(i\omega_n,k)\right]\,, \tag{A.5}$$

$$\Pi_{\rm L}(i\omega_n,k) \equiv \hat{M}_{\rm D}^2\left[1-\mathcal{T}(i\omega_n,k)\right]\,, \tag{A.6}$$

$$\tag{A.7}$$

where we also define the HTL functions for bosons $\mathcal{T}$ as

$$\mathcal{T}(i\omega_n,k) \equiv \frac{\Gamma(\frac{3}{2}-\epsilon)}{\Gamma(\frac{3}{2})\Gamma(1-\epsilon)}\int_0^1 dc\,(1-c^2)^{-\epsilon}\frac{(i\omega_n)^2}{(i\omega_n)^2-k^2c^2} \tag{A.8}$$

$$= {}_2F_1\left(\tfrac{1}{2},1;\tfrac{3}{2}-\epsilon;\frac{k^2}{(i\omega_n)^2}\right)\xrightarrow{\epsilon\to 0}\frac{i\omega_n}{k}Q_0\left(\frac{i\omega_n}{k}\right)=\frac{i\omega_n}{2k}\ln\frac{i\omega_n+k}{i\omega_n-k}\,. \tag{A.9}$$

Note that the HTL function involves the dimensional regularized form as they originate from the angular integrals in the $3-2\epsilon$ dimensions. Small ϵ dependence in the hypergeometric function will be important when calculating the temperature/density-independent part of the pressure (which we denote $P^\star$ below).

By carrying out the Matsubara sums and integrals, we will arrive at the one-loop expression of presssure calculated within the HTLpt.

$$\begin{aligned}P_{\rm g}(T,\mu_f) =& \frac{\hat{M}_{\rm D}^4}{64\pi^2}\left(\ln\frac{\bar{\Lambda}}{\hat{M}_{\rm D}}+C_{\rm g}\right)+\frac{1}{2\pi^3}\int_0^\infty d\omega\,\frac{1}{e^{\beta\omega}-1}\int_\omega^\infty dk\,k^2(2\phi_{\rm T}-\phi_{\rm L})\\ &-\frac{T}{2\pi^2}\int_0^\infty dk\,k^2\left[2\ln\left(1-e^{-\beta\omega_{\rm T}}\right)+\ln\left(1-e^{-\beta\omega_{\rm L}}\right)\right]-\frac{\pi^2T^4}{90}\,.\end{aligned} \tag{A.10}$$

Here the constants are evaluated numerically $C_{\rm g}\approx 1.17201$ and $C_{\rm q}\approx -0.03653$. Also we define the functions $\phi_{\rm T}$ and $\phi_{\rm L}$ as

$$\phi_{\rm T}(\omega,k;\hat{M}_{\rm D}^2)=\arctan\left[\frac{\frac{\pi\hat{M}_{\rm D}^2\omega}{4k^3}(k^2-\omega^2)}{k^2-\omega^2+\frac{\hat{M}_{\rm D}^2\omega^2}{2k^2}\left[1+\frac{k^2-\omega^2}{2k\omega}\ln\left(\frac{k+\omega}{k-\omega}\right)\right]}\right], \tag{A.11}$$

$$\phi_{\rm L}(\omega,k;\hat{M}_{\rm D}^2)=\arctan\left[\frac{\frac{\pi\hat{M}_{\rm D}^2\omega}{2k}}{k^2+\hat{M}_{\rm D}^2\left[1-\frac{\omega}{2k}\ln\left(\frac{k+\omega}{k-\omega}\right)\right]}\right], \tag{A.12}$$

Dispersion relations $\omega_{\rm T}(k;\hat{M}_{\rm D}^2)$ and $\omega_{\rm L}(k;\hat{M}_{\rm D}^2)$ are given by the solutions to the following equations:

$$\omega_{\rm T}^2-k^2-\frac{\hat{M}_{\rm D}^2\omega_{\rm T}^2}{2k^2}\left[1-\frac{\omega_{\rm T}^2-k^2}{2\omega_{\rm T}k}\ln\left(\frac{\omega_{\rm T}+k}{\omega_{\rm T}-k}\right)\right]=0\,, \tag{A.13}$$

$$k^2+\hat{M}_{\rm D}^2\left[1-\frac{\omega_{\rm L}}{2k}\ln\left(\frac{\omega_{\rm L}+k}{\omega_{\rm L}-k}\right)\right]=0\,. \tag{A.14}$$

We will derive each terms below.

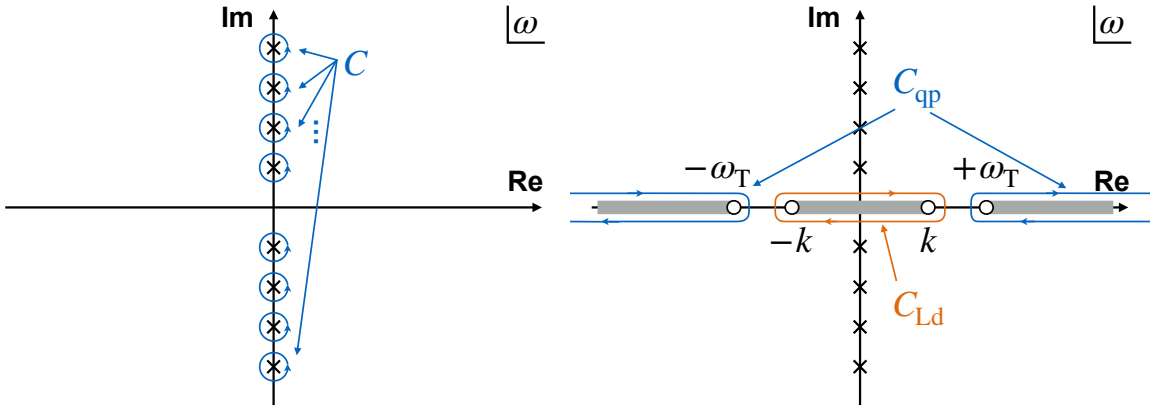

Fig. A.1: (Left) Integration contour of Matsubara sum; (Right) Contour after deformation.

A.1 Transverse gluons

We will start from the transverse gluon pressure in Eq. (A.2). We can rewrite the Matsubara sum into the contour integral by isolating the Matsubara zero mode $\omega_{n=0}$.

$$
\begin{aligned}
P_{\rm T}(T,\mu_f) &= -\frac{1}{2}\sum\!\!\!\!\!\!\int_K \ln\left[K^2+\Pi_{\rm T}(i\omega_n,k)\right] \\
&= -\frac{1}{2}\sum\!\!\!\!\!\!\int_K \ln\left[k^2+\omega_{n=0}^2+\Pi_{\rm T}(i\omega_{n=0},k)\right] - \frac{1}{2}\sum\!\!\!\!\!\!\int_K \ln\left[\frac{k^2+\omega_{n\neq0}^2+\Pi_{\rm T}(i\omega_{n\neq0},k)}{k^2+\omega_{n=0}^2+\Pi_{\rm T}(i\omega_{n=0},k)}\right] \\
&= -\frac{1}{2}\sum\!\!\!\!\!\!\int_K \ln\left(k^2\right) - \frac{1}{2}\sum\!\!\!\!\!\!\int_K \ln\left[\frac{k^2+\omega_{n\neq0}^2+\Pi_{\rm T}(i\omega_{n\neq0},k)}{k^2}\right] \\
&= -\frac{1}{2}\int_{\boldsymbol{k}} T\sum_{n\neq0}\ln\left[\frac{k^2+\omega_n^2+\Pi_{\rm T}(i\omega_n,k)}{k^2}\right] \\
&= -\frac{1}{4}\int_{\boldsymbol{k}}\oint_C\frac{d\omega}{2\pi i}\ln\left[\frac{k^2-\omega^2+\Pi_{\rm T}(\omega,k)}{k^2}\right]\coth\left(\frac{\beta\omega}{2}\right)
\end{aligned}
\tag{A.15}
$$

where we have used the relations $\Pi_{\rm T}(i\omega_n=0,k)=0$ and $\sum\!\!\!\!\!\!\int_K \ln(k^2) = \sum_n \lim_{\mu\to0}\int_{\boldsymbol{k}}\ln(k^2+\mu^2) = \frac{1}{(4\pi)^{d/2}}\frac{2}{d}\Gamma(1-\frac{d}{2})(\mu^2)^{d/2}=0$. The contour C is depicted in Fig. A.1 (Left). Now, by contour deformation, we can change the integration path C into $C_{\rm qp}\cup C_{\rm Ld}$, the one shown in Fig. A.1 (Right). We identify the term coming from the contour $C_{\rm qp}$ with the quasi-particle contribution and the one from the contour $C_{\rm Ld}$ with the Landau damping contribution:

$$
P_{\rm T,qp} = -\frac{1}{4}\int_{\boldsymbol{k}}\oint_{C_{\rm qp}}\frac{d\omega}{2\pi i}\ln\left[\frac{k^2-\omega^2+\Pi_{\rm T}(\omega,k)}{k^2}\right]\coth\left(\frac{\beta\omega}{2}\right), \tag{A.16}
$$

$$
P_{\rm T,Ld} = -\frac{1}{4}\int_{\boldsymbol{k}}\oint_{C_{\rm Ld}}\frac{d\omega}{2\pi i}\ln\left[\frac{k^2-\omega^2+\Pi_{\rm T}(\omega,k)}{k^2}\right]\coth\left(\frac{\beta\omega}{2}\right) \tag{A.17}
$$

Quasi-particle contribution

$$
\begin{aligned}
P_{\mathrm{T,qp}} &= -\frac{1}{4}\int_{\boldsymbol{k}}\oint_{C_{\mathrm{qp}}}\frac{d\omega}{2\pi i}\ln\left(\frac{k^2-\omega^2+\Pi_{\mathrm{T}}(\omega,k)}{k^2}\right)\coth\left(\frac{\beta\omega}{2}\right)\\
&= -\frac{1}{4}\int_{\boldsymbol{k}}\left\{\int_{\omega_{\mathrm{T}}}^{\infty}\frac{d\omega}{2\pi i}\left[\ln\left|\frac{k^2-\omega^2+\Pi_{\mathrm{T}}(\omega,k)}{k^2}\right|+i\arg\left(\frac{k^2-(\omega+i0^+)^2+\Pi_{\mathrm{T}}(\omega+i0^+,k)}{k^2}\right)\right]\coth\left(\frac{\beta\omega}{2}\right)\right.\\
&\quad+\int_{\infty}^{\omega_{\mathrm{T}}}\frac{d\omega}{2\pi i}\left[\ln\left|\frac{k^2-\omega^2+\Pi_{\mathrm{T}}(\omega,k)}{k^2}\right|+i\arg\left(\frac{k^2-(\omega-i0^+)^2+\Pi_{\mathrm{T}}(\omega-i0^+,k)}{k^2}\right)\right]\coth\left(\frac{\beta\omega}{2}\right)\\
&\quad+\int_{-\infty}^{-\omega_{\mathrm{T}}}\frac{d\omega}{2\pi i}\left[\ln\left|\frac{k^2-\omega^2+\Pi_{\mathrm{T}}(\omega,k)}{k^2}\right|+i\arg\left(\frac{k^2-(\omega+i0^+)^2+\Pi_{\mathrm{T}}(\omega+i0^+,k)}{k^2}\right)\right]\coth\left(\frac{\beta\omega}{2}\right)\\
&\quad\left.+\int_{-\omega_{\mathrm{T}}}^{-\infty}\frac{d\omega}{2\pi i}\left[\ln\left|\frac{k^2-\omega^2+\Pi_{\mathrm{T}}(\omega,k)}{k^2}\right|+i\arg\left(\frac{k^2-(\omega-i0^+)^2+\Pi_{\mathrm{T}}(\omega-i0^+,k)}{k^2}\right)\right]\coth\left(\frac{\beta\omega}{2}\right)\right\}\\
&= -\frac{1}{4}\int_{\boldsymbol{k}}\int_{\omega_{\mathrm{T}}}^{\infty}\frac{d\omega}{2\pi}\left[\arg\left(\frac{k^2-(\omega+i0^+)^2+\Pi_{\mathrm{T}}(\omega+i0^+,k)}{k^2}\right)-\arg\left(\frac{k^2-(\omega-i0^+)^2+\Pi_{\mathrm{T}}(\omega-i0^+,k)}{k^2}\right)\right]\\
&\qquad\times\left[\coth\left(\frac{\beta\omega}{2}\right)-\coth\left(-\frac{\beta\omega}{2}\right)\right]\\
&= -\frac{1}{4}\int_{\boldsymbol{k}}\int_{\omega_{\mathrm{T}}}^{\infty}\frac{d\omega}{2\pi}(-2\pi)\left(\frac{4}{e^{\beta\omega}-1}+2\right)\\
&= \int_{\boldsymbol{k}}\int_{\omega_{\mathrm{T}}}^{\infty}d\omega\left(\frac{1}{e^{\beta\omega}-1}+\frac{1}{2}e^{-\omega\delta}\right)\\
&= -\int_{\boldsymbol{k}}\left[T\ln\left(1-e^{-\beta\omega_{\mathrm{T}}}\right)-\frac{1}{2\delta}+\frac{\omega_{\mathrm{T}}(k)}{2}\right]
\end{aligned}
\tag{A.18}
$$

where in the intermediate steps, we have used the relations $\Pi_{\mathrm{T}}(-\omega,k)=\Pi_{\mathrm{T}}(\omega,k)$ and $\coth(\beta\omega/2)=\coth(-\beta\omega/2)=2/(e^{\beta\omega}-1)+1$. The dispersion relation for transverse gluons ω_{T} is obtained by solving Eq. (A.13). In the penultimate line, we have introduced the convergence factor $e^{-\omega\delta}$ and it gives out the $-1/2\delta$ contritbuion in the last line. This divergent term $-1/2\delta$ vanishes owing to dimensional regularization.

Landau damping contribution

$$
\begin{aligned}
P_{\mathrm{T,Ld}} &= -\frac{1}{4}\int_{\boldsymbol{k}}\oint_{C_{\mathrm{Ld}}}\frac{d\omega}{2\pi i}\ln\left[\frac{k^2-\omega^2+\Pi_{\mathrm{T}}(\omega,k)}{k^2}\right]\coth\left(\frac{\beta\omega}{2}\right)\\
&= -\frac{1}{4}\int_{\boldsymbol{k}}\left\{\int_{-k}^{k}\frac{d\omega}{2\pi i}\left[\ln\left|\frac{k^2-\omega^2+\Pi_{\mathrm{T}}(\omega,k)}{k^2}\right|+i\arg\left(\frac{k^2-(\omega+i0^+)^2+\Pi_{\mathrm{T}}(\omega+i0^+,k)}{k^2}\right)\right]\coth\left(\frac{\beta\omega}{2}\right)\right.\\
&\qquad\left.+\int_{k}^{-k}\frac{d\omega}{2\pi i}\left[\ln\left|\frac{k^2-\omega^2+\Pi_{\mathrm{T}}(\omega,k)}{k^2}\right|+i\arg\left(\frac{k^2-(\omega-i0^+)^2+\Pi_{\mathrm{T}}(\omega-i0^+,k)}{k^2}\right)\right]\coth\left(\frac{\beta\omega}{2}\right)\right\}\\
&= -\frac{1}{4}\int_{\boldsymbol{k}}\int_{-k}^{k}\frac{d\omega}{2\pi}\,\mathrm{Disc}\,\arg\left(\frac{k^2-\omega^2+\Pi_{\mathrm{T}}(\omega,k)}{k^2}\right)\coth\left(\frac{\beta\omega}{2}\right)\\
&= -\frac{1}{4}\int_{\boldsymbol{k}}2\int_{0}^{k}\frac{d\omega}{2\pi}\,\mathrm{Disc}\,\arctan\left[\frac{\mathrm{Im}\left[k^2-\omega^2+\Pi_{\mathrm{T}}(\omega,k)\right]}{\mathrm{Re}\left[k^2-\omega^2+\Pi_{\mathrm{T}}(\omega,k)\right]}\right]2\left(\frac{1}{e^{\beta\omega}-1}+\frac{1}{2}\right)\\
&= -\int_{\boldsymbol{k}}\int_{0}^{k}\frac{d\omega}{2\pi}\,\mathrm{Disc}\,\arctan\left[\frac{\frac{\hat{M}_{\mathrm{D}}^2}{2}\frac{k^2-\omega^2}{k^2}\,\mathrm{Im}\,{}_2F_1(\frac{1}{2},1;\frac{3}{2};\frac{k^2}{\omega^2})}{k^2-\omega^2+\frac{\hat{M}_{\mathrm{D}}^2}{2}\frac{\omega^2}{k^2}\left[1+\frac{k^2-\omega^2}{\omega^2}\,\mathrm{Re}\,{}_2F_1(\frac{1}{2},1;\frac{3}{2};\frac{k^2}{\omega^2})\right]}\right]\left(\frac{1}{e^{\beta\omega}-1}+\frac{1}{2}\right)\\
&= \frac{1}{\pi}\int_{\boldsymbol{k}}\int_{0}^{k}d\omega\,\phi_{\mathrm{T}}(\omega,k;\hat{M}_{\mathrm{D}}^2)\left(\frac{1}{e^{\beta\omega}-1}+\frac{1}{2}\right)
\end{aligned}
\tag{A.19}
$$

where in the penultimate step, we have used the facts

$$
\mathrm{Im}\,{}_2F_1(\tfrac{1}{2},1;\tfrac{3}{2};\tfrac{k^2}{(\omega\pm i0^+)^2}) = \mp\frac{i\pi\omega}{2k}\,,\quad \mathrm{Re}\,{}_2F_1(\tfrac{1}{2},1;\tfrac{3}{2};\tfrac{k^2}{(\omega\pm i0^+)^2}) = \frac{\omega}{2k}\ln(\frac{k+\omega}{k-\omega})\,. \tag{A.20}
$$

Now the angle ϕ_{T} is defined as in Eq. (A.11).

Temperature and chemical potential independent part

$$
\begin{aligned}
P_{\mathrm{T}}^{\star} &= -\frac{1}{2}\int_{-\infty}^{\infty}\frac{d\omega_{\mathrm{E}}}{2\pi}\int_{\boldsymbol{k}}\ln\left[k^2+\omega_{\mathrm{E}}^2+\Pi_{\mathrm{T}}(i\omega_{\mathrm{E}},k)\right]\\
&= -\int_{0}^{\infty}\frac{d\omega_{\mathrm{E}}}{2\pi}\int_{\boldsymbol{k}}k\ln\left[(1+\omega_{\mathrm{E}}^2)k^2+\Pi_{\mathrm{T}}(i\omega_{\mathrm{E}},1)\right]\\
&= \frac{\bar{\Lambda}^{2\epsilon}e^{\gamma_{\mathrm{E}}\epsilon}}{16\pi^{5/2}}\frac{\Gamma(2-\epsilon)\Gamma(\epsilon-2)}{\Gamma(\frac{3}{2}-\epsilon)}\int_{0}^{\infty}d\omega_{\mathrm{E}}\left(\frac{\Pi_{\mathrm{T}}(i\omega_{\mathrm{E}},1)}{1+\omega_{\mathrm{E}}^2}\right)^{2-\epsilon}
\end{aligned}
\tag{A.21}
$$

in the penultimate line, we have rescaled as $\omega_{\mathrm{E}}\to k\omega_{\mathrm{E}}$. Now we define the function f_{T} in the integrand above as:

$$
f_{\mathrm{T}}(\omega_{\mathrm{E}}) = \frac{2-2\epsilon}{\hat{M}_{\mathrm{D}}^2}\frac{\Pi_{\mathrm{T}}(i\omega_{\mathrm{E}},1)}{1+\omega_{\mathrm{E}}^2}\,. \tag{A.22}
$$

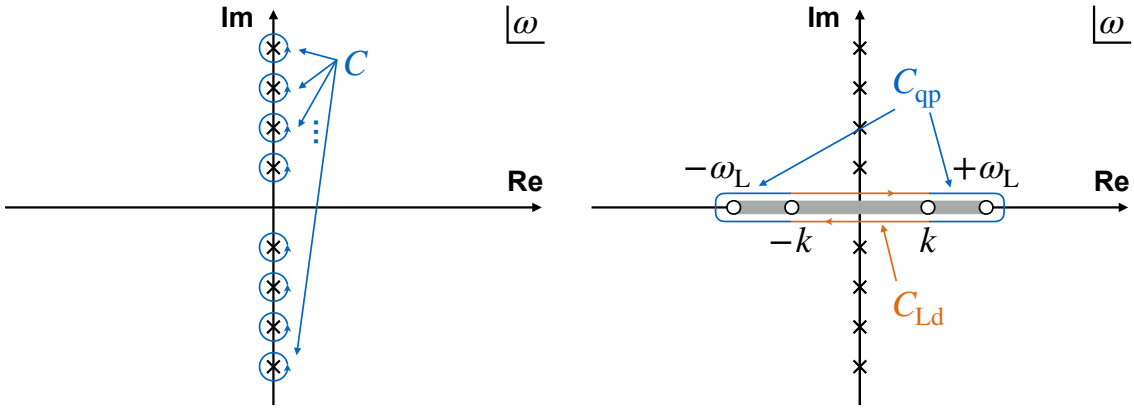

Fig. A.2: (Left) Integration contour of Matsubara sum; (Right) Contour after deformation.

We note here that this function f_T carrys the ϵ dependence (though not written explicitly). By expanding the integrand as the power of ϵ, we obtain

$$\begin{aligned}(2-2\epsilon)P_T^\star =& \frac{\bar{\Lambda}^{2\epsilon}e^{\gamma_E\epsilon}}{16\pi^{5/2}}\frac{\Gamma(2-\epsilon)\Gamma(\epsilon-2)}{\Gamma(\frac{3}{2}-\epsilon)}\frac{\hat{M}_D^{4-2\epsilon}}{(2-2\epsilon)^{1-\epsilon}}\left[\int_0^\infty d\omega_E\, f_T^2(\omega_E) - \epsilon\int_0^\infty d\omega_E\left(f_T^2\ln f_T - 2f_T\frac{\partial f_T}{\partial\epsilon}\right)\right]\\ =& \frac{\hat{M}_D^4}{32\pi^3}\left(\frac{1}{\epsilon}+\ln\frac{\bar{\Lambda}^2}{\hat{M}_D^2}+\frac{7}{2}-\ln 2\right)\left[\int_0^\infty d\omega_E\, f_T^2(\omega_E) - \epsilon\int_0^\infty d\omega_E\left(f_T^2\ln f_T - 2f_T\frac{\partial f_T}{\partial\epsilon}\right)\right]\end{aligned} \tag{A.23}$$

Here we define the constant as

$$\kappa_T = -\int_0^\infty d\omega_E\left(f_T^2\ln f_T - 2f_T\frac{\partial f_T}{\partial\epsilon}\right) \tag{A.24}$$

and using the value

$$\int_0^\infty d\omega_E\, f_T^2(\omega_E) = \frac{\pi}{12}(8\ln 2 - 5)\,, \tag{A.25}$$

we arrive at the expression

$$(2-2\epsilon)P_T^\star = \frac{\hat{M}_D^4}{64\pi^2}\left[\frac{8\ln 2-5}{6}\left(\frac{1}{\epsilon}+\ln\frac{\bar{\Lambda}^2}{\hat{M}_D^2}+\frac{7}{2}-\ln 2\right)+\frac{2\kappa_T}{\pi}\right] \tag{A.26}$$

A.2 Longitudinal gluons

We will start from the longitudinal gluon pressure in Eq. (A.3). We can rewrite the Matsubara sum into the contour integral by isolating the Matsubara zero mode $\omega_{n=0}$.

$$
\begin{aligned}
P_{\mathrm{L}}(T,\boldsymbol{\mu}_f) &= -\frac{1}{2}\sum\!\!\!\!\!\!\int_K \ln\left[k^2+\Pi_{\mathrm{L}}(i\omega_n,k)\right] \\
&= -\frac{1}{2}\int_{\boldsymbol{k}} \ln\left[k^2+\Pi_{\mathrm{L}}(i\omega_{n=0},k)\right] - \frac{1}{2}\sum\!\!\!\!\!\!\int_K \ln\left[k^2+\Pi_{\mathrm{L}}(i\omega_{n\neq 0},k)\right] \\
&= -\frac{1}{4}\int_{\boldsymbol{k}}\oint_C \frac{d\omega}{2\pi i}\ln\left[\frac{k^2+\Pi_{\mathrm{L}}(\omega,k)}{k^2+\hat{M}_{\mathrm{D}}^2}\right]\coth\left(\frac{\beta\omega}{2}\right)
\end{aligned}
\tag{A.27}
$$

where in the intermediate step, we have used the relation $\Pi_{\mathrm{L}}(i\omega_n = 0, k) = \hat{M}_{\mathrm{D}}^2$. The contour C is depicted in Fig. A.2 (Left). Note that the contribution from the Matsubara zero mode enters the final contour integral expression with the opposite sign because zero mode contour, which is the circle wrapping around the origin, can be deformed into $-C$. Here, further deforming the contour C, we can change the integration path into $C_{\mathrm{qp}} \cup C_{\mathrm{Ld}}$ as shown in Fig. A.2 (Right). As for the case in transverse gluons, we identify the term coming from the contour C_{qp} and C_{Ld} with the quasi-particle contribution and the Landau damping contribution, respectively:

$$
P_{\mathrm{L,qp}} = -\frac{1}{4}\int_{\boldsymbol{k}}\oint_{C_{\mathrm{qp}}} \frac{d\omega}{2\pi i}\ln\left[\frac{k^2+\Pi_{\mathrm{L}}(\omega,k)}{k^2+\hat{M}_{\mathrm{D}}^2}\right]\coth\left(\frac{\beta\omega}{2}\right), \tag{A.28}
$$

$$
P_{\mathrm{L,Ld}} = -\frac{1}{4}\int_{\boldsymbol{k}}\oint_{C_{\mathrm{Ld}}} \frac{d\omega}{2\pi i}\ln\left[\frac{k^2+\Pi_{\mathrm{L}}(\omega,k)}{k^2+\hat{M}_{\mathrm{D}}^2}\right]\coth\left(\frac{\beta\omega}{2}\right) \tag{A.29}
$$

Quasi-particle contribution

$$
\begin{aligned}
P_{\mathrm{L,qp}} &= -\frac{1}{4}\int_{\boldsymbol{k}}\oint_{C_{\mathrm{qp}}}\frac{d\omega}{2\pi i}\ln\left(\frac{k^2+\Pi_{\mathrm{L}}(\omega,k)}{k^2+\hat{M}_{\mathrm{D}}^2}\right)\coth\left(\frac{\beta\omega}{2}\right)\\
&= -\frac{1}{4}\int_{\boldsymbol{k}}\left\{\int_k^{\omega_{\mathrm{L}}}\frac{d\omega}{2\pi i}\left[\ln\left|\frac{k^2+\Pi_{\mathrm{L}}(\omega,k)}{k^2+\hat{M}_{\mathrm{D}}^2}\right|+i\arg\left(\frac{k^2+\Pi_{\mathrm{L}}(\omega+i0^+,k)}{k^2+\hat{M}_{\mathrm{D}}^2}\right)\right]\coth\left(\frac{\beta\omega}{2}\right)\right.\\
&\quad+\int_{\omega_{\mathrm{L}}}^{k}\frac{d\omega}{2\pi i}\left[\ln\left|\frac{k^2+\Pi_{\mathrm{L}}(\omega,k)}{k^2+\hat{M}_{\mathrm{D}}^2}\right|+i\arg\left(\frac{k^2+\Pi_{\mathrm{L}}(\omega-i0^+,k)}{k^2+\hat{M}_{\mathrm{D}}^2}\right)\right]\coth\left(\frac{\beta\omega}{2}\right)\\
&\quad+\int_{-\omega_{\mathrm{L}}}^{-k}\frac{d\omega}{2\pi i}\left[\ln\left|\frac{k^2+\Pi_{\mathrm{L}}(\omega,k)}{k^2+\hat{M}_{\mathrm{D}}^2}\right|+i\arg\left(\frac{k^2+\Pi_{\mathrm{L}}(\omega+i0^+,k)}{k^2+\hat{M}_{\mathrm{D}}^2}\right)\right]\coth\left(\frac{\beta\omega}{2}\right)\\
&\quad\left.+\int_{-k}^{-\omega_{\mathrm{L}}}\frac{d\omega}{2\pi i}\left[\ln\left|\frac{k^2+\Pi_{\mathrm{L}}(\omega,k)}{k^2}\right|+i\arg\left(\frac{k^2+\Pi_{\mathrm{L}}(\omega-i0^+,k)}{k^2+\hat{M}_{\mathrm{D}}^2}\right)\right]\coth\left(\frac{\beta\omega}{2}\right)\right\}\\
&= -\frac{1}{4}\int_{\boldsymbol{k}}\int_k^{\omega_{\mathrm{L}}}\frac{d\omega}{2\pi}\left[\arg\left(\frac{k^2+\Pi_{\mathrm{L}}(\omega+i0^+,k)}{k^2+\hat{M}_{\mathrm{D}}^2}\right)-\arg\left(\frac{k^2+\Pi_{\mathrm{L}}(\omega-i0^+,k)}{k^2+\hat{M}_{\mathrm{D}}^2}\right)\right]\\
&\qquad\times\left[\coth\left(\frac{\beta\omega}{2}\right)-\coth\left(-\frac{\beta\omega}{2}\right)\right]\\
&= -\frac{1}{4}\int_{\boldsymbol{k}}\int_k^{\omega_{\mathrm{L}}}\frac{d\omega}{2\pi}(2\pi)\left(\frac{4}{e^{\beta\omega}-1}+2\right)\\
&= -\int_{\boldsymbol{k}}\int_k^{\omega_{\mathrm{L}}}d\omega\left(\frac{1}{e^{\beta\omega}-1}+\frac{1}{2}\right)\\
&= -\int_{\boldsymbol{k}}\left[T\ln\left(\frac{1-e^{-\beta\omega_{\mathrm{L}}}}{1-e^{-\beta k}}\right)+\frac{1}{2}(\omega_{\mathrm{L}}(k)-k)\right]
\end{aligned}
\tag{A.30}
$$

where in the intermediate steps we have used the relations $\Pi_{\mathrm{L}}(-\omega,k)=\Pi_{\mathrm{L}}(\omega,k)$ and $\coth(\beta\omega/2)=-\coth(-\beta\omega/2)=2/(e^{\beta\omega}-1)+1$. The dispersion relation for longitudinal gluons ω_{L} is given by solving Eq. (A.14).

Landau damping contribution

$$
\begin{aligned}
P_{\mathrm{L,Ld}} &= -\frac{1}{4}\int_{\boldsymbol{k}}\oint_{C_{\mathrm{Ld}}}\frac{d\omega}{2\pi i}\ln\left(\frac{k^2+\Pi_{\mathrm{L}}(\omega,k)}{k^2+\hat{M}_{\mathrm{D}}^2}\right)\coth\left(\frac{\beta\omega}{2}\right)\\
&= -\frac{1}{4}\int_{\boldsymbol{k}}\left\{\int_{-k}^{k}\frac{d\omega}{2\pi i}\left[\ln\left|\frac{k^2+\Pi_{\mathrm{L}}(\omega,k)}{k^2+\hat{M}_{\mathrm{D}}^2}\right|+i\arg\left(\frac{k^2+\Pi_{\mathrm{L}}(\omega+i0^+,k)}{k^2+\hat{M}_{\mathrm{D}}^2}\right)\right]\coth\left(\frac{\beta\omega}{2}\right)\right.\\
&\qquad\left.+\int_{k}^{-k}\frac{d\omega}{2\pi i}\left[\ln\left|\frac{k^2+\Pi_{\mathrm{L}}(\omega,k)}{k^2+\hat{M}_{\mathrm{D}}^2}\right|+i\arg\left(\frac{k^2+\Pi_{\mathrm{L}}(\omega-i0^+,k)}{k^2+\hat{M}_{\mathrm{D}}^2}\right)\right]\coth\left(\frac{\beta\omega}{2}\right)\right\}\\
&= -\frac{1}{4}\int_{\boldsymbol{k}}\int_{-k}^{k}\frac{d\omega}{2\pi}\,\mathrm{Disc}\,\arg\left(\frac{k^2+\Pi_{\mathrm{L}}(\omega,k)}{k^2+\hat{M}_{\mathrm{D}}^2}\right)\coth\left(\frac{\beta\omega}{2}\right)\\
&= \frac{1}{4}\int_{\boldsymbol{k}}2\int_{0}^{k}\frac{d\omega}{2\pi}\,\mathrm{Disc}\,\arctan\left[\frac{\hat{M}_{\mathrm{D}}^2\,\mathrm{Im}\,{}_2F_1(\frac{1}{2},1;\frac{3}{2};\frac{k^2}{\omega^2})}{k^2+\hat{M}_{\mathrm{D}}^2-\hat{M}_{\mathrm{D}}^2\,\mathrm{Re}\,{}_2F_1(\frac{1}{2},1;\frac{3}{2};\frac{k^2}{\omega^2})}\right]2\left(\frac{1}{e^{\beta\omega}-1}+\frac{1}{2}\right)\\
&= -\frac{1}{\pi}\int_{\boldsymbol{k}}\int_{0}^{k}d\omega\,\phi_{\mathrm{L}}(\omega,k;\hat{M}_{\mathrm{D}}^2)\left(\frac{1}{e^{\beta\omega}-1}+\frac{1}{2}\right)
\end{aligned}
\tag{A.31}
$$

where in the penultimate line, we used the relations

$$
\mathrm{Im}\,{}_2F_1(\tfrac{1}{2},1;\tfrac{3}{2};\tfrac{k^2}{(\omega\pm i0^+)^2}) = \mp\frac{i\pi\omega}{2k}\,,\quad \mathrm{Re}\,{}_2F_1(\tfrac{1}{2},1;\tfrac{3}{2};\tfrac{k^2}{(\omega\pm i0^+)^2}) = \frac{\omega}{2k}\ln(\frac{k+\omega}{k-\omega})\,. \tag{A.32}
$$

The angle ϕ_{L} is defined in Eq. (A.12).

Temperature and chemical potential independent part

$$
\begin{aligned}
P_{\mathrm{L}}^{\star} &= -\frac{1}{2}\int_{-\infty}^{\infty}\frac{d\omega_{\mathrm{E}}}{2\pi}\int_{\boldsymbol{k}}\ln\left[k^2+\Pi_{\mathrm{L}}(i\omega_{\mathrm{E}},k)\right]\\
&= -\int_{0}^{\infty}\frac{d\omega_{\mathrm{E}}}{2\pi}\int_{\boldsymbol{k}}k\ln\left[k^2+\Pi_{\mathrm{L}}(i\omega_{\mathrm{E}},1)\right]\\
&= \frac{\bar{\Lambda}^{2\epsilon}e^{\gamma_{\mathrm{E}}\epsilon}}{16\pi^{5/2}}\frac{\Gamma(2-\epsilon)\Gamma(\epsilon-2)}{\Gamma(\frac{3}{2}-\epsilon)}\int_{0}^{\infty}d\omega_{\mathrm{E}}\,\left(\Pi_{\mathrm{L}}(i\omega_{\mathrm{E}},1)\right)^{2-\epsilon}
\end{aligned}
\tag{A.33}
$$

in the penultimate line, we have rescaled as $\omega_{\mathrm{E}}\to k\omega_{\mathrm{E}}$. Now we define the function f_{L} in the integrand above as:

$$
f_{\mathrm{L}}(\omega_{\mathrm{E}}) = \hat{M}_{\mathrm{D}}^{-2}\Pi_{\mathrm{L}}(i\omega_{\mathrm{E}},1)\,. \tag{A.34}
$$

We note here that this function $f_{\rm L}$ carrys the ϵ dependence (though not written explicitly). By expanding the integrand as the power of ϵ, we obtain

$$\begin{aligned} P_{\rm L}^{\star} =& \frac{\bar{\Lambda}^{2\epsilon} e^{\gamma_{\rm E}\epsilon}}{16\pi^{5/2}} \frac{\Gamma(2-\epsilon)\Gamma(\epsilon-2)}{\Gamma(\frac{3}{2}-\epsilon)} \hat{M}_{\rm D}^{4-2\epsilon} \left[\int_0^\infty d\omega_{\rm E}\, f_{\rm L}^2(\omega_{\rm E}) - \epsilon \int_0^\infty d\omega_{\rm E} \left(f_{\rm L}^2 \ln f_{\rm L} - 2 f_{\rm L} \frac{\partial f_{\rm L}}{\partial \epsilon} \right) \right] \\ =& \frac{\hat{M}_{\rm D}^4}{16\pi^3} \left(\frac{1}{\epsilon} + \ln \frac{\bar{\Lambda}^2}{\hat{M}_{\rm D}^2} + \frac{5}{2} - 2\ln 2 \right) \left[\int_0^\infty d\omega_{\rm E}\, f_{\rm L}^2(\omega_{\rm E}) - \epsilon \int_0^\infty d\omega_{\rm E} \left(f_{\rm L}^2 \ln f_{\rm L} - 2 f_{\rm L} \frac{\partial f_{\rm L}}{\partial \epsilon} \right) \right] \end{aligned} \tag{A.35}$$

Here we define the constant as

$$\kappa_{\rm L} = - \int_0^\infty d\omega_{\rm E} \left(f_{\rm L}^2 \ln f_{\rm L} - 2 f_{\rm L} \frac{\partial f_{\rm L}}{\partial \epsilon} \right) \tag{A.36}$$

and using the value

$$\int_0^\infty d\omega_{\rm E}\, f_{\rm L}^2(\omega_{\rm E}) = \frac{\pi}{3}(1 - \ln 2)\,, \tag{A.37}$$

we arrive at the expression

$$P_{\rm L}^{\star} = \frac{\hat{M}_{\rm D}^4}{64\pi^2} \left[\frac{4 - 4\ln 2}{3} \left(\frac{1}{\epsilon} + \ln \frac{\bar{\Lambda}^2}{\hat{M}_{\rm D}^2} + \frac{5}{2} - 2\ln 2 \right) + \frac{4\kappa_{\rm L}}{\pi} \right] \tag{A.38}$$

Appendix B

The structure equations of neutron stars

In this chapter we will present for completeness the description of the structure equations of neutron stars from the reduction of the Einstein equation.

B.1 Equilibrium configuration: mass and radius

B.1.1 Derivation of the TOV equation

The geometry of spacetime of a static and spherical symmetric star can be described by the following metric:

$$ds^2 = -e^{\nu(r)}dt^2 + e^{\lambda(r)}dr^2 + r^2(d\theta^2 + \sin^2\theta\, d\phi^2). \tag{B.1}$$

The energy-momentum tensor is given by

$$T_{\mu\nu} = (\varepsilon + P)u_\mu u_\nu + P\eta_{\mu\nu}, \tag{B.2}$$

where ε and P are density and pressure, and u_μ is the velocity four-vector, defined so that $u_\mu u^\nu = -1$. Ricci tensor associated with this metric can be calculated as follows

$$R_0^0 = -e^{-\lambda(r)}\left(\frac{\nu''}{2} + \frac{\nu'}{r} + \frac{\nu'^2}{4} - \frac{\nu'\lambda'}{4}\right), \tag{B.3}$$

$$R_1^1 = -e^{-\lambda(r)}\left(\frac{\nu''}{2} - \frac{\lambda'}{r} + \frac{\nu'^2}{4} - \frac{\nu'\lambda'}{4}\right), \tag{B.4}$$

$$R_i^i = -e^{-\lambda(r)}\left(\frac{\nu' - \lambda'}{2r} + \frac{1}{r^2}\right) + \frac{1}{r^2}, \quad (i = 2, 3). \tag{B.5}$$

The prime denote the differentiation in terms of r. Ricci scalars are

$$R = R_\mu^\mu = -e^{-\lambda(r)}\left(\nu'' + \frac{2(\nu' - \lambda')}{r} + \frac{\nu'^2}{2} - \frac{\nu'\lambda'}{2} + \frac{2}{r^2}\right) + \frac{2}{r^2} \tag{B.6}$$

Thus now one can write the Einstein equation:

$$G^{\mu}_{\nu} = 8\pi T^{\mu}_{\nu}, \tag{B.7}$$

where G^{μ}_{ν} is the Einstein tensor

$$G^{\mu}_{\nu} = R^{\mu}_{\nu} - \frac{1}{2}\delta^{\mu}_{\nu}R. \tag{B.8}$$

Each component ((0,0), (1,1) and $(i,i), i = 2,3$) reads

$$e^{-\lambda(r)}\left(\frac{1}{r^2} - \frac{\lambda'}{r}\right) - \frac{1}{r^2} = -8\pi\varepsilon \tag{B.9}$$

$$e^{-\lambda(r)}\left(\frac{\nu'}{r} + \frac{1}{r^2}\right) - \frac{1}{r^2} = 8\pi P \tag{B.10}$$

$$e^{-\lambda(r)}\left(\frac{\nu''}{2} + \frac{\nu' - \lambda'}{2r} + \frac{\nu'^2}{4} - \frac{\nu'\lambda'}{4}\right) = 8\pi P \tag{B.11}$$

Here we define $\Phi(r)$ and $m(r)$ instead of $\nu(r)$ and $\lambda(r)$

$$e^{\nu(r)} =: e^{2\Phi(r)}, \qquad e^{-\lambda(r)} =: 1 - \frac{2m(r)}{r}. \tag{B.12}$$

Plugging these in Eq. (B.9) and (B.10) gives

$$\frac{dm(r)}{dr} = 4\pi r^2 \varepsilon(r) \tag{B.13}$$

$$\frac{d\Phi(r)}{dr} = \frac{m + 4\pi r^3 P}{r(r - 2m)} \tag{B.14}$$

The derivative of p in terms of r result from the conservation of the momentum:

$$\nabla_{\nu} T^{1\nu} = 0 \quad \rightarrow \quad \frac{dP}{dr} = -(\varepsilon + P)\frac{d\Phi}{dr} \tag{B.15}$$

This completes the derivation of the TOV equations:

$$\frac{dm}{dr} = 4\pi r^2 \varepsilon, \tag{B.16}$$

$$\frac{dP}{dr} = -\frac{m\varepsilon}{r^2}\left(1 + \frac{P}{\varepsilon}\right)\left(1 + \frac{4\pi r^3 P}{m}\right)\left(1 - \frac{2m}{r}\right)^{-1}, \tag{B.17}$$

$$\frac{d\Phi}{dr} = -\frac{1}{\varepsilon + P}\frac{dP}{dr}. \tag{B.18}$$

As a remark, these equations (B.16-B.18) yield the well-known Schwarzschild metric:

$$ds^2 = -\left(1 - \frac{r_s}{r}\right)dt^2 + \left(1 - \frac{r_s}{r}\right)^{-1} dr^2 + r^2(d\theta^2 + \sin^2\theta\, d\phi^2), \tag{B.19}$$

where r_s is Schwarzschild radius $r_s := 2M$ and $M := m(R)$ is the mass of star up to the stellar radius $r = R$.

B.1.2 Gravitational redshift

In the geometry described by the Schwarzschild metric, a proper time interval is

$$d\tau = \left(1 - \frac{r_s}{r}\right)^{1/2} dt \tag{B.20}$$

Assume signals of frequency

$$\nu(r = R) = \frac{dN}{d\tau} = \left(1 - \frac{r_s}{R}\right)^{-1/2} \frac{dN}{dt} \tag{B.21}$$

are emitted from the neutron star surface ($r = R$), where dN is the number of signals over a time interval $d\tau$. A distant observer will detect signals of frequency

$$\nu_\infty = \frac{dN}{dt}, \tag{B.22}$$

since the geometry becomes asymptotically flat at infinity. Thus, the gravitational redshift of signals emitted from the surface is

$$\nu_\infty = \left(1 - \frac{r_s}{R}\right)^{1/2} \nu(R), \quad z := \frac{\nu(R)}{\nu_\infty} - 1 = \left(1 - \frac{r_s}{R}\right)^{-1/2} - 1. \tag{B.23}$$

B.2 Static linearized perturbations: tidal deformability

B.2.1 Perturbations due to an external tidal field

In this section, the behavior of the equilibrium configuration under linearized perturbations due to an external quadrupolar tidal field is examined following [307, 308]. The full metric of the geometry is given by

$$g_{\mu\nu} = \eta_{\mu\nu} + h_{\mu\nu}, \tag{B.24}$$

where $h_{\mu\nu}$ is a linearized metric perturbation. Here we analyze the angular dependence of the components of $h_{\mu\nu}$ into spherical harmonics $Y_l^m(\theta, \phi)$. Introducing a $l = 2$ and $m = 0$ perturbation without loss of generality onto the spherically symmetric geometry (B.1) results in a static (zero-frequency),

even-parity perturbation of the metric:

$$ds^2 = -e^{\nu(r)}[1 + H(r)Y_2^0(\theta,\phi)]dt^2 + e^{\lambda(r)}[1 - H(r)Y_2^0]dr^2 + r^2[1 - K(r)Y_2^0(\theta,\phi)](d\theta^2 + \sin^2\theta\, d\phi^2), \tag{B.25}$$

where $K(r)$ is related to $H(r)$ by $K'(r) = H'(r) + H(r)\nu'(r)$. The corresponding perturbations of the energy momentum tensor (B.2) are

$$\delta T_0^0 = -\delta\varepsilon(r)Y_2^0(\theta,\phi), \quad \delta T_i^i = \delta P(r)Y_2^0(\theta,\phi). \tag{B.26}$$

From the perturbed Einstein equation $\delta G_\nu^\mu = 8\pi\delta T_\nu^\mu$, one obtains the differential equation for $H(r)$:

$$H'' + H'\left[\frac{2}{r} + e^\lambda\left(\frac{2m(r)}{r^2} + 4\pi r\,(P-\varepsilon)\right)\right] + H\left[-\frac{6e^\lambda}{r^2} + 4\pi e^\lambda\left(5\varepsilon + 9P + \frac{\varepsilon+P}{(dP/d\varepsilon)}\right) - \nu'^2\right] = 0, \tag{B.27}$$

This second-order differential equation is separated into two first-order equations by defining the additional functions $\beta(r) = dH/dr$ and becomes:

$$\frac{dH}{dr} = \beta \tag{B.28}$$

$$\begin{aligned}\frac{d\beta}{dr} = {} & 2\left(1-\frac{2m}{r}\right)^{-1} H\left\{2\pi\left[5\varepsilon + 9P + (\varepsilon+P)\frac{d\varepsilon}{dP}\right] + \frac{3}{r^2} + 2\left(1-\frac{2m}{r}\right)^{-1}\left(\frac{m}{r^2} + 4\pi r^2 P\right)^2\right\} \\ & + \frac{2\beta}{r}\left(1-\frac{2m}{r}\right)^{-1}\left\{-1 + \frac{m}{r} + 2\pi r^2(\varepsilon - P)\right\}.\end{aligned} \tag{B.29}$$

These equations are augmented with Eqs. (B.16) and (B.17), and solved simultaneously with a boundary condition

$$H(r) = a_0 r^2\left[1 - \frac{2\pi}{7}\left(5\varepsilon_c + 9P_c + \frac{\varepsilon_c + P_c}{(dP/d\varepsilon)_c}\right)r^2 + O(r^3)\right], \tag{B.30}$$

at r slightly away from $r = 0$, where ε_c and P_c are the energy density and pressure at the stellar center. The constant a_0 determines how much the star is deformed and can be chosen arbitrarily as it cancels in the expression for the Love number k_2.

B.2.2 Calculation of the tidal Love number

Once we get the solution $m(r), P(r), H(r)$ and $\beta(r)$ solving the Eqs. (B.16), (B.17), (B.28), and (B.29), the tidal Love number k_2 can be calculated by the following procedure.

H has an analytical solution outside the star $r \geq R$, where $T_{\mu\nu} = 0$:

$$\begin{aligned}H &= c_1\left(\frac{r}{M}\right)^2\left(1-\frac{2M}{r}\right)\left[-\frac{M(M-r)(2M^2+6Mr-3r^2)}{r^2(2M-r)^2} + \frac{3}{2}\ln\left(\frac{r}{r-2M}\right)\right] + 3c_2\left(\frac{r}{M}\right)^2\left(1-\frac{2M}{r}\right), \\ &= c_1\frac{1-2C}{C^2}\left[-\frac{C(C-1)(2C^2+6C-3)}{(1-2C)^2} - \frac{3}{2}\ln(1-2C)\right] + 3c_2\frac{1-2C}{C^2},\end{aligned} \tag{B.31}$$

where $C = M/R$ is the compactness of the star. From the asymptotic behavior of this expression, the coefficients c_1 and c_2 are matched as follows [307]:

$$c_1 = \frac{15}{8}\frac{1}{M^3}\lambda\mathcal{E}, \quad c_2 = \frac{1}{3}M^2\mathcal{E}, \tag{B.32}$$

so that one can solve Eq. (B.31) and its derivative in terms of λ and obtain (remember $k_2 = (3/2)\lambda/R^5$):

$$\begin{aligned} k_2 =& \frac{8C^5}{5}\frac{c_1}{6c_2} \qquad\qquad (B.33)\\ =& \frac{8C^5}{5}(1-2C)^2[2+2C(y-1)-y] \\ &\times\Big\{2C[6-3y+3C(5y-8)]+4C^3[13-11y+C(3y-2)+2C^2(1+y)] \\ &\qquad +3(1-2C)^2[2-y+2C(y-1)]\ln(1-2C)\Big\}^{-1}, \qquad\qquad (B.34)\end{aligned}$$

where y is defined as

$$y = \frac{R\beta(R)}{H(R)} = \frac{R\,H'(R)}{H(R)}. \tag{B.35}$$

Bibliography

[1] Y. Fujimoto and K. Fukushima, *Equation of state of cold and dense QCD matter in resummed perturbation theory*, *Phys. Rev. D* **105** (2022) 014025, arXiv:2011.10891 [hep-ph].

[2] M. Y. Han and Y. Nambu, *Three Triplet Model with Double SU(3) Symmetry*, *Phys. Rev.* **139** (1965) B1006–B1010.

[3] H. Fritzsch, M. Gell-Mann, and H. Leutwyler, *Advantages of the Color Octet Gluon Picture*, *Phys. Lett. B* **47** (1973) 365–368.

[4] J. C. Pati and A. Salam, *Unified Lepton-Hadron Symmetry and a Gauge Theory of the Basic Interactions*, *Phys. Rev. D* **8** (1973) 1240–1251.

[5] J. C. Pati and A. Salam, *Lepton Number as the Fourth Color*, *Phys. Rev. D* **10** (1974) 275–289. [Erratum: Phys.Rev.D 11, 703–703 (1975)].

[6] S. Weinberg, *Nonabelian Gauge Theories of the Strong Interactions*, *Phys. Rev. Lett.* **31** (1973) 494–497.

[7] E. Braaten and R. D. Pisarski, *Soft Amplitudes in Hot Gauge Theories: A General Analysis*, *Nucl. Phys. B* **337** (1990) 569–634.

[8] Y. Nambu and G. Jona-Lasinio, *Dynamical Model of Elementary Particles Based on an Analogy with Superconductivity. 1.*, *Phys. Rev.* **122** (1961) 345–358.

[9] Y. Nambu and G. Jona-Lasinio, *DYNAMICAL MODEL OF ELEMENTARY PARTICLES BASED ON AN ANALOGY WITH SUPERCONDUCTIVITY. II*, *Phys. Rev.* **124** (1961) 246–254.

[10] **LIGO Scientific, Virgo** Collaboration, B. P. Abbott *et al.*, *GW170817: Observation of Gravitational Waves from a Binary Neutron Star Inspiral*, *Phys. Rev. Lett.* **119** (2017) 161101, arXiv:1710.05832 [gr-qc].

[11] M. R. Drout *et al.*, *Light Curves of the Neutron Star Merger GW170817/SSS17a: Implications for R-Process Nucleosynthesis*, *Science* **358** (2017) 1570–1574, arXiv:1710.05443 [astro-ph.HE].

[12] E. Pian *et al.*, *Spectroscopic identification of r-process nucleosynthesis in a double neutron star merger*, *Nature* **551** (2017) 67–70, arXiv:1710.05858 [astro-ph.HE].

[13] D. J. Gross and F. Wilczek, *Ultraviolet Behavior of Nonabelian Gauge Theories*, *Phys. Rev. Lett.* **30** (1973) 1343–1346.

[14] H. D. Politzer, *Reliable Perturbative Results for Strong Interactions?*, *Phys. Rev. Lett.* **30** (1973) 1346–1349.

[15] J. C. Collins and M. J. Perry, *Superdense Matter: Neutrons Or Asymptotically Free Quarks?*, *Phys. Rev. Lett.* **34** (1975) 1353.

[16] G. Baym and S. A. Chin, *Can a Neutron Star Be a Giant MIT Bag?*, *Phys. Lett. B* **62** (1976) 241–244.

[17] N. Itoh, *Hydrostatic Equilibrium of Hypothetical Quark Stars*, *Prog. Theor. Phys.* **44** (1970) 291.

[18] N. Cabibbo and G. Parisi, *Exponential Hadronic Spectrum and Quark Liberation*, *Phys. Lett. B* **59** (1975) 67–69.

[19] R. Hagedorn, *Statistical thermodynamics of strong interactions at high-energies*, *Nuovo Cim. Suppl.* **3** (1965) 147–186.

[20] N. Ishii, S. Aoki, and T. Hatsuda, *The Nuclear Force from Lattice QCD*, *Phys. Rev. Lett.* **99** (2007) 022001, arXiv:nucl-th/0611096.

[21] M. Asakawa and K. Yazaki, *Chiral Restoration at Finite Density and Temperature*, *Nucl. Phys. A* **504** (1989) 668–684.

[22] A. Barducci, R. Casalbuoni, S. De Curtis, R. Gatto, and G. Pettini, *Chiral Symmetry Breaking in QCD at Finite Temperature and Density*, *Phys. Lett. B* **231** (1989) 463–470.

[23] F. Wilczek, *Application of the renormalization group to a second order QCD phase transition*, *Int. J. Mod. Phys. A* **7** (1992) 3911–3925. [Erratum: Int.J.Mod.Phys.A 7, 6951 (1992)].

[24] M. Kitazawa, T. Koide, T. Kunihiro, and Y. Nemoto, *Chiral and color superconducting phase transitions with vector interaction in a simple model*, *Prog. Theor. Phys.* **108** (2002) 929–951, arXiv:hep-ph/0207255. [Erratum: Prog.Theor.Phys. 110, 185–186 (2003)].

[25] T. Hatsuda, M. Tachibana, N. Yamamoto, and G. Baym, *New critical point induced by the axial anomaly in dense QCD*, *Phys. Rev. Lett.* **97** (2006) 122001, arXiv:hep-ph/0605018.

[26] D. Bailin and A. Love, *Superfluidity and Superconductivity in Relativistic Fermion Systems*, *Phys. Rept.* **107** (1984) 325.

[27] M. Iwasaki and T. Iwado, *Superconductivity in the quark matter*, *Phys. Lett. B* **350** (1995) 163–168.

[28] M. G. Alford, K. Rajagopal, and F. Wilczek, *QCD at finite baryon density: Nucleon droplets and color superconductivity*, *Phys. Lett. B* **422** (1998) 247–256, arXiv:hep-ph/9711395.

[29] R. Rapp, T. Schäfer, E. V. Shuryak, and M. Velkovsky, *Diquark Bose condensates in high density matter and instantons*, *Phys. Rev. Lett.* **81** (1998) 53–56, arXiv:hep-ph/9711396.

[30] M. G. Alford, K. Rajagopal, and F. Wilczek, *Color flavor locking and chiral symmetry breaking in high density QCD*, *Nucl. Phys. B* **537** (1999) 443–458, arXiv:hep-ph/9804403.

[31] M. G. Alford, A. Schmitt, K. Rajagopal, and T. Schäfer, *Color superconductivity in dense quark matter*, *Rev. Mod. Phys.* **80** (2008) 1455–1515, arXiv:0709.4635 [hep-ph].

[32] M. A. Stephanov, *Non-Gaussian fluctuations near the QCD critical point*, *Phys. Rev. Lett.* **102** (2009) 032301, arXiv:0809.3450 [hep-ph].

[33] M. A. Stephanov, *On the sign of kurtosis near the QCD critical point*, *Phys. Rev. Lett.* **107** (2011) 052301, arXiv:1104.1627 [hep-ph].

[34] **STAR** Collaboration, J. Adam *et al.*, *Nonmonotonic Energy Dependence of Net-Proton Number Fluctuations*, *Phys. Rev. Lett.* **126** (2021) 092301, arXiv:2001.02852 [nucl-ex].

[35] L. McLerran and R. D. Pisarski, *Phases of cold, dense quarks at large N(c)*, *Nucl. Phys. A* **796** (2007) 83–100, arXiv:0706.2191 [hep-ph].

[36] D. T. Son and M. A. Stephanov, *QCD at finite isospin density*, *Phys. Rev. Lett.* **86** (2001) 592–595, arXiv:hep-ph/0005225.

[37] B. Borderie and J. D. Frankland, *Liquid–Gas phase transition in nuclei*, *Prog. Part. Nucl. Phys.* **105** (2019) 82–138, arXiv:1903.02881 [nucl-ex].

[38] M. Gyulassy and L. McLerran, *New forms of QCD matter discovered at RHIC*, *Nucl. Phys. A* **750** (2005) 30–63, arXiv:nucl-th/0405013.

[39] A. Andronic, P. Braun-Munzinger, K. Redlich, and J. Stachel, *Decoding the phase structure of QCD via particle production at high energy*, *Nature* **561** (2018) 321–330, arXiv:1710.09425 [nucl-th].

[40] P. Braun-Munzinger, J. Stachel, and C. Wetterich, *Chemical freezeout and the QCD phase transition temperature*, *Phys. Lett. B* **596** (2004) 61–69, arXiv:nucl-th/0311005.

[41] Y. Aoki, Z. Fodor, S. D. Katz, and K. K. Szabo, *The QCD transition temperature: Results with physical masses in the continuum limit*, *Phys. Lett. B* **643** (2006) 46–54, arXiv:hep-lat/0609068.

[42] S. Borsanyi, Z. Fodor, C. Hoelbling, S. D. Katz, S. Krieg, and K. K. Szabo, *Full result for the QCD equation of state with 2+1 flavors*, *Phys. Lett. B* **730** (2014) 99–104, arXiv:1309.5258 [hep-lat].

[43] **HotQCD** Collaboration, A. Bazavov *et al.*, *Equation of state in (2+1)-flavor QCD*, *Phys. Rev. D* **90** (2014) 094503, arXiv:1407.6387 [hep-lat].

[44] V. Vovchenko, *Hadron resonance gas with van der Waals interactions*, *Int. J. Mod. Phys. E* **29** (2020) 2040002, arXiv:2004.06331 [nucl-th].

[45] Y. Fujimoto, K. Fukushima, Y. Hidaka, A. Hiraguchi, and K. Iida, *Equation of state of neutron star matter and its warm extension with an interacting hadron resonance gas*, arXiv:2109.06799 [nucl-th].

[46] K. Hebeler and A. Schwenk, *Chiral three-nucleon forces and neutron matter*, *Phys. Rev. C* **82** (2010) 014314, arXiv:0911.0483 [nucl-th].

[47] S. Gandolfi, J. Carlson, and S. Reddy, *The maximum mass and radius of neutron stars and the nuclear symmetry energy*, *Phys. Rev. C* **85** (2012) 032801, arXiv:1101.1921 [nucl-th].

[48] I. Tews, T. Krüger, K. Hebeler, and A. Schwenk, *Neutron matter at next-to-next-to-next-to-leading order in chiral effective field theory*, *Phys. Rev. Lett.* **110** (2013) 032504, arXiv:1206.0025 [nucl-th].

[49] J. W. Holt, N. Kaiser, and W. Weise, *Nuclear chiral dynamics and thermodynamics*, *Prog. Part. Nucl. Phys.* **73** (2013) 35–83, arXiv:1304.6350 [nucl-th].

[50] G. Hagen, T. Papenbrock, A. Ekström, K. Wendt, G. Baardsen, S. Gandolfi, M. Hjorth-Jensen, and C. Horowitz, *Coupled-cluster calculations of nucleonic matter*, *Phys. Rev. C* **89** (2014) 014319, arXiv:1311.2925 [nucl-th].

[51] A. Roggero, A. Mukherjee, and F. Pederiva, *Quantum Monte Carlo calculations of neutron matter with non-local chiral interactions*, *Phys. Rev. Lett.* **112** (2014) 221103, arXiv:1402.1576 [nucl-th].

[52] G. Wlazł owski, J. Holt, S. Moroz, A. Bulgac, and K. Roche, *Auxiliary-Field Quantum Monte Carlo Simulations of Neutron Matter in Chiral Effective Field Theory*, *Phys. Rev. Lett.* **113** (2014) 182503, arXiv:1403.3753 [nucl-th].

[53] I. Tews, J. Carlson, S. Gandolfi, and S. Reddy, *Constraining the speed of sound inside neutron stars with chiral effective field theory interactions and observations*, *Astrophys. J.* **860** (2018) 149, arXiv:1801.01923 [nucl-th].

[54] C. Drischler, R. J. Furnstahl, J. A. Melendez, and D. R. Phillips, *How Well Do We Know the Neutron-Matter Equation of State at the Densities Inside Neutron Stars? A Bayesian Approach with Correlated Uncertainties*, *Phys. Rev. Lett.* **125** (2020) 202702, arXiv:2004.07232 [nucl-th].

[55] C. Drischler, J. W. Holt, and C. Wellenhofer, *Chiral Effective Field Theory and the High-Density Nuclear Equation of State*, *Ann. Rev. Nucl. Part. Sci.* **71** (2021) 403–432, arXiv:2101.01709 [nucl-th].

[56] B. A. Freedman and L. D. McLerran, *Fermions and Gauge Vector Mesons at Finite Temperature and Density. 1. Formal Techniques*, *Phys. Rev. D* **16** (1977) 1130.

[57] B. A. Freedman and L. D. McLerran, *Fermions and Gauge Vector Mesons at Finite Temperature and Density. 2. The Ground State Energy of a Relativistic electron Gas*, *Phys. Rev. D* **16** (1977) 1147.

[58] B. A. Freedman and L. D. McLerran, *Fermions and Gauge Vector Mesons at Finite Temperature and Density. 3. The Ground State Energy of a Relativistic Quark Gas*, *Phys. Rev. D* **16** (1977) 1169.

[59] V. Baluni, *Nonabelian Gauge Theories of Fermi Systems: Chromotheory of Highly Condensed Matter*, *Phys. Rev. D* **17** (1978) 2092.

[60] A. Kurkela, P. Romatschke, and A. Vuorinen, *Cold Quark Matter*, *Phys. Rev. D* **81** (2010) 105021, arXiv:0912.1856 [hep-ph].

[61] E. S. Fraga, A. Kurkela, and A. Vuorinen, *Interacting quark matter equation of state for compact stars*, *Astrophys. J. Lett.* **781** (2014) L25, arXiv:1311.5154 [nucl-th].

[62] T. Gorda, A. Kurkela, P. Romatschke, M. Säppi, and A. Vuorinen, *Next-to-Next-to-Next-to-Leading Order Pressure of Cold Quark Matter: Leading Logarithm*, *Phys. Rev. Lett.* **121** (2018) 202701, arXiv:1807.04120 [hep-ph].

[63] T. Gorda, A. Kurkela, R. Paatelainen, S. Säppi, and A. Vuorinen, *Soft Interactions in Cold Quark Matter*, *Phys. Rev. Lett.* **127** (2021) 162003, arXiv:2103.05658 [hep-ph].

[64] T. Gorda, A. Kurkela, R. Paatelainen, S. Säppi, and A. Vuorinen, *Cold quark matter at N3LO: Soft contributions*, *Phys. Rev. D* **104** (2021) 074015, arXiv:2103.07427 [hep-ph].

[65] J. Ghiglieri, A. Kurkela, M. Strickland, and A. Vuorinen, *Perturbative Thermal QCD: Formalism and Applications*, *Phys. Rept.* **880** (2020) 1–73, arXiv:2002.10188 [hep-ph].

[66] A. Akmal, V. R. Pandharipande, and D. G. Ravenhall, *The Equation of state of nucleon matter and neutron star structure*, *Phys. Rev. C* **58** (1998) 1804–1828, arXiv:nucl-th/9804027.

[67] H. Togashi, K. Nakazato, Y. Takehara, S. Yamamuro, H. Suzuki, and M. Takano, *Nuclear equation of state for core-collapse supernova simulations with realistic nuclear forces*, *Nucl. Phys. A* **961** (2017) 78–105, arXiv:1702.05324 [nucl-th].

[68] F. Douchin and P. Haensel, *A unified equation of state of dense matter and neutron star structure*, *Astron. Astrophys.* **380** (2001) 151, arXiv:astro-ph/0111092.

[69] B. D. Serot and J. D. Walecka, *Recent progress in quantum hadrodynamics*, *Int. J. Mod. Phys. E* **6** (1997) 515–631, arXiv:nucl-th/9701058.

[70] M. Drews and W. Weise, *Functional renormalization group studies of nuclear and neutron matter*, *Prog. Part. Nucl. Phys.* **93** (2017) 69–107, arXiv:1610.07568 [nucl-th].

[71] L. Tolos and L. Fabbietti, *Strangeness in Nuclei and Neutron Stars*, *Prog. Part. Nucl. Phys.* **112** (2020) 103770, arXiv:2002.09223 [nucl-ex].

[72] G. F. Burgio, I. Vidana, H. J. Schulze, and J. B. Wei, *Neutron stars and the nuclear equation of state*, *Prog. Part. Nucl. Phys.* **120** (2021) 103879, arXiv:2105.03747 [nucl-th].

[73] J. C. Collins, A. Duncan, and S. D. Joglekar, *Trace and Dilatation Anomalies in Gauge Theories*, *Phys. Rev. D* **16** (1977) 438–449.

[74] G. Aarts, *Introductory lectures on lattice QCD at nonzero baryon number*, *J. Phys. Conf. Ser.* **706** (2016) 022004, arXiv:1512.05145 [hep-lat].

[75] K. Nagata, *Finite-density lattice QCD and sign problem: current status and open problems*, arXiv:2108.12423 [hep-lat].

[76] B. B. Brandt, G. Endrodi, and S. Schmalzbauer, *QCD phase diagram for nonzero isospin-asymmetry*, *Phys. Rev. D* **97** (2018) 054514, arXiv:1712.08190 [hep-lat].

[77] Y. Ashida, Z. Gong, and M. Ueda, *Non-Hermitian physics*, *Adv. Phys.* **69** (2021) 249–435, arXiv:2006.01837 [cond-mat.mes-hall].

[78] C. M. Bender and S. Boettcher, *Real spectra in nonHermitian Hamiltonians having PT symmetry*, *Phys. Rev. Lett.* **80** (1998) 5243–5246, arXiv:physics/9712001.

[79] Y. L. Dokshitzer, V. A. Khoze, A. H. Mueller, and S. I. Troian, *Basics of perturbative QCD*. 1991.

[80] Y. L. Dokshitzer, *Calculation of the Structure Functions for Deep Inelastic Scattering and e+ e- Annihilation by Perturbation Theory in Quantum Chromodynamics.*, *Sov. Phys. JETP* **46** (1977) 641–653.

[81] V. N. Gribov and L. N. Lipatov, *Deep inelastic e p scattering in perturbation theory*, *Sov. J. Nucl. Phys.* **15** (1972) 438–450.

[82] G. Altarelli and G. Parisi, *Asymptotic Freedom in Parton Language*, *Nucl. Phys. B* **126** (1977) 298–318.

[83] L. N. Lipatov, *Reggeization of the Vector Meson and the Vacuum Singularity in Nonabelian Gauge Theories*, *Sov. J. Nucl. Phys.* **23** (1976) 338–345.

[84] E. A. Kuraev, L. N. Lipatov, and V. S. Fadin, *The Pomeranchuk Singularity in Nonabelian Gauge Theories*, *Sov. Phys. JETP* **45** (1977) 199–204.

[85] I. I. Balitsky and L. N. Lipatov, *The Pomeranchuk Singularity in Quantum Chromodynamics*, *Sov. J. Nucl. Phys.* **28** (1978) 822–829.

[86] A. H. Mueller, *Soft gluons in the infinite momentum wave function and the BFKL pomeron*, *Nucl. Phys. B* **415** (1994) 373–385.

[87] L. V. Gribov, E. M. Levin, and M. G. Ryskin, *Semihard Processes in QCD*, *Phys. Rept.* **100** (1983) 1–150.

[88] A. H. Mueller and J.-w. Qiu, *Gluon Recombination and Shadowing at Small Values of x*, *Nucl. Phys. B* **268** (1986) 427–452.

[89] I. Balitsky, *Operator expansion for high-energy scattering*, *Nucl. Phys. B* **463** (1996) 99–160, arXiv:hep-ph/9509348.

[90] Y. V. Kovchegov, *Unitarization of the BFKL pomeron on a nucleus*, *Phys. Rev. D* **61** (2000) 074018, arXiv:hep-ph/9905214.

[91] J. Jalilian-Marian, A. Kovner, A. Leonidov, and H. Weigert, *The BFKL equation from the Wilson renormalization group*, *Nucl. Phys. B* **504** (1997) 415–431, arXiv:hep-ph/9701284.

[92] J. Jalilian-Marian, A. Kovner, A. Leonidov, and H. Weigert, *The Wilson renormalization group for low x physics: Towards the high density regime*, *Phys. Rev. D* **59** (1998) 014014, arXiv:hep-ph/9706377.

[93] J. Jalilian-Marian, A. Kovner, A. Leonidov, and H. Weigert, *Unitarization of gluon distribution in the doubly logarithmic regime at high density*, *Phys. Rev. D* **59** (1999) 034007, arXiv:hep-ph/9807462. [Erratum: Phys.Rev.D 59, 099903 (1999)].

[94] A. Kovner, J. G. Milhano, and H. Weigert, *Relating different approaches to nonlinear QCD evolution at finite gluon density*, *Phys. Rev. D* **62** (2000) 114005, arXiv:hep-ph/0004014.

[95] E. Iancu, A. Leonidov, and L. D. McLerran, *Nonlinear gluon evolution in the color glass condensate. 1.*, *Nucl. Phys. A* **692** (2001) 583–645, arXiv:hep-ph/0011241.

[96] E. Iancu, A. Leonidov, and L. D. McLerran, *The Renormalization group equation for the color glass condensate*, *Phys. Lett. B* **510** (2001) 133–144, arXiv:hep-ph/0102009.

[97] E. Ferreiro, E. Iancu, A. Leonidov, and L. McLerran, *Nonlinear gluon evolution in the color glass condensate. 2.*, *Nucl. Phys. A* **703** (2002) 489–538, arXiv:hep-ph/0109115.

[98] K. J. Golec-Biernat and M. Wusthoff, *Saturation effects in deep inelastic scattering at low Q**2 and its implications on diffraction*, *Phys. Rev. D* **59** (1998) 014017, arXiv:hep-ph/9807513.

[99] Y. V. Kovchegov and E. Levin, *Quantum chromodynamics at high energy*, vol. 33. Cambridge University Press, 8, 2012.

[100] J.-P. Blaizot, *High gluon densities in heavy ion collisions*, *Rept. Prog. Phys.* **80** (2017) 032301, arXiv:1607.04448 [hep-ph].

[101] J. W. Negele and H. Orland, *Quantum Many-Particle Systems*. CRC Press, 1988.

[102] M. Gell-Mann and K. A. Brueckner, *Correlation Energy of an Electron Gas at High Density*, *Phys. Rev.* **106** (1957) 364–368.

[103] K. Kajantie and J. I. Kapusta, *Behavior of Gluons at High Temperature*, *Annals Phys.* **160** (1985) 477.

[104] R. Kobes, G. Kunstatter, and A. Rebhan, *QCD plasma parameters and the gauge dependent gluon propagator*, *Phys. Rev. Lett.* **64** (1990) 2992–2995.

[105] O. K. Kalashnikov and V. V. Klimov, *Polarization Tensor in QCD for Finite Temperature and Density*, *Sov. J. Nucl. Phys.* **31** (1980) 699.

[106] D. J. Gross, R. D. Pisarski, and L. G. Yaffe, *QCD and Instantons at Finite Temperature*, *Rev. Mod. Phys.* **53** (1981) 43.

[107] E. Braaten and R. D. Pisarski, *Resummation and Gauge Invariance of the Gluon Damping Rate in Hot QCD*, *Phys. Rev. Lett.* **64** (1990) 1338.

[108] R. D. Pisarski, *Scattering Amplitudes in Hot Gauge Theories*, *Phys. Rev. Lett.* **63** (1989) 1129.

[109] R. D. Pisarski, *Resummation and the gluon damping rate in hot QCD*, *Nucl. Phys. A* **525** (1991) 175–188.

[110] J. O. Andersen and M. Strickland, *The Equation of state for dense QCD and quark stars*, *Phys. Rev. D* **66** (2002) 105001, arXiv:hep-ph/0206196.

[111] K. Hebeler, J. M. Lattimer, C. J. Pethick, and A. Schwenk, *Constraints on neutron star radii based on chiral effective field theory interactions*, *Phys. Rev. Lett.* **105** (2010) 161102, arXiv:1007.1746 [nucl-th].

[112] K. Hebeler, J. M. Lattimer, C. J. Pethick, and A. Schwenk, *Equation of state and neutron star properties constrained by nuclear physics and observation*, *Astrophys. J.* **773** (2013) 11, arXiv:1303.4662 [astro-ph.SR].

[113] Y. Fujimoto, K. Fukushima, and K. Murase, *Mapping neutron star data to the equation of state using the deep neural network*, *Phys. Rev. D* **101** (2020) 054016, arXiv:1903.03400 [nucl-th].

[114] P. Bedaque and A. W. Steiner, *Sound velocity bound and neutron stars*, *Phys. Rev. Lett.* **114** (2015) 031103, arXiv:1408.5116 [nucl-th].

[115] "BUQEYE collaboration." https://github.com/buqeye/nuclear-matter-convergence.

[116] W. G. Lynch and M. B. Tsang, *Decoding the Density Dependence of the Nuclear Symmetry Energy*, arXiv:2106.10119 [nucl-th].

[117] P. Demorest, T. Pennucci, S. Ransom, M. Roberts, and J. Hessels, *Shapiro Delay Measurement of A Two Solar Mass Neutron Star*, *Nature* **467** (2010) 1081–1083, arXiv:1010.5788 [astro-ph.HE].

[118] E. Fonseca *et al.*, *The NANOGrav Nine-year Data Set: Mass and Geometric Measurements of Binary Millisecond Pulsars*, *Astrophys. J.* **832** (2016) 167, arXiv:1603.00545 [astro-ph.HE].

[119] J. Antoniadis *et al.*, *A Massive Pulsar in a Compact Relativistic Binary*, *Science* **340** (2013) 1233232, arXiv:1304.6875 [astro-ph.HE].

[120] H. T. Cromartie *et al.*, *Relativistic Shapiro delay measurements of an extremely massive millisecond pulsar*, *Nature Astron.* **4** (2019) 72–76, arXiv:1904.06759 [astro-ph.HE].

[121] M. G. Alford, G. Burgio, S. Han, G. Taranto, and D. Zappalà, *Constraining and applying a generic high-density equation of state*, *Phys. Rev. D* **92** (2015) 083002, arXiv:1501.07902 [nucl-th].

[122] K. Yako *et al.*, *Determination of the Gamow-Teller quenching factor from charge exchange reactions on Zr-90*, *Phys. Lett. B* **615** (2005) 193–199, arXiv:nucl-ex/0411011.

[123] J. Yasuda *et al.*, *Extraction of the Landau-Migdal Parameter from the Gamow-Teller Giant Resonance in Sn132*, *Phys. Rev. Lett.* **121** (2018) 132501.

[124] M. Kortelainen, T. Lesinski, J. More, W. Nazarewicz, J. Sarich, N. Schunck, M. V. Stoitsov, and S. Wild, *Nuclear Energy Density Optimization*, *Phys. Rev. C* **82** (2010) 024313, arXiv:1005.5145 [nucl-th].

[125] P. Möller, W. D. Myers, H. Sagawa, and S. Yoshida, *New Finite-Range Droplet Mass Model and Equation-of-State Parameters*, *Phys. Rev. Lett.* **108** (2012) 052501.

[126] L.-W. Chen, C. M. Ko, B.-A. Li, and J. Xu, *Density slope of the nuclear symmetry energy from the neutron skin thickness of heavy nuclei*, *Phys. Rev. C* **82** (2010) 024321, arXiv:1004.4672 [nucl-th].

[127] A. Tamii *et al.*, *Complete electric dipole response and the neutron skin in 208Pb*, *Phys. Rev. Lett.* **107** (2011) 062502, arXiv:1104.5431 [nucl-ex].

[128] X. Roca-Maza, M. Centelles, X. Viñas, M. Brenna, G. Colò, B. K. Agrawal, N. Paar, J. Piekarewicz, and D. Vretenar, *Electric dipole polarizability in ^{208}Pb: Insights from the droplet model*, *Phys. Rev. C* **88** (2013) 024316, arXiv:1307.4806 [nucl-th].

[129] L. Trippa, G. Colo, and E. Vigezzi, *The Giant Dipole Resonance as a quantitative constraint on the symmetry energy*, *Phys. Rev. C* **77** (2008) 061304, arXiv:0802.3658 [nucl-th].

[130] P. Danielewicz, P. Singh, and J. Lee, *Symmetry Energy III: Isovector Skins*, *Nucl. Phys. A* **958** (2017) 147–186, arXiv:1611.01871 [nucl-th].

[131] M. B. Tsang, Y. Zhang, P. Danielewicz, M. Famiano, Z. Li, W. G. Lynch, and A. W. Steiner, *Constraints on the density dependence of the symmetry energy*, *Phys. Rev. Lett.* **102** (2009) 122701, arXiv:0811.3107 [nucl-ex].

[132] J. M. Lattimer and Y. Lim, *Constraining the Symmetry Parameters of the Nuclear Interaction*, *Astrophys. J.* **771** (2013) 51, arXiv:1203.4286 [nucl-th].

[133] J. M. Lattimer and A. W. Steiner, *Constraints on the symmetry energy using the mass-radius relation of neutron stars*, *Eur. Phys. J. A* **50** (2014) 40, arXiv:1403.1186 [nucl-th].

[134] I. Tews, J. M. Lattimer, A. Ohnishi, and E. E. Kolomeitsev, *Symmetry Parameter Constraints from a Lower Bound on Neutron-matter Energy*, *Astrophys. J.* **848** (2017) 105, arXiv:1611.07133 [nucl-th].

[135] A. W. Steiner, M. Prakash, J. M. Lattimer, and P. J. Ellis, *Isospin asymmetry in nuclei and neutron stars*, *Phys. Rept.* **411** (2005) 325–375, arXiv:nucl-th/0410066.

[136] K. Oyamatsu and K. Iida, *Empirical properties of asymmetric nuclear matter to be obtained from unstable nuclei*, *Nucl. Phys. A* **718** (2003) 363–366.

[137] P. Danielewicz, *Surface symmetry energy*, *Nucl. Phys. A* **727** (2003) 233–268, arXiv:nucl-th/0301050.

[138] W. D. Myers and W. J. Swiatecki, *Average nuclear properties*, *Annals Phys.* **55** (1969) 395.

[139] **PREX** Collaboration, D. Adhikari *et al.*, *Accurate Determination of the Neutron Skin Thickness of ^{208}Pb through Parity-Violation in Electron Scattering*, *Phys. Rev. Lett.* **126** (2021) 172502, arXiv:2102.10767 [nucl-ex].

[140] B. T. Reed, F. J. Fattoyev, C. J. Horowitz, and J. Piekarewicz, *Implications of PREX-2 on the Equation of State of Neutron-Rich Matter*, *Phys. Rev. Lett.* **126** (2021) 172503, arXiv:2101.03193 [nucl-th].

[141] P.-G. Reinhard, X. Roca-Maza, and W. Nazarewicz, *Information Content of the Parity-Violating Asymmetry in Pb208*, *Phys. Rev. Lett.* **127** (2021) 232501, arXiv:2105.15050 [nucl-th].

[142] J. Piekarewicz, *Implications of PREX-2 on the electric dipole polarizability of neutron-rich nuclei*, *Phys. Rev. C* **104** (2021) 024329, arXiv:2105.13452 [nucl-th].

[143] E. Lipparini and S. Stringari, *Sum rules and giant resonances in nuclei*, *Phys. Rept.* **175** (1989) 103–261.

[144] E. E. Kolomeitsev *et al.*, *Transport theories for heavy ion collisions in the 1-A-GeV regime*, *J. Phys. G* **31** (2005) S741–S758, arXiv:nucl-th/0412037.

[145] J. Xu *et al.*, *Understanding transport simulations of heavy-ion collisions at 100A and 400A MeV: Comparison of heavy-ion transport codes under controlled conditions*, *Phys. Rev. C* **93** (2016) 044609, arXiv:1603.08149 [nucl-th].

[146] Y.-X. Zhang *et al.*, *Comparison of heavy-ion transport simulations: Collision integral in a box*, *Phys. Rev. C* **97** (2018) 034625, arXiv:1711.05950 [nucl-th].

[147] A. Ono *et al.*, *Comparison of heavy-ion transport simulations: Collision integral with pions and Δ resonances in a box*, *Phys. Rev. C* **100** (2019) 044617, arXiv:1904.02888 [nucl-th].

[148] B.-A. Li, L.-W. Chen, and C. M. Ko, *Recent Progress and New Challenges in Isospin Physics with Heavy-Ion Reactions*, *Phys. Rept.* **464** (2008) 113–281, arXiv:0804.3580 [nucl-th].

[149] M. B. Tsang *et al.*, *Isospin Diffusion and the Nuclear Symmetry Energy in Heavy Ion Reactions*, *Phys. Rev. Lett.* **92** (2004) 062701.

[150] S. Nagamiya, M. C. Lemaire, E. Moller, S. Schnetzer, G. Shapiro, H. Steiner, and I. Tanihata, *Production of Pions and Light Fragments at Large Angles in High-Energy Nuclear Collisions*, *Phys. Rev. C* **24** (1981) 971–1009.

[151] J. W. Harris *et al.*, *PION PRODUCTION AS A PROBE OF THE NUCLEAR MATTER EQUATION OF STATE*, *Phys. Lett. B* **153** (1985) 377–381.

[152] N. Ikeno, A. Ono, Y. Nara, and A. Ohnishi, *Probing neutron-proton dynamics by pions*, *Phys. Rev. C* **93** (2016) 044612, arXiv:1601.07636 [nucl-th]. [Erratum: Phys.Rev.C 97, 069902 (2018)].

[153] Y. Liu, Y. Wang, Y. Cui, C.-J. Xia, Z. Li, Y. Chen, Q. Li, and Y. Zhang, *Insights into the pion production mechanism and the symmetry energy at high density*, *Phys. Rev. C* **103** (2021) 014616, arXiv:2006.15861 [nucl-th].

[154] R. Stock, *Particle Production in High-Energy Nucleus Nucleus Collisions*, *Phys. Rept.* **135** (1986) 259–315.

[155] **SπRIT** Collaboration, J. Estee *et al.*, *Probing the Symmetry Energy with the Spectral Pion Ratio*, *Phys. Rev. Lett.* **126** (2021) 162701, arXiv:2103.06861 [nucl-ex].

[156] J.-Y. Ollitrault, *Anisotropy as a signature of transverse collective flow*, *Phys. Rev. D* **46** (1992) 229–245.

[157] **STAR** Collaboration, L. Adamczyk *et al.*, *Beam-Energy Dependence of the Directed Flow of Protons, Antiprotons, and Pions in Au+Au Collisions*, *Phys. Rev. Lett.* **112** (2014) 162301, arXiv:1401.3043 [nucl-ex].

[158] Y. Nara and A. Ohnishi, *JAM mean-field update: mean-field effects on collective flow in high-energy heavy-ion collisions at $\sqrt{s_{NN}} = 2 - 20$ GeV energies*, arXiv:2109.07594 [nucl-th].

[159] P. Danielewicz, R. Lacey, and W. G. Lynch, *Determination of the equation of state of dense matter*, *Science* **298** (2002) 1592–1596, arXiv:nucl-th/0208016.

[160] **LIGO Scientific, Virgo** Collaboration, B. P. Abbott *et al.*, *GW170817: Measurements of neutron star radii and equation of state*, *Phys. Rev. Lett.* **121** (2018) 161101, arXiv:1805.11581 [gr-qc].

[161] A. W. Steiner, J. M. Lattimer, and E. F. Brown, *The Neutron Star Mass-Radius Relation and the Equation of State of Dense Matter*, *Astrophys. J.* **765** (2013) L5, arXiv:1205.6871 [nucl-th].

[162] F. Özel and P. Freire, *Masses, Radii, and the Equation of State of Neutron Stars*, *Ann. Rev. Astron. Astrophys.* **54** (2016) 401–440, arXiv:1603.02698 [astro-ph.HE].

[163] Y. Fujimoto, K. Fukushima, and K. Murase, *Extensive Studies of the Neutron Star Equation of State from the Deep Learning Inference with the Observational Data Augmentation*, *JHEP* **03** (2021) 273, arXiv:2101.08156 [nucl-th].

[164] L. Lindblom, *Determining the nuclear equation of state from neutron-star masses and radii*, *Astrophys. J.* **398** (1992) 569–573.

[165] F. Özel, G. Baym, and T. Guver, *Astrophysical Measurement of the Equation of State of Neutron Star Matter*, *Phys. Rev. D* **82** (2010) 101301, arXiv:1002.3153 [astro-ph.HE].

[166] A. W. Steiner, J. M. Lattimer, and E. F. Brown, *The Equation of State from Observed Masses and Radii of Neutron Stars*, *Astrophys. J.* **722** (2010) 33–54, arXiv:1005.0811 [astro-ph.HE].

[167] F. Ozel, D. Psaltis, T. Guver, G. Baym, C. Heinke, and S. Guillot, *The Dense Matter Equation of State from Neutron Star Radius and Mass Measurements*, *Astrophys. J.* **820** (2016) 28, arXiv:1505.05155 [astro-ph.HE].

[168] S. Bogdanov, C. O. Heinke, F. Özel, and T. Güver, *Neutron Star Mass-Radius Constraints of the Quiescent Low-mass X-ray Binaries X7 and X5 in the Globular Cluster 47 Tuc*, *Astrophys. J.* **831** (2016) 184, arXiv:1603.01630 [astro-ph.HE].

[169] M. Miller, *Astrophysical Constraints on Dense Matter in Neutron Stars*, arXiv:1312.0029 [astro-ph.HE].

[170] M. C. Miller and F. K. Lamb, *Observational Constraints on Neutron Star Masses and Radii*, *Eur. Phys. J. A* **52** (2016) 63, arXiv:1604.03894 [astro-ph.HE].

[171] **Virgo, LIGO Scientific** Collaboration, B. P. Abbott *et al.*, *GW170817: Observation of Gravitational Waves from a Binary Neutron Star Inspiral*, *Phys. Rev. Lett.* **119** (2017) 161101, arXiv:1710.05832 [gr-qc].

[172] **LIGO Scientific, Virgo** Collaboration, B. Abbott *et al.*, *GW190425: Observation of a Compact Binary Coalescence with Total Mass $\sim 3.4 M_\odot$*, *Astrophys. J. Lett.* **892** (2020) L3, arXiv:2001.01761 [astro-ph.HE].

[173] T. E. Riley *et al.*, *A NICER View of PSR J0030+0451: Millisecond Pulsar Parameter Estimation*, *Astrophys. J. Lett.* **887** (2019) L21, arXiv:1912.05702 [astro-ph.HE].

[174] M. Miller *et al.*, *PSR J0030+0451 Mass and Radius from NICER Data and Implications for the Properties of Neutron Star Matter*, *Astrophys. J. Lett.* **887** (2019) L24, arXiv:1912.05705 [astro-ph.HE].

[175] M. C. Miller *et al.*, *The Radius of PSR J0740+6620 from NICER and XMM-Newton Data*, *Astrophys. J. Lett.* **918** (2021) L28, arXiv:2105.06979 [astro-ph.HE].

[176] T. E. Riley *et al.*, *A NICER View of the Massive Pulsar PSR J0740+6620 Informed by Radio Timing and XMM-Newton Spectroscopy*, *Astrophys. J. Lett.* **918** (2021) L27, arXiv:2105.06980 [astro-ph.HE].

[177] K. Yagi and N. Yunes, *I-Love-Q*, *Science* **341** (2013) 365–368, arXiv:1302.4499 [gr-qc].

[178] K. Yagi and N. Yunes, *I-Love-Q Relations in Neutron Stars and their Applications to Astrophysics, Gravitational Waves and Fundamental Physics*, *Phys. Rev. D* **88** (2013) 023009, arXiv:1303.1528 [gr-qc].

[179] K. Yagi and N. Yunes, *Approximate Universal Relations for Neutron Stars and Quark Stars*, *Phys. Rept.* **681** (2017) 1–72, arXiv:1608.02582 [gr-qc].

[180] L. Baiotti, *Gravitational waves from neutron star mergers and their relation to the nuclear equation of state*, *Prog. Part. Nucl. Phys.* **109** (2019) 103714, arXiv:1907.08534 [astro-ph.HE].

[181] R. C. Tolman, *Static solutions of Einstein's field equations for spheres of fluid*, *Phys. Rev.* **55** (1939) 364–373.

[182] J. R. Oppenheimer and G. M. Volkoff, *On Massive neutron cores*, *Phys. Rev.* **55** (1939) 374–381.

[183] D. Alvarez-Castillo, A. Ayriyan, S. Benic, D. Blaschke, H. Grigorian, and S. Typel, *New class of hybrid EoS and Bayesian M-R data analysis*, *Eur. Phys. J. A* **52** (2016) 69, arXiv:1603.03457 [nucl-th].

[184] C. A. Raithel, F. Özel, and D. Psaltis, *From Neutron Star Observables to the Equation of State: An Optimal Parametrization*, *Astrophys. J.* **831** (2016) 44, arXiv:1605.03591 [astro-ph.HE].

[185] C. A. Raithel, F. Özel, and D. Psaltis, *From Neutron Star Observables to the Equation of State. II. Bayesian Inference of Equation of State Pressures*, *Astrophys. J.* **844** (2017) 156, arXiv:1704.00737 [astro-ph.HE].

[186] G. Raaijmakers *et al.*, *Constraining the dense matter equation of state with joint analysis of NICER and LIGO/Virgo measurements*, *Astrophys. J. Lett.* **893** (2020) L21, arXiv:1912.11031 [astro-ph.HE].

[187] G. Raaijmakers *et al.*, *A NICER view of PSR J0030+0451: Implications for the dense matter equation of state*, *Astrophys. J. Lett.* **887** (2019) L22, arXiv:1912.05703 [astro-ph.HE].

[188] D. Blaschke, A. Ayriyan, D. E. Alvarez-Castillo, and H. Grigorian, *Was GW170817 a Canonical Neutron Star Merger? Bayesian Analysis with a Third Family of Compact Stars*, *Universe* **6** (2020) 81, arXiv:2005.02759 [astro-ph.HE].

[189] P. Landry and R. Essick, *Nonparametric inference of the neutron star equation of state from gravitational wave observations*, *Phys. Rev. D* **99** (2019) 084049, arXiv:1811.12529 [gr-qc].

[190] R. Essick, P. Landry, and D. E. Holz, *Nonparametric Inference of Neutron Star Composition, Equation of State, and Maximum Mass with GW170817*, *Phys. Rev. D* **101** (2020) 063007, arXiv:1910.09740 [astro-ph.HE].

[191] R. Essick, I. Tews, P. Landry, S. Reddy, and D. E. Holz, *Direct Astrophysical Tests of Chiral Effective Field Theory at Supranuclear Densities*, *Phys. Rev. C* **102** (2020) 055803, arXiv:2004.07744 [astro-ph.HE].

[192] Y. Fujimoto, K. Fukushima, and K. Murase, *Methodology study of machine learning for the neutron star equation of state*, *Phys. Rev. D* **98** (2018) 023019, arXiv:1711.06748 [nucl-th].

[193] M. Ferreira and C. Providência, *Unveiling the nuclear matter EoS from neutron star properties: a supervised machine learning approach*, *JCAP* **07** (2021) 011, arXiv:1910.05554 [nucl-th].

[194] F. Morawski and M. Bejger, *Neural network reconstruction of the dense matter equation of state derived from the parameters of neutron stars*, *Astron. Astrophys.* **642** (2020) A78, arXiv:2006.07194 [astro-ph.HE].

[195] S. Traversi and P. Char, *Structure of Quark Star: A Comparative Analysis of Bayesian Inference and Neural Network Based Modeling*, *Astrophys. J.* **905** (2020) 9, arXiv:2007.10239 [nucl-th].

[196] I. A. Akhiezer and S. V. Peletminskii, *Use of the methods of quantum field theory for the investigation of the thermodynamical properties of a gas of electrons and photons*, *Zh. Eksp. Teor. Fiz.* **38** (1960) 1829–1839.

[197] E. E. Salpeter, *Energy and Pressure of a Zero-Temperature Plasma*, *Astrophys. J.* **134** (1961) 669–682.

[198] G. Baym and S. A. Chin, *Landau Theory of Relativistic Fermi Liquids*, *Nucl. Phys. A* **262** (1976) 527–538.

[199] E. S. Fraga, R. D. Pisarski, and J. Schaffner-Bielich, *Small, dense quark stars from perturbative QCD*, *Phys. Rev. D* **63** (2001) 121702, arXiv:hep-ph/0101143.

[200] E. S. Fraga and P. Romatschke, *The Role of quark mass in cold and dense perturbative QCD*, *Phys. Rev. D* **71** (2005) 105014, arXiv:hep-ph/0412298.

[201] A. D. Linde, *Infrared Problem in Thermodynamics of the Yang-Mills Gas*, *Phys. Lett. B* **96** (1980) 289–292.

[202] L. Fernandez and J.-L. Kneur, *All order resummed leading and next-to-leading soft modes of dense QCD pressure*, arXiv:2109.02410 [hep-ph].

[203] J.-L. Kneur, M. B. Pinto, and T. E. Restrepo, *Renormalization group improved pressure for cold and dense QCD*, *Phys. Rev. D* **100** (2019) 114006, arXiv:1908.08363 [hep-ph].

[204] J. O. Andersen, E. Braaten, and M. Strickland, *Hard thermal loop resummation of the free energy of a hot gluon plasma*, *Phys. Rev. Lett.* **83** (1999) 2139–2142, arXiv:hep-ph/9902327.

[205] J. O. Andersen, E. Braaten, and M. Strickland, *Hard thermal loop resummation of the thermodynamics of a hot gluon plasma*, *Phys. Rev.* **D61** (2000) 014017, arXiv:hep-ph/9905337.

[206] J. O. Andersen, E. Braaten, and M. Strickland, *Hard thermal loop resummation of the free energy of a hot quark - gluon plasma*, *Phys. Rev. D* **61** (2000) 074016, arXiv:hep-ph/9908323.

[207] J. O. Andersen, E. Braaten, E. Petitgirard, and M. Strickland, *HTL perturbation theory to two loops*, *Phys. Rev. D* **66** (2002) 085016, arXiv:hep-ph/0205085.

[208] J. O. Andersen, E. Petitgirard, and M. Strickland, *Two loop HTL thermodynamics with quarks*, *Phys. Rev. D* **70** (2004) 045001, arXiv:hep-ph/0302069.

[209] J. O. Andersen, M. Strickland, and N. Su, *Gluon Thermodynamics at Intermediate Coupling*, *Phys. Rev. Lett.* **104** (2010) 122003, arXiv:0911.0676 [hep-ph].

[210] J. O. Andersen, M. Strickland, and N. Su, *Three-loop HTL gluon thermodynamics at intermediate coupling*, *JHEP* **08** (2010) 113, arXiv:1005.1603 [hep-ph].

[211] J. O. Andersen, L. E. Leganger, M. Strickland, and N. Su, *NNLO hard-thermal-loop thermodynamics for QCD*, *Phys. Lett. B* **696** (2011) 468–472, arXiv:1009.4644 [hep-ph].

[212] J. O. Andersen, L. E. Leganger, M. Strickland, and N. Su, *Three-loop HTL QCD thermodynamics*, *JHEP* **08** (2011) 053, arXiv:1103.2528 [hep-ph].

[213] S. Mogliacci, J. O. Andersen, M. Strickland, N. Su, and A. Vuorinen, *Equation of State of hot and dense QCD: Resummed perturbation theory confronts lattice data*, *JHEP* **12** (2013) 055, arXiv:1307.8098 [hep-ph].

[214] N. Haque, J. O. Andersen, M. G. Mustafa, M. Strickland, and N. Su, *Three-loop pressure and susceptibility at finite temperature and density from hard-thermal-loop perturbation theory*, *Phys. Rev. D* **89** (2014) 061701, arXiv:1309.3968 [hep-ph].

[215] N. Haque, A. Bandyopadhyay, J. O. Andersen, M. G. Mustafa, M. Strickland, and N. Su, *Three-loop HTLpt thermodynamics at finite temperature and chemical potential*, *JHEP* **05** (2014) 027, arXiv:1402.6907 [hep-ph].

[216] G. Baym, *Selfconsistent approximation in many body systems*, *Phys. Rev.* **127** (1962) 1391–1401.

[217] B. Vanderheyden and G. Baym, *Selfconsistent approximations in relativistic plasmas: Quasiparticle analysis of the thermodynamic properties*, *J. Statist. Phys.* **93** (1998) 843, arXiv:hep-ph/9803300.

[218] J. P. Blaizot, E. Iancu, and A. Rebhan, *The Entropy of the QCD plasma*, *Phys. Rev. Lett.* **83** (1999) 2906–2909, arXiv:hep-ph/9906340.

[219] J. P. Blaizot, E. Iancu, and A. Rebhan, *Selfconsistent hard thermal loop thermodynamics for the quark gluon plasma*, *Phys. Lett. B* **470** (1999) 181–188, arXiv:hep-ph/9910309.

[220] J. P. Blaizot, E. Iancu, and A. Rebhan, *Approximately selfconsistent resummations for the thermodynamics of the quark gluon plasma. 1. Entropy and density*, *Phys. Rev. D* **63** (2001) 065003, arXiv:hep-ph/0005003.

[221] J. P. Blaizot, E. Iancu, and A. Rebhan, *Quark number susceptibilities from HTL resummed thermodynamics*, *Phys. Lett. B* **523** (2001) 143–150, arXiv:hep-ph/0110369.

[222] A. Peshier, *HTL resummation of the thermodynamic potential*, *Phys. Rev. D* **63** (2001) 105004, arXiv:hep-ph/0011250.

[223] J. M. Luttinger and J. C. Ward, *Ground state energy of a many fermion system. 2.*, *Phys. Rev.* **118** (1960) 1417–1427.

[224] C. de Dominicis and P. C. Martin, *Stationary Entropy Principle and Renormalization in Normal and Superfluid Systems. I. Algebraic Formulation*, *J. Math. Phys.* **5** (1964) 14–30.

[225] J. M. Cornwall, R. Jackiw, and E. Tomboulis, *Effective Action for Composite Operators*, *Phys. Rev. D* **10** (1974) 2428–2445.

[226] C. Manuel, *Hard dense loops in a cold nonAbelian plasma*, *Phys. Rev. D* **53** (1996) 5866–5873, arXiv:hep-ph/9512365.

[227] R. Baier and K. Redlich, *Hard thermal loop resummed pressure of a degenerate quark gluon plasma*, *Phys. Rev. Lett.* **84** (2000) 2100–2103, arXiv:hep-ph/9908372.

[228] C. Drischler, S. Han, J. M. Lattimer, M. Prakash, S. Reddy, and T. Zhao, *Limiting masses and radii of neutron stars and their implications*, *Phys. Rev. C* **103** (2021) 045808, arXiv:2009.06441 [nucl-th].

[229] **HAL QCD** Collaboration, T. Inoue, S. Aoki, T. Doi, T. Hatsuda, Y. Ikeda, N. Ishii, K. Murano, H. Nemura, and K. Sasaki, *Equation of State for Nucleonic Matter and its Quark Mass Dependence from the Nuclear Force in Lattice QCD*, *Phys. Rev. Lett.* **111** (2013) 112503, arXiv:1307.0299 [hep-lat].

[230] M. Järvinen, *Holographic modeling of nuclear matter and neutron stars*, arXiv:2110.08281 [hep-ph].

[231] H. Hata and T. Kugo, *An Operator Formalism of Statistical Mechanics of Gauge Theory in Covariant Gauges*, *Phys. Rev. D* **21** (1980) 3333.

[232] M. Le Bellac, *Thermal Field Theory*. Cambridge Monographs on Mathematical Physics. Cambridge University Press, 1996.

[233] M. Laine and A. Vuorinen, *Basics of Thermal Field Theory*, vol. 925. Springer, 2016. arXiv:1701.01554 [hep-ph].

[234] V. V. Klimov, *Spectrum of Elementary Fermi Excitations in Quark Gluon Plasma. (In Russian)*, *Sov. J. Nucl. Phys.* **33** (1981) 934–935.

[235] V. V. Klimov, *Collective Excitations in a Hot Quark Gluon Plasma*, *Sov. Phys. JETP* **55** (1982) 199–204.

[236] H. A. Weldon, *Covariant Calculations at Finite Temperature: The Relativistic Plasma*, *Phys. Rev. D* **26** (1982) 1394.

[237] H. A. Weldon, *Effective Fermion Masses of Order gT in High Temperature Gauge Theories with Exact Chiral Invariance*, *Phys. Rev. D* **26** (1982) 2789.

[238] V. P. Silin, *On the electronmagnetic properties of a relativistic plasma*, *Sov. Phys. JETP* **11** (1960) 1136–1140.

[239] E. S. Fradkin, *Method of Green's functions in quantum field theory and quantum statistics*, *Trud. Fiz. Inst. Akad. Nauk SSSR (Fiz. Inst. Lebedev)* **29** (1965) 7–138.

[240] E. Braaten and R. D. Pisarski, *Deducing Hard Thermal Loops From Ward Identities*, *Nucl. Phys. B* **339** (1990) 310–324.

[241] J.-P. Blaizot and E. Iancu, *The Quark gluon plasma: Collective dynamics and hard thermal loops*, *Phys. Rept.* **359** (2002) 355–528, arXiv:hep-ph/0101103.

[242] J. Frenkel and J. C. Taylor, *High Temperature Limit of Thermal QCD*, *Nucl. Phys. B* **334** (1990) 199–216.

[243] J. P. Blaizot and E. Iancu, *Kinetic equations for long wavelength excitations of the quark - gluon plasma*, *Phys. Rev. Lett.* **70** (1993) 3376–3379, arXiv:hep-ph/9301236.

[244] J. P. Blaizot and E. Iancu, *Soft collective excitations in hot gauge theories*, *Nucl. Phys. B* **417** (1994) 608–673, arXiv:hep-ph/9306294.

[245] C.-x. Zhai and B. M. Kastening, *The Free energy of hot gauge theories with fermions through g**5*, *Phys. Rev. D* **52** (1995) 7232–7246, arXiv:hep-ph/9507380.

[246] E. Braaten and A. Nieto, *Free energy of QCD at high temperature*, *Phys. Rev. D* **53** (1996) 3421–3437, arXiv:hep-ph/9510408.

[247] J. C. Taylor and S. M. H. Wong, *The Effective Action of Hard Thermal Loops in QCD*, *Nucl. Phys. B* **346** (1990) 115–128.

[248] R. Efraty and V. P. Nair, *The Secret Chern-Simons action for the hot gluon plasma*, *Phys. Rev. Lett.* **68** (1992) 2891–2894, arXiv:hep-th/9201058.

[249] R. Efraty and V. P. Nair, *Chern-Simons theory and the quark - gluon plasma*, *Phys. Rev. D* **47** (1993) 5601–5614, arXiv:hep-th/9212068.

[250] A. Kurkela and A. Vuorinen, *Cool quark matter*, *Phys. Rev. Lett.* **117** (2016) 042501, arXiv:1603.00750 [hep-ph].

[251] F. Karsch, A. Patkos, and P. Petreczky, *Screened perturbation theory*, *Phys. Lett. B* **401** (1997) 69–73, arXiv:hep-ph/9702376.

[252] S. Chiku and T. Hatsuda, *Optimized perturbation theory at finite temperature*, *Phys. Rev. D* **58** (1998) 076001, arXiv:hep-ph/9803226.

[253] R. P. Feynman and H. Kleinert, *Effective Classical Partition Functions*, *Phys. Rev. A* **34** (1986) 5080–5084.

[254] N. Su, *A brief overview of hard-thermal-loop perturbation theory*, *Commun. Theor. Phys.* **57** (2012) 409, arXiv:1204.0260 [hep-ph].

[255] T. D. Lee and C. N. Yang, *Many-Body Problem in Quantum Statistical Mechanics. 4. Formulation in Terms of Average Occupation Number in Momentum Space*, *Phys. Rev.* **117** (1960) 22–36.

[256] A. Arrizabalaga and J. Smit, *Gauge fixing dependence of Phi derivable approximations*, *Phys. Rev. D* **66** (2002) 065014, arXiv:hep-ph/0207044.

[257] **Particle Data Group** Collaboration, P. A. Zyla *et al.*, *Review of Particle Physics*, *PTEP* **2020** (2020) 083C01.

[258] E. Petitgirard, *Massive fermion dispersion relation at finite temperature*, *Z. Phys. C* **54** (1992) 673–678.

[259] G. Baym, J.-P. Blaizot, and B. Svetitsky, *Emergence of new quasiparticles in quantum electrodynamics at finite temperature*, *Phys. Rev. D* **46** (1992) 4043–4051.

[260] J.-P. Blaizot and J.-Y. Ollitrault, *Collective fermionic excitations in systems with a large chemical potential*, *Phys. Rev. D* **48** (1993) 1390–1408, arXiv:hep-th/9303070.

[261] C. Quimbay and S. Vargas-Castrillon, *Fermionic dispersion relations in the standard model at finite temperature*, *Nucl. Phys. B* **451** (1995) 265–304, arXiv:hep-ph/9504410.

[262] M. Comadran and C. Manuel, *Mass corrections to the hard thermal or dense loops*, *Phys. Rev. D* **104** (2021) 076006, arXiv:2106.08904 [hep-ph].

[263] E. Braaten, *Effective field theory for plasmas at all temperatures and densities*, *Can. J. Phys.* **71** (1993) 215–218, arXiv:hep-ph/9303261.

[264] A. Chodos, R. L. Jaffe, K. Johnson, C. B. Thorn, and V. F. Weisskopf, *A New Extended Model of Hadrons*, *Phys. Rev. D* **9** (1974) 3471–3495.

[265] T. A. DeGrand, R. L. Jaffe, K. Johnson, and J. E. Kiskis, *Masses and Other Parameters of the Light Hadrons*, *Phys. Rev. D* **12** (1975) 2060.

[266] T. Kojo, *QCD equations of state and speed of sound in neutron stars*, *AAPPS Bull.* **31** (2021) 11, arXiv:2011.10940 [nucl-th].

[267] J.-E. Christian and J. Schaffner-Bielich, *Twin Stars and the Stiffness of the Nuclear Equation of State: Ruling Out Strong Phase Transitions below* $1.7n_0$ *with the New NICER Radius Measurements*, *Astrophys. J. Lett.* **894** (2020) L8, arXiv:1912.09809 [astro-ph.HE].

[268] C. Drischler, S. Han, and S. Reddy, *Large and massive neutron stars: Implications for the sound speed in dense QCD*, arXiv:2110.14896 [nucl-th].

[269] L. McLerran and S. Reddy, *Quarkyonic Matter and Neutron Stars*, *Phys. Rev. Lett.* **122** (2019) 122701, arXiv:1811.12503 [nucl-th].

[270] M. Hippert, E. S. Fraga, and J. Noronha, *Insights on the peak in the speed of sound of ultradense matter*, *Phys. Rev. D* **104** (2021) 034011, arXiv:2105.04535 [nucl-th].

[271] T. Kojo, *Stiffening of matter in quark-hadron continuity*, *Phys. Rev. D* **104** (2021) 074005, arXiv:2106.06687 [nucl-th].

[272] E. Annala, T. Gorda, A. Kurkela, J. Nättilä, and A. Vuorinen, *Evidence for quark-matter cores in massive neutron stars*, *Nature Phys.* **16** (2020) 907–910, arXiv:1903.09121 [astro-ph.HE].

[273] E. Annala, T. Gorda, A. Kurkela, J. Nättilä, and A. Vuorinen, *Constraining the properties of neutron-star matter with observations*, *Mem. Soc. Ast. It.* **90** (2019) 81–86, arXiv:1904.01354 [astro-ph.HE].

[274] G. Baym, T. Hatsuda, T. Kojo, P. D. Powell, Y. Song, and T. Takatsuka, *From hadrons to quarks in neutron stars: a review*, *Rept. Prog. Phys.* **81** (2018) 056902, arXiv:1707.04966 [astro-ph.HE].

[275] M. Alford, M. Braby, M. W. Paris, and S. Reddy, *Hybrid stars that masquerade as neutron stars*, *Astrophys. J.* **629** (2005) 969–978, arXiv:nucl-th/0411016.

[276] U. Vogl and W. Weise, *The Nambu and Jona Lasinio model: Its implications for hadrons and nuclei*, *Prog. Part. Nucl. Phys.* **27** (1991) 195–272.

[277] T. Hatsuda and T. Kunihiro, *QCD phenomenology based on a chiral effective Lagrangian*, *Phys. Rept.* **247** (1994) 221–367, arXiv:hep-ph/9401310.

[278] M. Buballa, *NJL model analysis of quark matter at large density*, *Phys. Rept.* **407** (2005) 205–376, arXiv:hep-ph/0402234.

[279] N. K. Glendenning, *First order phase transitions with more than one conserved charge: Consequences for neutron stars*, *Phys. Rev. D* **46** (1992) 1274–1287.

[280] K. Masuda, T. Hatsuda, and T. Takatsuka, *Hadron-Quark Crossover and Massive Hybrid Stars with Strangeness*, *Astrophys. J.* **764** (2013) 12, arXiv:1205.3621 [nucl-th].

[281] K. Masuda, T. Hatsuda, and T. Takatsuka, *Hadron–quark crossover and massive hybrid stars*, *PTEP* **2013** (2013) 073D01, arXiv:1212.6803 [nucl-th].

[282] T. Kojo, P. D. Powell, Y. Song, and G. Baym, *Phenomenological QCD equation of state for massive neutron stars*, *Phys. Rev. D* **91** (2015) 045003, arXiv:1412.1108 [hep-ph].

[283] T. Kojo, *Phenomenological neutron star equations of state: 3-window modeling of QCD matter*, *Eur. Phys. J. A* **52** (2016) 51, arXiv:1508.04408 [hep-ph].

[284] G. Baym, S. Furusawa, T. Hatsuda, T. Kojo, and H. Togashi, *New Neutron Star Equation of State with Quark-Hadron Crossover*, *Astrophys. J.* **885** (2019) 42, arXiv:1903.08963 [astro-ph.HE].

[285] T. Kojo, G. Baym, and T. Hatsuda, *QHC21 equation of state of neutron star matter - in light of 2021 NICER data*, arXiv:2111.11919 [astro-ph.HE].

[286] T. Schäfer and F. Wilczek, *Continuity of quark and hadron matter*, *Phys. Rev. Lett.* **82** (1999) 3956–3959, arXiv:hep-ph/9811473.

[287] M. G. Alford, G. Baym, K. Fukushima, T. Hatsuda, and M. Tachibana, *Continuity of vortices from the hadronic to the color-flavor locked phase in dense matter*, *Phys. Rev. D* **99** (2019) 036004, arXiv:1803.05115 [hep-ph].

[288] C. Chatterjee, M. Nitta, and S. Yasui, *Quark-hadron continuity under rotation: Vortex continuity or boojum?*, *Phys. Rev. D* **99** (2019) 034001, arXiv:1806.09291 [hep-ph].

[289] A. Cherman, S. Sen, and L. G. Yaffe, *Anyonic particle-vortex statistics and the nature of dense quark matter*, *Phys. Rev. D* **100** (2019) 034015, arXiv:1808.04827 [hep-th].

[290] Y. Hirono and Y. Tanizaki, *Quark-Hadron Continuity beyond the Ginzburg-Landau Paradigm*, *Phys. Rev. Lett.* **122** (2019) 212001, arXiv:1811.10608 [hep-th].

[291] Y. Fujimoto, K. Fukushima, and W. Weise, *Continuity from neutron matter to two-flavor quark matter with ${}^1S_0$ and ${}^3P_2$ superfluidity*, *Phys. Rev. D* **101** (2020) 094009, arXiv:1908.09360 [hep-ph].

[292] Y. Fujimoto, *Continuity from neutron matter to color-superconducting quark matter with ${}^3P_2$ superfluidity*, *Nucl. Phys. A* **1005** (2021) 121757, arXiv:2002.08073 [hep-ph].

[293] K. S. Jeong, L. McLerran, and S. Sen, *Dynamically generated momentum space shell structure of quarkyonic matter via an excluded volume model*, *Phys. Rev. C* **101** (2020) 035201, arXiv:1908.04799 [nucl-th].

[294] D. C. Duarte, S. Hernandez-Ortiz, and K. S. Jeong, *Excluded-volume model for quarkyonic Matter: Three-flavor baryon-quark Mixture*, *Phys. Rev. C* **102** (2020) 025203, arXiv:2003.02362 [nucl-th].

[295] T. Zhao and J. M. Lattimer, *Quarkyonic Matter Equation of State in Beta-Equilibrium*, *Phys. Rev. D* **102** (2020) 023021, arXiv:2004.08293 [astro-ph.HE].

[296] G. Cao and J. Liao, *A field theoretical model for quarkyonic matter*, *JHEP* **10** (2020) 168, arXiv:2007.02028 [nucl-th].

[297] K. Fukushima, T. Kojo, and W. Weise, *Hard-core deconfinement and soft-surface delocalization from nuclear to quark matter*, *Phys. Rev. D* **102** (2020) 096017, arXiv:2008.08436 [hep-ph].

[298] Y.-L. Ma and M. Rho, *Towards the hadron–quark continuity via a topology change in compact stars*, *Prog. Part. Nucl. Phys.* **113** (2020) 103791, arXiv:1909.05889 [nucl-th].

[299] M. Hoffberg, A. E. Glassgold, R. W. Richardson, and M. Ruderman, *Anisotropic Superfluidity in Neutron Star Matter*, *Phys. Rev. Lett.* **24** (1970) 775.

[300] R. Tamagaki, *Superfluid State in Neutron Star Matter. I. Generalized Bogoliubov Transformation and Existence of $^3P_2$ Gap at High Density*, *Prog. Theor. Phys.* **44** (1970) 905–928.

[301] E. H. Fradkin and S. H. Shenker, *Phase Diagrams of Lattice Gauge Theories with Higgs Fields*, *Phys. Rev.* **D19** (1979) 3682–3697.

[302] S. Elitzur, *Impossibility of Spontaneously Breaking Local Symmetries*, *Phys. Rev. D* **12** (1975) 3978–3982.

[303] K. Rajagopal and F. Wilczek, *The Condensed matter physics of QCD*, pp. 2061–2151. 11, 2000. arXiv:hep-ph/0011333.

[304] Y. Fujimoto and M. Nitta, *Non-Abelian Alice strings in two-flavor dense QCD*, *Phys. Rev. D* **103** (2021) 054002, arXiv:2011.09947 [hep-ph].

[305] Y. Fujimoto and M. Nitta, *Vortices penetrating two-flavor quark-hadron continuity*, *Phys. Rev. D* **103** (2021) 114003, arXiv:2102.12928 [hep-ph].

[306] Y. Fujimoto and M. Nitta, *Topological confinement of vortices in two-flavor dense QCD*, *JHEP* **09** (2021) 192, arXiv:2103.15185 [hep-ph].

[307] T. Hinderer, *Tidal Love numbers of neutron stars*, *Astrophys. J.* **677** (2008) 1216–1220, arXiv:0711.2420 [astro-ph].

[308] T. Hinderer, B. D. Lackey, R. N. Lang, and J. S. Read, *Tidal deformability of neutron stars with realistic equations of state and their gravitational wave signatures in binary inspiral*, *Phys. Rev. D* **81** (2010) 123016, arXiv:0911.3535 [astro-ph.HE].

[309] J. S. Read, B. D. Lackey, B. J. Owen, and J. L. Friedman, *Constraints on a phenomenologically parameterized neutron-star equation of state*, *Phys. Rev. D* **79** (2009) 124032, arXiv:0812.2163 [astro-ph].

[310] M. F. O'Boyle, C. Markakis, N. Stergioulas, and J. S. Read, *Parametrized equation of state for neutron star matter with continuous sound speed*, *Phys. Rev. D* **102** (2020) 083027, arXiv:2008.03342 [astro-ph.HE].

[311] A. Kurkela, E. S. Fraga, J. Schaffner-Bielich, and A. Vuorinen, *Constraining neutron star matter with Quantum Chromodynamics*, *Astrophys. J.* **789** (2014) 127, arXiv:1402.6618 [astro-ph.HE].

[312] E. Annala, T. Gorda, A. Kurkela, and A. Vuorinen, *Gravitational-wave constraints on the neutron-star-matter Equation of State*, *Phys. Rev. Lett.* **120** (2018) 172703, arXiv:1711.02644 [astro-ph.HE].

[313] E. Annala, T. Gorda, E. Katerini, A. Kurkela, J. Nättilä, V. Paschalidis, and A. Vuorinen, *Multimessenger constraints for ultra-dense matter*, arXiv:2105.05132 [astro-ph.HE].

[314] O. Komoltsev and A. Kurkela, *How perturbative QCD constrains the Equation of State at Neutron-Star densities*, arXiv:2111.05350 [nucl-th].

[315] X.-G. Wu, S. J. Brodsky, and M. Mojaza, *The Renormalization Scale-Setting Problem in QCD*, *Prog. Part. Nucl. Phys.* **72** (2013) 44–98, arXiv:1302.0599 [hep-ph].

[316] D. T. Son, *Superconductivity by long range color magnetic interaction in high density quark matter*, *Phys. Rev. D* **59** (1999) 094019, arXiv:hep-ph/9812287.

[317] A. Bzdak, S. Esumi, V. Koch, J. Liao, M. Stephanov, and N. Xu, *Mapping the Phases of Quantum Chromodynamics with Beam Energy Scan*, *Phys. Rept.* **853** (2020) 1–87, arXiv:1906.00936 [nucl-th].

[318] A. R. Bodmer, *Collapsed nuclei*, *Phys. Rev. D* **4** (1971) 1601–1606.

[319] E. Witten, *Cosmic Separation of Phases*, *Phys. Rev. D* **30** (1984) 272–285.

[320] E. Farhi and R. L. Jaffe, *Strange Matter*, *Phys. Rev. D* **30** (1984) 2379.

[321] V. A. Novikov, M. A. Shifman, A. I. Vainshtein, and V. I. Zakharov, *Are All Hadrons Alike?* , *Nucl. Phys. B* **191** (1981) 301–369.

[322] J. Steinheimer, M. Mitrovski, T. Schuster, H. Petersen, M. Bleicher, and H. Stoecker, *Strangeness fluctuations and MEMO production at FAIR*, *Phys. Lett. B* **676** (2009) 126–131, arXiv:0811.4077 [hep-ph].